Real-time studies of DNA repair kinetics following low-LET short-pulse electron radiation



A thesis presented for the degree of Doctor of Philosophy

By

Carlos Daniel Martins

Supervisors:
Professor Peter O'Neill
Professor Borivoj Vojnovic

Jesus College
CR-UK/MRC Oxford Institute for Radiation Oncology,
Department of Oncology,
University of Oxford

Trinity Term 2014





Dedication

Para a minha mãe que sempre foi a fonte da minha força, e para
o meu pai que sempre me apoiou e acreditou em mim.

To my mother who is my strength, and my father who
always believed in me and supported me.

Acknowledgements

First of all I would like to thank Cancer Research UK and the Medical Research Council for funding this project. A big thanks to both my supervisors, Professor Peter O'Neill and Professor Boris Vojnovic, two of the most if not the smartest people I have met in my life. Thank you for giving me the opportunity to be part of such a multidisciplinary and challenging project. I will never forget all the help and support, and the trust you put in me to be a part of this project. I would like to thank all the former members of the DNA Damage group, in particular Jennifer Anderson and Pamela Reynolds who taught me most of the biological techniques I have acquired throughout my PhD. I would also like to thank Lisa, Sarah, Martine, Luca, Ela, Laura and all the others for being such great colleagues to work with. In particular I would like to leave a thank you of approximately my shoe size to Siobhan Cunniffe. More than a colleague you are a dear friend, you are family, and you made my time during this degree far more enjoyable than I could have hoped for. This is just the beginning my friend ☺.

I would also like to thank all the members of the Advanced Technology Development group, a big thanks to Linda, also to Iain for all the patience and help in every step of the project. You are too smart for your own good ☺, to Paul Barber for support and an incredible help with the development, to Rob for simply making it all work you are a star ☺. I would also like to leave a thank you to Anthony for helping me, and for the good times as well, to Roger Nathan for getting me into Monte-Carlo, to Davide for being such a great help and an amazing fellow student. I would like to say a big thank you to Stuart Gilchrist who was a tremendous help with the linac, and the robot, and for the great chats as well. I could not go without thanking the workshop personnel, Gerry who built too much stuff for me, who is an amazing person and always has a nice word to say to you. To John Prentice what can I say, my friend you, like Siobhan were the great discoveries during this PhD, and I am truly blessed for having met you. Thank you for all the patience and for building so much stuff for me, and for all the great times we spent together. More fun ahead ☺.

I would also like to thank former members of the institute such as Jose, Rita, Maria, Isabel Garth, Guy, Becky, Steven, Simon, Lydia, amongst many others, and thank you so much for the enjoyable times. I would also like to thank current members of the institute such as Sarah, Martin, Blaz and the rest of the Kilties, Angelos, Nikola and the O'Neills, Cindy, Joana, Kasia, Stefan and the Hammonds. Thank you to Irina, Arnaud, Mattia, Enni and Svetlana. I would like to thank Andy Ryan and Anika Weber for all the help in generating my beautiful Geminin-mCherry cell line, and for so many other pieces of advice. Thank you to Mark Hill, Jamie, Graeme, and Luke for all the help and advice. Thank you to Sarah Norman, Eric O'Neill, Niki Sibson, Ester and Tim Humphrey for all the help and advice.

To the MSc crowd, thanks so much to Mark and Stav for being such great friends. A big big thank you to Emma for being such a great friend, and for being so understanding.

To the Jeune street family obviously I would like to thank Monica for all the good times and conversations. I would like to give a big thank you to my great friend Torben for all the fun times during our time together in Oxford. A lot more fun to come my friend. To my

brother Selva, for being there for me in every single moment of this journey, with either a hug, a plate of food, an apple or simply a kind word to make me feel better. You are one of the most amazing people I have ever had the pleasure to meet and I hope to have the opportunity to prolong this friendship for the rest of my life.
To the Bartlemas road crowd, I would like to thank Aswin, Iosifina and Sofia (who now brushes her teeth with parma ham) for all the fun times and for accepting me into your home.
A big thank you to the Portuguese crowd, Henrique, Patricia, Bruno and Carina, for all the help and support, and for the great times we have spent together, hopefully with many more to come.
Thank you to Hans Zimmer for the Dark Knight Trilogy soundtrack which inspired me during the writing process.
I have no words to thank Giulia for all the patience, care, love, support, and help that you have given me. This journey would not have been the same without you, and if I am where I am and if I have a future to look forward to I owe it to you. This is just the beginning of a beautiful journey ahead of us. You were my rock, my strength, and my motivation to overcome the difficulties I faced during this time. For all of this I can never thank you enough. From the bottom of my heart thank you ☺
Hugo meu irmao, obrigado pela paciencia e por todo o apoio. Para todos os meus amigos impecaveis pelos bons momentos e pelo apoio que me deram durante este doutoramento. Quero agradecer ao meu irmao Nelinho, e irmas Tininha e Licinha por terem tanta paciencia comigo devido a minha constante ausencia. Eu prometo que farei por estar mais presente no futuro. Obrigado pelo vosso apoio e compreensao.
Nao posso deixar de agradecer a minha mae por me ter dado a forca necessaria para embarcar nesta viagem, e espero que todos os sacrificios tenham valido a pena e que contribuam para um futuro mais risonho. Um tremendo obrigado para o meu pai sem quem teria sido impossivel chegar aqui. Peco desculpa por nao ligar mais vezes e nao estar mais presente, mas espero que de futuro eu tenha uma vida menos complexa e que isso me permita que nos vejamos bem mais frequentemente. O meu muito obrigado por todo o seu apoio, carinho e compreensao, e devido a si e a mae que aqui cheguei, e disso nunca me esquecerei.

To all of you my sincere THANK YOU! OBRIGADO!

Abstract

Carlos Daniel Martins Doctor of Philosophy
Jesus College, Trinity Term 2014 University of Oxford

Real-time studies of DNA repair kinetics following low-LET short-pulse electron radiation

Radiation-induced damage to the genomic DNA of cells may lead to errors in transcription and replication and, if not repaired correctly, these may result in mutations, genomic instability and cell death. Laser microbeams have generally been used by many research groups to investigate the real-time dynamics of protein recruitment in response to DNA insults in mammalian cells; however, such irradiations induce a plethora of DNA damage (including UV base damage, base damage, SSBs and DSBs and complex damage). A novel experimental setup has been designed capable of following the dynamics of protein recruitment in response to DNA insults in mammalian cells shortly following sub-microsecond-pulsed electron irradiation of living mammalian cells, not possible using conventional irradiation techniques. This arrangement was developed based on a 6 MeV electron pulse linear accelerator, to deliver sparsely ionising radiation, coupled to an automated, time-lapse inverted epifluorescence microscope imaging system. An integrated robotic system contained within a physiological environment of 37°C and 5% CO_2 was used to transfer remotely and repetitively custom-designed cell dishes containing the mammalian cells between irradiation and imaging locations.

Following the development of the linear accelerator and associated imaging devices, preliminary 'proof-of-principle' investigations were carried out using living HT1080 mammalian cells containing YFP-tagged 53BP1, an established biomarker of DSB, to follow the recruitment and loss of 53BP1 to sites of radiation-induced DNA damage in real-time. This novel experimental setup has allowed for the first time observations of the appearance and disappearance of radiation-induced foci in the same cell population at very early times. These single-foci studies have provided evidence for the formation of not only promptly formed DSBs but also late appearing DNA damage signalled by 53BP1. These data highlight different classes of DSBs formed in response radiation damage.

Additionally, the role of cell cycle on the repair kinetics was undertaken using HT1080-53BP1-YFP cells which also express Geminin-mCherry under appropriate selection. Geminin is increasingly expressed from early S-phase onwards, but is degraded following mitosis. Geminin-associated fluorescence can be used as a marker of progression through the cell cycle. 53BP1 repair kinetics were characterised in response to radiation damage in combination with ATM and PARP inhibitors. These studies provided supporting evidence for the existence of different classes of DSBs, potentially assigned to radiation-induced replication breaks and DSBs formed by enzymatic conversion of clustered damage.

These preliminary 'proof-of-principle' findings using DNA damage repair as an example, emphasize the use of this novel technology to explore the dynamics of numerous other biochemical processes in living cells in real-time with the knowledge of being able to quantify the range of damage induced by IR coupled with accurate dosimetry. The knowledge obtained may be used to identify potential biological targets coupled with drug discovery for translation into adjuncts for radiotherapy.

Table of contents

Dedication ..... **I**

Acknowledgements ..... **II**

Abstract ..... **IV**

Table of contents ..... **V**

List of figures ..... **X**

List of tables ..... **XIV**

List of abbreviations ..... **XV**

1. Introduction **1**

1.1 Genome instability and cancer development 1

1.2 DNA damage 3

1.2.1 DNA lesions 7
1.2.2 DNA damaging agents 8
1.2.2.1 Ionising radiation (IR) 8
1.2.2.2 Ultraviolet (UV) radiation 11
1.3 Spatiotemporal observation of DNA repair 14

1.3.1 Live cell imaging following laser microbeam irradiation 15
1.3.2 Repair of heavy ion-induced DNA lesions 18
1.3.3 Recruitment of DNA repair factors to USXR-induced damage 19
1.3.4 DNA repair kinetics observations following immunostaining 20
1.3.5 Rationale for DNA repair kinetics studies using the linac experiment system 21
1.4 Mechanisms of repair of base lesions and SSB 22

1.4.1 Single-strand break repair (SSBR) pathway 23
1.4.2 Base excision repair (BER) pathway 24
1.4.3 PARP-1 role in maintaining genomic integrity 25
1.5 Mechanisms of DSB repair 28

1.5.1 Homologous recombination (HR) repair pathway 29
1.5.1.1 HR role in cancer development and treatment 34
1.5.2 Classical non-homologous end-joining (NHEJ) repair pathway 36
1.5.2.1 Microhomology-mediated end-joining (MMEJ) 40

1.5.2.2 Clinical impact of NHEJ deficiencies 41
1.6 DNA damage response (DDR) 44

1.6.1 DNA damage sensing 45
1.6.2 DDR signal transduction 47
1.6.2.1 DNA DSB recognition by ATM 48
1.6.2.1.1 Mediators: DNA damage foci 48

1.6.2.1.2 53BP1-BRCA1 regulation of DSB repair 50

1.6.2.2 ATR activation by DNA damage and replication stress 51
1.6.3 Interplay between ATM and ATR 53
1.7 Aims of the study 54

2. Linac experiment system 56

2.1 Introduction 56

2.2 Linear accelerator 56

2.3 Cell dishes and sample holder 59

2.4 Irradiation setup 61

2.5 Epifluorescence imaging system 63

2.6 Automated sample transfer unit 66

2.7 Čerenkov dose monitor 67

2.8 Environmental enclosure 70

2.9 Discussion 73

3. Validation of the experimental setup 76

3.1 Introduction 76

3.2 Results 77

3.2.1 Sample repositioning following automated sample transfer 77
3.2.2 Cell detachment and damage formation monitoring due to automated sample transfer 78
3.2.3 Sample irradiation optimisation 80
3.2.3.1 HD810 Gafchromic film dosimetry 82
3.2.3.2 Scattering foil 83
3.2.3.3 Monte-Carlo simulations validation 85
3.2.3.4 Beam collimation determination 89
3.2.3.5 Biological validation of beam collimation 90
3.2.4 Dosimetry 94

3.2.4.1 Thermoluminescent dosimetry (TLD) 94
3.2.4.2 Fricke dosimetry 99
3.2.4.3 Čerenkov dose monitor calibration 100
3.2.4.4 53BP1 dose response 100
3.3 Discussion 103

4. Biological materials & methods 107

4.1 Cell lines and cell culture reagents 107

4.1.1 Antibiotics, inhibitors and other reagents 107
4.2 Dishes for cell culture of mammalian cells 107

4.2.1 Cell line maintenance and sub-culture 109
4.2.2 Storage of mammalian cells in liquid nitrogen 110
4.3 Sub-cloning, amplification and purification of plasmid DNA 110

4.3.1 Sub-cloning of plasmid DNA 111
4.3.2 Amplification and purification of plasmid DNA 114
4.4 Stable transfection of mammalian cells with plasmid DNA 116

4.5 Irradiation of exponentially growing mammalian cells 118

4.6 Immunocytochemistry for protein and DNA labelling with fluorescent molecules. 118

4.6.1 53BP1, γ-H2AX and Cyclin A labelling 119
4.6.2 RAD51 labelling 119
4.6.3 EdU labelling 121
4.7 Western blotting 122

4.7.1 Western blotting reagents 122
4.7.1.1 Lysis buffer 122
4.7.1.2 Laemmli buffer (2X) 122
4.7.1.3 Tris-Glycine-SDS running buffer (10X) 122
4.7.1.4 Tris-Glycine transfer buffer (10X) 122
4.7.2 Sample preparation 122
4.7.3 Electrophoresis 123
4.7.4 Western blotting 124
4.7.5 Blocking and antibody probing 124
4.7.6 ECL detection and X-ray imaging 125
4.7.7 Near-infrared imaging of membranes 126
4.8 Fluorescence activated cell sorting (FACS)-cell cycle analysis 126

4.8.1 BrdU incorporation/7-Aminoactinomycin D (7-AAD) staining 126
4.8.2 FACS analysis 128
4.9 Clonogenic survival assay 129

4.10 Scratch-wound assay 131

4.11 Cell proliferation assay 133

4.12 Fluorescence microscopy 133

4.12.1 Imaging of γ-H2AX/RAD51 and 53BP1 labelled samples 134
4.12.2 Imaging of Cyclin A/EdU labelled samples 134
4.12.3 Image analysis 134
4.13 Statistical analysis 137

5. Dynamics of 53BP1-YFP recruitment to DNA damage sites at the single focus level 138

5.1 Introduction 138

5.2 Results 140

5.2.1 Optimisation of image processing 140
5.2.2 Stability of YFP to light exposure 141
5.2.3 Cell mobility minimisation: Src-inhibition 142
5.2.3.1 Saracatinib inhibitory effect 145
5.2.3.2 Saracatinib effect on cell migration 146
5.2.3.3 Saracatinib effect on cell proliferation 149
5.2.3.4 Saracatinib effect on 53BP1 recruitment to sites of damage following irradiation 149
5.2.4 53BP1-YFP recruitment kinetics to radiation-induced DNA damage in real-time 155
5.2.5 53BP1 single-foci mapping to sites of damage in individual cells following irradiation 157
5.3 Discussion 159

6. Specificity of DNA repair kinetics on phase of the cell cycle 168

6.1 Introduction 168

6.2 Results 172

6.2.1 HT1080-53BP1-YFP-Geminin-mCherry cell line establishment 172
6.2.1.1 Impact of Geminin-mCherry on cell cycle progression 172
6.2.1.2 S-phase duration measurements: BrdU incorporation 173
6.2.1.3 Geminin co-localisation with S/G2/M marker: Cyclin A 174
6.2.1.4 Cell cycle profile determination using EdU and Geminin-mCherry 174
6.2.1.5 Radiation resistance: clonogenic cell survival 176
6.2.2 53BP1-YFP recruitment kinetics following irradiation: G1 vs. S/G2 180
6.2.3 Dependence of 53BP1 kinetics at sites of radiation-induced DNA damage in response to DNA-PKcs inhibition 181
6.2.3.1 Dependence of 53BP1 kinetics at sites of DNA damage in response to DNA-PKcs inhibition: effects of cell cycle 186
6.2.4 ATM kinase activity inhibition results in 53BP1 foci formation delay 190
6.2.4.1 ATM kinase inhibition: effects of cell cycle 194
6.2.5 PARP inhibition induces collapsed replication forks 195
6.3 Discussion 202

6.3.1 53BP1-YFP recruitment kinetics following irradiation: effects of cell cycle .. 202
6.3.2 DNA-PKcs inhibition leads to compromised repair efficiency 209
6.3.3 ATM kinase activity inhibition impairs 53BP1 recruitment to prompt radiation-induced DSBs 212
6.3.4 PARP inhibition leads to damage accumulation in S/G2 cells 213
6.3.5 Summary 215

7. General discussion 222

7.1 Single-foci studies as a qualitative measure of DNA DSBs 223

7.2 Radiation-induced ATM to ATR switch? 224

7.3 Future work 226

References 228

Appendix 256

A1 Photon budget calculations 256

A1.1 Excitation intensity 256
A1.2 Imaging collection efficiency and microscope losses 256
A1.3 Imager quantum efficiency and conversion factors 257
A1.4 Fluorescence yields 257
A2 TRI2 automated foci analysis 259

A3 List of publications 260

List of figures

1. Introduction 1

Figure 1.1 Schematic depicting the hallmarks of cancer as proposed by Hanahan and Weinberg 4

Figure 1.2 Classes of DSBs caused by radiation-induced DNA damage 6

Figure 1.3 Schematic depicting effects of increasing LET radiation leading to DSB and non-DSB lesions induced to DNA 13

Figure 1.4 Repair of single-strand break (SSB) lesions 26

Figure 1.5 DSB repair via homologous recombination (HR) 35

Figure 1.6 DSB repair via non-homologous end-joining (NHEJ) 42

Figure 1.7 DNA damage response (DDR) signalling pathway 46

2. Linac experiment system 56

Figure 2.1 Linear accelerator 58

Figure 2.2 Sample dish, sample holder and stage inserts 62

Figure 2.3 Irradiation setup 64

Figure 2.4 Epifluorescence imaging system 68

Figure 2.5 Automated sample transfer unit 69

Figure 2.6 Čerenkov dose monitor 71

Figure 2.7 Linac experiment system environmental enclosure 74

Figure 2.8 Environmental enclosure temperature and CO_2 monitoring 75

3. Validation of the experimental setup 76

Figure 3.1 Kinematic sample repositioning accuracy 79

Figure 3.2 Sample handling control tests using live HT1080-53BP1-YFP cells 81

Figure 3.3 Diagram representing the model used in Fluka for Monte-Carlo simulations 84

Figure 3.4 Scattering foil effect on beam homogeneity 86

Figure 3.5 Relative dose percentage dependence on scattering foil thickness 88

Figure 3.6 Dose distribution comparison between film irradiation and Monte-Carlo simulations using a 4 mm diameter spot beam 92

Figure 3.7 Collimator height determination by Monte-Carlo and film dosimetry 93

Figure 3.8 Biological validation of Monte-Carlo simulations using HT1080-53BP1-YFP cells 96

Figure 3.9 TLD calibration curves 97

Figure 3.10 Linear accelerator dosimetry using TLD chips 98

Figure 3.11 Comparison between Fricke and TLD dosimetry 101

Figure 3.12 Calibration of Čerenkov monitor photodiode output against TLD dose 102

Figure 3.13 Dose response comparison between ^{137}Cs gamma-source and linear accelerator 104

4. Biological materials & methods 107

Figure 4.1 Generation of pRetroX-SG2M-Geminin-mCherry-Puro 113

Figure 4.2 Cell cycle analyses by flow cytometry using ModFit, and FlowJo 130

Figure 4.3 Scratch-wound assay description and analysis 135

Figure 4.4 Cell proliferation assay analysis 136

5. Dynamics of 53BP1-YFP recruitment to DNA damage sites at the single focus level 138

Figure 5.1 Image processing: blind deconvolution 143

Figure 5.2 Image processing: cell segmentation and registration 144

Figure 5.3 53BP1-YFP photobleaching kinetics 147

Figure 5.4 Saracatinib concentration titration 148

Figure 5.5 Scratch-wound assay in response to Saracatinib treatment 150

Figure 5.6 Saracatinib-induced reduction in cell motility 151

Figure 5.7 Proliferation assay in response to Saracatinib treatment 153

Figure 5.8 The effect of Saracatinib on cell proliferation 154

Figure 5.9 Saracatinib effect on 53BP1 following IR treatment 156

Figure 5.10 53BP1-YFP kinetics in response to 0.5 Gy 160

Figure 5.11 53BP1 single-foci mapping following irradiation 161

Figure 5.12 53BP1 single-foci mapping following irradiation (selected foci from figure 5.11) 166

Figure 5.13 DSB repair kinetics following radiation treatment 167

6. Specificity of DNA repair kinetics on phase of the cell cycle 168

Figure 6.1 Geminin-mCherry expression throughout the cell cycle 175

Figure 6.2 Cell cycle profile comparison between 53BP1-YFP and Geminin-mCherry cells 177

Figure 6.3 S-phase duration and 53BP1/Geminin expression levels 178

Figure 6.4 Geminin co-localisation with Cyclin A 179

Figure 6.5 Cell cycle profile determination via immunofluorescence and flow cytometry 182

Figure 6.6 Radiation resistance determination of HT1080-*wt*, 53BP1-YFP, and Geminin-mCherry cells 183

Figure 6.7 Cell cycle phase-specific 53BP1-YFP kinetics in response to radiation 185

Figure 6.8 DNA-PKcsi titration and time course in response to radiation treatment 188

Figure 6.9 53BP1-YFP kinetics in response to 0.5 Gy in combination with DNA-PKcsi 189

Figure 6.10 DNA-PKcsi induces 53BP1 foci persistence following radiation damage 191

Figure 6.11 DNA-PKcsi induces γ-H2AX foci persistence following radiation damage 192

Figure 6.12 ATMi titration and time course in response to radiation treatment 196

Figure 6.13 53BP1-YFP kinetics in response to 0.5 Gy in combination with ATMi.... 197

Figure 6.14 ATMi results in 53BP1 foci formation delay in response to radiation treatment 198

Figure 6.15 PARPi concentration titration 203

Figure 6.16 PARPi leads to increased levels of 53BP1 foci in S/G2 cells 204

Figure 6.17 PARPi leads to increased levels of 53BP1 foci in S/G2 cells 205

Figure 6.18 PARPi leads to p53BP1-S1778 accumulation following radiation damage 206

Figure 6.19 PARPi induces RAD51 foci in S/G2 cells following radiation damage 207

Figure 6.20 Different classes of DSBs caused by radiation-induced DNA damage 217

Figure 6.21 DNA damage response in G1 and S/G2 cells following radiation treatment in combination with ATMi, DNA-PKcsi, and PARPi..... 219

Figure 6.22 53BP1 single-foci mapping following irradiation: effects of cell cycle 220

Figure 6.23 Proposed model for the signalling and repair of different types of DSBs that can arise with radiation damage 221

Appendix 256

Figure A2.1 Comparison between manual and automated γ-H2AX foci count 259

List of tables

1. Introduction 1

Table 1.1 Cancer predispositions associated with DNA damage response defects 5

4. Biological materials & methods 107

Table 4.1 Reagents used in conjunction with cell culture based experiments 108

Table 4.2 Gamma Service GSR D1 irradiator dose rates 120

Table 4.3 Details of the antibodies used for western blotting. 127

Table 4.4 Seeding densities per radiation dose used in the clonogenic survival assay.. 132

List of abbreviations

µM	Micromolar
53BP1	P53 binding protein 1
9-1-1	RAD9-HUS1-RAD1
ADU	Analogue to digital unit
A-NHEJ	Alternative-NHEJ
AP	Apurinic or apyrimidinic
APE1	AP endonuclease 1
APLF	Aprataxin and PNKP-like factor
A-T	Ataxia telangiectasia
ATM	Ataxia telangiectasia mutated
ATMi	ATM inhibitor
ATR	Ataxia telangiectasia and RAD3-related
ATRIP	ATR-interacting protein
BER	Base excision repair
BIR	Break-induced replication
BLM	Bloom
B-NHEJ	Backup-NHEJ
BRCA1/2	Breast and ovarian cancer susceptibility protein 1/2
BrdU	Bromodeoxyuridine
BSA	Bovine serum albumin
CCD	Charge-coupled device
CDK	Cyclin-dependent kinase
CML	Chronic myelogenous leukaemia
CtIP	CTBP-interacting protein
DDR	DNA damage response
dHJ	Double Holliday junction
DMEM	Dulbecco's Modified Eagle Medium
DMSO	Dimethyl sulfoxide
DNA	Deoxyribonucleic acid
DNA2	DNA replication helicase/nuclease 2
DNA-PKcs	Catalytic subunit of the DNA-dependent protein kinase
DNA-PKcsi	DNA-PKcs inhibitor
DPSS	Diode-pumped solid-state
dRP	Deoxyribose-phosphate
DSBs	Double-strand breaks
dsDNA	Double-stranded DNA
ECL	Enzymatic chemiluminescence
EDTA	Ethylenediaminetetraacetic acid
EGFR	Epidermal growth factor receptor
Exo1	Exonuclease 1
FBS	Foetal bovine serum

FEN1	Flap endonuclease 1
FOV	Field of view
FSG	Fish skin gelatin
FWHM	Full width half maximum
Gy	Gray
h	Hours
HR	Homologous recombination
HRP	Horseradish peroxidase
Hs	Homo sapiens
HU	Hydroxyurea
ICLs	Interstrand crosslinks
IR	Ionising radiation
IRIF	Ionising radiation-induced foci
J	Joule
KAP1	KRAB-associated protein 1
LET	Linear energy transfer
LFS	Li-Fraumeni syndrome
LigI	Ligase I
LigIIIα	Ligase IIIα
LigIV	Ligase IV
LOH	Loss of heterozygosity
MDC1	Mediator DNA-damage checkpoint 1
MEFs	Mouse embryonic fibroblasts
MEM	Modified Essential Medium
min	Minutes
MMEJ	Microhomology-mediated end-joining
MMR	Mismatch repair
MRN	MRE11-RAD50-NBS1
NA	Numerical aperture
NDIR	Non-dispersive infrared
NER	Nucleotide excision repair
NHEJ	Non-homologous end-joining
NIR	Near infrared
nM	Nanomolar
OD	Optical density
OH	Hydroxyl
PAR	Poly (ADP-ribose)
PARG	Poly (ADP-ribose) glycohydrolase
PARP-1	Poly (ADP-ribose) polymerase 1
PARPi	PARP inhibitor
PBLs	Peripheral blood lymphocytes
PBS	Phosphate buffered saline
PCNA	Proliferating cell nuclear antigen
PDMS	Polydimethylsiloxane
PFA	Paraformaldehyde
PFGE	Pulsed-field gel electrophoresis
PI3KK	Phosphatidylinositol-3-kinase-like kinase
PID	Proportional-integral-derivative
PNKP	Polynucleotide kinase phosphatase

Polβ	Polymerase β
pRb	Retinoblastoma protein
RAD51AP1	RAD51-associated protein 1
RBE	Relative biological effectiveness
RIF1	RAP1-interacting factor 1
RMI1/2	RecQ mediated genome instability 1/2
ROS	Reactive oxygen species
RPA	Replication protein A
RS-SCID	Radiosensitive severe combined immunodeficiency
RWD	Relative wound density
S.E.M.	Standard error of the mean
S/Ser	Serine
Sc	*Saccharomyces cerevisiae*
SCID	Severe combined immunodeficiency
SDS	Sodium dodecyl sulphate
SDSA	Synthesis-dependent strand annealing
sec	Seconds
Sp	*Schizosaccharomyces pombe*
SSA	Single-strand annealing
SSBR	Single-strand break repair
SSBs	Single-strand breaks
ssDNA	Single-stranded DNA
T/Thr	Threonine
t-AML	Therapy-related acute myeloid leukaemia
TDP1	Tyrosyl-DNA phosphodiesterase 1
TLDs	Thermoluminescent dosimeters
TOP1/2/3	Topoisomerase 1/2/3
TopBP1	Topoisomerase 2 binding protein 1
TP53	Tumour protein 53
USXR	Ultrasoft X-rays
UV	Ultraviolet
WCE	Whole cell extract
WT	Wild-type
XLF	XRCC4-like factor
XPF	Xeroderma pigmentosum group f
XRCC1	X-ray cross-complementing protein 1
Y/Tyr	Tyrosine
YFP	Yellow fluorescent protein

1. Introduction

1.1 Genome instability and cancer development

Cancer is one of the main causes of death worldwide. Even though many efforts have been made in terms of research and therapy over the years, a large number of people still develop and perish from this disease (Mistry *et al.*, 2011). According to Cancer Research UK statistics, 14.1 million people worldwide were diagnosed with cancer in 2012, and it is estimated that in the UK alone more than one in three people will be diagnosed with cancer during the course of their lives. These numbers highlight the complexity of this disease and the mechanisms by which cells acquire tumorigenic traits and eventually give rise to such malignancies, thus complicating therapeutic approaches.

Hanahan and Weinberg highlighted the complexity of such disease by attributing a variety of hallmarks to cancer cells (Hanahan and Weinberg, 2000). Such cells are capable of sustaining proliferative signalling by deregulating signals mostly orchestrated by growth factors regulating cell cycle progression and cell growth. Such cells also possess the capacity of evading growth suppressor signals by deregulating the function of genes involved in controlling cell proliferation. Tumour protein 53 (TP53) and retinoblastoma protein (pRb) are two tumour suppressor genes involved in such regulation, and malfunction of these genes can lead to persistent cell proliferation (Burkhart and Sage, 2008; Levine *et al.*, 1991). Associated to the capacity of uncontrolled proliferation, cancer cells are also capable of escaping signals, which promote cell death. TP53 also plays an important role in promoting cell death by apoptosis (Lowe *et al.*, 1993). Abnormalities to the function of this gene can allow cells to resist cell death. Cancer cells are also thought to

possess what Hanahan and Weinberg named a replicative immortality, by up-regulating telomerase (Hanahan and Weinberg, 2000; Harley *et al.*, 1994). Irrespectively of this acquired immortality, cells still require oxygen and nutrient supply to subsist. Cancer cells promote angiogenesis rearranging the vasculature surrounding the tumour, guaranteeing their survival (Hanahan and Weinberg, 2000). Another common characteristic of cancer cells is the invasive phenotype, promoting the development of other tumours in tissues different from that of the original tumour. E-cadherin (cell to cell adhesion molecule) loss is an example of a deregulation that enhances the metastatic potential of cancer cells (Onder *et al.*, 2008). All of these hallmarks are common traits of cancer cells, which contribute to the potentiation of their growth and survival.

Cancer development can be mainly attributed to what Hanahan and Weinberg described as enabling characteristics (Hanahan and Weinberg, 2011). These are thought to be genome instability, and tumour promoting inflammation. Inflammation leads to changes to the tumour microenvironment potentiating its growth and survival (see **figure 1.1**). Genome instability is correlated with repair and misrepair of DNA lesions promoting mutagenesis (Negrini *et al.*, 2010). The genomic DNA of cells is exposed to several types of lesions on a daily basis, such as single-strand breaks (SSBs), DNA adducts, crosslinking and potentially low levels of DNA double-strand breaks (DSBs) (Bennett *et al.*, 2004; Bennett *et al.*, 2005; Lindahl and Barnes, 2000). Different damaging agents of endogenous and exogenous nature can cause these lesions. Endogenous factors are mainly replication fork stalling, topoisomerase malfunctions, and reactive oxygen species (ROS) produced during metabolic processes (Jackson and Bartek, 2009). Exogenous forms of damage encompass ionising radiation (IR), chemotherapeutic agents, and ultraviolet (UV) light exposure (Eastman and Barry, 1992; Jackson and Bartek, 2009). Amongst the described lesions, DSBs are thought to be the most deleterious to cells, and their misrepair can potentiate cell

death (Rich *et al.*, 2000). It is therefore important to repair such lesions in order to preserve genomic integrity.

In response to DSBs, cells can potentiate repair via two highly conserved repair mechanisms named homologous recombination (HR) and non-homologous end-joining (NHEJ) (Mladenov and Iliakis, 2011). There are a variety of factors involved in the repair of DSBs by these mechanisms, and complete loss or compromised activity of genes involved in these forms of repair can lead to mutagenesis and ultimately to cancer (Ciccia and Elledge, 2010; Kastan, 2008). **Table 1.1** provides a snapshot of some of the cancers, which can be developed when genes, which are involved in damage signalling or its repair, are mutated.

It is therefore important to address the mechanisms by which cancer cells cope with exogenous forms of damage, circumventing commitment to cell death, promoting incessant proliferation. The study of such mechanisms is valuable to deepen the understanding of the intricate processes behind tumour development.

1.2 DNA damage

DNA damage can be divided into two categories: simple and complex (when two or more lesions locate within one or two helical turns of the DNA) (Gulston *et al.*, 2004). Simple damage includes base damages such as apurinic or apyrimidinic (AP) sites, single-strand breaks (SSBs) and double-strand breaks (DSBs). The term DSB has been generally used to describe chemically different DSB, namely two-ended DSB induced promptly by IR and one-ended DSB, formed at stalled replication forks (**figure 1.2**). The latter types of breaks are called replication-induced DSBs. Such alterations to a cell's genetic code may lead to genomic instability, mutations and even cell death (Roos and Kaina, 2006).

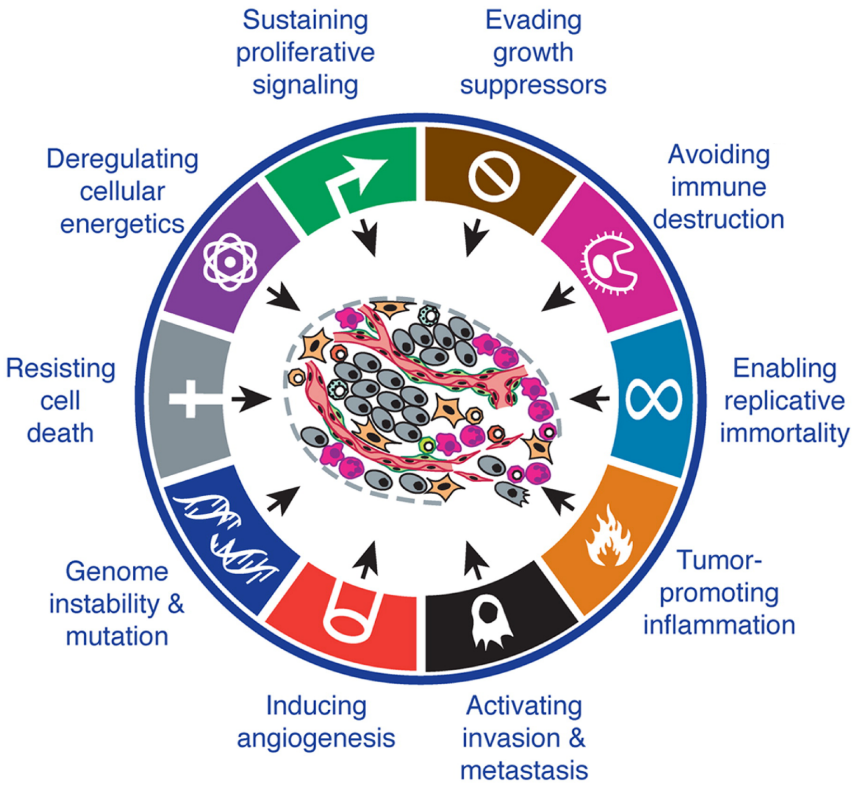


Figure 1.1 Schematic depicting the hallmarks of cancer as proposed by Hanahan and Weinberg. Reprinted from Hanahan, D., and Weinberg, R.A. (2011). Hallmarks of cancer: the next generation. Cell 144, 646-674 with permission from Elsevier.

Syndrome	Mutated gene	Defect	Cancer
Familial breast cancer	ATM, BCRA1, BCRA2, CHK2, NBS1, RAD51C, RAD50	HR, damage signalling	Breast cancer, ovarian cancer
Bloom syndrome	BLM	HR	Carcinomas, leukaemias, lymphomas
Werner syndrome	WRN	HR, BER	Sarcomas
Ligase IV syndrome	LigIV	NHEJ	All, lymphomas
Radiosensitive severe combined immunodeficiency (RS-SCID)	ARTEMIS	NHEJ	Lymphomas
Ataxia telangiectasia (A-T)	ATM	Damage signalling, DSB repair, oxidative stress	Lymphomas, leukaemias, breast cancer
Li-Fraumeni syndrome (LFS)	TP53	DNA damage signalling, DSB repair	Brain and breast cancer, sarcomas

Table 1.1 Cancer predispositions associated with DNA damage response defects. Adapted from (Ciccia and Elledge, 2010).

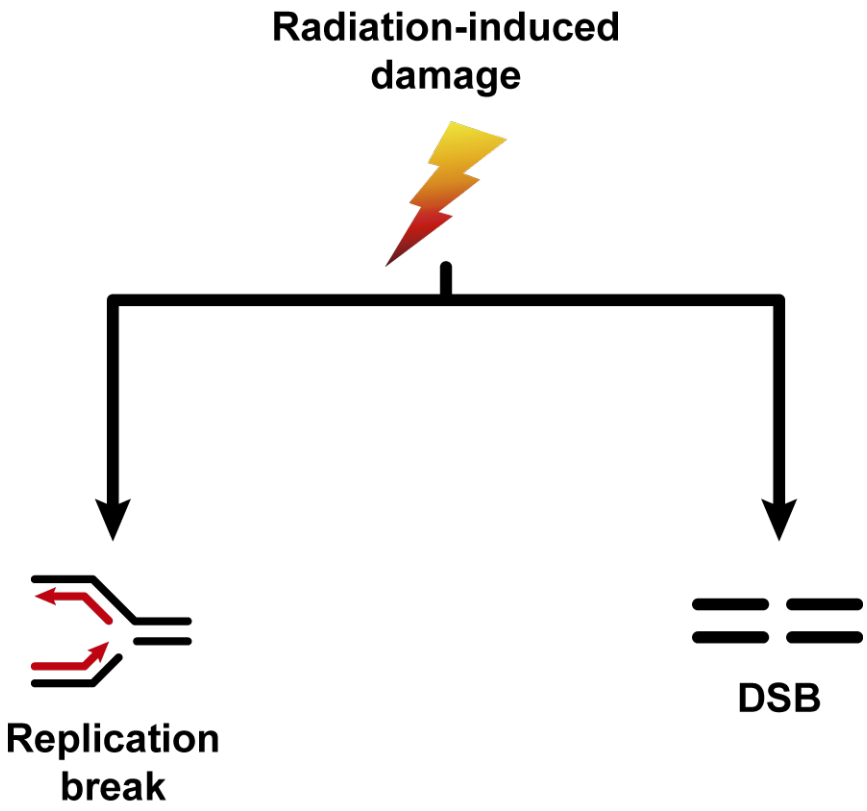


Figure 1.2 Classes of DSBs caused by radiation-induced DNA damage. Radiation can lead to the formation of two-ended DSBs induced promptly by IR and one-ended DSBs, formed at stalled replication forks.

These types of damage can be induced directly to the DNA molecules or indirectly by the interaction with reactive oxygen species (ROS) that are within 4 nm of a DNA molecule (Wiseman and Halliwell, 1996). Several exogenous agents such as ionising radiation, chemotherapeutic agents, and ultraviolet (UV) light exposure can induce direct DNA damage (Ciccia and Elledge, 2010). Cytotoxic drugs that directly kill cancer cells are the most common form of chemotherapy and have been used for the past 50 years, resulting in increased survival rates. There are several kinds of cytotoxic agents, which have different interaction mechanisms to cause cell kill. Some different kinds of cytotoxic agents are: alkylating agents, antimetabolites, antimicrotubule agents and topoisomerase inhibitors. Helleday *et al.* reviewed in detail the clinical use of different chemotherapeutic agents (Helleday *et al.*, 2008).

1.2.1 DNA lesions

The DNA structure reported by Watson and Crick provided an early perception of the DNA being a highly stable molecule (Watson and Crick, 1953). Irrespectively of the high fidelity that characterises the DNA metabolic processes, failures during these can lead to DNA aberrations (Friedberg, 2003). These processes are DNA replication (creation of a DNA copy prior to cell division), recombination (exchanges between different DNA molecules within the same nucleus), and DNA repair mechanisms (restoration of an altered DNA molecule) (Friedberg, 2003). DNA mismatches arising during DNA replication, and strand-breaks introduced due to topoisomerase 1 and 2 (TOP1/2) activity failures are some of the examples. Lindahl and Barnes have also highlighted a number of other processes such as hydrolytic reactions, and non-enzymatic methylations, which are in the nature of some of the DNA-base lesions naturally occurring in cells (Lindahl and Barnes, 2000).

Base damage can be further aggravated as cells progress through S-phase during DNA replication, proportionating the formation of single nucleotide (point) mutations. Most of the common replication errors such as base mismatches, insertions, and deletions are normally corrected by the mismatch repair (MMR) machinery. This repair mechanism was reviewed in detail by Jiricny (Jiricny, 2006). Intrastrand crosslinks and bulky DNA adducts are corrected via the nucleotide excision repair (NER) pathway. This pathway was reviewed in detail by Friedberg (Friedberg, 2001). Altered bases, abasic sites, and SSBs are tackled by base excision repair (BER) (Dianov and Hubscher, 2013; Friedberg, 2003; Jackson and Bartek, 2009; Maynard *et al.*, 2009). This repair pathway is described in more detail in **section 1.4**.

Reactive oxygen species (ROS) resultant from oxidative respiration or produced by neutrophils and macrophages at sites of inflammation and infection can also attack the DNA leading to strand breaks (Kawanishi *et al.*, 2006). When two SSBs are in close proximity of ~10 bp or less, or when the replication machinery is faced with such lesions or certain others, these processes can result in the most deleterious type of lesion denominated double-strand break (DSB). The two pathways by which these lesions can be repaired are described in detail in **section 1.5**.

1.2.2 DNA damaging agents

Lesions to the genomic DNA can be induced by a variety of damaging agents.

1.2.2.1 Ionising radiation (IR)

Ionising radiation is a double-edged sword since it can lead to mutations ultimately promoting cancer development, but it is also commonly used to induce DNA damage in most clinical settings to kill preferentially tumour cells. Aside from surgery, radiation therapy remains as the most effective form of cancer treatment (James *et al.*, 2012). The

effects of irradiation have been widely characterised over the years, highlighting the different forms of DNA damage induced by different types of ionising radiation (Cadet *et al.*, 2008; Cadet *et al.*, 2012; O'Neill and Wardman, 2009). Ionising radiation consists of energy high enough to promote the ejection of electrons from atoms/molecules, therefore causing ionisation. This energy can come from a particle or from a high-energy photon. There are two different types of ionising radiation: electromagnetic radiation (photons), and particle radiation (particles). Electromagnetic radiation consists mostly of X-rays or gamma (γ) rays. Photon interaction with matter occurs mainly through Compton scattering, where part of the photon energy is transferred to an outer shell electron, which is ejected, and the incident photon is deflected assuming a new direction with lower energy. Photon interaction can also occur via photoelectric effect, where the photon energy is transferred to an inner shell electron, which is ejected with a kinetic energy equal to the difference between the photon energy and the orbital binding energy (Rosenberg, 2008). The probability of photon interaction with matter occurring via photoelectric effect is directly proportional to Z^4 (where Z represents the atomic number), and inversely proportional to the cubed energy of the incident photon (Rosenberg, 2008). This latter process involves emission of characteristic X-rays or Auger electrons with specific energies. Efforts have been made towards enhancing radiotherapy treatment and more recently by using kV X-rays in combination with gold nanoparticles (high Z) present within the tumour, enhancing the photoelectric effect cross-section, thus increasing the absorbed dose at the tumour level (Butterworth *et al.*, 2012; Jain *et al.*, 2014; Jain *et al.*, 2011; McMahon *et al.*, 2011; McMahon *et al.*, 2008).

Within particle radiation there are several types to be considered. Ionisation processes mostly generate electrons, which have a negative charge. Electron beams are used for therapy and are generally produced by linear accelerators, with beams being aimed at a

high Z target leading to characteristic X-ray production conventionally used in most clinical settings. Neutrons have approximately the same mass as protons (positive charge) but do not have a charge. Neutrons are obtained by accelerating atoms against a target. Alpha (α) particles are Helium atoms with two protons and two neutrons. These particles are products of the alpha decay of unstable nuclei, which emit alpha particles in order to reach a more stable form (Rasmussen, 1959). The emitted particles and photons have a specific Linear Energy Transfer (LET) which represents the energy transfer as a function of the distances covered within the target. LET depends on several different factors such as the photon energy, the particle's velocity, atomic number and electron density of the target (in case of charged particles) (Lehnert, 2007). High-LET radiation (neutrons, protons, alpha particles and heavy ions) produces fewer tracks (ionisations along tissue) per unit dose but is considered to be more lethal compared to the same dose of low-LET radiation. The density of the energy depositions increases as the LET increases and as a consequence it was proposed that clustered damage sites are formed with increasing complexity as the LET increased (Goodhead, 1989; Nikjoo *et al.*, 2001). Protons' and heavy ions' depth-dose curve is defined by a Bragg peak which allows a finer energy deposition within a smaller area, where the penetration depth is defined by the beam energy, with beam deposition occurring at the track end (Schulz-Ertner *et al.*, 2006). Relative biological effectiveness (RBE) is used to compare different LET values of radiation in terms of biological effects such as cell killing. Radiation forms with a higher RBE are generally more detrimental as the LET increases (see **figure 1.3a**).

From the types of damage to DNA caused by ionising radiation, the most important ones are SSBs, DSBs, base damage and clustered damage. OH radicals have been shown to be responsible for approximately 70% of the DNA damage induced in mammalian cells by ionising radiation under normal oxygen conditions for low-LET (Delara *et al.*, 1995; Roots

and Okada, 1975), highlighting the importance of the presence of oxygen to enhance radiation damage (Hirayama *et al.*, 2013). On increasing the LET of the radiation, the majority of the DNA damage is induced by direct energy deposition in the DNA with a reduced contribution of diffusible OH radicals.

DSBs and clustered damage are the most commonly related lesions to mutagenic potential of the radiation. Clustered damage represents a combination of two or more lesions formed within one or two helical turns of the DNA by a single radiation track (Gulston *et al.*, 2004). This particular kind of damage includes not only DSBs but also a SSB in close proximity to base lesions on both strands and the later clustered damage sites have been shown experimentally to be formed in irradiated cells (Gulston *et al.*, 2002; Sutherland *et al.*, 2000; Sutherland *et al.*, 2002). Clustered damage occurrence may increase with the ionisation potential of the radiation used, although difficulties in their detection when using high-LET radiation have posed difficulties to demonstrate such premise. Approximately 30% of the DSBs induced by low-LET radiation are complex due to additional breaks. This number increases to 70% when high-LET radiation is used. A single Gy of low-LET ionising radiation induces approximately 1,000 SSBs, and 20-40 DSBs (Nikjoo *et al.*, 2001). The plethora and complexity of damage induced by different ionisation density of ionising radiation highlight the deleterious effects this damaging agent poses to genomic DNA as shown in **figures 1.3a** and **1.3b**.

1.2.2.2 Ultraviolet (UV) radiation

Soft and hard X-rays lead to different forms of DNA damage due to different wavelengths. Similarly, the DNA damage induced by ultraviolet (UV) and visible radiation also depends on the wavelength of the exciting light (Kielbassa *et al.*, 1997; Will *et al.*, 1999). Laser light has more recently been used to induce cell DNA damage to follow the processes

induced using real-time observations (Bekker-Jensen *et al.*, 2006; Lan *et al.*, 2004; Lukas *et al.*, 2005). Lasers are based on the principle of electron excitation from lower to higher energy levels. The energy difference between the levels is emitted through photons, which can cause further excitation processes. The photon wavelength is inversely proportional to its energy. DNA mainly absorbs light in the UV range (200 to 300 nm); however there is low penetration due to the high absorption rates at this wavelength range. The type of DNA lesions depends on the wavelength of the UV radiation utilised, and the laser power. For wavelengths between 290 and 340 nm, the observed lesions are mainly photoproducts, a small yield of SSBs, and lesions excised by the glycosylase Fpg. At wavelengths above 340 nm the number of photoproducts generated decreases, with an increase in the number of Fpg sensitive lesions reaching its maximum for wavelengths between 400 and 450 nm. When laser microbeams are used in conjunction with photosensitizers such as bromodeoxyuridine (BrdU) and Hoechst, base lesions, SSBs, and DSBs are generated, minimising the contribution of UV-type damage (Reynolds *et al.*, 2013).

For higher light penetration, near infrared (NIR) light can be used, as there is only minimal cell absorption of light in the NIR range (Lan *et al.*, 2004). NIR light has a lower energy than light in the UV range; therefore in order to achieve direct DNA damage in the NIR range, multiple photons must be simultaneously absorbed for multiphoton excitation. This technique uses high repetition rate, ultrashort laser pulses to correlate the photons in time and space. The number of photons that are absorbed by DNA and their wavelength determine how comparable the damage will be with UV single photons. Near infrared range (600-1047 nm), photons of 760 nm were found to induce the higher DNA damage (Mohanty *et al.*, 2002).

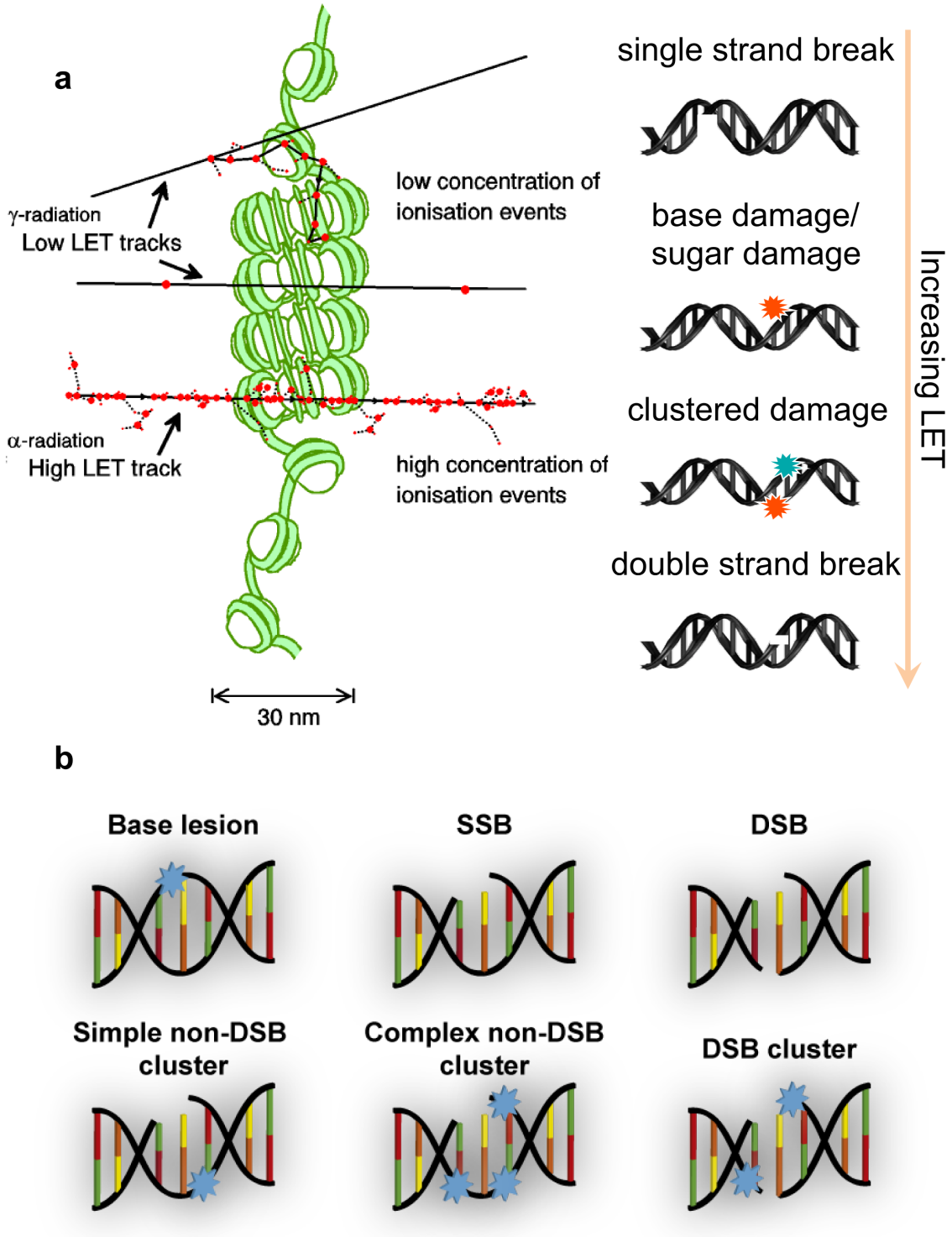


Figure 1.3 Schematic depicting effects of increasing LET radiation leading to DSB and non-DSB lesions induced to DNA. a) Schematic depicting ionisation events (red dots) at the DNA level caused by different forms of radiation with increasing LET. Adapted from (Goodhead, 1994). **b)** Base lesions, single-strand breaks (SSBs), and double-strand breaks (DSBs) can be generated endogenously. Cluster damage is characteristic of ionising radiation-induced damage. Simple clusters are composed of a base lesion in the vicinity of a SSB. Multiple base lesions in the proximity of a SSB compose a complex non-DSB cluster. A DSB cluster is characterised by base lesions surrounding a DSB.

The mechanism of DNA damage induction by NIR multiphoton systems can occur by direct 3-photon absorption, indirectly by the production of ROS which can cause DNA lesions if in close proximity to DNA molecules, and mainly by 2-photon absorption when photosensitizers are used. SSBs, UV products, base lesions, and DSBs are some of the lesions, which can be caused by direct 3-photon absorption.

Both multi- and mono-photonic systems are assumed to induce a higher yield of complex damage when compared to forms of low-LET ionising radiation. The potential issues of using these systems to mimic the effects of ionising radiation-induced DNA damage are addressed in **section 1.3.1**.

1.3 Spatiotemporal observation of DNA repair

The characterisation of the dynamics of recruitment of DNA repair factors to lesions caused by exogenous damaging agents can be of extreme importance to unveil the mechanisms by which mammalian cells resolve damage preventing genomic instability. The accumulation of repair factors at sites of DNA damage caused by low-LET ionising radiation leads to the formation of foci, which can be microscopically observed. These are normally referred to as ionising radiation-induced foci (IRIF). Such foci have been extensively studied in response to ionising radiation damage, using immunocytochemical approaches. However, cell fixation simply provides a snapshot at a given time of the recruitment of repair factors to DNA lesions. Spatiotemporal characterisation of such processes has been mainly performed using living cells with fluorescently-labelled factors involved in the signalling and repair of DNA lesions, in response to localised forms of damage induced by laser microbeams, high-LET heavy ions, and ultrasoft X-rays (USXR) (Reynolds *et al.*, 2013).

1.3.1 Live cell imaging following laser microbeam irradiation

Laser microbeams have become over recent years a valuable tool to perform DNA repair kinetics studies (Kong *et al.*, 2009; Meldrum *et al.*, 2003; Reynolds *et al.*, 2012). These systems induce highly localised DNA damage, and when coupled to imaging systems allow visualisation of the repair processes in a time-lapse fashion. Environmental enclosures guarantee physiological conditions for normal cell growth at 37°C and 5% CO_2 humidified air. UV (193-355 nm) (Gottschalk *et al.*, 2009; Kong *et al.*, 2009; Lan *et al.*, 2004), UVA (315-400 nm) lasers in combination with photosensitizers (Dinant *et al.*, 2007; Kong *et al.*, 2009; Lan *et al.*, 2004), and near infrared (NIR) multi-photon laser microbeam systems (600-1047 nm) (Bisby *et al.*, 2006; Botchway *et al.*, 2007; Tirlapur *et al.*, 2001) have been used to characterise the spatiotemporal aspects of DNA damage repair.

Laser microbeams can induce a plethora of different lesions to the genomic DNA. The profile of lesions is normally dependent on laser power and wavelength (Kong *et al.*, 2009; Reynolds *et al.*, 2013). As described in **section 1.2.2.2**, wavelengths between 290-340 nm mainly cause photoproducts. At higher wavelengths such as 400-450 nm, SSBs and oxidised purine products are induced and the yield of photoproducts is less prominent. Several studies have reported the use of photosensitizers such as BrdU and Hoechst in conjunction with laser microbeams, to generate indirect DNA damage (Dinant *et al.*, 2007; Kong *et al.*, 2009; Lan *et al.*, 2004). Photosensitizers give rise to lesions such as SSBs, DSBs, and base lesions, whilst reducing the yield of UV-type damage. Although, the presence of DNA interchelating agents may pose difficulties to DNA repair factors in accessing the damaged sites, compromising the correct repair of the induced lesions.

NIR laser microbeams are normally coupled to a confocal microscope system, with the laser being focused using a high numerical aperture (0.5-1.45) microscope objective (Botchway *et al.*, 2010). These systems are known to induce DNA damage via multiphoton excitation processes via 3-photon direct absorption or through the production of reactive oxygen species due to 2-photon absorption in the presence of photosensitizers. Direct 3-photon absorption has been reported to induce UV-type lesions, base lesions, single- and double-stranded breaks. Quantification of the yields of DNA lesions produced within the irradiated regions is yet to be fully characterised (Kong *et al.*, 2009; Reynolds *et al.*, 2013). Harper *et al.* have estimated the yields of DSB induction by multi-photon processes to be equivalent to that of 2 Gy low-LET ionising radiation, normally responsible for approximately 40-80 DSBs (Harper *et al.*, 2008). Beker-Jensen *et al*. have reported a DSB induction yield equivalent to 3 to 10 Gy of low-LET ionising radiation (approximately 60-200 DSBs) (Bekker-Jensen *et al.*, 2006). Splinter *et al.* have tested the same laser microbeam settings used in the work reported by Beker-Jensen *et al*., and reported a DSBs yield equivalent to that of several hundred Gy (Splinter *et al.*, 2010). Uematsu *et al.* and Kleppa *et al.* have estimated the DSB yield to be 1000-1500 for 800 nm for the used multiphoton system, and approximately 3000 DSBs for 365 nm laser system (Kleppa *et al.*, 2012; Uematsu *et al.*, 2007). These reports have led to the conclusion that the damage generated within the irradiated area of the nuclei is not only constituted of isolated lesions but also of clustered damage of a more complex nature. NIR microbeams have been shown to induce a high level of clustered damage sites, which are of a complex nature and therefore are more challenging to be appropriately resolved (Harper *et al.*, 2008; Reynolds *et al.*, 2012). The presence of such clusters impacts on the kinetics of resolution of the damage induced and therefore is not entirely representative of the spatiotemporal dynamics of the DNA damage repair processes in response to lesions generated by exposure to low-

LET ionising radiation. Such observations have been made when the recruitment of fluorescently labelled molecules such as the NHEJ sensor molecule Ku80 was followed in response to laser microbeam-induced damage at different wavelengths. The half-life of Ku80 was determined to be shorter when damage induction was performed with NIR systems, as opposed to UV lasers (Feng and Chen, 2012; Mari *et al.*, 2006; Reynolds *et al.*, 2012; Reynolds *et al.*, 2013). The higher complexity of damage was reflected in persistence of this molecule within the irradiated region for longer times. The same discrepancy was not observed when different systems were used to follow the recruitment kinetics of the catalytic subunit of the DNA-dependent protein kinase (DNA-PKcs) to damage sites, since this molecule is thought to be mainly involved in the resolution of complex DSBs (Reynolds *et al.*, 2013).

Another example of discrepancies involves the spatiotemporal dynamics of recruitment of X-ray cross-complementing protein 1 (XRCC1). XRCC1 is a scaffolding protein, which is heavily involved in the repair of SSBs by BER. When the recruitment of XRCC1 is followed in living cells in response to damage induced by a 365 nm laser microbeam and uranium ions, the results are confounding. There is a persistence of XRCC1 at the damage sites in contrast to what is observed in response to irradiation using uranium ions, reflecting the higher complexity of damage induced by laser microbeams (Jakob *et al.*, 2011; Lan *et al.*, 2004; Reynolds *et al.*, 2013).

The difficulties in using laser micro-irradiation are mainly associated with quantification of damage yields, photo damage induction, and laser setup conditions including power, and these all add to difficulties in terms of data reproducibility, interpretation, and comparison of data between laboratories. The repair kinetics characteristic of DNA damage induced by low-LET ionising radiation tend to be different to those determined following laser micro-irradiation.

1.3.2 Repair of heavy ion-induced DNA lesions

High-LET radiation has also been widely used to study DNA repair kinetics. Studies have been performed using different particles with LET that ranges from 200 keV/µm (Carbon ions) to 14300 keV/µm (Uranium ions) (Tobias *et al.*, 2010). High-LET particles deposit energy throughout their trajectories, which makes it possible to study the spatial organisation of the radiation-induced foci. Molecules such as XRCC1 and Aprataxin have been studied at shorter times post high-LET irradiation (Jakob *et al.*, 2011). XRCC1 forms radiation-induced foci within sec of high-LET irradiation (Harris *et al.*, 2009). Poly (ADP-ribose) polymerase 1 (PARP-1) recruitment to DNA SSBs was shown to lead to a fast recruitment of XRCC1 to the damage site. Recruitment of the DSB biomarker p53 binding protein 1 (53BP1) has also been shown to take longer which correlates with being activated downstream of several other events such as phosphorylation of histone H2AX (γ-H2AX), another DSB biomarker (FitzGerald *et al.*, 2009; Schultz *et al.*, 2000).

The damage complexity induced by high-LET radiation is greater than that caused by low-LET sparsely ionising radiation (Costes *et al.*, 2010; Goodhead, 1989; Nikjoo *et al.*, 2001). Using human fibroblasts, high-LET radiation (nitrogen ions) induces the maximal number of γ-H2AX foci 10-15 min after irradiation compared to low-LET radiation 30-45 min post irradiation (Costes *et al.*, 2006). The foci size was also shown to increase faster post exposure to high-LET radiation. The number of IRIF does not increase along the track for increasing LET, however a single focus might contain increasing numbers of DSBs due to the increased probability of producing two or more DSB in close proximity with an increase in LET (Jakob *et al.*, 2009). The repair times of DSB (Datta *et al.*, 2005b; Jenner *et al.*, 1993) or loss of foci (Costes *et al.*, 2010; Leatherbarrow *et al.*, 2006) are longer post high-LET irradiation, reaffirming the higher complexity of damage caused by more

densely ionising forms of radiation. Persistence of damage was also proposed from the observation of longer-lived γ-H2AX and 53BP1 foci in response to iron ions when compared to low-LET IR (Asaithamby *et al.*, 2011; Saha *et al.*, 2013). Alpha particle irradiation is more detrimental in terms of both cell survival and persistent DSBs following irradiation as determined by pulsed-field gel electrophoresis (PFGE) when compared to low-LET ionising radiation (Anderson *et al.*, 2010).

High-LET radiation has proven to be a valid resource to help unveiling the mechanisms involved in the repair of radiation-induced damage and its correlation to chromatin modifications. However, the fact that high-LET radiation induces a higher proportion of complex damage than seen with low-LET radiation poses difficulties in terms of assuming similar spatiotemporal dynamics of DNA damage repair occurs in response to low-LET ionising radiation.

1.3.3 Recruitment of DNA repair factors to USXR-induced damage

DNA repair has also been characterised in response to damage generated by X-rays with energies between 0.1 to 5 keV, normally designated as ultrasoft X-rays (USXR) (Badie *et al.*, 2009; Reynolds *et al.*, 2012; Sprung *et al.*, 2011; Tambini *et al.*, 2010). Such irradiations are generally performed through a shielded grid, inducing damage to localised regions within the different nuclei, with dose rates in the order of 0.3 Gy/sec. USXR interact with matter producing mainly low energy electrons and a characteristic Auger electron which has a restricted range between 7 and 500 nm depending on the energy of the USXR (Hamada *et al.*, 2006). For instance, 1.49 keV characteristic aluminium K-shell X-rays have a track length of 70 nm, and are found to have a RBE of 1.9-2.5 for DSB induction, as measured by PFGE (Botchway *et al.*, 1997; de Lara *et al.*, 2001).

Initial studies using such irradiation systems allowed observation of accumulation of DNA damage sensing and signalling factors at damage sites using immunocytochemistry methods. Phosphorylated histone H2AX (γ-H2AX), Rad50 and Mre11 recruitment was observed following USXR irradiation (Hamada *et al.*, 2006; Nelms *et al.*, 1998). This form of radiation has also been used for live-cell imaging experiments using fluorescently labelled factors to characterise in more detail the recruitment kinetics of highly abundant repair factors such as Ku80, DNA-PKcs, RAD51 and other tagged proteins (Badie *et al.*, 2009; Reynolds *et al.*, 2012; Tambini *et al.*, 2010). By inducing concentrated damage to small regions within the nuclei, it is possible to observe the recruitment of such factors above the background levels of fluorescence (Reynolds *et al.*, 2012).

The low dose rates associated with USXR irradiation pose issues regarding live-cell imaging experiments, because longer times are required for the irradiations, making it necessary to maintain the cells at low temperatures during the irradiation to minimise the repair processes during damage induction. The need for lower temperatures during irradiation introduces a delay in the repair processes, posing difficulties for the observation of fast recruitment of DNA repair associated molecules to damage sites following irradiation.

1.3.4 DNA repair kinetics observations following immunostaining

Immunocytochemistry methods are the most conventional approach used to monitor DNA signalling and repair following damage induction. Cells are normally exposed to different forms of irradiation with low- and high-LET ionising radiation to induce DNA damage in mammalian cells. Cells are then restored to a physiological environment at 37°C and 5% CO_2 humidified air. To minimise the repair processes cells are normally placed at 4°C before irradiation. Cells are then fixed at different times following irradiation (Anderson *et*

al., 2010; Harper *et al.*, 2010; Paull *et al.*, 2000; Saha *et al.*, 2013; Schultz *et al.*, 2000). This particular approach is useful to monitor damage induction by observing for example 53BP1 and γ-H2AX foci formation, although it is limited in terms of recruitment kinetics to sites of damage (Markova *et al.*, 2007; Rappold *et al.*, 2001; Wang *et al.*, 2002). Additionally, there is no prior knowledge of the damage present at the time of irradiation and this approach only provides a snapshot at any one time of the level of repair processes involved in the resolution of radiation-induced DNA damage. The time course for loss of foci is established from a series of individual experiments at different times after irradiation using different populations of cells. Contrastingly, live-cell imaging approaches as used in laser micro-irradiations allow observation of damage formation and disappearance in the same cells throughout a time course. Such approaches provide a better idea of the kinetics of recruitment of DNA damage repair associated molecules in response to multiple forms of damage induction and should allow questions on whether the onset of some of the processes are delayed following irradiation.

1.3.5 Rationale for DNA repair kinetics studies using the linac experiment system

Based on the above considerations with laser micro-irradiation, USXR and ion particles, a system based on a 6 MeV linear accelerator coupled to a fully automated epifluorescence microscope harboured within an environmental enclosure would be a novel approach to study DNA repair kinetics following damage induction by low-LET radiation.

In contrast to laser microbeams and high-LET heavy ions, a linear accelerator provides low-LET ionising radiation and the dose and dose rate can be quantified and as a consequence the level of DNA damage in cells may be quantified. Additionally, the damage induced by 6 MeV electrons is not contaminated by UV-type damage, as is the case with several laser microbeam approaches and it reproduces the types of damage

induced by accelerators used in clinical settings. The capacity to deliver doses at a high dose rate (sub-μs pulses) allows cells to be maintained under physiological conditions in contrast to maintain cells at lower temperatures during irradiation as is the case for many studies using immuno-staining. By operating under physiological conditions (37°C and 5% CO_2 humidified air), fast repair processes immediately following damage induction may be monitored. *In situ* imaging permits live-cell imaging in a time-lapse fashion, allowing monitoring of the recruitment of fluorescently labelled proteins to radiation-induced DNA damage sites. Whereas sparsely ionising radiation induces damage to localised regions of the nuclei resulting in homogeneous distribution of damage, laser microbeams, high-LET heavy ions and gridded-USXR approaches induced damage more heterogeneously in nucleus as 'tracks' or small region(s) containing high levels of damage. As a consequence, the cells irradiated with the linac would be able to be used for other types of assays. Development of such a facility would provide clinically relevant radiation with quantifiable damage, which can be monitored in living cells under physiological conditions.

1.4 Mechanisms of repair of base lesions and SSB

Base excision repair (BER) and single-strand break repair (SSBR) are responsible for maintaining genome stability through correct repair of base lesions, SSB and AP sites derived from oxidation and chemical alterations resulting from reactions with endogenous and exogenous DNA damaging agents (Krokan and Bjoras, 2013; Maynard *et al.*, 2009). Each cell on average has to repair 10,000–20,000 DNA lesions per day induced endogenously through oxygen metabolism (Lindahl, 1993). These repair pathways are important to minimise accumulation of unrepaired lesions which may pose difficulties for processes such as DNA replication and transcription and may lead to the development of

mutations, genomic instability, aging and cancer, amongst other diseases (Caldecott, 2008; Curtin and Szabo, 2013; Maynard *et al.*, 2009). There are multiple mechanisms used by cells to cope with these forms of lesions. These mechanisms differ mainly on the detection and end-processing step. BER normally processes indirect SSBs that are generated by enzymatic excision of the modified base. Direct SSBs result from sugar damage, generated by interaction with endogenously produced ROS and by exogenous agents such as ionising radiation, are repaired via the SSBR pathway (Almeida and Sobol, 2007; Caldecott, 2008). SSBs may also originate from Topoisomerase failure but they require a different set of repair proteins for end processing. Gap filling and ligation steps involve the same enzymes regardless of the origin of the SSB (Caldecott, 2008) (see **figure 1.4**).

1.4.1 Single-strand break repair (SSBR) pathway

SSBR pathway is described in more detail and is normally required for the resolution of SSB arising due to the interaction of the DNA with ROS, with exogenous agents, radicals induced by ionising radiation, and lesions arising due to topoisomerase malfunction (Caldecott, 2008; Dianov and Hubscher, 2013). This pathway differs from BER mainly in the initiation step, which does not involve DNA glycosylase processing. PARP-1 is thought to be the sensing molecule in this pathway, which rapidly binds to the SSBs and modifies itself and other targets with branched chains of poly (ADP-ribose) (PAR). The activity of PARP-1 at the DNA breaks is only transient since PARP-1 dissociates from the DNA and PAR chains are degraded by poly (ADP-ribose) glycohydrolase (PARG), retrieving PARP-1 to its de-ribosylated state, and available for the detection of further SSBs (Caldecott, 2008). End-processing is then performed in order to restore both 3' and 5' termini to 3'OH and 5'phosphate moieties required for gap filling and DNA ligation steps. A wide spectrum of molecules are involved in processing the DNA ends during

SSBR, reflecting the variety of damaged termini that can arise. Polymerase β (Polβ) is responsible for removing blocking 5'-sugar phosphates, AP endonuclease 1 (APE1) removes 3'-sugar phosphates, polynucleotide kinase phosphatase (PNKP) dephosphorylates 3'-ends and phosphorylates 5'OH ends. Aprataxin (APTX) also has a role in cleaning 5'-termini, which have been blocked by interrupted ligations. Tyrosyl-DNA phosphodiesterase 1 (TDP1) repairs SSBs which were generated by abortive topoisomerase reactions (Dianov and Hubscher, 2013). Following end processing, gap filling and ligation can occur either via short- or long-patch BER as described in **section 1.4.2** (Caldecott, 2008) (**figure 1.4**). TOP1-SSBs are DNA nicks therefore they might not require a gap filling step.

1.4.2 Base excision repair (BER) pathway

This pathway is generally used to repair base lesions as reviewed by Dianov and Hubscher, with 11 known human DNA glycosylases which are used in the initial step to recognise and process damaged DNA bases to be repaired by BER (Dianov and Hubscher, 2013). DNA glycosylases are thought to be consistently scanning the DNA, removing damaged DNA bases, thus creating AP sites. Following DNA-glycosylase activity, repair can be completed by either of two sub-pathways short-patch BER or long-patch BER. It is thought that the majority of lesions are repaired via short-patch BER (Almeida and Sobol, 2007; Dianov and Hubscher, 2013).

Short-patch BER is initiated by a glycosylase, which excises the base lesion and the subsequent AP site is hydrolysed by APE1. APE1 is responsible for catalysing the incision of the damaged strand, leaving a 3'hydroxyl (OH) and a 5'deoxyribose-phosphate (5'dRP) at the margins. The 5'dRP moiety is excised by Polβ, which also fills the nucleotide gap,

leaving the strand ready for ligation by a complex involving DNA ligase IIIα (LigIIIα) and XRCC1 (Almeida and Sobol, 2007; Dianov and Hubscher, 2013).

Oxidative lesions are normally removed by bi-functional DNA glycosylases, which also possess a 3' AP lyase activity. In this case, the DNA backbone can be incised 3' to the lesion, leaving a 3' unsaturated aldehyde, and a 5' phosphate at the termini. APE1 3' phosphodiesterase activity permits cleavage of the 3' terminus, leaving the strand ready for Polβ gap filling and ligation via LigIIIα/XRCC1 (Almeida and Sobol, 2007).

Long-patch BER is initiated by a DNA glycosylase in a similar fashion to short-patch BER. If Polβ cannot process the DNA end, it dissociates from the DNA strand allowing proliferating cell nuclear antigen (PCNA) together with polymerases Polε/Polδ, replication factor C (RF-C), flap endonuclease 1 (FEN1) and poly (ADP-ribose) polymerase 1 (PARP-1) to bind to the DNA. These proteins displace the DNA by addition of up to 12 nucleotides before the resulting DNA flap is cleaved by FEN1 endonuclease. The DNA backbone is then ligated by DNA ligase I (LigI) (Fortini *et al.*, 2003) (**figure 1.4** BER pathway). Incorrect repair of SSB and base lesions can lead to damage accumulation and ultimately to cancer development (Fortini *et al.*, 2003; Maynard *et al.*, 2009). Mutations in DNA polymerase β (Polβ) have been identified in approximately 30% of human tumours. X-ray cross-complementing protein 1 (XRCC1) polymorphisms and may be correlation to cancer development (Caldecott, 2008).

1.4.3 PARP-1 role in maintaining genomic integrity

Maintenance of genomic integrity depends on the correct resolution of both physiological and environmental challenges posed to the cells (Fortini *et al.*, 2003; Maynard *et al.*, 2009).

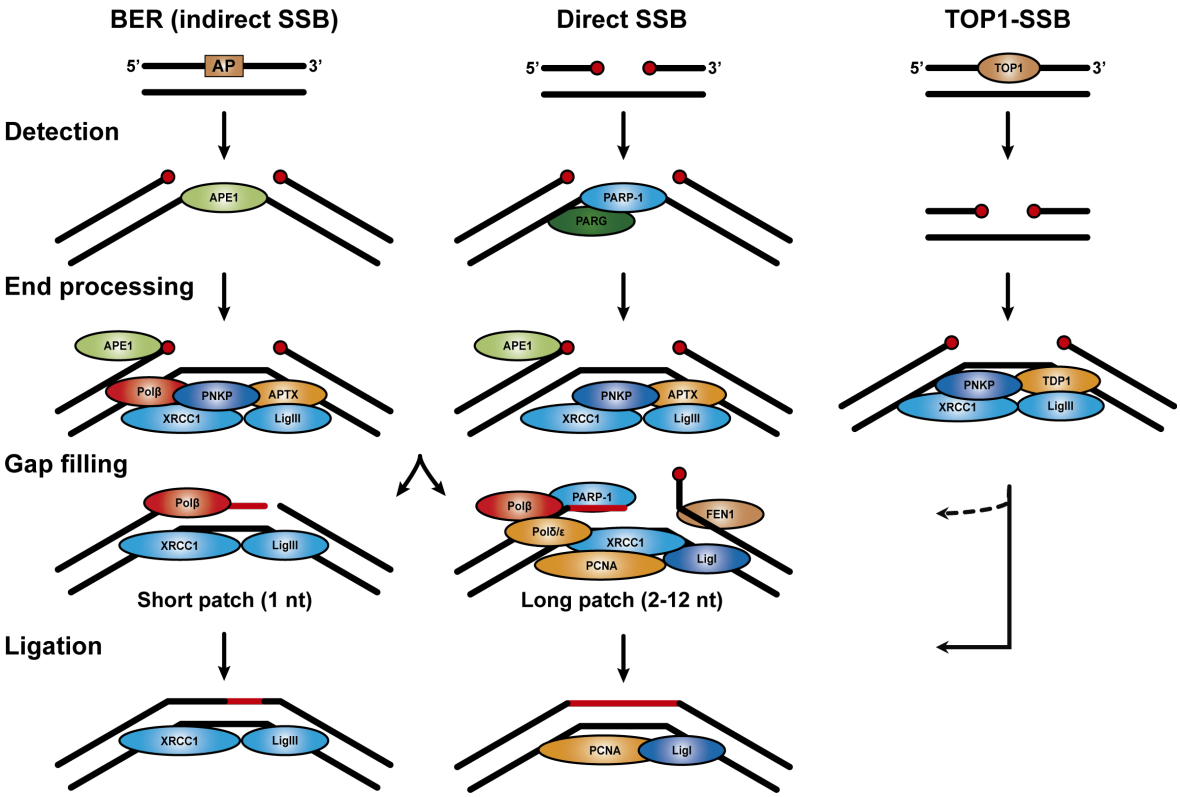


Figure 1.4 Repair of single-strand break (SSB) lesions. SSBs can arise indirectly following processing of an AP site by a DNA glycosylase, being repaired by BER. SSBs can also be directly generated via the interaction of reactive oxygen species with the DNA, or due to abortive topoisomerase 1 (TOP1) activity. During BER the glycosylase processed AP site is hydrolysed by APE1, also catalysing the incision of the damaged strand, leaving a 3'hydroxyl (OH) and a 5'deoxyribose-phosphate (5'dRP) at the margins. Polβ excises the 5' dRP moiety (red circle) during short-patch end processing. Direct breaks are detected by PARP-1, promoting rapid access and accumulation of other repair factors. PARG restores PARP-1 to its natural state in preparation for processing of further SSBs. SSBs generated by DNA glycosylases and due to abortive TOP1 activity occur in a scheduled fashion, therefore they might not require PARP-1 mediated detection. Following SSB detection end processing occurs. End processing of the damaged termini (red circles) present at indirect SSBs, is carried out by APE1, Polβ (which excises the 5' dRP moiety following APE1 processing during BER), PNKP, and APTX. During repair of direct SSBs, end processing is achieved by APE1, PNKP and APTX. TOP1-SSBs are processed by TDP1. The following step is gap filling, which is accomplished by Polβ for most SSBs, inserting the missing nucleotide – short patch repair. In case gap filling requires extension for 2-12 nucleotides, Polβ, and Polε/Polδ carry out nucleotide insertion – long patch repair. The generated flap of two or more displaced nucleotides is removed by FEN1 in a reaction catalysed PARP-1 and PCNA. Ligation is accomplished by LigIII during short patch repair, and by LigI during long patch repair. See text for further details. Adapted from (Caldecott, 2008).

Increasing levels of unrepaired SSBs can lead to the formation of deleterious replication-induced DSBs as cells undergo replication, overloading the cell repair capacity and leading to cell death (Dianov and Hubscher, 2013). When exposed to excessive amounts of DNA damage, the limited amounts of BER enzymes are still sufficient to repair damage above a physiological level. This is possible due to modulation of the BER capacity by PARP-1 molecules, which readily bind to SSBs leading to PAR synthesis subsequently allowing PARP-1 to dissociate from the DNA. PARP-1 also has a role in protecting the DNA SSBs from cell nucleases (Parsons *et al.*, 2005). If the molar amount of SSBs exceeds the molar amount to BER enzymes, PARP-1 protects the DNA ends from deterioration and prevents the formation of DSBs (Woodhouse and Dianov, 2008). PARP-1 activation and promotion of PAR chains leads to its dissociation from the DNA making way for the BER enzymes to access the damage sites, ensuring correct repair. The abundance of PARP-1 ensures protection of the DNA SSB ends, until the BER/SSBR machinery is available to undertake the repair process (Dianov and Hubscher, 2013). PARP-1 relevance in maintaining genomic integrity is demonstrated by PARP-1 knock-out mice which are extremely sensitive to alkylating agents and irradiation, highlighting a limiting capacity to cope with an increasing burden of DNA damage (de Murcia *et al.*, 1997; Wang *et al.*, 1995).

PARP-1 inhibition has been widely investigated when used concomitantly to radiation treatment, in particular breast cancer patients with a diminished capacity to repair replication DSBs through HR due to breast and ovarian cancer susceptibility protein 1/2 (BRCA1/2) deficiencies and mutations (Bryant *et al.*, 2005; Curtin and Szabo, 2013). PARP-1 inhibition leads to the accumulation of SSBs, which are converted into replication DSBs requiring the HR machinery for resolution (Helleday, 2011; Saleh-Gohari *et al.*, 2005), thus resulting in a significantly increased sensitivity to radiation. A deficiency in the HR repair pathway to overcome such lesions, results in an increased damage burden,

which may in turn lead to cell death. All of these aspects highlight the importance of PARP-1 in the maintenance of genomic integrity and the potential of PARP-1 inhibition in broadening radiation treatment therapeutic index by specifically sensitising cancer cells whilst sparing normal tissues (Curtin and Szabo, 2013; Dianov and Hubscher, 2013).

1.5 Mechanisms of DSB repair

DNA double strand breaks are considered the most deleterious and damaging lesions, which can threaten genomic integrity (Rothkamm *et al.*, 2003). These lesions can arise when cells are exposed to exogenous damaging agents such as ionising radiation and certain chemicals. DSBs induced endogenously through ROS are few if any (Bennett *et al.*, 2004; Bennett *et al.*, 2005). In contrast, replication DSBs can be endogenously generated as by-products of cell processes such as DNA replication, V(D)J recombination (Heyer *et al.*, 2010; Woodbine *et al.*, 2014). If DSBs are accumulated and remain unrepaired, they may result in cell cycle arrest, induction of apoptosis or mitotic cell death caused by loss of genomic information (Rothkamm *et al.*, 2003). Misrepair of DSBs can also promote genomic instability through translocations, inversions, or deletions, leading in the worst case scenario to inactivation of tumour suppressor genes or activation of oncogenes, thus promoting carcinogenesis (Bartkova *et al.*, 2005; Gorgoulis *et al.*, 2005; Helleday, 2010; Kasparek and Humphrey, 2011; Weterings and Chen, 2008).

Lesions that affect both DNA strands within one helical turn by a single radiation track are normally termed as clustered DNA damage (see **figure 1.3**) and are thought to be a signature of ionising radiation. DSBs are a form of clustered damage, which can be generated due to the formation of multiple SSBs in close proximity, as a result of accidental chemical modifications, or due to the enzymatic processing of base lesions. Additional base lesions and SSBs in the vicinity of a DSB increase complexity and as a

consequence pose difficulties for the repair processes (Datta *et al.*, 2006; Datta *et al.*, 2005a; Datta *et al.*, 2005b; Datta *et al.*, 2007; Dobbs *et al.*, 2008; Gulston *et al.*, 2004; Mladenov and Iliakis, 2011).

Higher eukaryotes mainly repair DSBs via two repair pathways, NHEJ and HR. In contrast to HR, NHEJ does not require the presence of a sister chromatid as a template to overcome the loss of genetic information and occurs throughout the cell cycle. This repair pathway promotes simple rejoining with little requirement for homology. On the other hand, HR mainly occurs during late S and G2 phases of the cell cycle, using a sister chromatid as a template to restore the sequence lost at the damage site. DSBs arising from collapsed replication forks, due to endogenous and exogenous forms of stress, constitute a chemically different form of DSBs, which also require HR for a complete resolution (Miyagawa, 2008; Mladenov and Iliakis, 2011; Thompson, 2012; West, 2003).

Defects in key factors involved in the repair pathways used for DSB and replicative DSB resolution (such as BRCA1/2) lead to cancer predisposition (**table 1.1**), highlighting that faithful repair of DSBs is indispensable to ensure genomic stability, guaranteeing cell survival and posing a barrier to cancer development (Ciccia and Elledge, 2010; Helleday, 2011).

1.5.1 Homologous recombination (HR) repair pathway

HR is a high fidelity metabolic process existent in most forms of life providing template-dependent repair or tolerance of DNA gaps, DSB including replicative DSB, and DNA interstrand crosslinks (ICLs) (Helleday, 2010; Heyer *et al.*, 2010; Miyagawa, 2008). HR is also involved in the recovery of stalled or broken replication forks. HR also processes lesions remaining from loss or improper operation of base excision repair and nucleotide excision repair or translesion synthesis during replication (Helleday, 2010). Studies based

on organisms such as *Saccharomyces cerevisiae* (*S. cerevisiae*) and *Schizosaccharomyces pombe* (*S. pombe*), which are rapidly grown and easily genetically manipulated, have contributed to the understanding of the mechanisms of recombination in eukaryotes (Filippo *et al.*, 2008; Kasparek and Humphrey, 2011; Rothkamm *et al.*, 2003; West, 2003; Wyman *et al.*, 2004).

The HR repair pathway requires the use of a sister chromatid, which is only present after DNA replication. Such requirement limits appropriate HR activity to S and G2 phases of the cell cycle. To avoid misuse of this repair pathway, HR is controlled by the DNA damage response signalling machinery, and by the cell cycle, relying on cyclin-dependent kinase (CDK) activity, which is limited to S, G2 and M phases of the cell cycle (Filippo *et al.*, 2008; Heyer *et al.*, 2010; Rothkamm *et al.*, 2003).

In response to DSB formation HR repair is promoted in human S and G2 cells with the initiation of resection, which occurs in multi-step processes involving MRE11-RAD50-NBS1 (MRN complex), CTBP-interacting protein (CtIP), exonuclease 1 (Exo1), DNA2 nuclease and Bloom syndrome protein (BLM) helicase (Heyer *et al.*, 2010; Kass and Jasin, 2010; Sartori *et al.*, 2007). CtIP phosphorylation at Ser-327 by CDK2 leads to initiation of end resection. This phosphorylation event allows CtIP to interact with breast and ovarian cancer susceptibility protein 1 (BRCA1) enhancing CtIP resection activity (Yun and Hiom, 2009). BRCA1 is reported to promote RPA-coated ssDNA formation through an interaction with the MRN complex and CtIP (Chen *et al.*, 2008; Schlegel *et al.*, 2006). In fission yeast *S. pombe* $Ctp1^{Sp}$/$CtIP^{Hs}$ is required for the formation of replication protein A (RPA) coated ssDNA at the double-stranded ends, indicating it functions in conjunction with the MRN complex in 5' to 3' resection (Limbo *et al.*, 2007; Takeda *et al.*, 2007). Knockdown of human CtIP in U2OS cells increases sensitivity to IR by 2-fold, indicating CtIP is necessary for end resection and optimal HR repair (Chen *et al.*, 2008). Two

complexes containing the BLM helicase carry out extensive end resection. In conjunction with Exo1, BLM promotes resection irrespectively of its helicase activity (Nimonkar *et al.*, 2008). Additionally, in association with DNA replication helicase/nuclease 2 (DNA2), BLM promotes resection by unwinding dsDNA (Nimonkar *et al.*, 2011). Single-stranded 3' ends resulting from resection are bound and protected by replication protein A (RPA). RPA is responsible for removing secondary structures, which are necessary for RAD51 filament formation (Iftode *et al.*, 1999; Wold, 1997).

RAD51 recombinase is a key factor in HR mediated repair. RAD51 is the eukaryotic homolog of *E. coli* RecA and responsible for homology search and DNA strand invasion (Filippo *et al.*, 2008; Shinohara *et al.*, 1992; West, 2003). RAD51 loading onto ssDNA is dependent on BRCA2, which is facilitated by BRCA1. BRCA2 aids strand invasion via its interaction with RAD51, promoting association of RAD51 to ssDNA in preference of dsDNA, and also favouring the growth of RAD51 filament formation in a 5' to 3' direction as bound RPA is displaced from ssDNA. RAD51 filament formation is promoted by five RAD51 paralogs, acting as accessory factors. These paralogs form two complexes containing RAD51C-XRCC3 and RAD51B-RAD51C-RAD51D-XRCC2 and SWS1 which was identified by sequence similarity with *S. cerevisiae* proteins which interact with yeast homologs RAD51D and XRCC2 (Martin *et al.*, 2006; Masson *et al.*, 2001; Miller *et al.*, 2002). These factors promote RAD51 foci formation in response to ionising radiation damage induction, highlighting their role in stabilising RAD51 filament formation during HR mediated repair of DSBs (Thompson, 2012). The importance of these factors in HR repair is highlighted by the decreased viability of RAD51 paralog mutant DT40 cell lines in response to agents such as cisplatin and ionising radiation (Takata *et al.*, 2001). Causal mutations in RAD51 paralog genes are identified in human cancers (Ingraham *et al.*, 1999; Meindl *et al.*, 2010).

The RAD51 filament searches and pairs with a homologous sequence on the neighbouring sister chromatid present during S and G2 phases of the cell cycle. The RAD54 dsDNA-dependent ATPase facilitates this process, playing an essential role in homologous pairing by interacting with RAD51 enhancing its ATPase activity (Mazin *et al.*, 2010; Tanaka *et al.*, 2002). RAD54 has been shown to form nuclear foci in response to ionising radiation which does not occur in mutants defective in RAD51 focus formation, such as BRCA2, XRCC2, XRCC3 and RAD51C mutants (van Veelen *et al.*, 2005).

RAD51-associated protein 1 (RAD51AP1) promotes the efficiency of RAD51 during HR repair by enhancing its ability to form heteroduplex DNA joints called D-loops (Thompson, 2012; Wiese *et al.*, 2007). POL3, the *S. cerevisiae* homolog of eukaryotic Polδ has been reported to be the main polymerase implicated in HR, carrying out DNA synthesis from the template sequence (Maloisel *et al.*, 2008).

When a second end is not present, the D-loop may become a fully-fledged replication fork in a process known as break-induced replication (BIR) (Heyer *et al.*, 2010; Kasparek and Humphrey, 2011). Despite chromosome integrity restoration, this process can lead to loss of heterozygosity (LOH) of the genetic information distal to the DSB (Kasparek and Humphrey, 2011) (**figure 1.5**).

Another possible outcome is the sub-pathway synthesis-dependent strand annealing (SDSA), on which the resolution of the heteroduplex occurs by releasing the invading strand with the assistance of RAD54, and reannealing to the second end, resulting in a non-crossover (no exchange of genetic material between homologous chromosomes) (Kasparek and Humphrey, 2011; West, 2003). The annealing step is facilitated by RAD52 as suggested by both in vivo and in vitro experiments (Mcllwraith and West, 2008; Stark *et al.*, 2004). RAD52 depletion does not affect RAD51 or RAD54 foci formation in response to IR (van Veelen *et al.*, 2005). However, when RAD52 deficiency is concomitant with

BRCA2 depletion, cells show little capability to proliferate and diminished RAD51 foci formation, highlighting a synthetic lethality between these two factors (Feng *et al.*, 2011) (**figure 1.5**).

RAD52 is also involved in the D-loop capture of the second resected end (Nimonkar and Kowalczykowski, 2009). In this particular case repair synthesis occurs on both sides of the D-loop. The resulting structure is a double Holliday junction (dHJ). BLM together with topoisomerase 3 (TOP3) and RecQ mediated genome instability 1/2 (RMI1/2) can promote dissolution of these structures (Wu and Hickson, 2003). The two junctions are migrated towards each other leading to a hemicatenate, which is dissolved by TOP3 (Thompson, 2012). Dissolution of these intermediates does not cause crossovers, avoiding potential rearrangements which can lead to translocations, deletions and inversions. Double Holliday junctions can also be resolved by structure-selective nucleases, which generate two nicks that are joined resulting in both crossovers and non-crossovers depending on the plane the dHJ is cut. Structure-specific nucleases are Gen1, SLX1-4, and Mus81-EME1 (Heyer *et al.*, 2010) (**figure 1.5**).

Single-strand annealing (SSA), a HR sub-pathway, can also restore chromosomal without strand invasion, with stretches of RPA-coated ssDNA being reannealed by RAD52 (West, 2003). A complex composed by xeroderma pigmentosum group f (XPF), and DNA excision repair protein ERCC1, processes generated ssDNA flaps (Heyer *et al.*, 2010) (**figure 1.5**). Kasparek and Humphrey extensively reviewed the different chromosomal rearrangements associated with HR repair including SSA, BIR, gene conversion and crossovers (Kasparek and Humphrey, 2011).

1.5.1.1 HR role in cancer development and treatment

Many cancers are normally characterised by gross gene rearrangements due to mutated HR genes (Helleday, 2010). Several proteins involved in HR repair such as BRCA1/2 are mutated in breast and ovarian cancer; RAD54 and CtIP are mutated in non-Hodgkin's lymphoma and colon cancer; as well as BLM and Nbs1 in other cancers. The mutation or silencing of HR genes can result in disruption of some of the HR sub-pathways, and likely promoting genetic instability, which can form the basis for cancer development.

As reviewed by Miyagawa, the HR repair pathway is responsible for resolving some of the damage caused by anti-cancer drugs at DNA replication forks (Miyagawa, 2008). Inactivation of this repair pathway can further sensitise cancer cells to treatment. For instance, ovarian cancers are extremely responsive to cisplatin treatment, which can be correlated with a lower expression of BRCA1 or mutations in BRCA1/2. High expression levels of RAD51 in small cell lung cancer cells confer an added resistance to etoposide (topoisomerase 2 inhibitor) treatment, often used to treat this type of cancer. RAD51 and its paralogs may be potential targets for the improvement of etoposide-based chemotherapy.

Therapy-related acute myeloid leukaemia (t-AML) results from a complication caused by chemotherapy and/or radiotherapy treatment of a primary tumour. T-AML development has been associated with high levels of RAD51 expression. RAD51 also interacts with BLM which is upregulated in chronic myelogenous leukaemia (CML) promoting resistance to cisplatin treatment (Miyagawa, 2008). BRCA1/2 deficiencies have been widely associated to breast cancer. BRCA1 upregulation in breast cancer cells can counteract cisplatin therapy, overcoming DNA damage induction.

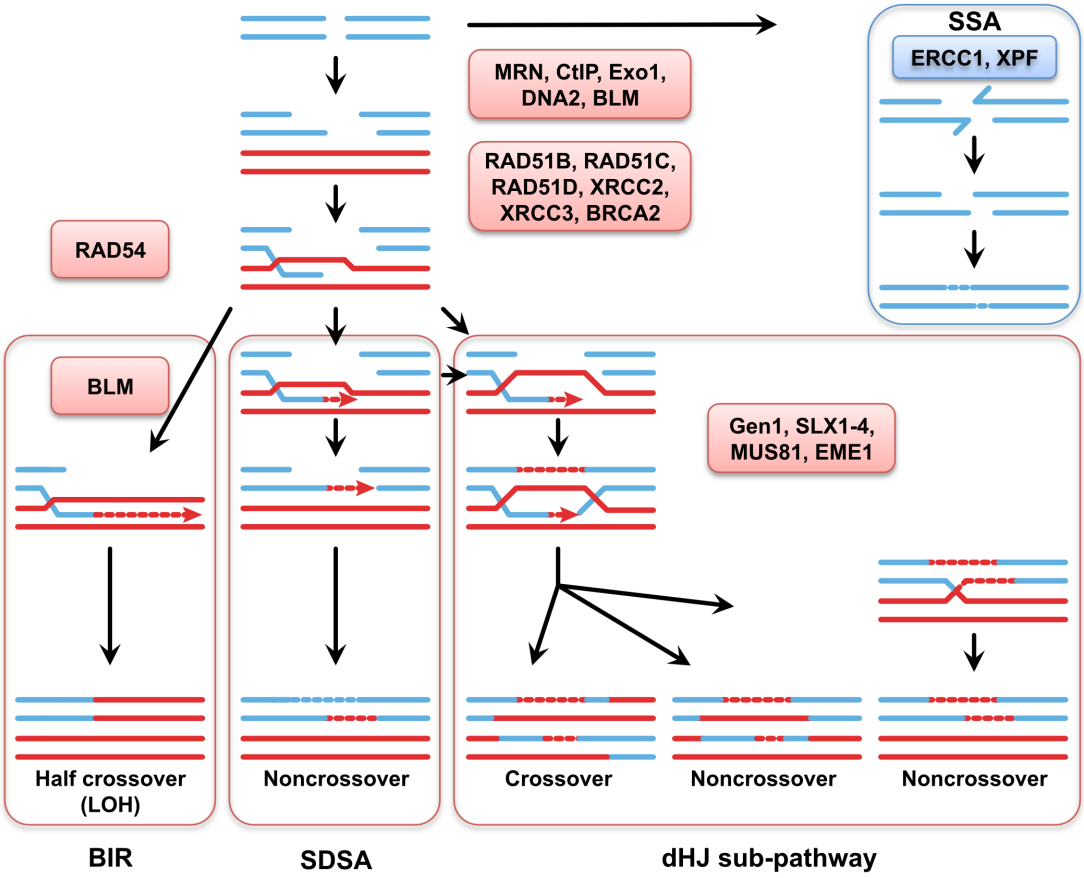


Figure 1.5 DSB repair via homologous recombination (HR). DSBs are detected and processed by the MRN complex. Initial resection is carried out in conjunction with CtIP followed by extensive resection processed by DNA2, Exo1 and BLM. Resulting stretches of ssDNA are coated by RPA. RPA displacement is achieved by RAD51 filament formation promoted by the RAD51 paralogs and BRCA2. RAD51 filament pairs and searches for homology in a process facilitated by RAD54, forming a D-loop structure. Failure in displacing the newly synthesized strand leads to break-induced replication (BIR), promoting replication of the invaded template DNA, potentially causing loss of heterozygosity (LOH). Alternatively the newly synthesized strand can be displaced leading to synthesis-dependent strand annealing (SDSA) leading to non-crossover products. Additionally, the second end can be captured with the aid of RAD52, originating a double Holliday junction, which can be resolved or dissolved leading to crossover and non-crossover products. Failure in RPA displacement by RAD51 filament, promotes a RAD52-dependent annealing of ssDNA stretches in a process termed single-strand annealing (SSA), which involves the formation of overhangs processed by a complex formed by XPF and ERCC1. This HR subpathway leads to the loss of genetic information. See text for further detail. Adapted from (Heyer *et al.*, 2010).

As described in **section 1.4.3**, these patients benefit from treatment with PARP inhibitors in the context of synthetic lethality. Similarly, lung cancer patients with low-levels of BRCA1 expression are more responsive to cisplatin therapy. These facts suggest BRCA1 can be used as a predictive marker for cisplatin resistance (Helleday, 2010).

Additionally, epidermal growth factor receptor (EGFR) inhibitors have been used concomitantly with radiotherapy for treatment of various forms of cancer, providing a survival benefit in lung, head and neck cancers. Erlotinib, an EGFR inhibitor, has been shown to inhibit radiation-induced activation of RAD51, confirming a role in HR-mediated repair in cell survival following radiation treatment (Chinnaiyan *et al.*, 2005).

HR repair is deeply associated with resistance to multiple forms of cancer therapy routinely used in most clinical settings. Similarly to the use of PARP inhibitions in a BRCA1/2 deficient background, exploiting defects in the HR machinery characteristic of specific forms of cancer can provide a rationale to maximise cancer cell killing (Helleday, 2010, 2011; Miyagawa, 2008).

1.5.2 Classical non-homologous end-joining (NHEJ) repair pathway

The classical NHEJ repair pathway is the main repair mechanism used by mammalian cells to resolve DSBs generated by exogenous sources such as ionising radiation or during cell processes such as V(D)J recombination and class switch recombination (Lieber, 2010; Lieber *et al.*, 2003; Woodbine *et al.*, 2014). Unlike HR repair, NHEJ does not require the presence of a sister chromatid and simply involves modification of the two broken DNA ends making them compatible prior to rejoining (Burma *et al.*, 2006; Weterings and van Gent, 2004). This mechanism encompasses a set of enzymes which are responsible for capturing both ends of the broken DNA molecules, followed by the formation of a molecular bridge that brings the two ends together prior to re-ligation of the molecule.

The initial step of this repair process involves binding of the Ku70/80 heterodimer to a DNA end. This heterodimer is highly abundant in the cell nucleus and it also possesses a high affinity to DNA ends (Anderson and Carter, 1996; Blier *et al.*, 1993; Mimori and Hardin, 1986). The ring structure characteristic of Ku70/80 allows it to slide over the ends of a broken DNA molecule (Ristic *et al.*, 2003; Walker *et al.*, 2001). It is thought that this molecule promotes NHEJ-mediated repair by binding to the DNA ends preventing other factors from accessing the substrate, stopping HR repair to occur (Fattah *et al.*, 2010). This particular process can be of great importance to prevent HR to occur prior to DNA replication (Burma *et al.*, 2006).

The DNA end bound Ku70/80 attracts the catalytic subunit of the DNA-dependent protein kinase (DNA-PKcs) and activates its protein kinase activity (Gell and Jackson, 1999; Singleton *et al.*, 1999; van Gent and van der Burg, 2007). Upon binding of DNA-PKcs, the Ku70/80 heterodimer moves approximately 10 base pairs inward, remaining associated with DNA-PKcs (Weterings and van Gent, 2004; Yaneva *et al.*, 1997; Yoo and Dynan, 1999). The assembled DNA-PK complex acquires the ability to phosphorylate a number of substrates. Amongst these substrates, DNA-PKcs autophosphorylation (e.g. Ser-2056) is of great importance for the appropriate functionality of the NHEJ repair pathway (Chan *et al.*, 2002; Ding *et al.*, 2003; Uematsu *et al.*, 2007; van Gent and van der Burg, 2007).

Several clusters of autophosphorylation sites have been mapped, with a cluster composed of seven phosphorylation sites between residues 2609 and 2647 having a great impact on remodelling the DNA-PK complex in order to make the DNA ends accessible for ligation (Block *et al.*, 2004; Ding *et al.*, 2003). Autophosphorylation in the region between residues 2023 and 2056 appears to be involved in reducing the access of nuclease activities to the DNA ends (Chen *et al.*, 2005). Phosphorylation of the 3950 residue has also been reported to influence joining efficiency (Douglas *et al.*, 2007). The presence of DNA-PKcs in its

unphosphorylated form at the DNA termini, blocks the access of processing enzymes and ligases to the DNA ends preventing re-ligation of the broken ends (Block *et al.*, 2004; Weterings and Chen, 2008; Weterings *et al.*, 2003). This phenomenon is thought to occur when the kinase activity of DNA-PKcs is chemically inhibited, allowing DNA-PKcs to be recruited to the DNA ends but blocking access to other repair enzymes due to its unphosphorylated state (Ciszewski *et al.*, 2014; Mahaney *et al.*, 2009; Zhao *et al.*, 2006). Mouse embryonic fibroblasts (MEFs) from DNA-PKcs-deficient mice display high rates of spontaneous chromosomal aberrations compared to DNA-PKcs-proficient cells (Burma *et al.*, 2006; Ferguson *et al.*, 2000; Martin *et al.*, 2005). DNA-PKcs activity in peripheral blood lymphocytes (PBLs) from lung cancer patients is reportedly lower than that of control PBLs (Auckley *et al.*, 2001). Such effect was also noted in uterine, cervix and breast cancer patients (Burma *et al.*, 2006). DNA-PKcs deficient mouse cells also display higher levels of telomeric fusions, highlighting a role for DNA-PKcs in telomere maintenance (Gilley *et al.*, 2001).

However, DNA-PKcs has been reported not to be necessary for all end-joining events, since blunt DNA ends are efficiently joined in DNA-PKcs deficient cells (Lieber *et al.*, 1988; van Gent and van der Burg, 2007). DNA repair in response to ionising radiation damage induction is also more efficient in cells lacking DNA-PKcs when compared to Ku80-deficient cells (Anderson *et al.*, 2010; Reynolds *et al.*, 2012; Riballo *et al.*, 2004). Consistent with these reports is the recent finding that simple DSB induced by radiation are repaired rapidly involving Ku70/80 and XRCC4/Ligase IV/ XRCC4-like factor (XLF) in contrast to complex DSBs which are repaired slowly and require not only Ku70/80 and XRCC4/Ligase IV/XLF but also DNA-PKcs (Reynolds *et al.*, 2012).

Successful ligation following DSB induction requires the presence of a 5’ phosphate and a 3’OH. However, most DNA damaging agents lead to a variety of DNA ends that often

require further processing of the DNA termini involving removal of one or a few damaged bases from the end prior to ligation (Nikjoo *et al.*, 1998). Polynucleotide kinase phosphatase (PNKP) phosphates 5'-OH ends and removes 3' phosphates to give 3'-OH ends, preparing the DNA ends for ligation (Koch *et al.*, 2004). Aprataxin also plays a role in DNA end processing by removing adenylates from 5' termini (Lieber, 2010; Rass *et al.*, 2008).

Artemis resects single-stranded overhangs arising during NHEJ (Jeggo and O'Neill, 2002). The Artemis nuclease was discovered as the mutated gene in the majority of radiosensitive severe combined immunodeficiency (SCID) patients (van Gent and van der Burg, 2007). This nuclease is also important for processing the DNA hairpin structures formed during V(D)J recombination (Ma *et al.*, 2002). Artemis nuclease activity is restricted to a 5' exonuclease activity in the absence of DNA-PKcs. However, Artemis and DNA-PKcs form a physical complex with DNA-PKcs being able to phosphorylate Artemis (Ma *et al.*, 2005). This complex has endonuclease activity at both 5' and 3' overhangs (Jeggo and O'Neill, 2002). Artemis activity is thought to be essential for the rejoining of approximately 15% of a subset of radiation-induced DSBs (Riballo *et al.*, 2004). Further processing can be carried out by Aprataxin and PNKP-like factor (APLF), which is an endonuclease and a 3' exonuclease, complementing the lack of Artemis 3' exonuclease activity (Lieber, 2010).

Damaged or missing bases often lead to non-complementarity, requiring addition of a few nucleotides as part of the NHEJ repair process. Short single-stranded DNA gaps present during NHEJ are normally filled by DNA polymerases Polμ and Polλ (van Gent and van der Burg, 2007).

The concluding step in the NHEJ repair pathway regards ligation performed by the ligase IV (LigIV) XRCC4 complex (**figure 1.6**). The efficiency of this repair pathway is minimal

in the absence of the ligation complex, with a defect in either LigIV or XRCC4 being embryonic lethal in mice (Frank *et al.*, 1998; Gao *et al.*, 1998). XRCC4 is absolutely required for LigIV activity since it provides stability and correct targeting of the DSBs (Hsu *et al.*, 2002; Teo and Jackson, 2000). An interaction between Ku70/80 heterodimer and the LigIV/XRCC4 complex promotes an efficient DNA end ligation. DNA-PKcs also provides additional stability to this complex through interactions with XRCC4 (Burma *et al.*, 2006; Weterings and Chen, 2008; Weterings and van Gent, 2004). XRCC4-like factor (XLF) has also been reported to stimulate NHEJ-mediated repair of DNA DSBs, being mainly important for non-complementary ends, but not an absolute requirement for the majority of DSBs (Gu *et al.*, 2007; van Gent and van der Burg, 2007).

1.5.2.1 Microhomology-mediated end-joining (MMEJ)

A DNA-PKcs and LigIV-independent NHEJ pathway can support a low level of end-joining (Iliakis, 2009). This pathway relies on patches of only a few base pairs of homology that may assist in alignment of the ends. This pathway is normally referred to as microhomology-mediated end-joining (MMEJ), alternative-NHEJ (A-NHEJ), or backup-NHEJ (B-NHEJ) (Mladenov and Iliakis, 2011). This repair mechanism is reportedly error-prone, as chromosomal translocations have been found to contain microhomologies at the junctions. The existence of this NHEJ sub-pathway correlates with the higher frequency of chromosomal translocations in cells with defects in NHEJ-associated factors (Mladenov and Iliakis, 2011; van Gent and van der Burg, 2007).

Ku70/80 is thought to be the main protein responsible for preventing the occurrence of MMEJ. Ku rapidly binds to the DNA ends suppressing MMEJ and HR DSB repair, regulating access to the substrate by other factors. In the absence of Ku, other repair factors can more freely access the DNA ends and pursue repair via other pathways (Fattah *et al.*,

2010). MMEJ is initiated with PARP-1 being recruited to the DSB particularly in the absence of Ku. In addition to the recruitment of DNA-PKcs, Ku also exerts DNA end alignment functions prior to ligation. Evidence that histone H1 facilitates end joining suggests a direct effect on MMEJ repair enhancing both PARP-1 and LigIII activity (Mladenov and Iliakis, 2011). Observations of the repair of etoposide-induced lesions specifically in G0/G1 cells, and end-resection events in XRCC4-deficient cells, provided further insight regarding the involvement of the MRN complex and CtIP in promoting end resection during the DNA end processing step of MMEJ repair (Quennet *et al.*, 2011; Xie *et al.*, 2009). Ligation is carried out by LigIII/XRCC1 complex (Bétermier *et al.*, 2014; Mladenov and Iliakis, 2011) (**figure 1.6**).

1.5.2.2 Clinical impact of NHEJ deficiencies

NHEJ is the main DSB repair pathway employed by mammalian cells to resolve DSBs arising endogenously or due to exposure to exogenous agents such as ionising radiation. The process of V(D)J recombination functions during the development of the immune response and involves the introduction and rejoining of programmed DSBs, which require NHEJ for their resolution (Lieber, 2010; Lieber *et al.*, 2003). Failure in rejoining such breaks leads to SCID. Amongst SCID patients there is a radiosensitive sub-class (RS-SCID). Mutations in factors such as LigIV, XLF, DNA-PKcs and Artemis, involved in NHEJ have been associated with the development of SCID.

Woodbine *et al.* have extensively reviewed the clinical impact of deficiencies in NHEJ-associated factors (Woodbine *et al.*, 2014). Loss of LigIV function is known to cause embryonic lethality in mice with extensive neuronal apoptosis (Frank *et al.*, 1998). Fibroblasts obtained from LigIV syndrome patients with lymphoid tumours show enhanced radiosensitivity reflecting compromised DSB repair capacity.

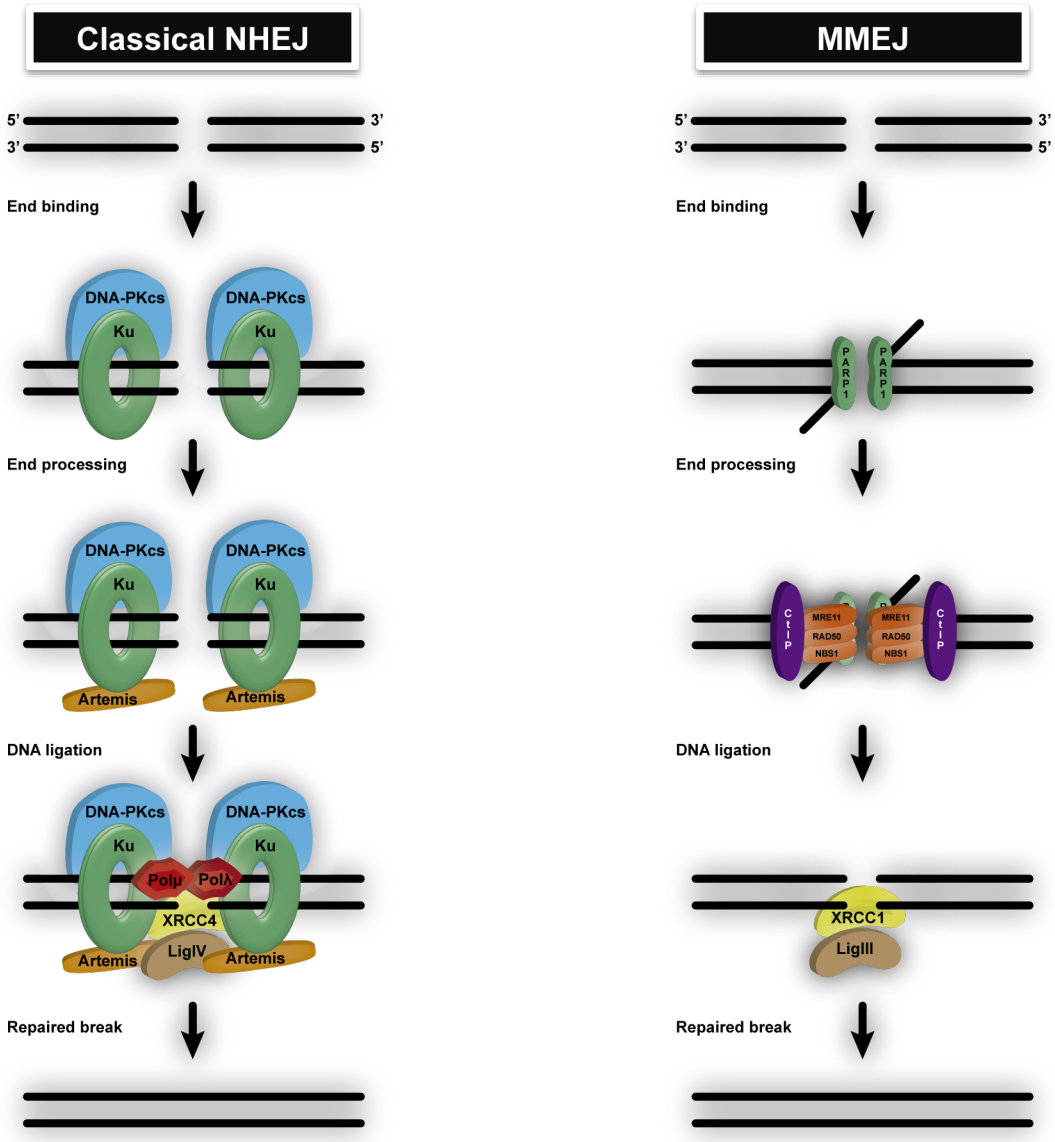


Figure 1.6 DSB repair via non-homologous end-joining (NHEJ). NHEJ repair can occur via either classical NHEJ or via microhomology-mediated end-joining (MMEJ). During classical NHEJ, Ku associates to the DNA ends promoting the recruitment and subsequent catalytic activation of DNA-PKcs. DNA-PKcs promotes end processing by the Artemis nuclease, preparing the DNA ends for ligation by the XRCC4/LigIV complex. In the absence of Ku, PARP-1 binds to the DNA ends promoting MMEJ. The MRN complex together with CtIP carry out resection, prior to ligation of the micro-homologous complementary DNA strands mediated by XRCC1/LigIII. See text for further details. Adapted from (Mladenov and Iliakis, 2011).

Additionally, LigIV deficiency in a p53-deficient background results in lymphoid tumours. XLF mutated patients display microcephaly and growth retardation. XLF-depletion in mice does not result in embryonic lethality, although the mice are characterised by spontaneous genomic instability and higher frequency of chromosomal translocations. Even though XLF may not be required for the repair of all NHEJ-processed DSBs, the loss of this factor profoundly impacts on this repair process. XLF inactivation has a similar clinical manifestation to that observed in a LigIV mutated setting. XLF-defective fibroblasts derived from patients display a similar level of radiosensitivity and DSB repair impairment to that observed in LigIV syndrome patients (van Gent and van der Burg, 2007; Woodbine *et al.*, 2014).

As mentioned before, Artemis deficient patients represent a common case of SCID and also exhibit increased sensitivity to ionising radiation. However, Artemis knock-out mice are viable, and Artemis-null cells derived from patients display a fraction of unrepaired DSBs in response to ionising radiation, which differs from the phenotype observed with LigIV syndrome and XLF-deficient patient cells (Jeggo and O'Neill, 2002; van Gent and van der Burg, 2007; Woodbine *et al.*, 2014). Similarly, DNA-PKcs depletion results in SCID development in mice with no additional phenotypes. Knowledge of the patient's genetic background can help to stratify treatment accordingly to the radiosensitive class of the patient. In general, identification of patients with difficulties in resolving DSBs via NHEJ repair, could in principle help to predict which patients would not respond well to the radiation doses necessary to overcome certain tumours, and serve to assign those patients to alternative forms of treatment (Woodbine *et al.*, 2014).

Moreover, being an error-prone repair pathway, NHEJ can result in chromosomal translocations compromising genetic stability. In case of a compromised NHEJ repair pathway, the frequency of chromosomal translocations is reported to increase (Mladenov

and Iliakis, 2011; van Gent and van der Burg, 2007). This effect suggests the incapacity of cells to resolve DSBs via the classical NHEJ repair pathway, paves the way for MMEJ repair. The elevated frequency of translocations observed in NHEJ impaired cells, suggest MMEJ is more prone to originate such aberrations. Aside from the clinical outcomes associated with mutations and loss of NHEJ-associated factors, the incapacity to repair DSBs via NHEJ leads to a higher dependency on the error-prone MMEJ repair pathway promoting increased levels of chromosomal translocations, contributing to genomic instability and ultimately cancer development (Mladenov and Iliakis, 2011; Woodbine *et al.*, 2014).

1.6 DNA damage response (DDR)

The DNA repair pathways are supported by an evolved and organised effort to overcome endogenous and exogenous stresses posed to genomic DNA named the DNA damage response (DDR). The DDR machinery is responsible for sensing and signalling problems in the DNA, promoting cell cycle arrest, DNA repair, cell death through apoptosis in case of extensive damage, or terminal differentiation through senescence (Ciccia and Elledge, 2010).

The cell response to DNA damage is regulated and coordinated by the DDR network, using signalling sensors, transducers, mediators and effectors (Harper and Elledge, 2007; Jackson and Bartek, 2009; Marechal and Zou, 2013). The DDR machinery is generally activated in the presence of DNA damage or replication stress. Additionally, the DDR sensing molecules are responsible for recognising compromised DNA structures and activating the most upstream DDR kinases, which initiate a signalling cascade with the aid of mediator molecules facilitating phosphorylation events. Effector molecules are generally substrates of the DDR kinases, promoting a plethora of cell processes such as DNA

replication, DNA repair and cell cycle control (Harper and Elledge, 2007; Jackson and Bartek, 2009; Marechal and Zou, 2013) (**figure 1.7**).

Numerous diseases and cancer-predisposition syndromes have been associated with mutations in DDR genes, highlighting the importance of this network in the maintenance of genomic integrity (Ciccia and Elledge, 2010).

1.6.1 DNA damage sensing

The MRN complex is the main damage sensor in response to DSB induction, being one of the first factors recruited to DSBs, promoting the recruitment of one of the major DDR kinases ataxia-telangiectasia-mutated (ATM) (Lee and Paull, 2005). In response to radiation damage the MRN complex recruits Tip60 (histone acetyltransferase) to nuclear foci (Chailleux *et al.*, 2010). Chromatin remodelling and acetylation by Tip60 lead to ATM activation and subsequent autophosphorylation at Ser-1981 (Sun *et al.*, 2005). ATM is a serine/threonine kinase member of the phosphatidylinositol-3-kinase-like kinase family (PI3KK). The MRN complex is required for rapid localisation of ATM to DSBs and subsequent activation. When recruited to DSBs, ATM, which generally exists as inactive dimers, dissociates and autophosphorylates on multiple residues (Bakkenist and Kastan, 2003). Such phosphorylation events are thought to be important to maintain ATM activity (Harper and Elledge, 2007). The requisite of dsDNA free ends by the MRN complex to successfully activate ATM is supported by in vitro studies, suggesting dsDNA ends stimulate MRN-mediated ATM activation in a length-dependent fashion (Jazayeri *et al.*, 2008; Lee and Paull, 2005). In response to replication stress, extensive RPA-coated ssDNA regions are formed promoting DNA replication responses mediated by another major PI3KK kinase ataxia-telangiectasia and RAD3-related (ATR).

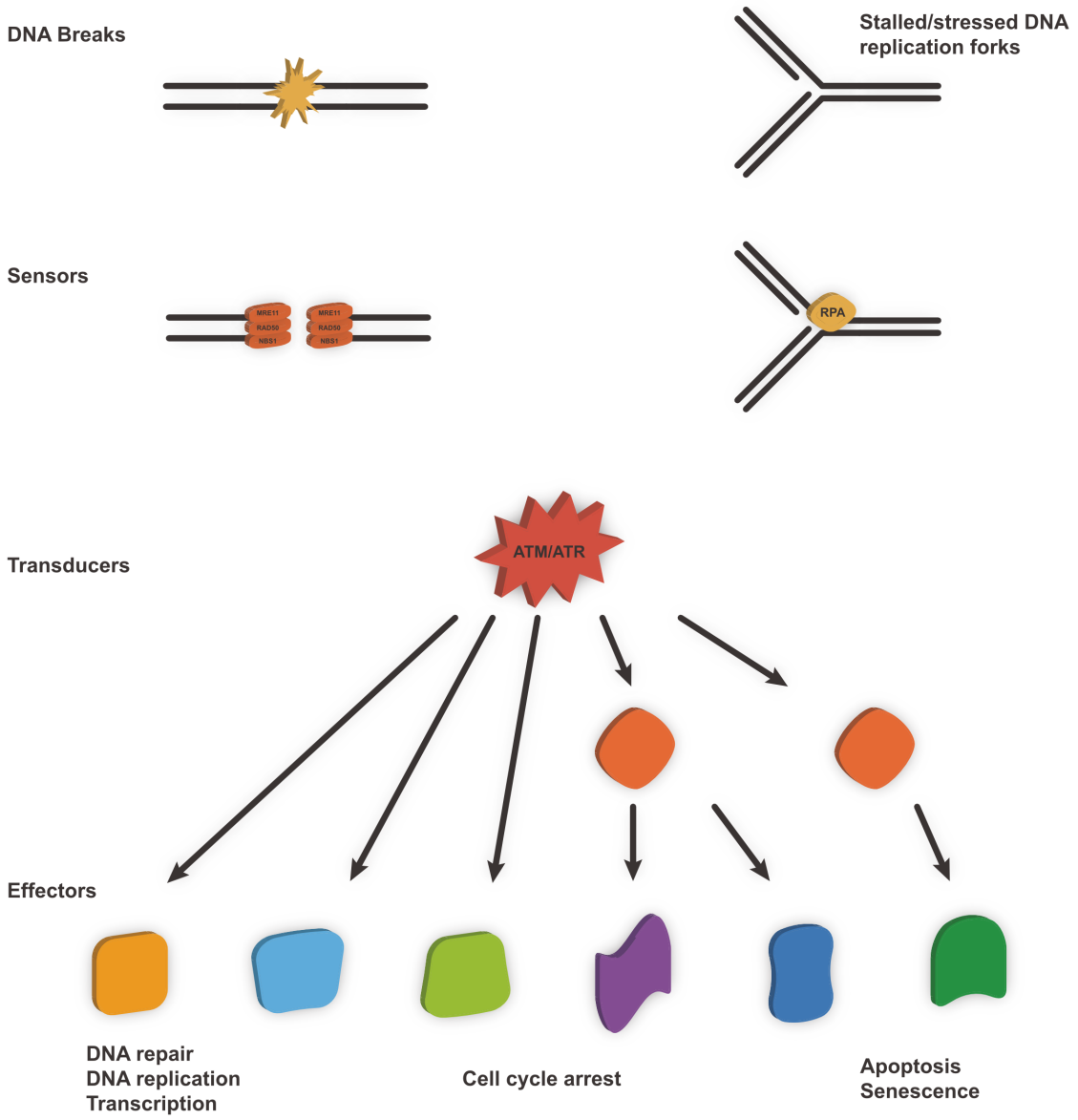


Figure 1.7 DNA damage response (DDR) signalling pathway. The DDR machinery is composed of signal sensors, transducers, and effectors. DNA breaks and stalled/stressed replication forks are sensed by the MRN complex and RPA respectively. Following sensing of the damage, the signalling is carried out by the transducer molecules ATM and ATR and their downstream kinases. The effectors of the DDR signalling pathway are substrates of ATM, ATR and their downstream kinases. The effectors are responsible for activating a plethora of cell processes such as DNA repair, cell cycle arrest, apoptosis and senescence, in an effort to maintain genomic stability. See text for further details. Adapted from (Marechal and Zou, 2013).

RPA-coated ssDNA regions recruit the ATR/ATR-interacting protein (ATRIP) complex localising it to the fork (Byun *et al.*, 2005; Zou and Elledge, 2003). ATR activity promotes activation of CHK1 and CHK2 kinase signalling, triggering phosphorylation events of multiple chromatin-bound factors, stimulating fork stability and restart of stalled or collapsed replication forks (Ciccia and Elledge, 2010; Cimprich and Cortez, 2008).

1.6.2 DDR signal transduction

The signal transduction is initiated following sensing of DNA damage and replication stress, setting in motion a cascade of events to protect the genomic integrity of cells. In an initial step both ATM and ATR phosphorylate mediator proteins, which aid in the recruitment of other ATM/ATR substrates, amplifying the DDR pathway (Ciccia and Elledge, 2010). Effector proteins promoting multiple physiological responses such as cell death and DNA repair are either directly phosphorylated by ATM/ATR or by the CHK1 and CHK2 kinases (Harper and Elledge, 2007). ATM and ATR activity is necessary to promote multiple DNA repair pathways and is also involved in the activation of WEE1 kinase and CDC25 phosphatases, regulating an inhibitory phosphorylation of cyclin-dependent kinases (CDK) CDK1 and CDK2, thus controlling progression into both S phase and mitosis (Harper and Elledge, 2007).

ATM and CHK2 are also known to regulate p53 in response to DNA DSBs induction. p53 can promote cell cycle arrest, apoptosis and senescence by transcriptionally regulating the activity of the CDK inhibitor p21 and the apoptotic-promoting factors BAX and PUMA amongst others (Ciccia and Elledge, 2010; Riley *et al.*, 2008). ATM cyclically regulates the activation of p53 through a negative regulatory circuit involving the WIP1 phosphatase and the MDM2 E3 ubiquitin ligase, which promotes p53 degradation by the ubiquitin-proteasome system (Batchelor *et al.*, 2009; Ciccia and Elledge, 2010).

1.6.2.1 DNA DSB recognition by ATM

As previously mentioned, DSBs are the most deleterious lesions cells can experience. ATM activation is a key event in the signalling cascade promoting the repair of such cytotoxic abnormalities. The significance of ATM activity is highlighted by the exacerbated radiosensitivity exhibited by ATM-deficient cells derived from ataxia-telangiectasia (AT) patients, and in response to ATM chemical inhibition such as the small molecule inhibitor KU55933. AT cells denote defective DSB repair as well as G1/S, intra-S and G2/M checkpoint activation (Hickson *et al.*, 2004; Lavin, 2008; Marechal and Zou, 2013; Shiloh, 2003).

Following damage sensing, the MRN complex recruits Tip60 (histone acetyltransferase) to nuclear foci (Chailleux *et al.*, 2010). Chromatin remodelling and acetylation by Tip60 lead to ATM activation and subsequent autophosphorylation at Ser-1981 (Sun *et al.*, 2005). ATM is rapidly localised to dsDNA ends being activated driving a series of phosphorylation events. Within or in close proximity to heterochromatic regions ATM facilitates DSB repair by phosphorylating KRAB-associated protein 1 (KAP1) on Ser-824 promoting chromatin decondensation thereby facilitating repair (Goodarzi *et al.*, 2008; Noon *et al.*, 2010; White *et al.*, 2006; Ziv *et al.*, 2006).

1.6.2.1.1 Mediators: DNA damage foci

Additionally, Histone H2A variant H2AX is phosphorylated on Ser-139, generally referred to as γ-H2AX (Rogakou *et al.*, 1998). H2AX phosphorylation is the most prominent DDR-associated histone modification. γ-H2AX is generally constrained to microscopically discernable structures known as ionising radiation-induced foci (IRIF) (Giglia-Mari *et al.*, 2011; Rogakou *et al.*, 1999). H2AX phosphorylation spreads over 1-2 megabases around DSBs in an ATM-dependent fashion (Harper and Elledge, 2007). γ-H2AX foci co-localise

with most of the DSB-associated DDR molecules, and are thought to serve as a docking platform for the assembly of DNA repair and signalling factors (Giglia-Mari *et al.*, 2011). These foci are generally thought to resemble DSB including replicative DSB present in the genomic DNA. The persistence of foci has generally been thought to reflect DSB processing during their repair, where γ-H2AX dephosphorylation has not yet occurred allowing checkpoint recovery (Downey and Durocher, 2006). γ-H2AX foci formation has been widely accepted as a DNA damage biomarker in response to different damaging agents, and used as a measure to estimate repair kinetics and sensitivity to treatment (Bonner *et al.*, 2008; Kinner *et al.*, 2008; Lobrich *et al.*, 2010) although some confusion in discerning the repair pathways may arise especially in S-phase cells if both DSB and replication DSB are present. γ-H2AX foci can be detected in early-stage tumours serving as a surrogate marker for the accumulation of DNA damage, thus allowing observation of genomic instability in the evolution of cancer (Bartek *et al.*, 2007). H2AX depletion prevents the formation of IRIF for most proteins but only a mild effect was observed on genomic stability and both DNA damage sensitivity and signalling (Harper and Elledge, 2007).

Moreover, ATM phosphorylates the mediator DNA-damage checkpoint protein 1 (MDC1), which directly binds to γ-H2AX and amplifies H2AX phosphorylation (Stewart *et al.*, 2003). MDC1 bound to γ-H2AX provides a platform for the initiation of ubiquitylation and SUMOylation cascades promoting the recruitment of BRCA1 and 53BP1 (Marechal and Zou, 2013; Stewart, 2009; Wang *et al.*, 2002).

p53 binding protein 1 (53BP1) is an important regulator of DSB signalling, being first described as a binding partner of the vastly characterised tumour suppressor p53 (Iwabuchi *et al.*, 1994). 53BP1 can be considered as both a mediator and an effector of the DDR pathway (Panier and Boulton, 2014). In response to DNA damage, ATM rapidly

phosphorylates 53BP1 on multiple residues including Ser-25 and Ser-1778 (Jowsey *et al.*, 2007; Matsuoka *et al.*, 2007; Ward *et al.*, 2003). In the first instance, 53BP1 behaves as a molecular scaffold for the recruitment of additional factors to DSB sites such as RAP1-interacting factor 1 (RIF1) (Silverman *et al.*, 2004). On the other hand, 53BP1 localisation at IRIF is known to amplify ATM activity and to promote checkpoint signalling in the presence of low levels of DNA damage (DiTullio *et al.*, 2002; Fernandez-Capetillo *et al.*, 2002; Mochan *et al.*, 2004). In the absence of 53BP1, the phosphorylation of ATM substrates such as p53, CHK2 and BRCA1 is reduced, resulting in G2/M checkpoint defects, leading to genomic instability (DiTullio *et al.*, 2002; Fernandez-Capetillo *et al.*, 2002).

53BP1 stimulates ATM activity via an interaction with the MRN complex, known to promote ATM localisation to DSB sites (Lee and Paull, 2007). Similarly to γ-H2AX, 53BP1 is rapidly localised to the damage sites in response to DSB induction, and its recruitment to nuclear foci can be microscopically detected (Rappold *et al.*, 2001; Schultz *et al.*, 2000). Additionally, the kinetics of resolution of 53BP1 foci is similar to the kinetics of DSB repair following IR treatment (Asaithamby *et al.*, 2008; Rappold *et al.*, 2001; Schultz *et al.*, 2000). Fluorescently labelled 53BP1 has been used as a surrogate marker for DSB and replication DSB repair following damage induction in living cells, with the advantage of allowing monitoring of damage formation and repair with prior knowledge of the damage present at the time of treatment (Asaithamby and Chen, 2009).

1.6.2.1.2 53BP1-BRCA1 regulation of DSB repair

53BP1 has been reported to be involved in promoting DSB repair via NHEJ when cells are present in G1 phase of the cell cycle. 53BP1 preserves the DSB ends blocking end resection, thus favouring NHEJ over HR repair (Bunting *et al.*, 2010). Recent reports have

suggested cooperation between 53BP1 and its effector RIF1 in promoting NHEJ repair in G1 cells (Chapman *et al.*, 2013; Escribano-Diaz *et al.*, 2013; Zimmermann *et al.*, 2013). Cells lacking RIF1 and both 53BP1 and RIF1 exhibit similar sensitivity to radiation treatment, and a comparable defect in NHEJ mediated repair (Chapman *et al.*, 2013; Escribano-Diaz *et al.*, 2013). Additionally, cells without RIF1 and 53BP1 independently or concomitantly, display increased ATR signalling at IR-induced DSBs suggesting extensive regions of RPA-coated ssDNA (Chapman *et al.*, 2013; Panier and Boulton, 2014).

53BP1 binding to DSBs blocks HR repair in BRCA1 deficient cells blocking resection (Bunting *et al.*, 2010). It has been observed by super-resolution microscopy that even though 53BP1 accumulates in DSBs arising in G1, S and G2, it is displaced from the core of S phase foci in a BRCA1-dependent manner (Chapman *et al.*, 2012). BRCA1 is known to form a complex with CtIP following phosphorylation of this factor on Ser-327 by CDK2, promoting the initiation of end resection, thus producing a substrate for HR and evicting pro-NHEJ factors such as 53BP1 and RIF1 from DSB sites (Escribano-Diaz *et al.*, 2013). 53BP1-RIF1 block accumulation of BRCA1 at DSB sites in G1 cells, promoting NHEJ, however upon entry into S phase BRCA1 promotes a switch in the repair of lesions by excluding 53BP1-RIF1 from the DSB sites, leading to extensive resection and the initiation of HR repair (Escribano-Diaz *et al.*, 2013). Several studies have also reported the HR defect in BRCA1-deficient cells can be circumvented by 53BP1 depletion providing further evidence for the balance between these two factors in regulating HR-mediated repair (Bouwman *et al.*, 2010; Bunting *et al.*, 2010; Cao *et al.*, 2009).

1.6.2.2 ATR activation by DNA damage and replication stress

In contrast to ATM, ATR has a seminal role in survival as demonstrated by the early embryonic lethality resultant from its deletion in both mouse and human cells (Brown and

Baltimore, 2000; Cortez *et al.*, 2001). ATR constantly monitors replication fork progression protecting cells from intrinsic forms of stress which can naturally occur during S phase of the cell cycle (Casper *et al.*, 2002). ATR aids to the maintenance of genomic stability by triggering a cascade of phosphorylation events, recruiting factors that operate at replication forks and origins. Such signal transduction aims to protect the genome during DNA synthesis by regulating nucleotide pools, fork progression, origin firing, and stimulating DNA repair mechanisms to act on stalled/collapsed replication forks (Marechal and Zou, 2013).

The ATR-ATRIP complex is recruited to regions of RPA-coated ssDNA following DNA damage and stressed replication forks (Zou and Elledge, 2003). Regions of RPA-coated ssDNA are generated at or behind replication forks when the interplay between helicases and polymerases is compromised by both intrinsic impediments and DNA damage. The capacity of the ATR-ATRIP complex in recognising RPA-coated ssDNA stretches confers it sensitivity to sensing DNA damage and replicative stress (Zou and Elledge, 2003). Additionally to RPA-ssDNA, ssDNA-dsDNA junctions are equally important in promoting ATR activation. These junctions, which accompany ssDNA regions, are recognised by the RAD17-RFC2-5 clamp loader complex, which promotes the recruitment of the RAD9-HUS1-RAD1 (9-1-1) heterotrimer stimulating ATR activity (Blaikley *et al.*, 2014; Zou *et al.*, 2003). ATR autophosphorylation on Thr-1989 creates a docking site for topoisomerase 2 binding protein 1 (TopBP1) (Liu *et al.*, 2011). TopBP1 is recruited to the damage sites following interaction with the 9-1-1 complex, functioning to stimulate ATR activity (Marechal and Zou, 2013). CHK1 activation is mediated by Claspin, a DNA replication protein, which becomes phosphorylated by ATR at sites of replication stress, leading to CHK1 binding and subsequent activation (Harper and Elledge, 2007). This multistep process leading on to ATR activation ensures ATR is only activated when both ssDNA and

ssDNA/dsDNA junctions are present at sites of damage and are recognised by DNA damage sensors, providing a fail-safe mechanism for full ATR activation (Marechal and Zou, 2013).

1.6.3 Interplay between ATM and ATR

ATM and ATR are both critical for checkpoint responses and DSB repair in response to damage, suggesting they complement each other in these functions. ATR is activated by RPA-coated ssDNA stretches, whereas the MRN complex promotes ATM activation following DSB formation (Lee and Paull, 2005; Zou and Elledge, 2003). ATM contributes to DSB repair both via HR and NHEJ (Marechal and Zou, 2013). During HR ATM stimulates efficient resection possibly by regulating CtIP and Exo1 (Bolderson *et al.*, 2010; You *et al.*, 2009). Consistent with the idea that DSB resection is important for ATR activation, depletion of ATM, MRE11, CtIP, Exo1 and DNA2 all result in a decrease in ATR activity following DSB induction (Marechal and Zou, 2013). DSB resection not only promotes ATR activation but also modulates the interplay between ATM and ATR at DSB sites. Double-stranded DNA was found to activate both ATM and ATR, although with the gradual lengthening of ssDNA stretches during DSB resection there is a switch from activating ATM to ATR (Shiotani and Zou, 2009). Activation of ATR following resection leads to the activation of its effector kinase CHK1 which has been suggested to phosphorylate RAD51 when DSBs arise at stalled replication forks, promoting their repair via HR (Sorensen *et al.*, 2005).

ATR has also been shown to phosphorylate histone H2AX in response to replication stress promoting the recruitment of ATM to the chromatin regions adjacent to the stressed replication regions (Ward and Chen, 2001). Conversely, ATM has been shown to phosphorylate TopBP1 and suggested to promote its recruitment to sites of DNA damage

via MDC1 and γ-H2AX, stimulating its interaction with ATR, known to enhance ATR activity (Marechal and Zou, 2013; Yoo *et al.*, 2007). Additionally ATM and ATR can be substrates of one another with ATR having been shown to phosphorylate ATM on Ser-1981 following replicative stress (Stiff *et al.*, 2006).

Even though ATM and ATR share some substrates the two kinases are thought to phosphorylate them in response to different types of stress or during different phases of the DDR. Genetic evidence suggests despite the crosstalk between these two kinases, their role in maintaining genomic stability is non-redundant (Marechal and Zou, 2013).

1.7 Aims of the study

The primary aim of this project was to develop a low-LET radiation facility based upon a 6 MeV linear accelerator, to deliver short pulses of low-LET radiation, coupled to an imaging system for real-time studies using mammalian cells under physiological conditions.

Following development, this system was validated through acquisition of preliminary data on the dynamics of repair of radiation induced DNA damage in mammalian cells in real-time. For validation, HT1080 mammalian cells, constitutively expressing 53BP1-YFP, were used to assess the recruitment of 53BP1 to DNA damage sites in a time-lapse fashion following short-pulse electron radiation.

Following validation, this setup allows time lapse studies to be undertaken in response to low-LET irradiation of mammalian cells to monitor promptly formed DSB and ask the question if DSB are formed at later times, indicative of replication DSB or DSB arising from processing of clustered DNA damage. Evidence for the latter has been previously reported (Gulston *et al.*, 2004).

A second aim was to develop a cell line by further transfecting HT1080-53BP1-YFP cells with Geminin-mCherry to be able to follow cell cycle phase-specific DNA damage formation and repair kinetics in living cells, in an effort to further understand the dynamics of radiation-induced damage leading to replicative stress. Preliminary data highlight the potential of such approach to follow the fate of each individual focus, the detection of which is not possible with present methods generally used based on immunostaining of proteins or laser micro-irradiation. In the latter approach, individual damage sites are not formed due to the heterogeneous formation of DNA damage.

From the 'proof-of-principle' experiments it is intended that the understanding of repair/signaling pathways at early times is extended. The use of this novel technology has potential to explore the dynamics of numerous biological processes. The knowledge obtained may be used to identify potential biological targets coupled with drug discovery for translation into adjuncts for radiotherapy.

The inevitably complex experimental setup described in this report was developed in collaboration with staff of the Advanced Technology Development Group. I was involved in all aspects of the post-accelerator setup and designed the details of the irradiation setup, sample holder, environmental enclosure, and contributed to the construction of the imaging system. I carried out all the experimental work presented in this thesis.

2. Linac experiment system

2.1 Introduction

This chapter addresses the different component parts of the linac experiment system, developed to perform DNA repair kinetics studies in living mammalian cells in response to low-LET radiation damage. The irradiation component of the linac experiment system is a 6 MeV electron linear accelerator capable of delivering biologically relevant doses in sub-microsecond pulses. Following damage induction, a common method to perform real-time DNA repair kinetics studies is to image living cells containing fluorescently labelled DNA damage markers (Asaithamby and Chen, 2009). The described experimental setup overcomes some of the issues involving irradiations at low dose-rates, where there is the possibility of repair processes occurring during damage induction. In contrast, high dose-rates allow monitoring of repair processes at short times post damage induction.

Fast imaging of repair processes is accomplished by an *in situ* microscope system. An integrated robotic unit allows automated sample transfer between irradiation and imaging locations. This system transfers remotely and repetitively custom-designed samples between irradiation and imaging locations within 2 sec. This setup is integrated within a custom-designed environmental enclosure to maintain physiological conditions appropriate for cell growth at 37°C and 5% CO_2 humidified air.

2.2 Linear accelerator

The radiation source used in this work is a 6 MeV electron linear accelerator (**figure 2.1a**), constructed from the waveguide, beam focus and radiofrequency systems from a clinical

Elekta SL75-5 accelerator (Vojnovic, 2011a). The accelerating structure is located within a Faraday cage. This system has a single-shot modulator producing user-defined electron pulse widths in the range of 20 ns to 1 μs (Vojnovic, 2011b). This modulator is used to raise the gun injection potential to ~50 kV (diode type of gun) and uses a double switch Blumlein delay line structure, capable of producing pulse widths defined by the delay between firing of two thyratrons (high voltage switches) at either end of a balanced delay line, in an arrangement similar to that described in (de Angelis *et al.*, 2008).

The beam shape, position, and orientation can be set using a quadrupole doublet focusing system (**figure 2.1d**). One of the quadrupole magnets focuses in the horizontal direction, the other in the vertical direction. The beam shape and dimensions can be viewed by monitoring Čerenkov emission (Cerenkov, 1937) from a silica disc with the aid of a periscope and Charge-Coupled Device (CCD) camera synchronised to the electron pulse (**figure 2.1b**). This system is used mainly for beam alignment purposes. The total charge leaving the accelerator can be measured with an inductive monitor (Vojnovic, 1984, 1987) in the output beam line (**figure 2.1c**). A large ferrite toroidal core, wound with a single layer of copper wire is placed around the beam line. This monitor is arranged as a tuned circuit which resonates when the beam pulse traverses the core. The peak circuit voltage is proportional to total pulse charge (Zimek, 1978). The charge monitor output was recorded and calibrated against physical dose measurements (**section 3.2.4**). The beam current can be monitored directly with a beam target, as shown in **figure 2.3b**. This setup allows irradiations using various beam shapes and pulse widths to deliver biologically relevant doses over the range of <0.1 Gy to >>100 Gy per pulse. Linac dosimetry is addressed in **section 3.2.4**.

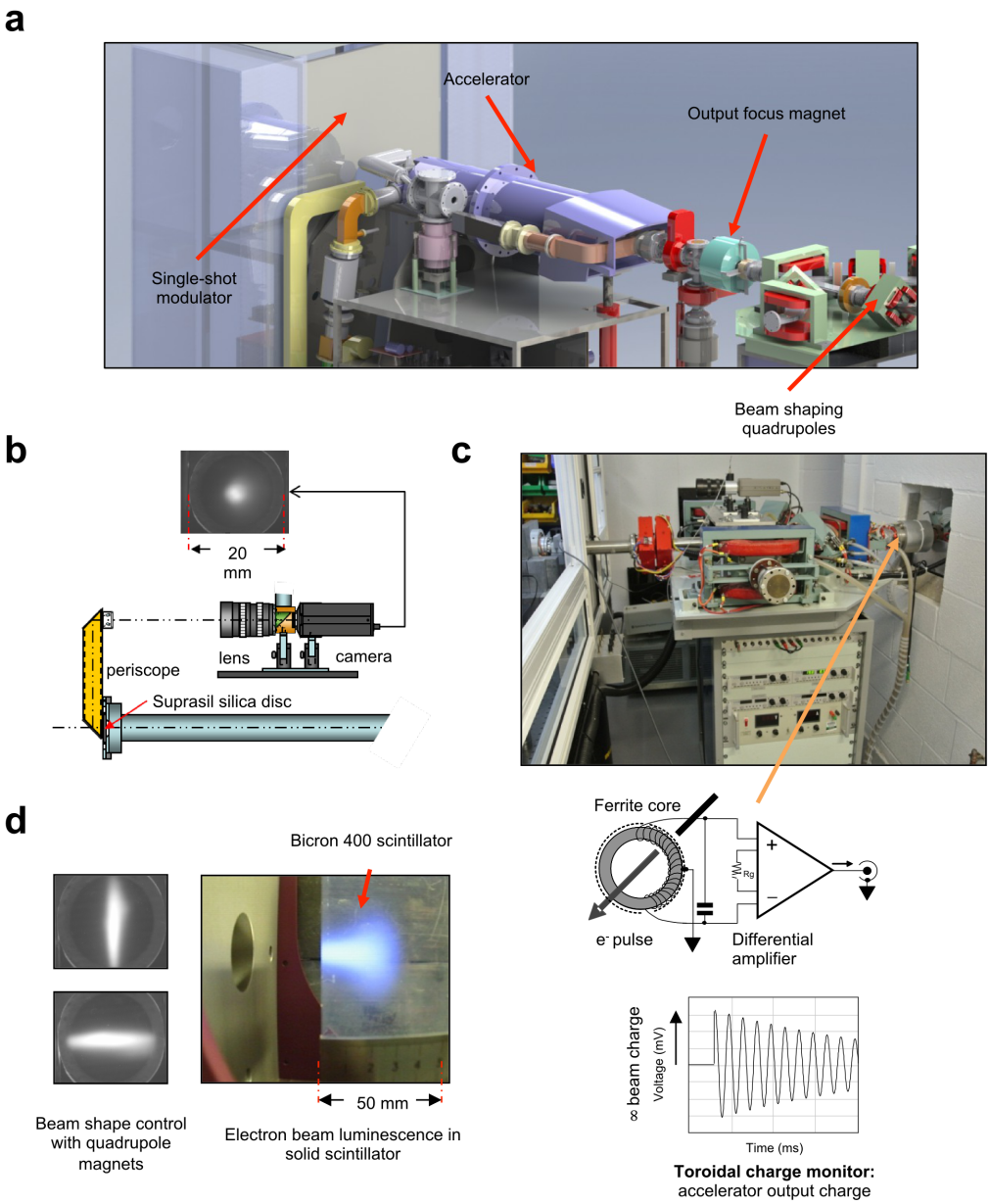


Figure 2.1 Linear accelerator. a) SolidWorks model of the linear accelerator. **b)** Diagram of the periscope arrangement used for beam alignment. **c)** Charge monitor system, used for beam delivery monitoring. **d)** Beam shapes obtained using different quadrupole magnets settings; beam luminescence observed by irradiation of a Bicron 400 scintillator block.

2.3 Cell dishes and sample holder

The cell dishes (samples) are irradiated orthogonally to allow manipulation of the dose distribution across the sample. The following issues were considered in the design of the cell dishes with the different dose distributions described in more detail in **section 3.2.3.4**. 6 MeV electrons penetrate through approximately 34 mm of water, at which point the deposited dose falls to approximately zero (Cygler *et al.*, 1997; Seymour H. Levitt *et al.*, 2008). Broad beams require ~5 mm of water-equivalent material for dose build-up. However, smaller beams require much less build-up. Following this, a relatively flat dose profile is obtained over ~10 mm (**figure 2.2a**) (Cygler *et al.*, 1997; Seymour H. Levitt *et al.*, 2008). The cell dishes were therefore designed to be of dimensions 12 x 12 mm square borosilicate glass tube (cut down to 10 mm high, Chance Glass Ltd, UK) with 1 mm thick walls providing a 10 x 10 x 10 mm inner sample volume (**figure 2.2c**). A borosilicate glass coverslip, (0.13-0.16 mm thick, No 1, Chance Glass Ltd), dimensions 11 x 11 mm, is attached to one of the open faces of the square tube using a radioresistant and biocompatible adhesive (Opti-tec 5006, Intertronics, UK), thus forming a five-sided cell dish (**figure 2.2c**). This adhesive exhibits a low degree of characteristic auto-fluorescence, therefore the amount used to attach the coverslips was minimised to avoid high levels of background fluorescence when imaging cells near the internal edges of the cell dish. These cell dishes can be re-used following coverslip cleaning by removal of the attached cells and sterilisation at 200°C for a period of 2 h.

A homogeneous dose depth of ~10 mm is obtained by exploiting material build-up using the 1 mm input wall thickness of the glass cell dish and the accelerator 0.2 mm thick titanium output window (**figure 2.2b**). By using a square sample, dosimetry issues related

to the different quartz thicknesses 'seen' by the electrons traversing the sample at different angles are avoided.

The microscope (described in **section 2.5**) used to image the cells prior to, and following irradiation is located to one side of the irradiation port to minimise irradiation of the optical components, particularly the imaging objective, and to facilitate other potential applications of the irradiation system. Long-term irradiation of glass induces colour centre formation (Speit *et al.*, 1992), resulting in unwanted and uncontrollable optical attenuation in the imaging path. Although this process occurs in the coverslips, they are thin enough, and irradiated only once, for the consequences of any radiation-induced attenuation to be negligible. Dishes therefore need to be transferred between the imaging and irradiation locations. A dish transfer system provides the additional advantage that several dishes can be used within a single experiment, allowing sample-multiplexed time-lapse microscopy to be performed. Correct positioning of dishes is simplified through the use of a cell dish holder which incorporates a number of features (Vojnovic *et al.*, 2011b). The cell dish holder is constructed from a radio-resistant material, 40% glass fibre-filled polyphenylene sulphide (PPS) (Watford Plastics Ltd, UK), a material soft enough not to cause cracking of the cell dishes (due to inevitable machining tolerances) when inserted. This particular material also has excellent machining properties. This design allows accurate and reproducible re-positioning permitting imaging of the same field(s) of view pre- and post-IR. The holder incorporates a Maxwell kinematic system (Maxwell, 1876) and contains 3 stainless steel spheres (Simply Bearings Ltd, UK), mated to 3 female 'vees' (each 'vee' consisting of 2 parallel stainless steel rods, Simply Bearings Ltd). These female 'vees' were constructed for both the imaging and irradiation locations (**figures 2.2d** and **2.2e**). The design uses pairs of stainless steel rods, which can be acquired with fine tolerances,

allowing more reproducible repositioning of the sample, compared to machined 'vee' grooves.

A flexible 0.4 mm thick plastic shim was attached on the top of the sample holder to minimise evaporation of the liquid inside the cell dish. All holder components were irradiated with doses >>1000 Gy to test their radiation resistance. No appreciable damage was found. The sample holder repositioning accuracy is assessed in **section 3.2.1**.

2.4 Irradiation setup

A key component of the irradiation assembly is the collimator placed in front of the sample. The collimator is made of 24 mm thick aluminium: this stops all of the 6 MeV stray electrons (Prasad *et al.*, 1988). The resulting photon dose is considered negligible (<0.1% contribution to total sample dose). The collimator has an adjustable collimator height (**figure 2.3d**) allowing modulation of the dose distribution across the sample (see **section 3.2.3**). It was necessary to develop an additional kinematic arrangement that facilitated sample repositioning. As described in **section 2.3**, this arrangement was based on a Maxwell kinematic system, identical to the custom-designed microscope stage (**figures 2.2e** and **2.4b)**. When the sample to be irradiated is in place, the coverslip on to which the cells are plated is aligned with the central axis of the beam (**figure 2.3c**). In order to obtain a homogeneous irradiation field, a 'dummy' cell dish was placed below the sample to be irradiated. This dish is filled with polydimethylsiloxane (PDMS) elastomer (Sylgard 184 Elastomer kit, Farnel UK Ltd, UK), which has a density of 0.965 g/cm^3, similar to that of liquid water. Beneath the 'dummy' sample a 45 degree 25 x 25 mm prism mirror (MRA25-G01, Thorlabs, Ltd, UK) was fitted. This prism reflects the light resulting from the Čerenkov emission of the irradiated sample into an optical train, described in **section 2.7** (**figures 2.3a** and **2.3c**).

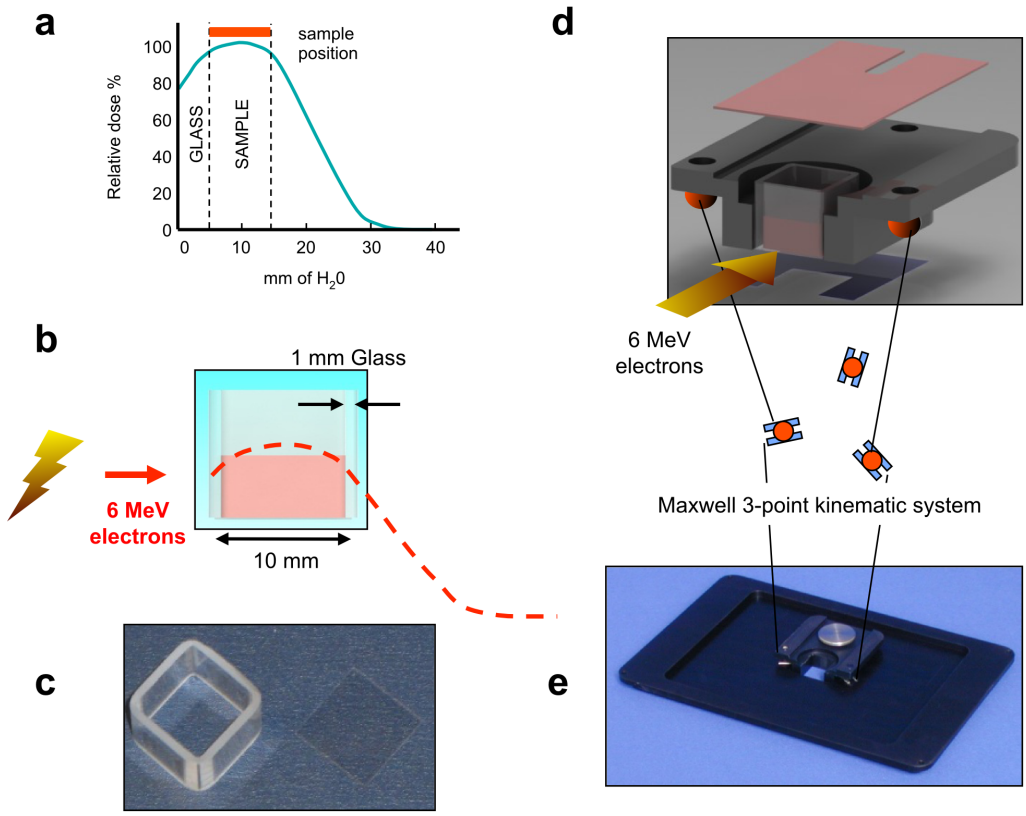


Figure 2.2 Sample dish, sample holder and stage inserts. a) Broad-field 6 MeV electron depth-dose curve, highlighting the ideal sample dimensions to assure a homogeneous dose distribution across the sample. **b)** SolidWorks representation of a sample dish. **c)** 12 x 12 mm glass sample dish and 11 x 11 mm type 1 borosilicate cover-slip. **d)** SolidWorks representation of a kinematic sample holder. **e)** Kinematic sample holder placed on custom-designed microscope stage insert.

A kinematic plate (KBT75/M, Thorlabs Ltd) is attached to the bottom of the irradiation assembly (made of Tufnol for insulation purposes, Watford Plastics Ltd, UK), and sits on a kinematic base (KBB75/M, Thorlabs Ltd). This mechanism shown in **figure 2.3b** allows rapid and accurate interchange of the irradiation assembly with the beam alignment periscope assembly (described in **section 2.2**) and, if required, a beam target (beam dump).

2.5 Epifluorescence imaging system

The imaging system (**figure 2.4**) consists of a custom-designed epifluorescence microscope equipped with a widefield camera, similar to that described before (Barber *et al.*, 2013). A Prior Lumen 200 (Prior Scientific Instruments Ltd, UK) continuous wave white light source provides fluorescence excitation, with the aid of conventional dichromatic 'cubes', used for filtering the excitation band and separating the fluorescence emission. Different cubes were used to image YFP, DAPI, Alexa 647 and mCherry. The YFP filter set (Semrock YFP-2427B-000, Laser 2000, UK) provides excitation at 500 ± 20 nm and filters the emission at 542 ± 13.5 nm. DAPI imaging was performed with a DAPI cube (Semrock LF405-A-000 Laser 2000, UK) allowing excitation at 390 ± 20 nm and imaging at 452 ± 22.5 nm. Alexa 647 was imaged with a Cy5 cube (Semrock Cy5-4040A-NTE, Laser 2000, UK) allowing excitation at 628 ± 20 nm and imaging at 692 ± 20 nm. Geminin-mCherry, as used in the biological systems described later was imaged with a Texas Red cube (Semrock TxRed-4040C-000 Laser 2000, UK) with excitation at 562 ± 20 nm and emission at 624 ± 20 nm. The microscopy system includes an integrated power meter, developed in-house, to monitor fluorescence excitation power at the back focal plane of the objective during imaging and to compensate for excitation lamp intensity variations from experiment to experiment (Vojnovic and Newman, 2007).

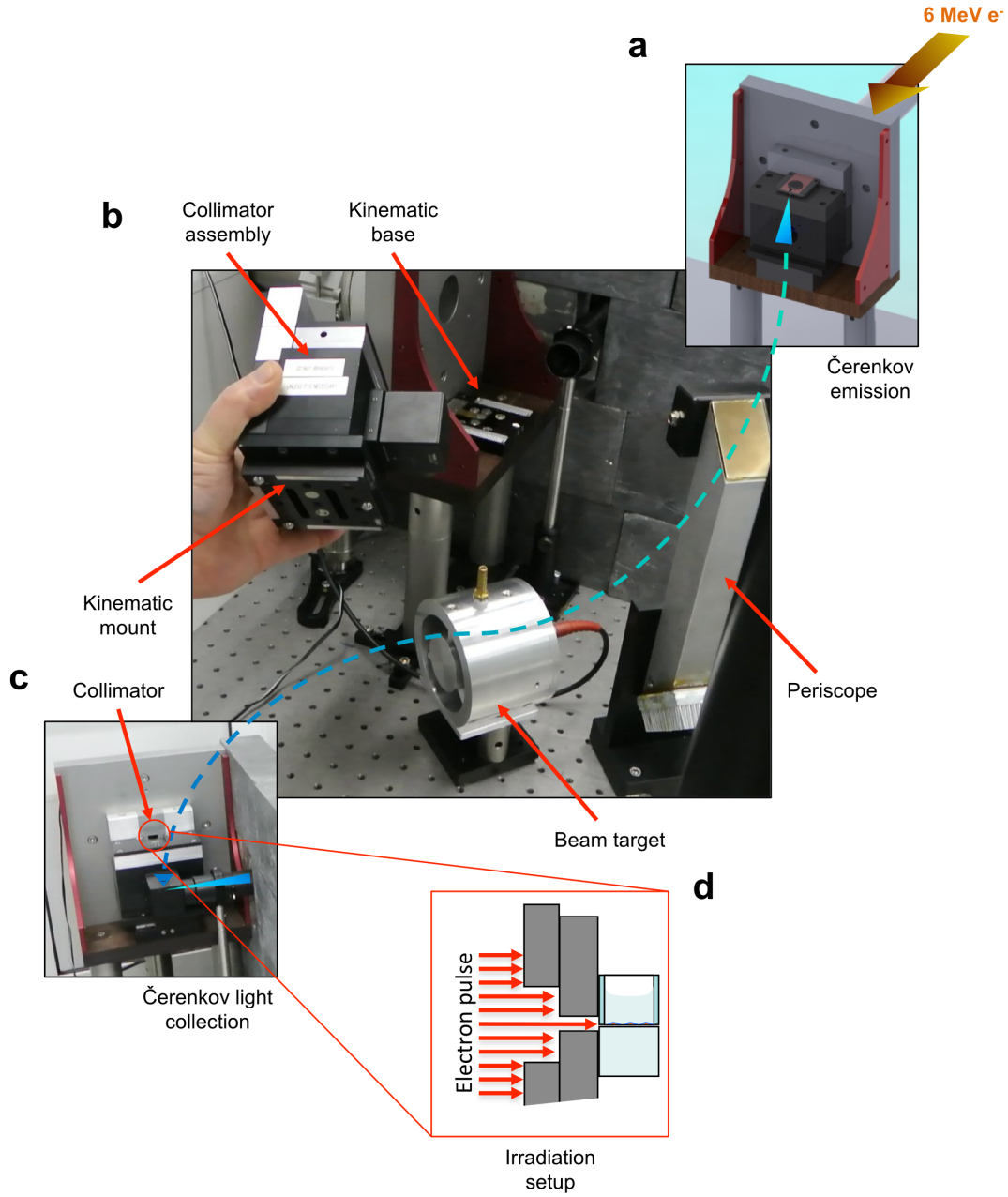


Figure 2.3 Irradiation setup. a) SolidWorks model of the collimator assembly. Čerenkov emission is highlighted in blue. **b)** Irradiation stand with a kinematic base. The irradiation assembly, beam target and periscope imager have kinematics mounts that couple to the kinematic base attached to the irradiation stand. **c)** Collimator assembly. Čerenkov emission is highlighted in blue, being collected into an optical train for signal detection. **d)** The diagram is a representation of sample irradiation (lateral perspective).

This imaging system has a motorised scanning stage for inverted microscopes (Märzhäuser Scan-IM powered by a Corvus driver, Märzhäuser Wetzlar GmbH & Co. KG, Germany) for remote and automated sample positioning. This stage has a travel of 120 x 100 mm, although a much smaller travel was usually used. A Nikon CFI S Fluor 40x 0.9 NA air objective (Nikon) is used for sample imaging, with its correction collar set to compensate spherical aberrations induced by the glass coverslip. Fine focusing is provided by a piezo-electric objective drive (MIPOS 500 SG-UD, Piezosystem Jena GmbH, Germany), allowing a ±200 μm focus range with nm resolution.

The focus drive system is complemented by a coarse focusing system, again developed in-house constructed from linear stages and a bell crank vertical drive powered by a DC motor-encoder (Vojnovic and Newman, 2010; Vojnovic *et al.*, 2008).

The imager is a Hamamatsu Orca-Flash 2.8 sCMOS camera (Hamamatsu Photonics UK Ltd, UK) (1920 x 1440 pixels), featuring <3-electron noise, sufficiently low for imaging on a low fluorescence background inherent to the experiments described here. The camera is used at a resolution of 1440 x 1440 pixels for compatibility issues, (or 720 x 720 pixels when 2 x 2 pixel binning is employed) to provide a field of view (FOV), corresponding to an imaged field of ~130 x 130 μm when the 40× objective is used. The 2 x 2 pixel binning is used during live-cell imaging experiments to increase sensitivity and minimise photobleaching. The spatial resolution of a system can be determined from the camera pixel dimensions, the microscope magnification and crucially, the objective NA. The Rayleigh criterion defines the optical resolution limit, determining the minimum distance at which two points can be resolved. If 500 nm light is assumed, then the Rayleigh criterion (resolution ≈0.6λ/NA) gives a resolution of 333 nm. This requires twice the sampling for full detail to be obtained (Born and Wolf, 1999). The 3.63 μm camera pixel resolution satisfies this when a 40x objective is used (3.63 μm / 40 = 91 nm, confirmed

with graticule measurement). The 2 x 2 binning used in the described experiments slightly exceeds the sampling limit (binned pixel resolution = 181.5 nm).

2.6 Automated sample transfer unit

Transfer of cell dishes between irradiation, imaging and resting locations is accomplished by the use of two coupled linear stages to provide sub-10 μm resolution motion in the horizontal (X) and vertical (Z) axes (**figure 2.5a**). The X-stage (Aerotech type PRO225-1200, Aerotech Ltd, UK) has a travel of 1200 mm, a repeatability of ±2.5 μm and allows accelerations above 1000 mm/s^2. The Z-stage (ATS100-200, Aerotech Ltd) has a travel of 200 mm with sub-micron repeatability, allowing accelerations above 500 mm/s^2. A 17 mm diameter electromagnet (SM series, Solentec Ltd, UK) is used to pick up the samples (**figures 2.5a** and **2.5b**), magnetising a soft iron disc attached to each cell dish holder (Vojnovic *et al.*, 2011b). When the sample is to be released, the disc is momentarily de-magnetized. The handling of the samples is controlled by software, developed in-house (Gilchrist and Vojnovic, 2011), which orchestrates the communication between the accelerator, the microscope system and the sample handling system. The software also allows optimisation of the motion paths and accelerations. When a sample is picked up from the holding area, it is directed to the imaging site, which sends a signal to the microscope stage to be moved to the defined 'pickup' coordinates. Once the sample is imaged and the relevant FOVs are selected and stored, the stage is returned to the 'pickup' coordinates and the X-Z stages transport the sample to the irradiation site. When this motion is completed, the linac irradiates the sample, using previously defined settings by the user. Following irradiation, the sample is transferred back to the microscope stage and the sample is time-lapse imaged (numbered path highlighted in blue in **figure 2.5a**). The holding area was also designed to be kinematic and holds up to 9 samples. Each sample

holder is assigned with an ID (for sample tracking purposes). Software developments are to be made in order to allow 9 samples to be controlled in an interleaved fashion, moving towards real-time DNA repair kinetics studies in a high-throughput fashion. The automated sample transfer repositioning accuracy is addressed in **section 3.2.1**. Potential cell detachment and DNA damage formation caused by the automated transfer unit are addressed in **section 3.2.2**.

2.7 Čerenkov dose monitor

The charge monitor described in **section 2.2** gives the user information about the charge leaving the accelerating structure of the linac. In order to monitor which fraction of this charge reaches the irradiated samples, a dose monitor was developed at the sample level. This monitor makes use of Čerenkov emission (Cerenkov, 1937; Frelin *et al.*, 2005), from the sample and from the transparent water-equivalent material (PDMS) placed just below the sample dish to monitor the dose delivered to the sample (**figure 2.3d**). The calibration of this dose monitoring system is achieved using a water-filled sample where the coverslip was replaced by a 200 μm thick EJ-212 scintillator (Southern Scientific Ltd, UK), enhancing the output. The calibration of this dose monitor against physical dose measurements is described in detail in **section 3.2.4.3**. The Čerenkov optical pulse is synchronous with the electron pulse and its detection provides an indication of the temporal profile and relative intensity of the pulse. Some of the Čerenkov light is collected at the bottom of the cell dish with a 100 mm focal length fused silica planoconvex lens (LA4380-UV, Thorlabs, Ltd), supplemented by a 300 mm focal length fused silica meniscus lens (LE4329-UV, Thorlabs, Ltd). The resulting light is filtered with a 555 nm low pass filter (FD1C filter, Thorlabs, Ltd) and re-imaged with a 75 mm fl quartz planoconvex lens (LA4725-UV, Thorlabs Ltd) onto a field-defining square aperture stop.

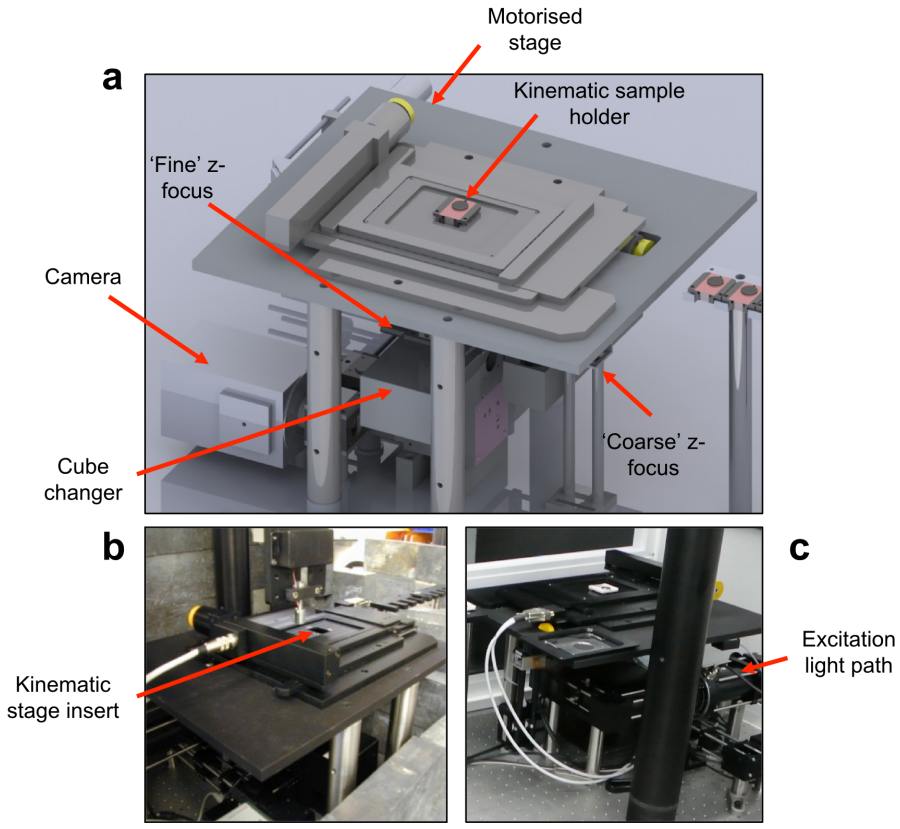


Figure 2.4 Epifluorescence imaging system. a) SolidWorks model of the linac experiment system microscope. Some of the key features are highlighted. **b)** Kinematic stage insert for accurate sample repositioning in place at the linac imaging system. **c)** Linac microscopy imaging system.

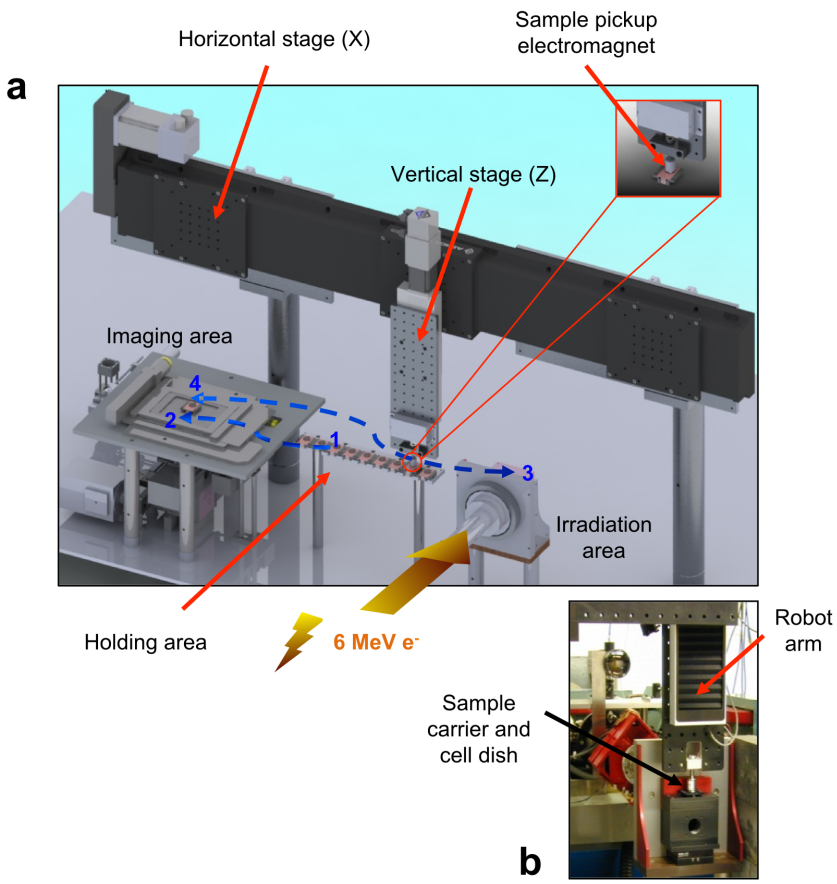


Figure 2.5 Automated sample transfer unit. a) SolidWorks model of the linac experiment system. The coupled stages and the electromagnet that constitute the automated sample transfer unit are highlighted. The numbered path highlighted in blue represents the order in which a sample is repositioned during a live cell imaging experiment in response to radiation treatment. **b)** Z-arm picking up sample in place at the irradiation site.

This stop is further re-imaged, through a motorised mirror switch (Vojnovic *et al.*, 2011a) onto one of several detectors (**figure 2.6**). (1) a photomultiplier (HC5700, Hamamatsu Photonics UK Ltd), coupled through a 25 mm focal length planoconvex lens (part 45504, Edmund Optics Ltd, UK) and a 1 mm diameter polymer optical fibre (Fibre Data, A19A52A0, Optoelectronic Manufacturing Corporation, UK), to monitor the pulse width; (2) a photodiode (OSD15-5T, Centronic Ltd, UK), coupled through a pair of 63 mm focal length planoconvex lenses (63PU40, Comar Instruments, UK) to monitor the integrated dose and (3) an electron pulse synchronised CCD camera (Cohu type 4910, Brian Reece Scientific Ltd, UK) and frame store (Brian Reece Scientific Ltd) to image the emission across the sample. The camera image can be used to monitor the dose distribution. The lateral deposited beam profile can be imaged with the camera using a 200 μm thick piece of EJ-212 scintillator (Southern Scientific Ltd, UK) replacing the glass coverslip in a water-filled 'dummy' cell dish. For routine work, the integrated photodiode output obtained with EJ-212 irradiations was calibrated against independently determined dose (**section 3.2.4.3**).

2.8 Environmental enclosure

In order to perform live-cell imaging experiments it was necessary to guarantee that the cells were kept under physiological conditions during experiments, i.e. at 37°C and 5% CO_2. To achieve such an environment it was necessary to model and construct an enclosure which could keep the environment at a constant temperature of 37°C and 5% CO_2 humidified air. The environmental enclosure is a 3.5 m^3 structure (Insuglaze Ltd, UK) composed of double-glazed (U-value of 1.2 W/°C m^2) and single-glazed windows (U-value of 5.8 W/°C m^2) and several insulating panels (U-value of 1.07 W/°C m^2) (**figure 2.7**).

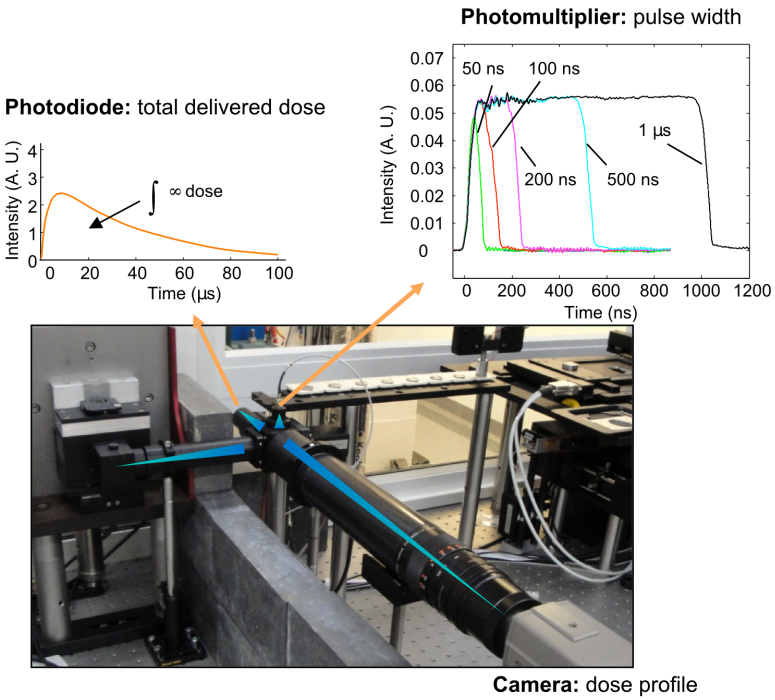


Figure 2.6 Čerenkov dose monitor. Representation of the Čerenkov dose monitor. The light is guided through an optical train into a mirror switch, which can guide the light into a photodiode, a photomultiplier, or a camera. The outputs can be respectively converted into dose, pulse width, or dose profiles according to the light path.

The total heat loss was determined to be approximately 370 W based on the U-values of the different components of the structure (**equation 2.1**). Assuming a load inside the enclosure of 3.5 m^3 of air (mass specific heat capacity, c_{Air} = 1.01 J/g°C), 450 kg of lead (c_{Pb} = 0.128 J/g°C, mainly used for radiation shielding purposes) and 50 kg of aluminium (c_{Al} = 0.902 J/g°C, microscope body), the power required to heat the enclosure up to 37°C was determined using **equations 2.2** and **2.3**. The power necessary to achieve a heat energy of 1.82 x 10^6 J (as determined by **equation 2.2**) within 30 min was determined to be ~1 kW (**equation 2.3**). Considering the power required and the heat losses of the system, four 400 W heaters (Stego Elektrotechnik, part 03112.0-00, RS Components Ltd, UK) with associated fans (EBM-Papst 4650NU, Farnell UK Ltd), distributed around the enclosure, were used to heat the enclosure. Temperature control is performed by a proportional-integral-derivative (PID) type of feedback controller (Omron E5CN series, Farnell UK Ltd), connected to a temperature sensor (Pt 100 type Labfacility DM-333, Farnell UK Ltd). A non-dispersive infrared (NDIR) sensor (Cozir W20-VH, Gas Sensing Solutions Ltd, UK) measures the CO_2 concentration within the enclosure. Both sensors are placed close to the microscope sample carrier. The concentration is maintained at the required level (usually 5%) with the aid of a second PID controller (Omron E5CN series, Farnell UK Ltd), which on turn alters the mark-space ratio of a solenoid-operated gas valve (SMC VDW21-5G-3-01F-Q, RS Components Ltd). The fans associated to the heaters help to re-circulate the gas within the enclosure. When the system is powered ‘on’, it takes ~100 min for the temperature and CO_2 to stabilise at 37°C and 5% respectively (**figure 2.8**). For live-cell imaging experiments, the samples are generally placed inside the environmental enclosure 2 h after the system was powered ‘on’. The introduction of the samples results in a negligible decrease in the CO_2 % within the enclosure, with the environment stabilising

within 10 min of closing the enclosure (**figure 2.8**). The detailed description of a similar arrangement was described by Vojnovic *et al.* (Vojnovic *et al.*, 2012).

Hl: *heat loss, W*
U: *U-Value, W/°C* m^2
A: *surface area,* m^2
ΔT: *temperature difference, 17 °C*

$$Hl = U \times A \times \Delta T \quad \textbf{2.1}$$

Q: *heat energy, J*
c: *specific heat capacity, J/g°C*
m: *mass, g*

$$Q = c \times m \times \Delta T \quad \textbf{2.2}$$

P: *power, W*
t: *time, sec*

$$P = \frac{Q}{t} \quad \textbf{2.3}$$

2.9 Discussion

In this chapter the different components of the linac experiment system were described. The high dose-rates delivered by the 6 MeV linac open the possibility to perform DNA repair kinetics studies at short times following irradiation when virtually no repair is on-going during the irradiation time. Beam alignment, and charge monitoring (charge monitor and Čerenkov dose monitor) facilitate radiation delivery monitoring and reproducibility between different experiments. The irradiation field can be manipulated using a quadrupole focusing system, or by changing the beam collimation. The dimensions of the samples to be irradiated were chosen based on the electron energy of the accelerator, in order to achieve a flat dose distribution across the sample. Each sample is associated with a kinematic holder permitting accurate repositioning and allowing imaging of the same cells pre- and post-irradiation. The remote transfer of the samples between imaging and irradiation locations is carried out via a robotic unit housed within a custom-designed environmental enclosure which keeps an environment of 37°C and 5% CO_2 humidified air. This approach based on a pump-probe method ensures the delivery of radiation within sub-μs (pump) allowing subsequent real-time detection (probe) of events in living cells using fluorescence microscopy.

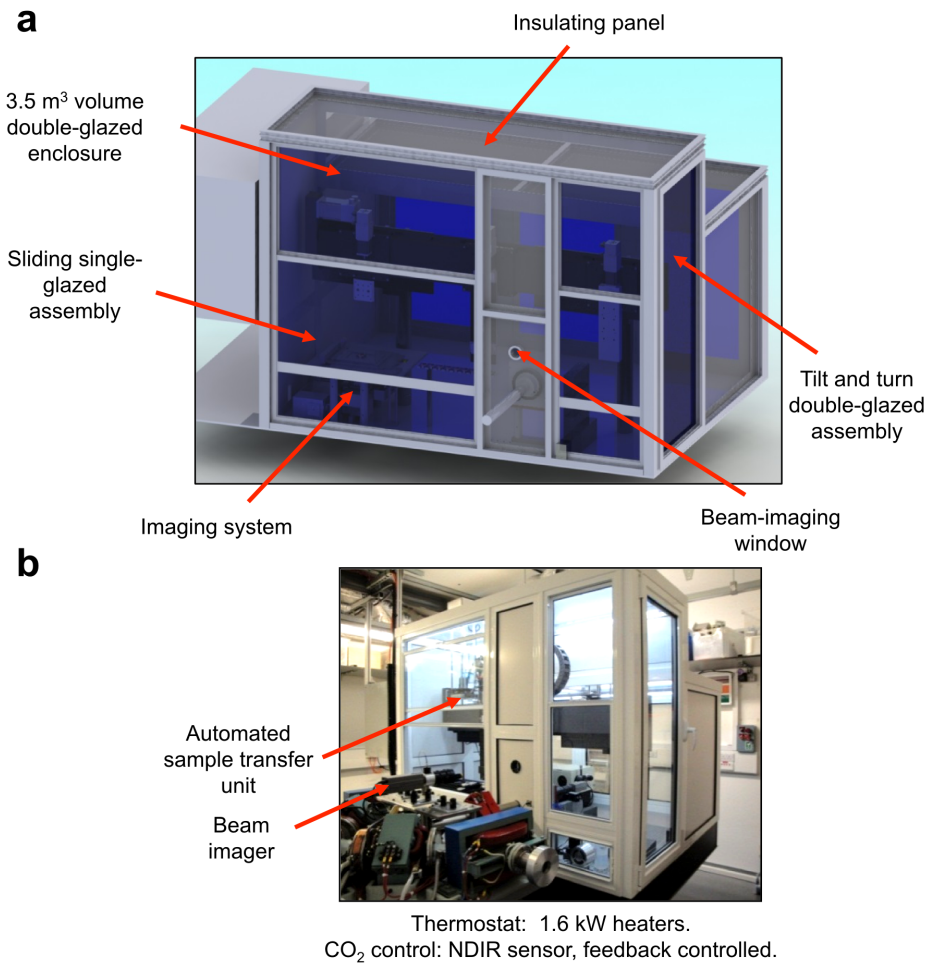


Figure 2.7 Linac experiment system environmental enclosure. a) SolidWorks model of the environmental enclosure composed of single and double-glazed windows, and insulating panels. **b)** Experiment system within the environmental enclosure. The camera used in combination with the periscope for beam alignment (**section 2.2**) is highlighted.

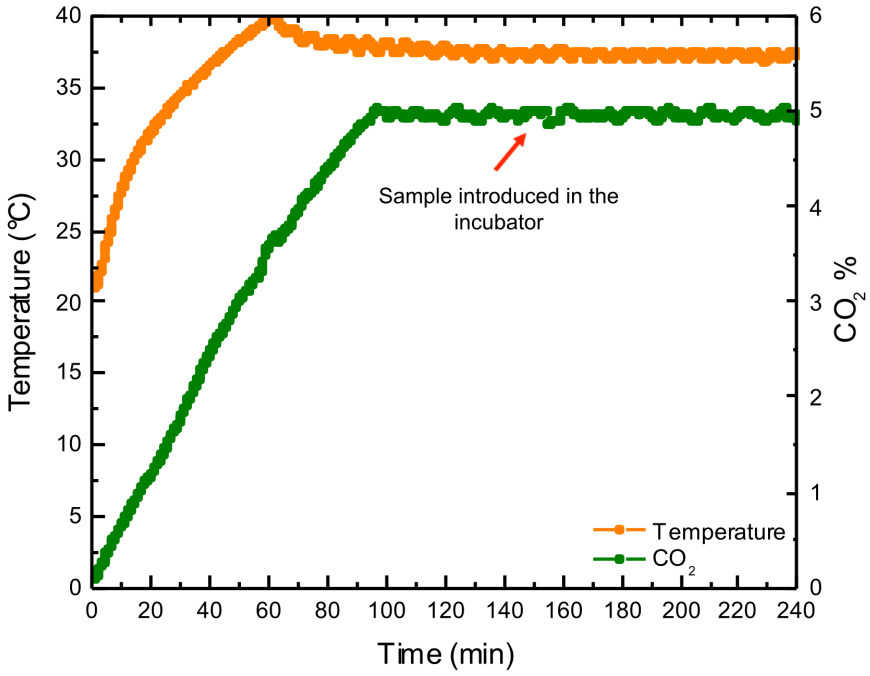


Figure 2.8 Environmental enclosure temperature and CO_2 monitoring. The plot displays the temperature and CO_2 rise over with time. The environment is stable at 37°C after 100 min. No significant drop in the CO_2 level is observed when the samples are introduced inside the environmental enclosure.

3. Validation of the experimental setup

3.1 Introduction

The work presented in this chapter addresses the feasibility of the use of the linac experiment system for DNA repair kinetics studies using living mammalian cells. As mentioned previously, studies of the kinetics of DNA repair in real-time in mammalian cells have used laser microbeam techniques to induce highly localised DNA damage in living cells. However, these studies have produced contradictory and often confusing results that are likely caused by the different laser systems used, reflecting in part the wavelength dependence of the damage induced (Kong *et al.*, 2009; Reynolds *et al.*, 2013). Moreover, in studies using low-LET ionising radiation, repair kinetics are mainly followed using fixed samples at different time points, displaying simply a 'snapshot' at one particular time of the repair process. In this chapter the capacity to image the same cells pre- and post-irradiation was assessed. The feasibility of using the linac experiment system without incurring additional damage to the cells by transferring them automatically between imaging and irradiation locations was addressed. Using a system based on a low-LET radiation delivery, coupled with accurate dosimetry, concomitant UV/visible induced damage is avoided and sparsely ionising radiation induces essentially homogeneously distributed damage. Dose distributions were assessed experimentally and with Monte-Carlo simulations, and physical dose measurements performed to ensure a reproducible, quantifiable and homogenous irradiation of the samples under physiological conditions at 37°C and 5% CO_2 humidified air.

3.2 Results

The capacity to accurately reposition the samples described in **section 2.3** was assessed using the microscope and the automated sample transfer unit described in **section 2.5** and **section 2.6** respectively. To exclude the possibility of inducing damage to the genomic DNA of the cells during sample transfer with the automated sample transfer unit, the HT1080-53BP1-YFP cells described in **section 4.1** were used to monitor the formation of 53BP1 foci. Gafchromic film dosimetry and Monte-Carlo particle tracking modelling were used to characterise and optimise the radiation dose distribution across the samples using the linac system. The physical dose delivered to the samples was determined using thermoluminescent dosimetry (TLD) and Fricke dosimetry. The physical dose measurements were confirmed by irradiating samples with a ^{137}Cs source and determining the number of 53BP1 foci formed in the nuclei of HT1080-53BP1-YFP in response to increasing radiation doses.

3.2.1 Sample repositioning following automated sample transfer

The same cell fields must be imaged pre- and post-irradiation, in order to assess background levels of damage prior to irradiation. In order to assess the feasibility of repositioning the custom-designed samples described in **section 2.3**, U2OS cells were plated and DAPI-stained as described in **section 4.6.1**. Following staining, the samples were placed on the resting area and brought to the microscope using the automated transfer unit. Three fields of view (FOV) were chosen per sample. The repositioning accuracy was tested by repetitively transferring the samples between irradiation, the resting and the imaging locations. Consecutive images of the DAPI-stained nuclei were acquired per sample at increasing lateral and vertical accelerations. The lateral and vertical accelerations ranged between 250-1000 and 250-500 mm/s^2 respectively. The images were analysed to

assess displacement using the Image Stabilizer (LI, 2008) optical flow estimation plugin for ImageJ (Schneider *et al.*, 2012). This plugin stabilised image jitter in sequential images using the Lucas-Kanade algorithm (Lucas and Kanade, 1981) and provided an output in the form of a direction vector, normalised to a real distance from knowledge of the image field dimensions. Micrographs representing the results obtained following sequential movements are shown in **figure 3.1a**. To illustrate the displacement to be determined, the result of the subtraction of the image obtained following a movement, and the original image is shown (**figure 3.1a**). The difference, which represents the displacement, is highlighted. As shown by the data plotted in **figure 3.1b**, the displacements were found to be <<500 nm and mostly <100 nm, confirming the capability to reposition and track the same cells over repeated dish moves.

3.2.2 Cell detachment and damage formation monitoring due to automated sample transfer

The linear stages used to transfer the dishes between the different locations available, are capable of accelerations exceeding 1 x g. It was important to assess whether such fast accelerations were capable of causing cell detachment from the samples or even result in damage formation in the form of DSBs. In order to assess this possibility, living HT1080-53BP1-YFP cells were plated onto the samples described in **section 2.3** as described in **section 4.5**. The samples were placed inside the environmental enclosure (described in **section 2.8**) at 37°C and 5% CO_2 humidified air, and were allowed to stabilise under physiological conditions for 1 h. The samples were then moved to the microscope and three FOVs were chosen per sample. The chosen FOVs were imaged for 53BP1-YFP every 15 min for a period of 1 h. Before each image acquisition, the samples were moved between resting and imaging locations (**figure 3.2a**).

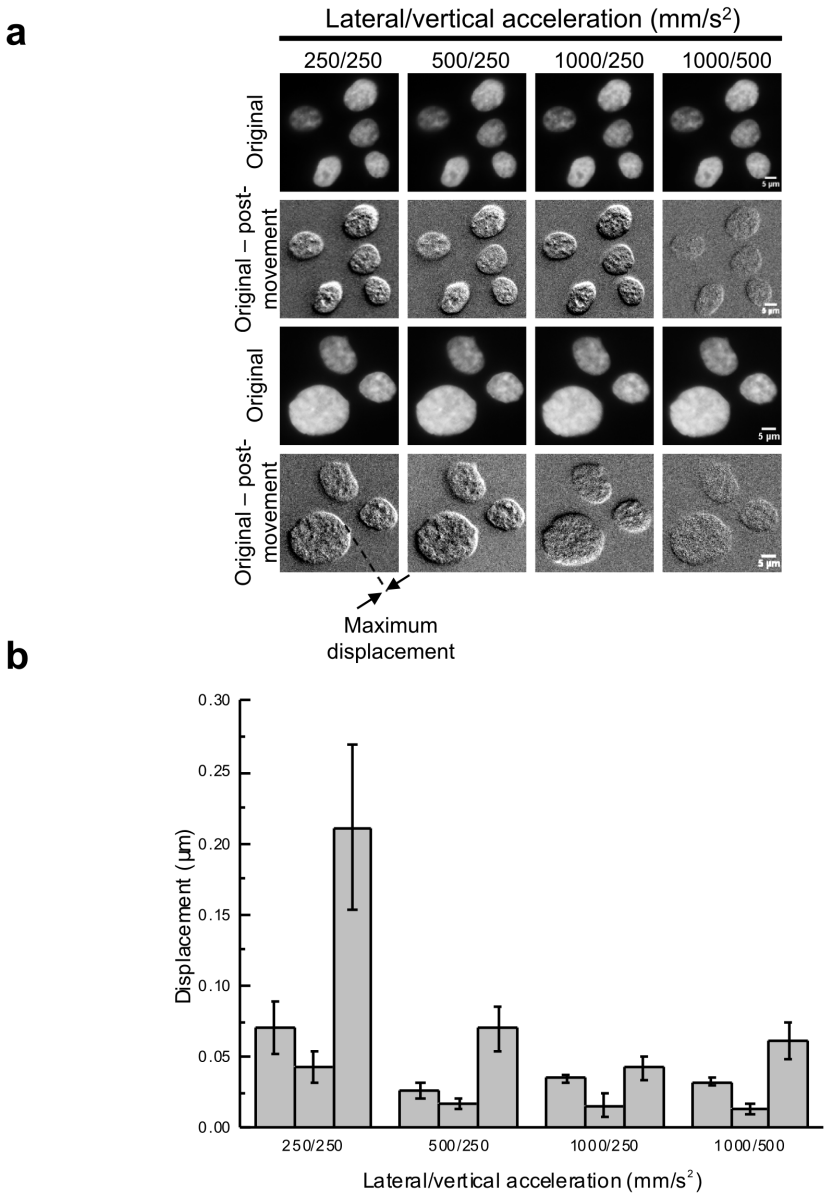


Figure 3.1 Kinematic sample repositioning accuracy. a) Micrographs representing DAPI-stained U2OS cells. The samples were moved between imaging and holding locations using different lateral and vertical accelerations. Sequential images were subtracted to illustrate the potential displacement. Scale bar = 5 µm. **b)** Quantification of the displacement between sequential images using optical flow estimations. Error bars represent the s.e.m. (n = 3 independent experiments).

This procedure was repeated for different lateral accelerations between 250 mm/s^2 and 1000 mm/s^2, at a constant vertical acceleration of 500 mm/s^2 (**figure 3.2b**). For each FOV, multiple z-slices were collected per time point. A total of 21 z-slices with a 'z' spacing of 350 nm were acquired per FOV per time point. A final collapsed image is obtained per time point. The optimisation of image acquisition is described in further detail in **section 5.2.1**. The cell detachment was monitored by counting the number of cells present in each FOV per time point.

As described in **chapter 1**, 53BP1 can be used as a probe for DSB formation (Huyen *et al.*, 2004; Mochan *et al.*, 2004). To monitor the formation of DSBs, the number of 53BP1 foci per cell was counted per time point as described in **section 4.12.3**. The cell numbers showed no alteration over time for the different lateral accelerations tested (**figure 3.2c**), confirming there was no cell detachment observed with increasing lateral accelerations. In terms of DSB formation, a small decrease in the number of foci was observed compared to the original image before the first movement (**figure 3.2d**). This may potentially represent the on-going repair of background foci associated with replication errors. These data confirmed the capability to use the automated sample transfer unit without cell detachment or significant changes to DSB formation.

3.2.3 Sample irradiation optimisation

A scattering foil was inserted in the beam path in order to minimise variations in the beam output between experiments, and to ensure beam homogeneity. As described in **section 2.3**, the sample dimensions were chosen based on existing data in the literature (Strydom *et al.*, 2005) in terms of relative dose percentage curves for 6 MeV electrons. It was hypothesised based on the depth-dose curve, that the dose distribution across 1 cm of H_2O was homogenous.

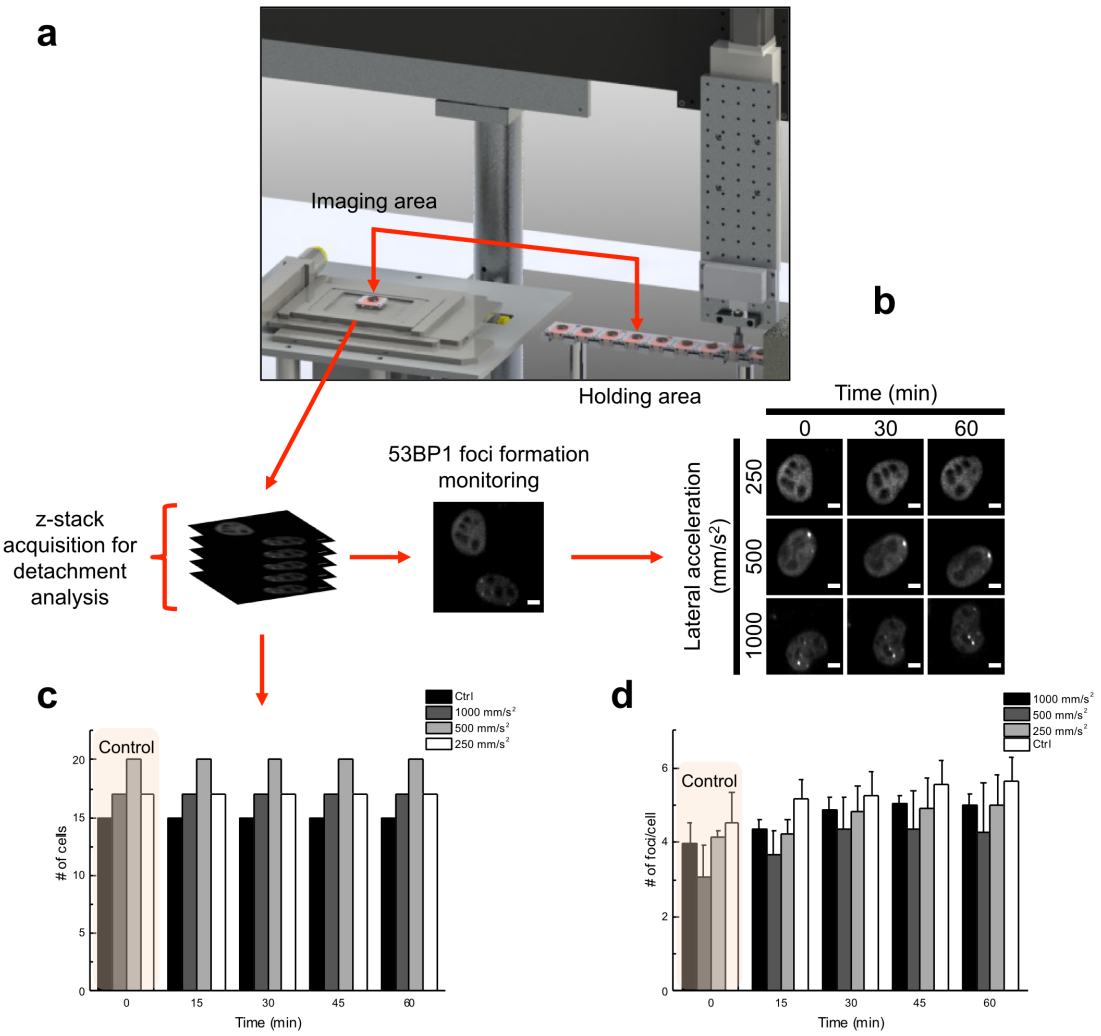


Figure 3.2 Sample handling control tests using live HT1080-53BP1-YFP cells. a) Schematic representing the experimental design. Samples were moved between imaging and holding areas at different lateral accelerations. z-stacks were acquired to detect cell detachment and visualize 53BP1 foci formation. **b)** Micrographs showing 53BP1 foci per time point for different lateral accelerations. Scale bar = 5 µm. **c)** Quantification of the number of cells per time point for the different accelerations. **d)** Quantification of the number of 53BP1 foci per cell per time point per acceleration. Error bars represent the s.e.m. (n = 3 independent experiments). Highlighted in **(c, d)** are the cell and foci numbers prior to any movement.

In order to assess the 2D dose distribution profiles and thus select appropriate beam collimation, Monte-Carlo simulations were performed, using Fluka particle tracking software (Battistoni *et al.*, 2007) (see model in **figure 3.3**). The simulated 2D dose profiles were confirmed by irradiating HD810 Gafchromic film (ISP Technologies Inc., USA). The dose distribution was further analysed by assessing 53BP1 foci numbers in fixed HT1080-53BP1-YFP cells in response to radiation damage.

3.2.3.1 HD810 Gafchromic film dosimetry

It is necessary to obtain a calibration curve to convert obtained optical density (OD) into dose in order to perform dosimetry using HD810 film. Optical densities were obtained by scanning the irradiated films with an Epson Expression 10000 XL scanner and its associated transparency unit (B12B813363) (Epson, Japan). Pixel intensities can range from 0 to 65,535. The films were scanned at resolution of 300 dots per inch, giving a size per pixel of 0.0847 mm x 0.0847 mm. The optical densities were calculated using **equation 3.1**. To convert optical densities into dose it was necessary to scan films irradiated with known doses ranging from 0 to 300 Gy using a ^{60}Co source (MRC Harwell). The resulting optical densities were plotted as a function of dose, and the data fitted to a third order polynomial curve (**equation 3.2**). For each experiment, following determination of optical densities, doses were calculated using **equation 3.2**. The optical densities were corrected per experiment, by scanning a blank film and subtracting the difference between the OD of the scanned blank, and the OD of un-irradiated film scanned to obtain the dose calibration curve. This procedure guaranteed correction for potential exposure to ambient light with time. To obtain 2D dose profiles, the doses were normalised to the maximum dose and displayed with a false colour map using Matlab. For relative

dose percentage curves or beam homogeneity curves, the doses were averaged across 2 mm (24 pixels), normalised to the maximum dose, and plotted as a function of distance.

OD: *optical density*
I_j: *transmission after j Gy*
I_0: *transmission after 0 Gy*

$$OD = -\log\left(\frac{I_j}{I_0}\right) \quad \textbf{3.1}$$

Dose: *dose, Gy*
A-D: *polynomial curve coefficients*

$$Dose = A \times OD^3 + B \times OD^2 + C \times OD + D \quad \textbf{3.2}$$

Dr. James Thompson and Stuart Gilchrist developed the Matlab code necessary to perform the calculations to obtain 2D dose maps, and to generate the dose calibration curves.

3.2.3.2 Scattering foil

As an electron beam passes through a medium, the electrons are subjected to multiple scattering due to the Coulomb force interactions between the electrons and the charged particles present in interacting medium (Strydom *et al.*, 2005). These interactions cause the electrons to lose energy and to gain an increasing angular spread. The ability of a given material to scatter electrons is directly proportional to the square of the atomic number of the interacting medium, and inversely proportional to the square of the kinetic energy of the electrons (Strydom *et al.*, 2005). To increase beam homogeneity, different thicknesses of gold (Au) were tested as a scattering foil. The dose distribution of the electron beam at the exit of the collimator was measured using HD810 Gafchromic film in order to assess the homogeneity achieved using each gold foil (25 μm and 50 μm thick). The film was placed close to the surface of the collimator, perpendicular to the beam axis (as illustrated in **figure 3.3**). Each film was irradiated using a broad beam with a charge monitor output of 105 mV, and a pulse duration of 1 μs. The numbers of pulses used were 5, 20 and 40, for 0 μm, 25 μm and 50 μm of gold respectively.

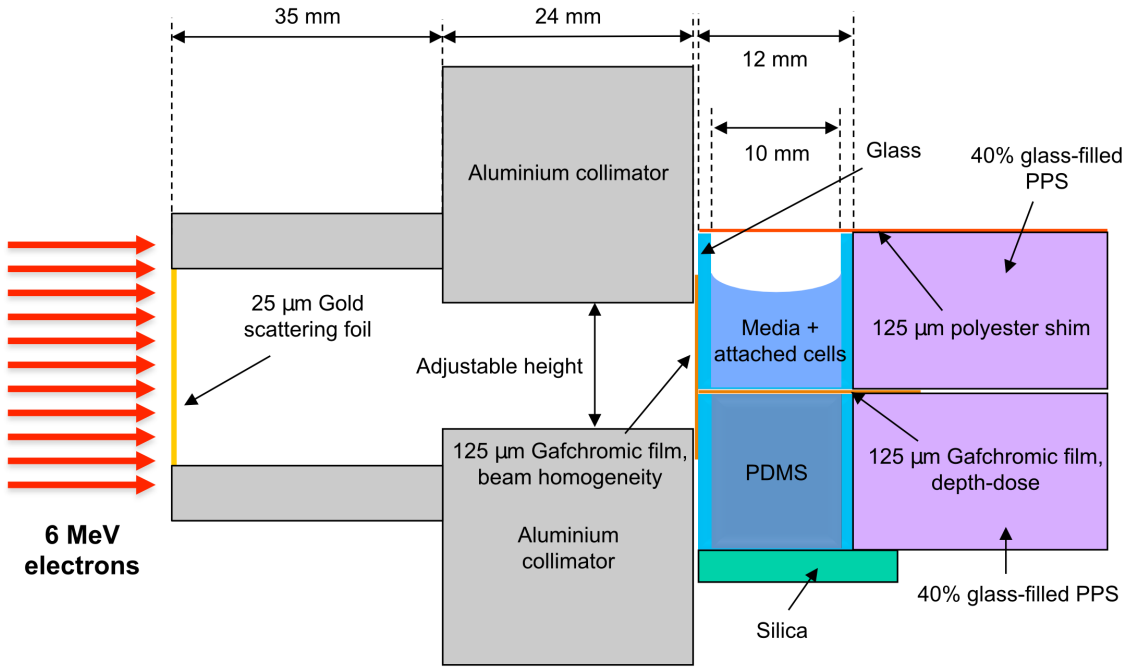


Figure 3.3 Diagram representing the model used in Fluka for Monte-Carlo simulations. The location of the Gafchromic film used to obtain the 2D dose profiles is indicated. The position of the scattering foil is also illustrated.

The number of pulses was increased with the foil thickness in order to account for the additional attenuation of the beam caused by the foils. It can be seen from the normalised 2D dose profiles (**figures 3.4a-c**), that there is an increase in the homogeneity of the beams when the scattering foil thickness is increased. The normalised doses were averaged over a 2 mm wide strip (indicated by the green dashed box in **figures 3.4a-c**), and plotted as a function of distance in order to assess the relative homogeneity of the beams (**figure 3.4d**). The most homogeneous distribution was observed for 50 μm thick gold. To observe the dose profile obtained in the plane of the sample, the HD810 film was placed between a water filled sample dish and the PDMS block, at the exit to the collimator, as illustrated in **figure 3.3**. The film was irradiated with 20 pulses and 40 pulses of 1 μs for 25 μm and 50 μm gold scattering foil respectively. These irradiations were performed using a beam collimation of 10 mm x 12 mm. The 2D dose profiles obtained for both 25 and 50 μm gold are shown in **figure 3.5a** and **figure 3.5b** respectively. The normalised profiles as a function of distance, showed a sharper dose falloff for the 50 μm gold scattering foil (**figure 3.5c**). Given the reduction in dose uniformity when the 50 μm thick scattering foil was used, the thickness chosen for the scattering foil was 25 μm.

3.2.3.3 Monte-Carlo simulations validation

Since the active layer of HD-810 Gafchromic film is affected by contact with water through the edges, it was not possible to use this method in order to assess the dose distributions inside the sample to be irradiated. To assess these dose distributions Monte-Carlo modelling was used. The beam used for all the experimental work carried out, was a sparse beam in order to achieve a more homogenous irradiation of the sample. Due to the non-homogenous nature of the beam it was hard to accurately model.

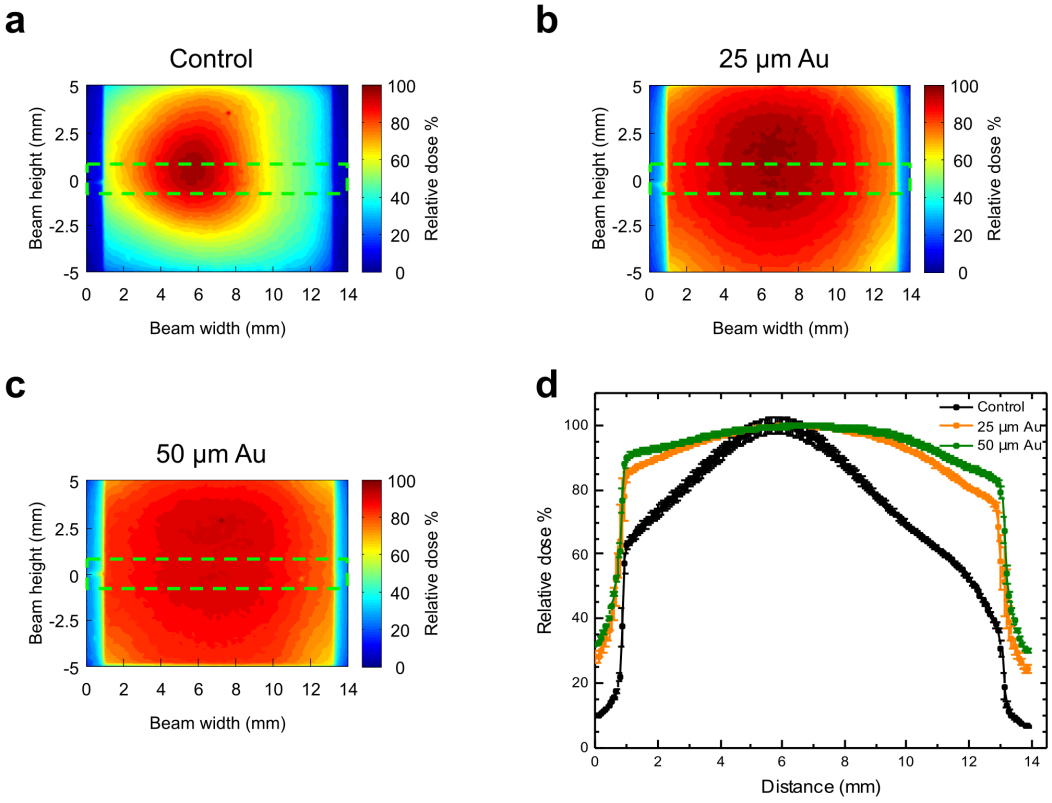


Figure 3.4 Scattering foil effect on beam homogeneity. a) False-colour map of the 2D dose profile obtained with Gafchromic film placed parallel to the exit of the collimator. This profile was obtained without the presence of a scattering foil. **b)** 2D dose profile obtained with a 25 µm thick gold scattering foil. **c)** 2D dose profile obtained with a 50 µm thick gold scattering foil. **d)** Plot of the normalised dose distribution integrated across the green dashed regions highlighted. Error bars represent the s.e.m. (n = 3 individual experiments).

As mentioned in **section 3.2.3.2**, the introduction of a scattering foil increases the angular spread and decreasing the electron fluence reaching the target (Connell *et al.*, 2012). To perform Monte-Carlo simulations, the irradiation setup described in **section 2.4** was modelled (**figure 3.3**) by defining each material by its elemental composition, in order to accurately represent the probable interactions for 6 MeV electrons through each media. A 4 mm full width half maximum (FWHM) beam was compared to a 25 mm x 25 mm flat beam in order to assess the fluence dependence on beam characteristics. Both 6 MeV electrons beams were incident on a 25 μm thick gold scattering foil and simulated with 6 x 10^6 electrons with a 20/300 mm grid along the beam axis. The integrated fluence of electrons across the thickness of the modelled Gafchromic film was found to be 54% less for the larger beam, and thus a larger number of electrons would be required to obtain the same statistics for the 2 different beams. Furthermore, the same 4 mm beam was simulated without a scattering foil, and the integrated electron fluence across it was found to be 80% higher. These data suggest that smaller beams require less total primaries in order to obtain a higher fluence at the target level, and the number of primaries has to be increased with beam size and scattering foil introduction, impacting on simulation time.

In order to test the feasibility of using Monte-Carlo simulations to predict 2D dose profiles, the 6 MeV electrons 4 mm FWHM Gaussian beam was used. The simulation was performed with 24 x 10^6 electrons in total, concurrently running on 4 CPUs in the same computer. The delta-ray production threshold was set for 10 keV, meaning the interactions for particles of 10 keV or less were not followed. A 25 μm scattering foil was introduced in the model as illustrated in **figure 3.3**. The dose was integrated over the thickness of the Gafchromic film (~125 μm) for the 2D profile obtained in **figure 3.6a**.

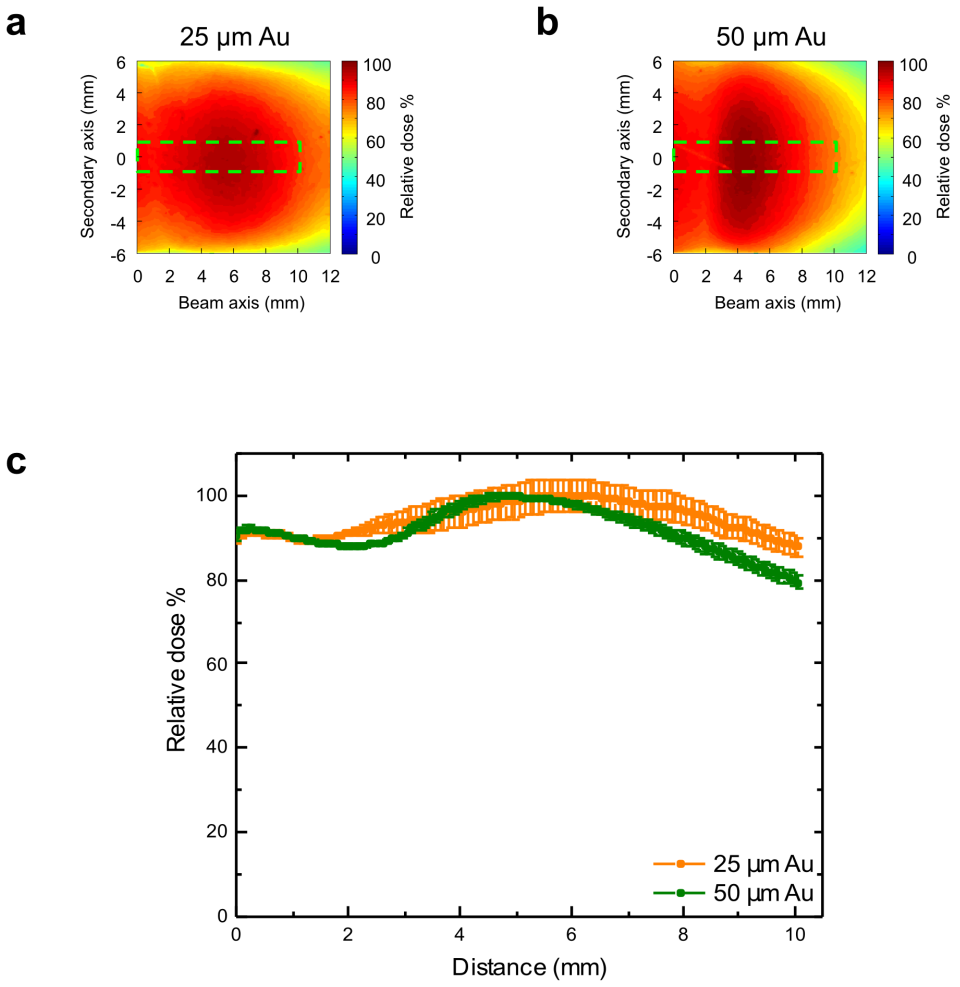


Figure 3.5 Relative dose percentage dependence on scattering foil thickness. a) False-colour map of the 2D relative dose profile obtained with 25 µm thick gold scattering foil, for Gafchromic film placed as illustrated in **figure 3.3**. **b)** 2D relative dose profile obtained with 50 µm thick gold scattering foil. **c)** Relative dose percentage curves integrated across 2 mm as indicated by the green dashed boxes. Error bars represent the s.e.m. (n = 3 individual experiments).

A 4 mm diameter spot beam was used to irradiate Gafchromic film in the same conditions as in the model used for the Monte-Carlo simulation. To experimentally confirm the characteristics of the beam incident on the scattering foil, Gafchromic film was placed in front of the beam line and irradiated with 5 pulses of 1 μs with 85 mV charge monitor output per pulse. The film was scanned as described in **section 3.2.3.1**. The beam profile is shown in **figure 3.6b**. To gather information about the 2D dose profile at the sample level, Gafchromic film was placed beneath the sample as illustrated in **figure 3.3**, and irradiated with 20 pulses of 1 μs. The normalised 2D dose profile obtained is shown in **figure 3.6c**. To compare the relative dose percentage curves obtained with simulation and Gafchromic film, both 2D dose profiles were integrated across 2 mm in the centre of the film (green dashed boxes in **figure 3.6a** and **figure 3.6c**). These data were plotted as a function of distance from the edge of the film closest to the beam line (**figure 3.6d**). Both 2D profiles and relative dose percentage curves were seen to be identical, proving the Monte-Carlo simulations in this particular configuration to be a good predictor of dose distributions.

3.2.3.4 Beam collimation determination

The beam collimation determines the volume of the sample to be irradiated, and impacts on the dose distribution obtained at the sample level. In order to assess the effect of the collimator height (illustrated in **figure 3.7a**) Monte-Carlo simulations and film irradiations were performed at different collimator heights: 2.5, 5 and 10 mm. As mentioned in **section 3.2.3.3**, for a larger beam with a scattering foil, the electrons fluence reaching the sample is dramatically reduced. To reduce simulation time, the scattering foil was not included in the model, and the incident beam was assumed as a flat rectangular 6 MeV electron beam with dimensions of 25 x 25 mm. For each collimation, the simulation was performed with 24 x 10^6 electrons in total and particles with energies below 10 keV were not followed. The 2D

dose profiles obtained with Monte-Carlo simulations are shown in **figure 3.7b**. Gafchromic film was irradiated with 20 pulses of 1 μs with 105 mV charge monitor output per pulse to assess beam collimation effects and the validity of the Monte-Carlo simulations. The film was scanned and processed as described in **section 3.2.3.1**. The 2D dose profiles obtained are shown in **figure 3.7c**. In order to compare the relative dose percentage curves obtained with simulation and Gafchromic film, the 2D dose profiles obtained for all collimations, were integrated across 2 mm in the centre of the film (green dashed boxes in **figure 3.7b** and **figure 3.7c**) and plotted as a function of distance from the edge of the film closest to the beam line (**figure 3.7d**). The profiles and relative dose percentage curves obtained with simulations and scanned films were seen to be identical, proving the validity of the simulations for all collimations and incident flat beam. Analysing the profiles, an increase in collimator height resulted in a more homogeneous dose distribution. Smaller collimations resulted in a sharper dose falloff closer to the irradiated edge. The relative dose percentage curve and 2D dose profile for the 10 mm x 12 mm showed a dose distribution across 10 mm between 85 and 100% of the maximum dose over an 88 mm^2 area, as opposed to smaller collimations which presented a sharper dose decay with distance from the irradiated edge. The relative dose percentage fell below 80% at 4.5 mm and 7 mm away from the irradiated edge, for 2.5 and 5 mm collimator height respectively. The collimation chosen for the experiments carried out in **chapter 5** and **chapter 6** was 10 mm x 12 mm.

3.2.3.5 Biological validation of beam collimation

As mentioned in **section 3.2.3.3** Gafchromic cannot be in contact with water and therefore it could not be used to predict the dose distribution across the plane where the cells are attached. Monte-Carlo simulations were performed to assess dose distributions at the

sample level. Simulations were run as described in **section 3.2.3.4**. The dose was integrated over 100 μm of water above the coverslip where the cells are attached in order to obtain relative dose percentage curves. The dose values were averaged over 2 mm across the centre of the sample (similar to examples illustrated in **figure 3.7b** and **figure 3.7c**). The relative dose percentage curves obtained were found to be similar to the curves obtained when the dose integration was performed across the Gafchromic film (black lines in **figures 3.8c, 3.8d** and **3.8e**). At the cell level, it was hypothesized the average number of 53BP1 foci could decrease with the distance from the irradiated edge, depending on the collimation. In order to confirm the results obtained with the Monte-Carlo simulations, HT1080-53BP1-YFP cells were plated in square dishes as described in **section 4.5**, 24 h before being irradiated using the linac. The samples were irradiated with 2.5, 5 and 10 mm collimator heights at an average dose of 1 Gy (dose determined as described in **section 3.2.4.1**). After irradiation, the samples were placed at 37°C and 5% CO_2 for 30 min. Following incubation, the samples were fixed and stained for 53BP1 as described in **section 4.6.1**. The samples were imaged with the imaging system described in **section 2.5**. The focus was set on the irradiated edge, and using the automated microscope stage, 6 FOVs were acquired per distance in steps of 500 μm away from the irradiated edge (**figure 3.8a**). The samples were imaged between 0.5 and 8.5 mm away from the irradiated edge (**figure 3.8b**). The number of 53BP1 foci per nucleus was manually counted (as described in **section 4.12.3**) and averaged over the 6 FOVs acquired per distance. Unirradiated samples were imaged to obtain the average number of background 53BP1 foci. The average number of radiation-induced 53BP1 foci was plotted as a function of distance from the irradiated edge per beam collimation (colour symbols in **figures 3.8c, 3.8d** and **3.8e**).

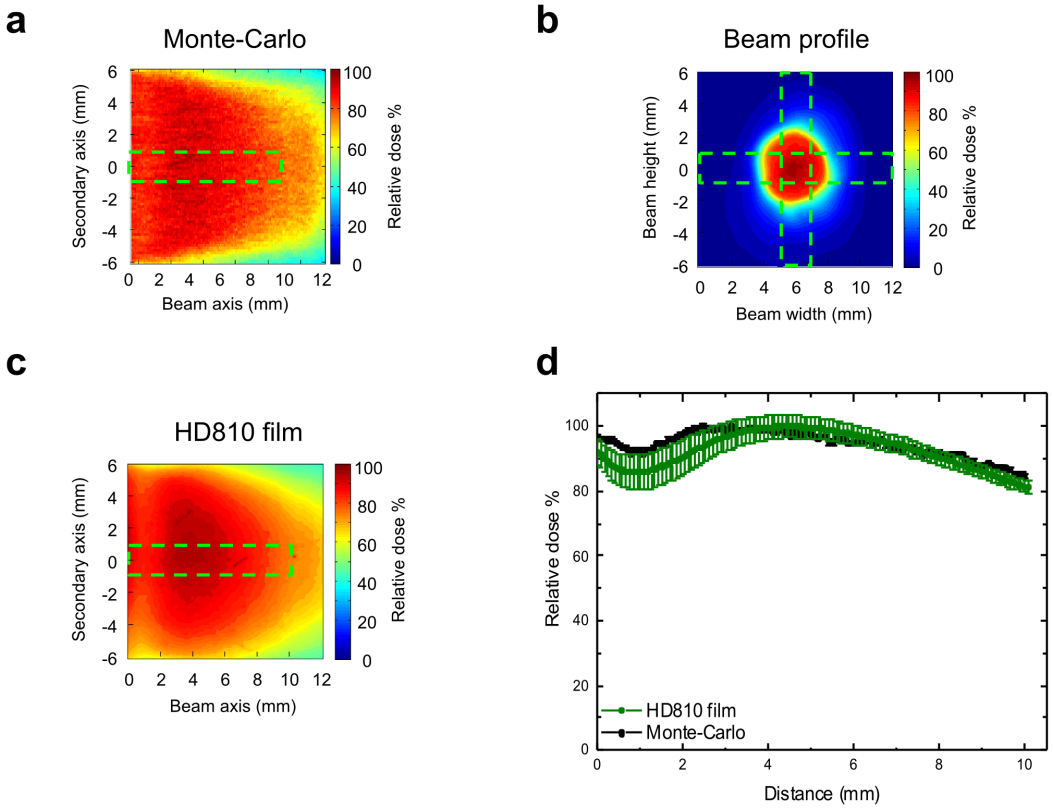


Figure 3.6 Dose distribution comparison between film irradiation and Monte-Carlo simulations using a 4 mm diameter spot beam. a) 2D relative dose profile obtained with Fluka, integrated over the Gafchromic film located as illustrated in **figure 3.3**. **b)** Characterisation of the 4 mm beam used experimentally, by irradiating film placed parallel to the collimator. **c)** 2D relative dose profile obtained with film irradiation, being the film located under the sample. **d)** Relative dose percentage curves obtained integrated across 2 mm as indicated by the green dashed boxes in **a** and **c**. Green error bars represent the s.e.m. (n = 3 individual experiments).

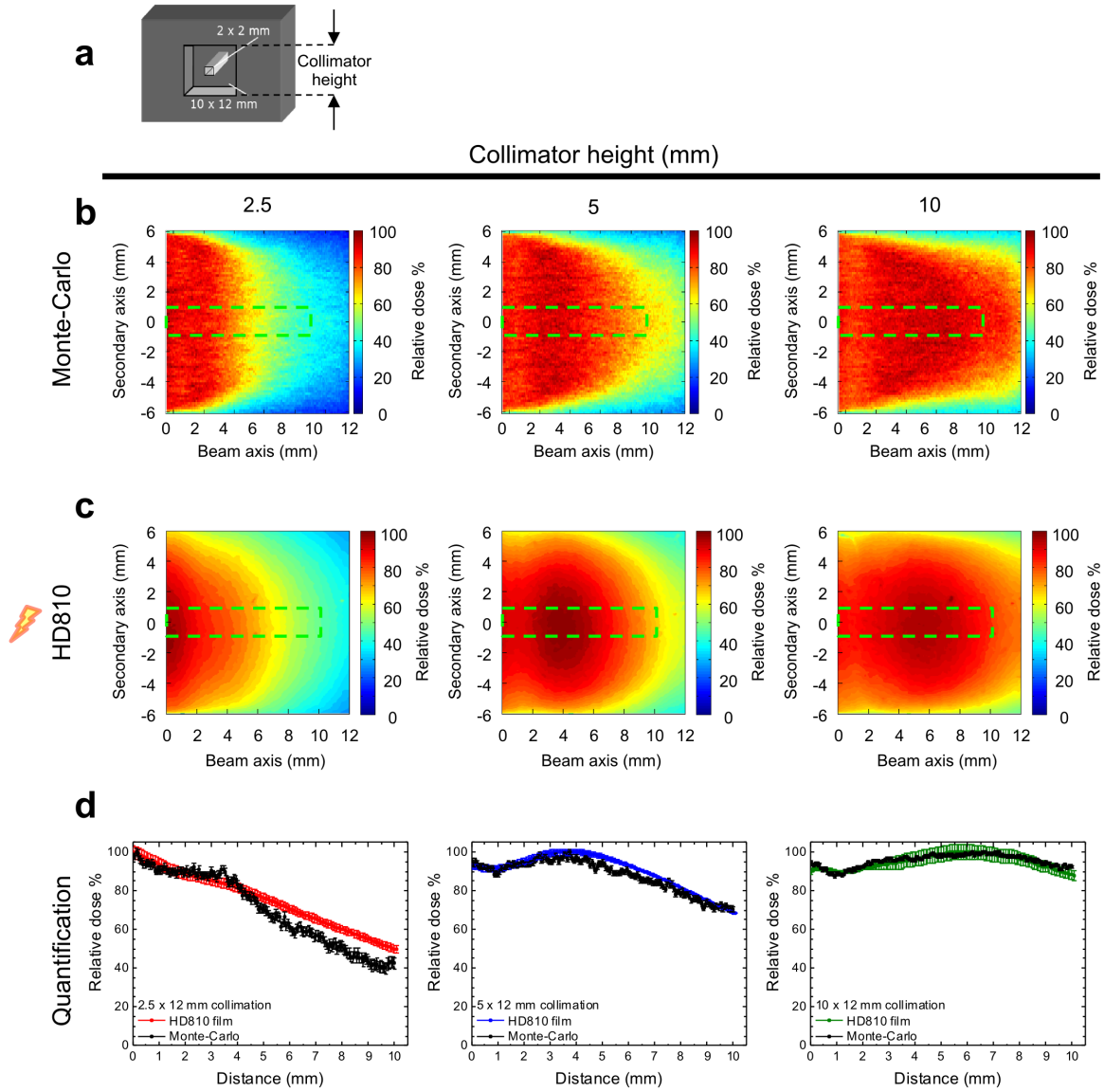


Figure 3.7 Collimator height determination by Monte-Carlo and film dosimetry. **a)** Schematic representing some of the different collimations that can be used. **(b, c)** Dose profiles obtained for different collimator heights using Fluka particle tracking software and scanned irradiated dosimetry film respectively. The film was placed as illustrated in **figure 3.3**. **d)** Comparison between the 2D dose profiles obtained with both methods. The green dashed lines in **(b, c)** represent the integrated areas used for the relative dose % curves plotted. Colour error bars represent the s.e.m. (n = 3 individual experiments).

The number of foci was seen to follow a similar trend to the relative dose percentage curves obtained with the simulated models. The number of radiation-induced foci decreased more abruptly with the distance from the irradiated edge for the 2.5 mm collimator height, and these numbers became more homogenous across the sample as the collimator height was increased. For a 10 mm x 12 mm collimation, the average number of 53BP1 foci was determined to be between 16 and 19 foci as a function of distance, compared to a simulated relative dose percentage between 85 and 100%. These data show a correlation between the number of 53BP1 foci and the dose distributions predicted by Fluka.

3.2.4 Dosimetry

As previously mentioned, one of the advantages of this experimental setup is that the radiation dose delivered can be accurately calibrated and monitored in Gy (J/kg). The radiation dose was determined using thermoluminescent dosimeters (TLDs) and Super Fricke dosimetry solution. The radiation dose obtained with these methods was calibrated to the voltage obtained with the charge monitor described in **section 2.2**. The output of the Čerenkov dose monitor photodiode was calibrated to the TLD dose measurements. The dosimetry was biologically validated by determining the average number of 53BP1 foci in response to increasing radiation doses using both the linac and a ^{137}Cs source.

3.2.4.1 Thermoluminescent dosimetry (TLD)

When heated following irradiation, TLDs emit visible light in proportion to dose. This light results from trapped electrons, forced to move to higher energy levels during irradiation. Once the TLD is heated, the electrons return to their ground state; this process is associated with photon emission at a wavelength corresponding to the difference between energy levels. The total amount of light emitted is proportional to the absorbed

dose. The crystals used in this work were lithium fluoride (TLD 100) and lithium borate (TLD 800), which can be used over dose ranges of 10 pGy to 10 Gy and 0.5 mGy to 10^5 Gy respectively (Qados Ltd, UK). After each irradiation, the TLDs were read out with a Harshaw TLD reader model 5500 (Qados Ltd). After each measurement, the chips were annealed by heating to 400°C for 2.5 h. Before calibration, the response of each chip to the same dose was assessed in different days. All TLD 100 chips were irradiated with 2 Gy and TLD 800 with 10 Gy using a ^{137}Cs source. The TLDs were grouped in sets of 4 chips based on their response. The chips were grouped so that the difference in outputs measured amongst the chips for the same dose was less than 2%. The TLD chips were then calibrated using a clinical Varian Clinac (Varian Medical Systems, UK) by irradiation with 6 MeV electrons at doses ranging from 0.25 to 10 Gy (TLD 100 chips), and 4 to 30 Gy (TLD 800 chips) using 4 chips per dose point. These were introduced into a packet and inserted in between water equivalent material (WTE material, Barts Water, UK) applicable to electron irradiation and a 1 cm thick bolus, as illustrated in **figure 3.9a**. Irradiations were performed using a Varian 15 cm x 15 cm electron applicator. Calibration curves were determined per chip type (**figure 3.9b** and **3.9c**). Post calibration, the TLDs were irradiated using the experimental linac with a 25 μm gold scattering foil and 10 mm x 12 mm collimation, at increasing voltages measured with the charge monitor described in **section 2.2**. TLDs however, should not be in contact with water therefore the chips were placed in WTE material as illustrated in **figure 3.10a**. The TLD responses were measured and the doses determined using the obtained calibration curves based on chip type. The doses measured using TLD dosimetry were plotted as a function of the voltage measured using the charge monitor (**figure 3.10b**). The doses measured ranged from 0.1 Gy for a single 50 ns pulse with 3.4 mV charge monitor output, to 15.5 Gy for a single 1 μs pulse with 465 mV charge monitor output.

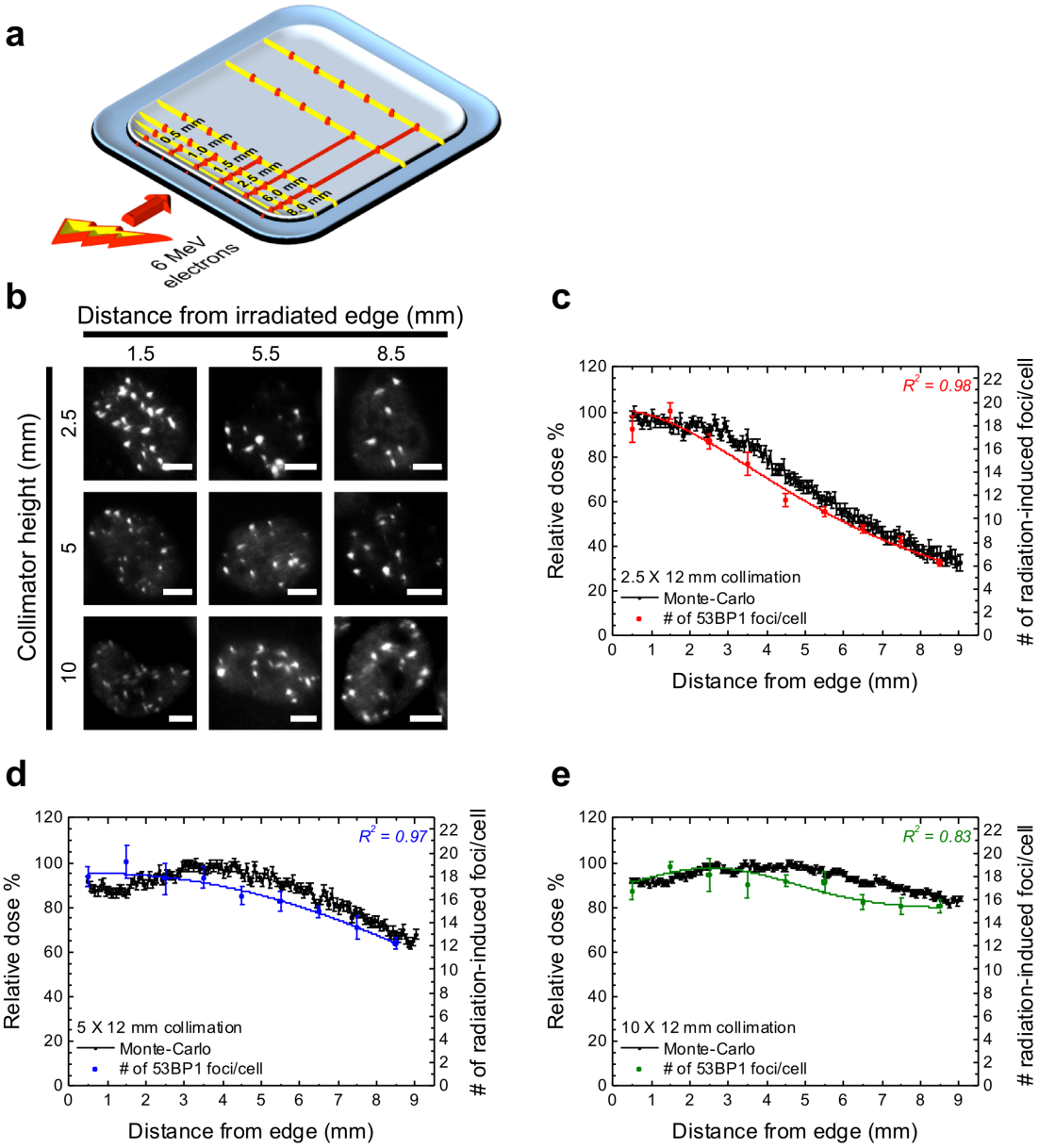


Figure 3.8 Biological validation of Monte-Carlo simulations using HT1080-53BP1-YFP cells. a) Illustration of the image acquisition process. Each red dot represents an acquired image. **b)** Micrographs displaying HT1080 cells stained against 53BP1 30 min after being irradiated with 1 Gy. Scale bar = 5 µm. **(c, d** and **e)** Comparison between Monte-Carlo obtained relative dose % curves and the number of 53BP1 foci across the sample for 2.5, 5 and 10 mm collimator height respectively. Cell number >> 100. The coloured error bars represent the s.e.m. (n = 3 independent experiments).

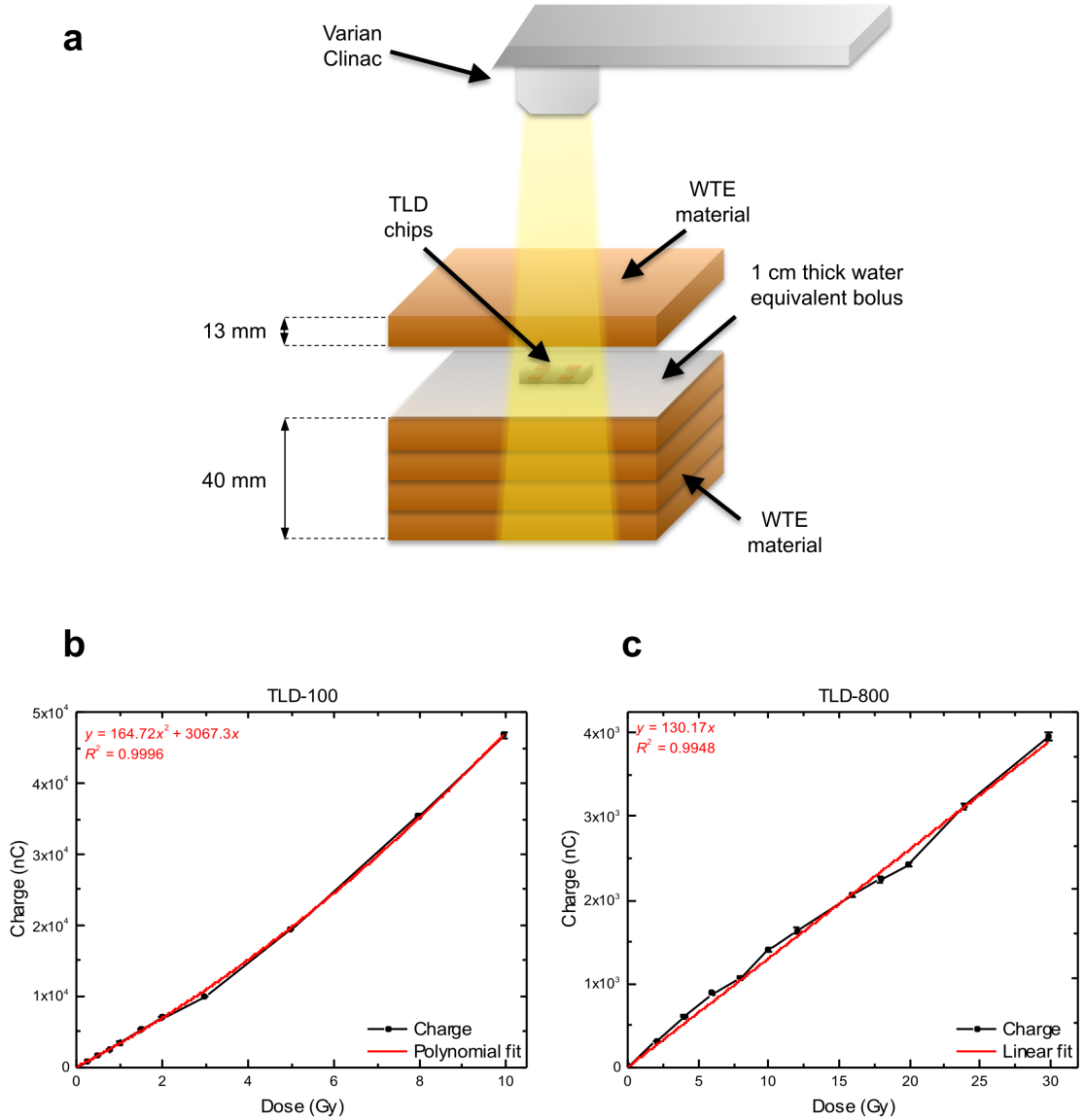


Figure 3.9 TLD calibration curves. a) Diagram illustrating the setup used to irradiate TLD chips using a Varian Clinac. **b)** Calibration curve obtained for TLD-100 chips. **c)** Calibration curve obtained for TLD-800 chips. Error bars represent the s.e.m. (n = 3 individual experiments, with 4 TLD chips per dose point).

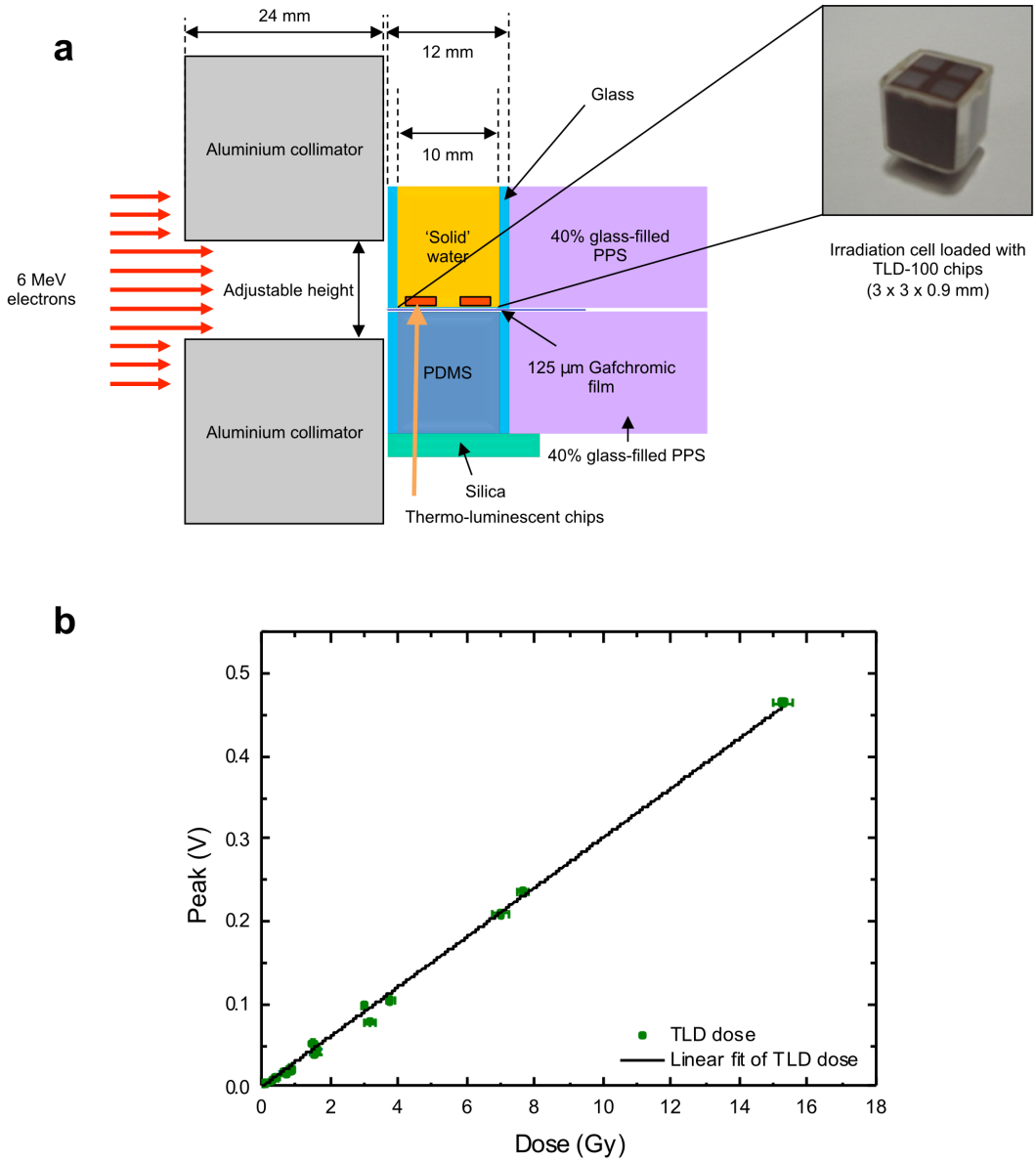


Figure 3.10 Linear accelerator dosimetry using TLD chips. a) Schematic of the irradiation assembly with TLD chips inserted in 'solid' water in a sample dish. **b)** Quantification of dose using TLD chips against charge monitor signal. Error bars represent s.e.m. (n = 3 independent experiments, with 4 TLD chips per dose point).

3.2.4.2 Fricke dosimetry

Fricke dosimetry was used in an attempt to confirm the doses measured with TLDs. Super-Fricke dosimetry solution (10^{-2} M of ferrous sulphate) when irradiated, causes the conversion of ferrous ions (Fe^{2+}) to ferric ions (Fe^{3+}). NaCl is used to remove impurities at high dose rates. The optical density of ferric ions at 304 nm can be translated into the average dose over the irradiated volume. The OD is proportional to the concentration of ferric ions, which in turn depends on the delivered dose. The result represents the average dose delivered to the irradiated volume. In order to perform these measurements, 800 µl of Fricke solution was irradiated by the linac per dose point, in triplicate. The output of the charge monitor was also recorded. The OD at 304 nm was measured, using a 1 cm path length cuvette and a 8453 UV-Vis spectrophotometer (Agilent Technologies UK Ltd, UK). The OD was corrected by subtracting the value read for unirradiated solution. The ODs were plotted as a function of the charge monitor output. These data were fitted with a linear regression line, and the slope (V^{-1}) was used to determine the dose rate in Gy/V using **equation 3.3** (O'Donnell and Sangster, 1970). The dose per irradiation was obtained using **equation 3.4**. The data were plotted as a function of the charge monitor output, together with the doses measured using TLDs (**figure 3.11**). The doses measured by the 2 different methods were found to be in agreement within ± 3.5%.

D_{rate}: *dose rate, Gy/V*
ΔOD: *slope of optical density fitted curve, V^{-1}*
ε_m: *molar extinction coefficient, 220 mol^{-1} m^2 at 25 °C*
G(Fe^{3+}): *chemical yield of Fe^{3+}, 1.61 x 10^{-6} mol J^{-1}*
ρ: *density of 0.4 M H_2SO_4, 1024 kg m^{-3}*
d: *optical path length, 0.01 m*

$$D_{rate} = \frac{\Delta OD}{\varepsilon_m \times G(Fe^{3+}) \times \rho \times d} \qquad \textbf{3.3}$$

Dose: *dose, Gy*
V_j: *voltage for pulse j*

$$Dose = D_{rate} \times V_j \qquad \textbf{3.4}$$

3.2.4.3 Čerenkov dose monitor calibration

As mentioned in **section 2.7**, the photodiode of the dose monitoring system can be used as a probe for dose measurements. For routine work, the integrated photodiode output was used, having been calibrated against TLD determined dose. To perform the calibration, a 200 μm thick piece of EJ-212 scintillator (Southern Scientific Ltd, UK) replaced the glass coverslip in a water-filled 'dummy' cell dish. This scintillator has an output of 10,000 photons per 1 MeV electron, with wavelengths ranging from 400 to 520 nm. The maximum emission occurs at 423 nm. Irradiations were performed for the same charge monitor outputs recorded during TLD irradiations. The photodiode output was recorded using a PicoScope model 6403 (Picotech, UK). The maximum value of the integrated signal (in μVs) was recorded and plotted as a function of the TLD dose measurements (**figure 3.12**). The output of the photodiode was calibrated to a maximum dose of approximately 4 Gy, before the photodiode signal was saturated. This calibration was used to facilitate routine dose checks at the sample level. The output of the photodiode was determined to be 5-fold lower when no scintillator is present in the sample to be irradiated. The damage contribution of the UV light resultant from Čerenkov emission required consideration when UV-hypersensitive model systems are used (Michael *et al.*, 1981; Petin *et al.*, 2011).

3.2.4.4 53BP1 dose response

In order to assess the dose measurements at the biological level, HT1080-53BP1-YFP cells were plated for irradiation on square dishes as described in **section 4.5**. Samples were irradiated with doses ranging from 0.5 to 2 Gy with the experimental linac and a ^{137}Cs source. The samples were allowed to repair the induced damage for 30 min at 37°C and 5% CO_2 humidified air.

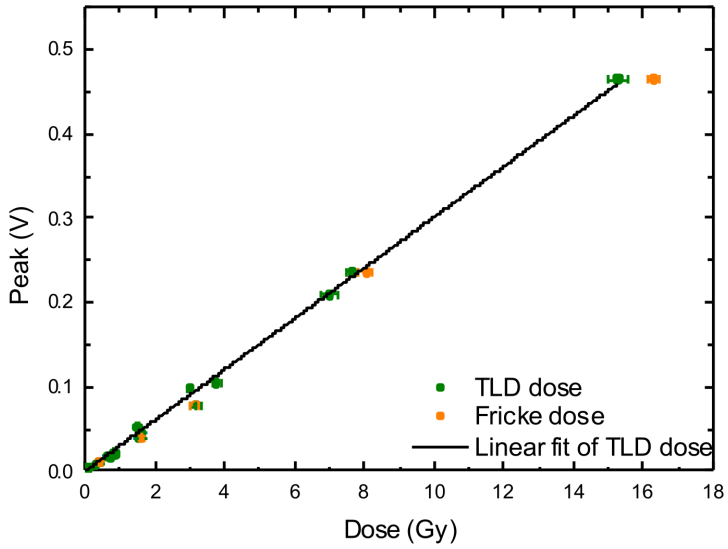


Figure 3.11 Comparison between Fricke and TLD dosimetry. Quantification of dose using TLD chips and Fricke dosimetry, against charge monitor signal. The differences between TLDs and Fricke were found not to be significant (p-values >> 0.05 using one-way Anova statistical analysis). Error bars represent s.e.m. (n = 3 independent experiments, with 4 TLD chips, and 3 Fricke samples per dose point).

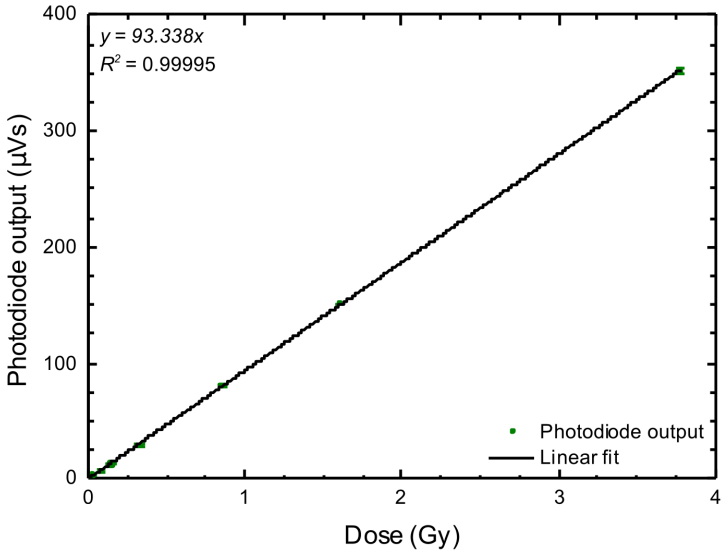


Figure 3.12 Calibration of Čerenkov monitor photodiode output against TLD dose. Integrated photodiode signal per dose point as a function of dose measured using TLD chips. Error bars represent s.e.m. (n = 3 individual experiments).

Following incubation, the cells were fixed and stained for imaging of 53BP1 foci, as described in **section 4.6.1**. The samples were imaged with the system described in **section 2.5** and the number of 53BP1 foci per cell was counted, as described in **section 4.12.3** (**figure 3.13a**). Control samples were also analysed in order to assess the background levels of 53BP1 foci, which were subtracted from the radiation-induced foci. The number of radiation-induced foci was plotted as a function of dose per irradiation system (**figure 3.13b**). At doses higher than 1 Gy the number of 53BP1 foci begins to saturate. These data confirmed the linac dosimetry at a biological level.

3.3 Discussion

In this chapter, the experimental system was validated in terms of automatically handling and irradiating the samples. The automatic handling unit was shown to be able to accurately reposition the samples mostly with accuracy below 100 nm at increasing lateral and vertical accelerations (**figure 3.1**). This capability allows the same FOVs to be followed pre- and post-irradiation with low-LET radiation. This represents a great advantage in terms of prior knowledge of the damage present at time of irradiation. More commonly, the samples are irradiated and then transported to a microscope in a separate location. This approach has issues associated temperature stability of the sample, on-going repair post-irradiation, and almost no information regarding the background damage prior to irradiation (Asaithamby and Chen, 2009). Furthermore, studies using HT1080-53BP1-YFP showed that no cell detachment is caused by automatic sample handling, and no additional damage is incurred by the cells, as monitored by the formation of 53BP1 foci in living cells (**figure 3.2**). The introduction of a scattering foil was assessed, in order to minimise potential beam variability during the irradiation process, and to obtain a homogenous distribution across the irradiated sample.

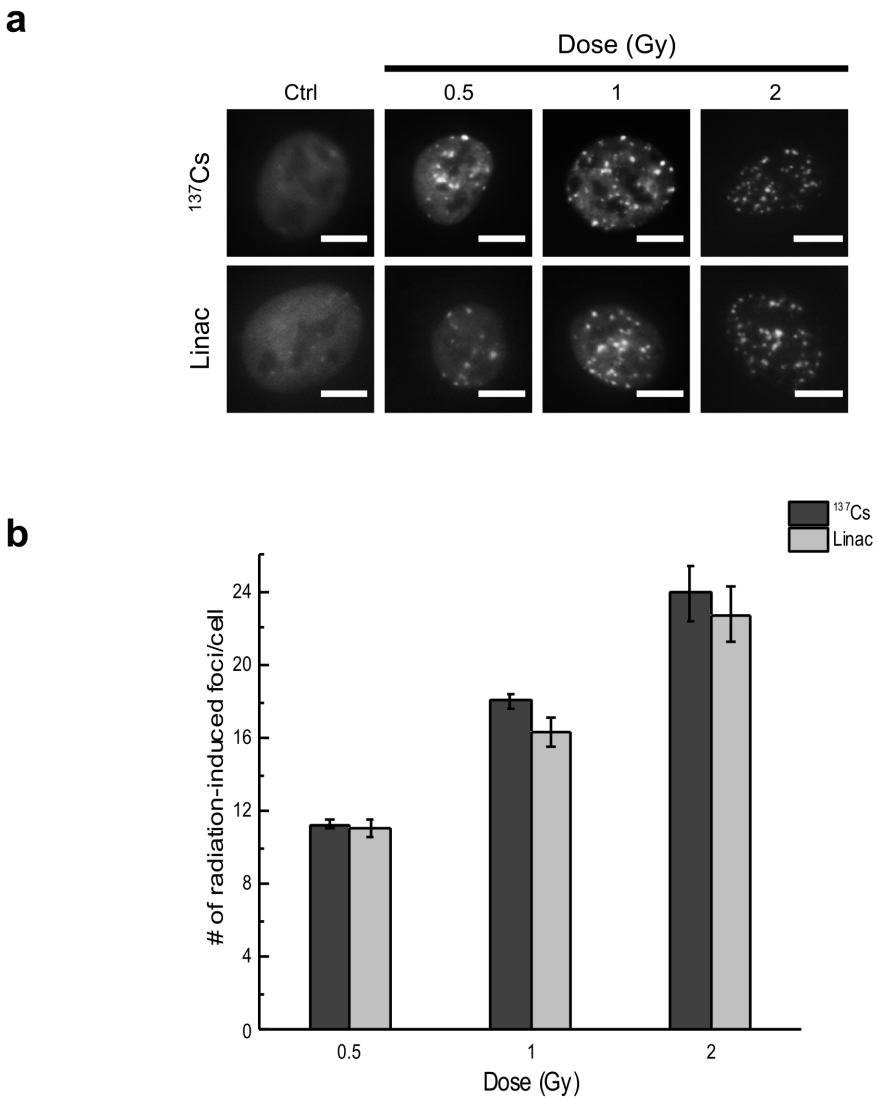


Figure 3.13 Dose response comparison between ^{137}Cs gamma-source and linear accelerator. a) Micrographs displaying HT1080-53BP1-YFP cells which were fixed 30 min after irradiation and immuno-stained against 53BP1. Scale bar = 10 µm. **b)** Quantification of the observed 53BP1 foci for different doses using both irradiation setups. Background foci numbers were subtracted to the radiation-induced foci. The differences in foci numbers observed with both systems were found not to be significant (p-values >> 0.05 using one-way Anova statistical analysis). The error bars represent the s.e.m. (n = 3 independent experiments).

Compared to the original beam, a 25 μm gold scattering foil ensured a homogenous distribution of the beam (**figure 3.4**), and a more homogenous distribution across the sample, as shown by the percentage depth-dose curve shown in **figure 3.5b**. With an increasing thickness of gold scattering foil, the Bremsstrahlung contributions to the dose at the entrance level of the sample may become more prominent. With the added thickness of gold, the resulting energy drop may also become more evident, contributing to a higher dose deposited at the sample entrance and resulting in a sharper dose decay across the sample.

Dose distributions were further characterised using Monte-Carlo simulations with Fluka particle tracking software. The validity of the simulations was proven using 4 mm diameter spot beam with a 25 μm scattering foil, showing similar dose distribution and relative dose percentage profiles to those obtained with irradiated Gafchromic HD810 film with the same beam settings (**figure 3.6**). As described in **section 3.2.3**, beam size and scattering foil impact on the fluence of electrons reaching the simulated Gafchromic film. This would in turn increase the time taken per simulation. The simulations to assess the dose distribution at the sample level in response to beam collimation were carried out using a model without a scattering foil and a flat rectangular 6 MeV electron beam with dimensions of 25 x 25 mm^2. The dose distribution was found to be more homogenous for a collimator height of 10 mm with dose across the sample within 85% of the maximum delivered dose (**figure 3.7**). For collimator heights of 2.5 and 5 mm, the relative dose percentage curves showed a sharper decrease in dose with distance from the irradiated edge. Whilst compromising on dose homogeneity across sample, the dose distributions obtained with smaller collimations may be useful for different types of experiments. With a 2.5 collimator height, the dose percentage was found to be approximately 40% of the maximum dose. Having prior knowledge of the dose percentage at a particular distance

from the irradiated edge could enable repair kinetics studies at different doses within the same sample. Moreover, the simulated data were found to be in agreement with the data obtained by Gafchromic film irradiation (**figure 3.7**), confirming the feasibility of using the Monte-Carlo model as a probe for the dose distributions at the sample level. The dose distributions, obtained with Fluka for different collimator heights, were also compared to a biological model. The number of 53BP1 foci in response to 1 Gy, as a function of distance from the irradiated edge, showed the same trend as the relative dose percentage curves obtained with Fluka for all different collimator heights (**figure 3.8**). These data further confirmed the capacity to translate the predicted dose distributions to a biological system.

As previously mentioned, most of the current DNA repair kinetics studies are performed by other workers, using laser microbeam irradiation. This type of approach has problems such as dose quantification, and wavelength-dependent damage induction, making it complicated to translate the resulting data from one institution to another (Reynolds *et al.*, 2013). TLDs were used to perform dosimetry with the linac experiment system. The doses, measured with TLDs (**figure 3.10**) were confirmed by Fricke dosimetry, and seen to be similar to within ±3.5% (**figure 3.11**). To perform regular dosimetry checks, the photodiode output (part of the Čerenkov dose monitor system described in **section 2.7**) was calibrated to the doses measured by thermoluminescent dosimetry. The dosimetry was validated at a biological level by irradiating HT1080-53BP1-YFP cells with increasing doses of radiation using both the linac and a ^{137}Cs source. These data showed the numbers of 53BP1 foci formed 30 min after irradiation using the same dose on both systems was identical.

The work presented in this chapter supports the feasibility of using the developed system to induce damage in the genomic DNA of cells in a repeatable and controlled fashion.

4. Biological materials & methods

4.1 Cell lines and cell culture reagents

The HT1080-53BP1-YFP human fibrosarcoma cells which were stably transfected with 53BP1-YFP, were kindly donated by Professor David Chen, and have been described previously by Asaithamby *et al.* (Asaithamby and Chen, 2009). HT1080-53BP1-YFP-Geminin-mCherry cells described in **section 4.3** were originated from the 53BP1-YFP cells. HT1080-*wild-type* (*wt*) cells were used as controls. U2OS human osteosarcoma cells were used for the sample repositioning studies described in **section 3.2.1**.

4.1.1 Antibiotics, inhibitors and other reagents

All antibiotics and inhibitors were diluted from stock solutions for use in culture and experiments using Modified Eagle's Medium media. **Table 4.1** lists all of the antibiotics, inhibitors and other reagents that were used during this study, including stock and final concentrations and storage conditions. The solvent and supplier are also indicated.

4.2 Dishes for cell culture of mammalian cells

All of the plastic ware used for cell culture was purchased from Falcon (BD Biosciences, UK) unless otherwise stated. The square glass dishes, used when the cells were irradiated using the linear accelerator facility, were purchased from Chance Glass (Chance Glass Ltd, UK) and assembled as described in **section 2.3**. For γ-irradiation, unless otherwise stated, cells were commonly plated onto type 1 glass coverslips glued onto 30 mm diameter glass-walled dishes using Araldite AT1 (Ciba-Geigy, UK).

Reagent (abbreviation)	Supplier	Stock Solution (Solvent)	Storage	Final Concentration
Geneticin, G418	PAA Laboratories Ltd, UK	50 mg/ml (H_2O)	4°C	0.4 mg/ml
Puromycin (Puro)	Sigma Aldrich, UK	1 mM (H_2O)	-20°C	0.5 μg/ml
KU-55933, ATM inhibitor (ATMi)	Calbiochem, EMD Milipore, USA	10 mM (DMSO)	-20°C	10 μM (IC_{50}: 13 nM)
AZD-2281, Olaparib, PARP inhibitor (PARPi)	Stratech Scientific Ltd, UK	10 mM (DMSO)	-20°C	5 μM (PARP-1/2 IC_{50}: 5 nM/1 nM,)
NU7441, DNA-PKcs inhibitor (DNA-PKcsi)	Stratech Scientific Ltd, UK	1 mM (DMSO)	-20°C	1 μM (IC_{50}: 14 nM)
AZD-0530, Saracatinib, Src inhibitor (Srci)	LC Laboratories, USA	10 mM (DMSO)	-20°C	5 μM (IC_{50}: 2.7 nM)
Bromodeoxyuridine (BrdU)	Sigma Aldrich, UK	10 mg/ml (H_2O)	-20°C	10 μM

Table 4.1 Reagents used in conjunction with cell culture based experiments. G418 and Puro concentrations were determined assessing the maximum cell killing of wild-type cells without an antibiotic resistance vector within 2-3 day incubation. Final inhibitor concentrations used in the experiments were determined by titration to establish the minimum concentration required to give a significant inhibitory effect as observed by western blotting.

4.2.1 Cell line maintenance and sub-culture

HT1080-*wt* derived cells and U2OS cells were cultured in Minimum Essential Medium (MEM) (Gibco, USA), and Dulbecco's Modified Eagle Medium (DMEM) (Sigma Aldrich, UK) respectively. The media were supplemented with 10% of foetal bovine serum (FBS) (Gibco), 100 units/ml penicillin, 100 μg/ml streptomycin and 2 mM L-Glutamine (Gibco) in the absence of phenol red. All cells were maintained at 37°C with 5% CO_2 humidified air, and handled in a class II laminar flow hood (Thermo Fisher Scientific Inc., UK). The 53BP1-YFP cells were also kept under selection medium supplemented with 0.4 mg/ml G418 (PAA Laboratories Ltd, UK). The Geminin-mCherry cells were supplemented with 0.5 μg/ml Puro (Sigma Aldrich, UK) and 0.4 mg/ml G418. All the cell lines were routinely cultured in T175 flasks (Corning, USA), which have a growth area of 175 cm^2. Cells were typically passaged 2-3 times a week once they had reached about 80% confluence, determined using an inverted microscope (Nikon Eclipse TS100, Nikon UK Ltd, UK), in order to maintain exponential growth. To passage each cell line, the medium was aspirated from the flask and the cell monolayer washed using 8 ml of phosphate buffered saline (PBS) (Fisher Scientific Inc., UK) at 37°C and pH 8.0 to remove any remaining of FBS which would inhibit the enzymatic action of Trypsin. Cells were then detached from the surface of the flask using 2 ml of 2x Trypsin/ethylenediaminetetraacetic acid (EDTA) (Gibco) and subsequently incubated at 37°C for approximately 2 min to allow Trypsin to hydrolyse the peptide bonds that are formed when adherent-type cells attach to the surface of the flask. This action causes the cells to detach from the surface of the flask so they can then be transferred to a 50 ml centrifuge tube (Corning) and diluted with 8 ml of culture medium. For experiments, the number of cells per ml was calculated using a haemocytometer (SLS Ltd, UK). Once the number of cells/ml had been determined, the

cells were plated 24 h before each experiment, and kept at 37°C and 5% CO_2 humidified air. Routinely, to maintain the cell line growing, 1/10 of the cell suspension was plated on a T175 flask without counting cell numbers. HT1080 derived cells were generally cultured up to 18-20 passages.

4.2.2 Storage of mammalian cells in liquid nitrogen

For long-term cryogenic storage, cells were harvested, transferred into a 50 ml centrifuge tube and counted as described in **section 4.2.1**. The cell suspension was centrifuged at 1100 rpm for 5 min (relative centrifugal force of 189) using an Eppendorf 5702R centrifuge (Eppendorf UK Ltd, UK). The growth medium was then aspirated and the cell pellet re-suspended to give a dilution of approximately $1x10^6$ cells/ml in growth medium containing 10%v/v dimethyl sulfoxide (DMSO) (Sigma Aldrich, UK) (a cryoprotectant). Subsequently, 1 ml aliquots were transferred to cryogenic Fisher vials, which were placed in a cryo container containing isopropanol (Fisher Scientific UK Ltd, UK) with a cooling rate of 1°C/min to prevent crystallization and cell lysis due to rapid freezing when placed at -80°C. The cells were maintained at -80°C for 24 h and then transferred to liquid nitrogen (-192°C).

4.3 Sub-cloning, amplification and purification of plasmid DNA

In order to generate a stable cell line co-expressing 53BP1-YFP and Geminin-mCherry, it was necessary for the 53BP1-YFP and Geminin-mCherry plasmids to confer resistance to different antibiotics. This would allow selection of cells that are positive for both 53BP1-YFP and Geminin-mCherry as only those co-expressing cells would maintain resistance to both antibiotics. To generate the Geminin-mCherry cell line with a Puro resistance cassette described in **section 4.1,** pRetroX-SG2M-Cyan (Geminin-Cyan) and pRetroX-G1-Red (Cdt1-mCherry) plasmids available in the lab were sub-cloned (Clonentech, USA).

4.3.1 Sub-cloning of plasmid DNA

To generate this vector it was necessary to perform enzymatic reactions to extract both Cyan and mCherry fragments from the respective vectors, and enzymatically ligate the mCherry fragment with the pRetroX-Geminin backbone. Following ligation, it was also necessary to replace the Neomycin resistance cassette with a Puro resistance cassette, due to the fact that the 53BP1-YFP vector present in the HT1080 cells already confers the latter cells Geneticin resistance (see **section 4.2.1**). For this purpose, both vectors were digested overnight at 37°C on a heat block (Thermo Fisher Scientific Inc.) with NotI and AscI restriction enzymes (for Cyan and mCherry extraction) or with HindIII restriction enzyme (for extraction of the Puro and Neomycin resistance cassettes) (Fermentas, UK). The restriction sites are highlighted in the vectors displayed in **figure 4.1**. The DNA concentration was measured using a NanoDrop 1000 detecting the absorbance at 260 nm (Thermo Fisher Scientific Inc.). The digestion reaction for Cyan and mCherry extractions was prepared in nuclease-free water (Life Technologies) in a total volume of 20 µl, containing 1 µg of DNA, 4 fold-excess NotI enzyme (2 µl, 20 U), and 2 fold-excess AscI (1 µl, 10 U) enzyme, and 2 µl of buffer R (10 mM Tris HCl, pH 8.5 at 37°C, 10 mM $MgCl_2$, 100 mM KCl, 0.1 mg/ml BSA) (Fermentas). For extraction of both Puro and Neomycin resistance cassettes, the digestions were also prepared in nuclease-free water in a total volume of 20 µl containing 1 µg of DNA, HindIII enzyme (0.5 µl, 5 U) and 2 µl of buffer R (Fermentas). The overnight reaction was stopped by heating the samples to 65°C for 20 min on a heat block.

The digests (100 ng) were then prepared to give a final concentration of 2X using 10X BlueJuice loading buffer (Life Technologies, USA), run on a 1% agarose (Sigma Aldrich) gel in 0.5X Tris-Borate-EDTA (TBE) buffer (Sigma Aldrich), for 1 h at 100 V using a

horizontal Bio-Rad kit (Bio-Rad, USA). The gel was then stained with ethidium bromide (0.5 μg/ml) (Life Technologies) for 5 min. The gel was illuminated with a UV trans-illuminator (Fotodyne Inc., USA) and the DNA fragments excised with a scalpel. The DNA was extracted using a QIAquick gel extraction kit (QIAGEN, USA). After excising the desired DNA fragment, 3 volumes of buffer QG (100 mg of 1% agarose gel per 100 μl of buffer) were added to the fragment which was incubated at 50°C on a heat block for 10 min, vortexing every 2-3 min to help dissolving the gel, before adding 1 gel volume of isopropanol (Fisher Scientific Inc.) to the sample. A QIAquick column was placed in a 2 ml collection tube and the sample was added to it. Using an Eppendorf 5415R centrifuge, the sample was centrifuged for 1 min at 16,400 x g (13,300 rpm). The flow-through was discarded and an additional 0.5 ml of buffer QG (containing 5.5 M guanidine thiocyanate (GuSCN), and 20 mM Tris HCl at pH 6.6) was added to the sample before centrifuging again for 1 min to remove all traces of agarose gel. The sample was washed by adding 0.75 ml of buffer PE to the column and centrifuging for 1 min. After discarding the flow-through, the sample was centrifuged for an additional 1 min. The column was then transferred to a new 1.5 ml microcentrifuge tube (Greiner Bio-One, UK) before eluting the DNA by addition of 50 μl of buffer EB (10 mM Tris-Cl, pH 8.5) and centrifuging for 1 min. After extraction, the ligation reaction was prepared to give a total volume of 20 μl. The mCherry fragment was ligated into the pRetroX-Geminin backbone using a 2:1 ratio (100:50 ng of DNA) of the mCherry fragment to the Geminin backbone, with 0.5 μl of T4 DNA ligase in 1X T4 DNA ligase buffer (Fermentas). The ligation was performed at room temperature for 30 min and stopped by heating to 70°C for 5 min on a heat block. The Puro resistance cassette fragment was ligated using a ratio of 5:1 (250:50 ng of DNA) into the pRetroX-Geminin-mCherry backbone (which had been depleted of the Neomycin resistance cassette) using 2 μl of T4 DNA ligase.

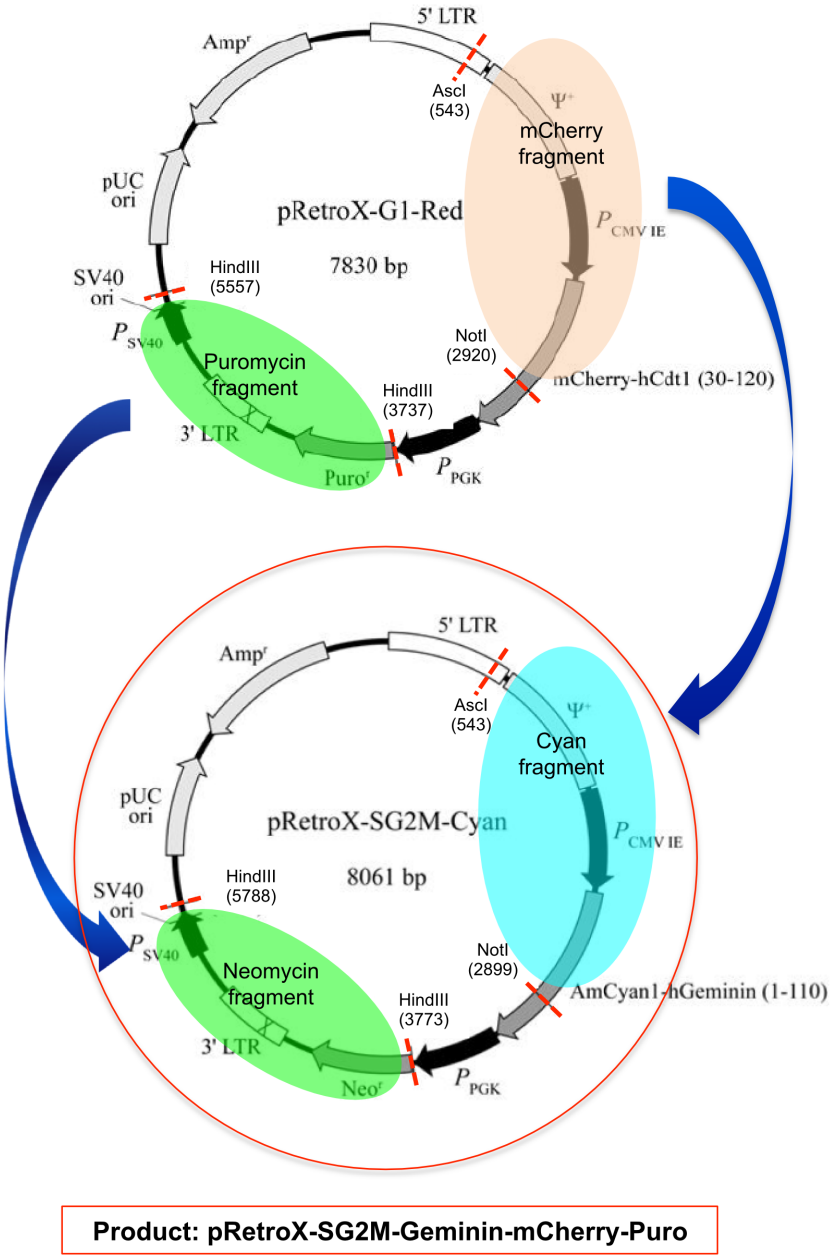


Figure 4.1 Generation of pRetroX-SG2M-Geminin-mCherry-Puro. Illustrations of the sub-cloned vectors used to generate Geminin-mCherry. The coloured regions highlight the fragments, which are flanked by the parenting restriction sites. The arrows indicate the insertion of the mCherry and Puromycin fragments into pRetroX-SG2M-Geminin.

Since both Puromycin and Neomycin cassettes were flanked by HindIII restriction sites, there was the possibility of the vector backbone to ligate itself and not with the Puro resistance cassette. To increase the probability of ligation between the backbone and the Puro resistance cassette, the amount of the Puro resistance cassette was increased.

4.3.2 Amplification and purification of plasmid DNA

In order to amplify plasmid DNA, 10 ng (8 µl) of the ligation reactions containing pRetroX-Geminin-mCherry-Puro plasmid were transformed into a 50 µl aliquot of chemically competent sub-cloning efficient DH5α E. Coli (Life Technologies). Following addition of the DNA, the aliquot was kept on ice for 30 min before a 20 sec heat-shock at 42°C on a water bath (Thermo Fisher Scientific Inc.). The tube was then kept on ice for a further 2 min before the addition of 450 µl of SOB medium (2% w/v tryptone, 0.5% w/v yeast extract, 10 mM NaCl, 2.5 mM KCl, pH 7). The sample was incubated in an Eppendorf ThermoMixer Comfort (Eppendorf) for 1 h at 37°C and 300 rpm. 200 µl of bacteria were spread on LB Agar (Sigma Aldrich) plates containing 100 µg/ml of ampicillin, used for growth selection due to the presence of an ampicillin resistance cassette in the transformed plasmid DNA. The plates were incubated at 37°C overnight. A single colony was picked the next day and added to 5 ml of LB medium (Sigma Aldrich) containing 100 µg/ml of ampicillin. The sample was incubated overnight in a shaking incubator (225 rpm, New Brunswick Scientific model innova 4230) at 37°C. The plasmid DNA was purified using a QIAGEN Plasmid Mini Kit (QIAGEN) to confirm successful incorporation of the plasmid on bacteria by running on a 1% agarose gel. Once correct incorporation had been confirmed, a further purification was performed to generate more DNA using a Plasmid Midi Kit (QIAGEN). Both kits have similar protocols, with the differences lying on the QIAGEN tips and the volumes of the different buffers added to the

sample. To purify the DNA using a Plasmid Mini/Midi Kit, it was necessary to harvest the bacterial cells by centrifuging them at 4°C for 15 min at 6,000 x g (6,800 rpm) (Eppendorf 5804R centrifuge) and resuspending the pellet in 0.3 ml (Mini Kit) or 4 ml (Midi Kit) of buffer P1 (resuspension buffer containing 50 mM Tris-Cl at pH 8.0, 10 mM EDTA, and 100 μg/ml RNase A). The sample was transferred to a 1.5 ml microcentrifuge tube. A volume of 0.3 ml (Mini) or 4 ml (Midi) of buffer P2 (lysis buffer containing 200mM NaOH, and 1% Sodium dodecyl sulphate) was added and the sample was left at room temperature for 5 min. Subsequently, 0.3 ml (Mini) or 4 ml (Midi) of buffer P3 (neutralisation buffer containing 3 M K-acetate at pH 5.5) was added to the sample, followed by a 5 min (Mini) or 15 min (Midi) incubation on ice. The sample was then centrifuged at 16,400 x g for 10 min at room temperature (Mini) or 30 min at 4°C (Midi) using an Eppendorf 5415R centrifuge. When using the Midi Kit, the supernatant was transferred to a new microcentrifuge tube and spun again for a further 15 min at 4°C. While the sample was being centrifuged a QIAGEN-tip 20 (Mini) or QIAGEN-tip 100 (Midi) was equilibrated by adding 1 ml (Mini) or 4ml (Midi) of buffer QBT (equilibration buffer containing 750 mM NaCl, 50 mM MOPS, pH 7.0, 15% of isopropanol, and 0.15% of Triton X-100) and allowing the column to empty by gravity flow. The sample supernatant was added to the column allowing it to enter the resin present in the column by gravity flow. The column was then washed 2 times with 2 ml (Mini) or 10 ml (Midi) of buffer QC (wash buffer containing 1 M NaCl, 50 mM MOPS, pH 7.0, 15% of isopropanol). After washing, the DNA was eluted into a microcentrifuge tube (Mini) or a 50 ml tube (Midi), using 0.8 ml or 5 ml of buffer QF (elution buffer containing 1.25 M NaCl, 50 mM MOPS, pH 8.5, 15% of isopropanol). Following elution, 0.56 ml (Mini) or 3.5 ml (Midi) of isopropanol was added to the sample and centrifuged at 15,000 x g for 30 min at 4°C. The supernatant was removed, and 1 ml (Mini) or 2 ml (Midi) of 70% ethanol

was added to wash the DNA pellet. The sample was centrifuged for 10 min at 15,000 x g. The supernatant was removed and the pellet was left to air-dry for 5-10 min before addition of 50 µl (Mini) or 250 µl (Midi) of buffer EB. The DNA concentration was then determined using a NanoDrop 1000 at 260 nm, and the sample stored at -20°C.

4.4 Stable transfection of mammalian cells with plasmid DNA

Prior to transfection, the created plasmid pRetroX-Geminin-mCherry-Puro was linearized for 3 h at 37°C with XmnI restriction enzyme in nuclease-free water in a total volume of 20 µl, containing 1 µg of DNA, 2 fold-excess XmnI enzyme (1 µl, 10 U), and 2 µl of buffer Tango (33 mM Tris-acetate, pH 7.9 at 37°C, 10 mM Mg-acetate, 66 mM K-acetate, and 0.1 mg/mL BSA) (Fermentas). The reaction was stopped by heating the sample to 65°C for 20 min on a heat block. Linearization was performed to facilitate correct vector integration. Before transfection, HT1080-53BP1-YFP cells were plated at a density of $2x10^5$ cells on a 6 cm diameter dish (Corning), in 5 ml of complete MEM media, and left to grow overnight at 37°C and under 5% CO_2 humidified air. On the following day, 1 µg of the linearized plasmid was diluted with Opti-MEM I Reduced Serum Medium (Life Technologies) to a total volume of 150 µl, following by addition of 20 µl of the transfection reagent Superfect (QIAGEN). The transfection complex was allowed to form for 10 min at room temperature. During this period, the cells to be transfected were washed twice in 4 ml of PBS. Following formation of the transfection complex, 1 ml of complete growth medium was added to the reaction. The transfection complex was then transferred to the 6 cm diameter dish and incubated for 3 h at 37°C in 5% CO_2 humidified air. The transfection complex was then aspirated, the cells washed with PBS and full growth medium was added. The cells were allowed to grow for a further 24 h before the addition of 0.5 µg/ml of Puro (selection for cells which incorporated Geminin-mCherry) and 0.4 mg/ml of G418

(selection for cells with incorporated 53BP1-YFP). After 4 days, the cells were trypsinized and counted as described in **section 4.2.1** and then serially diluted to give an average of 1 cell per 100 µl. Following dilution, 200 µl total volume containing 100 µl of cell suspension and 100 µl of complete growth medium were plated per well on 2 individual 96-well plates (Costar, Corning). Puromycin and G418 were added to the solution to give a final concentration of 0.5 µg/ml of Puromycin and 0.4 mg/ml of G418 per well. It was necessary to plate 1 cell per well in order to be able to generate clones, which derived from a single cell. The rationale was to achieve a more homogenous distribution of expression of the transfected plasmid across the whole population. After 4 days, the plates were checked using an inverted microscope (Nikon Eclipse TS100), to determine in which wells cell growth was derived from a single cell. The cells were allowed to grow for 10 days in total with the media being replaced with fresh full growth media containing selection agents every 2 days. After 10 days, the single colonies were trypsinized and transferred to individual T25 flasks (surface growth area of 25 cm^2) (Corning). Once each flask reached 80% confluence, the cells were trypsinized and plated into 30 mm glass-walled dishes (**section 4.2**) containing a total volume of 3 ml of full growth medium. The individual clones were checked for fluorescence of both 53BP1-YFP and Geminin-mCherry using the microscope in the linac experiment system, described in **section 2.5**. The selected clones showed a homogenous expression of both fluorophores amongst the population. The selected clones were then irradiated with 1 Gy of γ-radiation as described in **section 4.5** to assess those clones, which formed detectable 53BP1 foci in response to radiation. The selected clones were allowed to grow and preserved as described in **section 4.2.2**.

4.5 Irradiation of exponentially growing mammalian cells

During this project, cells were primarily irradiated using the linear accelerator described in **section 2.2**. When using this system, the dose delivered was determined as described in **section 3.4.3**. For such irradiations, cells were plated 24 h prior to irradiation at a density of 4 x 10^4 cells in the sample dishes as described in **section 2.3** to give a total volume of 800 µl of full growth medium, containing either 0.4 mg/ml of G418 only or additionally 0.5 µg/ml of Puromycin. Cells to be irradiated with γ-radiation were plated, unless otherwise stated, either in 3 cm diameter glass-walled dishes described in **section 4.2** (for immunofluorescence staining, **section 4.6**), or in 10 cm diameter dishes (Costar, Corning) (for western blotting, **section 4.7**). The irradiations were performed using a Gamma Service GSR D1 irradiator containing a ^{137}Cs source. The Radiation Biophysics core group at the Oxford Institute for Radiation Oncology determined the characteristic dose rates according to the vessel used and its position relative to the source, as described in **table 4.2**. Before irradiation and immediately afterwards, the samples were placed on ice to minimize cell processes including DNA repair. The medium was replaced with pre-warmed (at 37°C) full growth medium, and the samples were then incubated at 37°C in 5% CO_2 humidified air for the times stated on each experiment, and further processed for immunofluorescent staining (**section 4.6**) or western blotting (**section 4.7**).

4.6 Immunocytochemistry for protein and DNA labelling with fluorescent molecules

Immunofluorescent labelling was mainly applied to cells plated in the 3 cm diameter glass-walled dishes described in **section 4.2**. The cells that were irradiated prior to labelling were incubated for different times at 37°C and in 5% CO_2 humidified air before fixing the cells ready for the treatments described in **sections 4.6.1** and **section 4.6.2**.

4.6.1 53BP1, γ-H2AX and Cyclin A labelling

After incubation for the specified amount of time post γ-irradiation, the cells were washed in 1 ml of PBS and fixed in 3% paraformaldehyde (PFA) (made in PBS) (Sigma Aldrich) and kept at 4°C for at least 30 min. The cells were washed 3 times with 1 ml of PBS for 5 min at room temperature, before permeabilization with 0.5 ml of 1% Triton-X-100 (Sigma Aldrich) in PBS for 10 min. The cells were washed 3 times for 5 min in PBS at room temperature and then incubated with 0.5 ml of a blocking solution composed of 1% BSA (Sigma Aldrich) and 1% Fish skin gelatin (FSG) (Sigma Aldrich) in PBS for 1 h at room temperature. Primary antibodies, rabbit anti-53BP1 (Bethyl Labs, USA), mouse anti-phospho-H2A.X (Milipore, USA) and mouse anti-Cyclin A (Vector Labs Inc., USA), were diluted 1:500, 1:1000 and 1:50 respectively in blocking solution, and 150 µl added to each sample. The samples were incubated at 4°C overnight or for a 2 h period at room temperature. The cells were washed 3 times with 1ml of PBS for 5 min at room temperature. The secondary antibody Alexa Fluor 647 goat anti-mouse IgG (Life Technologies) was diluted 1:2000 in blocking solution. 150 µl were pipetted into each dish and left at room temperature for 1 h. Subsequently, the samples were washed 3 times with 1ml of PBS for 5 min at room temperature. A drop of Vectashield Mounting Medium with DAPI (Vector Labs Inc.) was added to each dish and covered with a glass coverslip. The samples were imaged as described in **section 4.12**.

4.6.2 RAD51 labelling

After treatment, the cells were washed in 1 ml of PBS and then fixed in 3% paraformaldehyde, made up in PBS-T (PBS plus 0.1% Triton X-100) (Sigma Aldrich), for 15 min. After fixation, the cells were washed twice in PBS for 10 min. Subsequently, the cells were permeabilized with PBS-T (0.3% Triton X-100) for 10 min.

Dose (Gy)	Vessel	Time (sec)	Position
0.5	3 cm ø	15	Centre
1	3 cm ø	34	Centre
2	3 cm ø	74	Centre
2	10 cm ø	87	Corner
4	10 cm ø	179	Corner
6	10 cm ø	271	Corner
8	10 cm ø	362	Corner

Table 4.2 Gamma Service GSR D1 irradiator dose rates. Dose is determined by the time that the sample is exposed to the source, and by the relative position to the source. In a more central position the samples are irradiated separately, as opposed to the corner positions when up to 4 samples may be irradiated simultaneously.

The samples were then blocked for 40 min in 3% Bovine Serum Albumin (BSA) (Sigma Aldrich) made up in PBS. The primary mouse antibody anti-RAD51 (GeneTex International Corp., USA) was diluted 1:500 in 3% BSA in PBS, and incubated at 4°C overnight. The following day, the samples were washed 3 times in PBS for 10 min. The secondary antibody Alexa Fluor 647 goat anti-mouse IgG (Life Technologies) was diluted 1:2000 in 3% BSA in PBS and 150 µl was added to each sample, and incubated for 1 h at room temperature. The samples were washed 3 times with PBS for 10 min, before staining with DAPI. The samples were imaged with the system described in **section 4.12**.

4.6.3 EdU labelling

In order to label cells in S-phase of the cell cycle, an EdU labelling protocol was followed using a Click-iT EdU Alexa Fluor 647 Imaging Kit (Life Technologies). After treatment, the cells were washed with PBS prior to fixation in 3% PFA in PBS for 15 min at room temperature. Post fixation, the cells were washed twice for 5 min in 3% BSA in PBS. Permeabilization was performed by a 20 min incubation at room temperature in 0.5% Triton X-100 in PBS. Following permeabilization, the samples were washed twice for 5 min with 3% BSA in PBS before addition of the Click-iT reaction cocktail, prepared according to the manufacturer's instructions, using a total of 500 µl per 3 samples. This cocktail consisted of 430 µl of 1X Click-iT reaction buffer, 20 µl of copper sulphate ($CuSO_4$), 1.2 µl of Alexa Fluor Azide (containing Alexa Fluor 647) and 50 µl of reaction buffer additive. The reaction cocktail was evenly distributed per sample and incubated for 30 min at room temperature in the dark. Following incubation, samples were washed once for 5 min with 3% BSA in PBS, followed by nuclear staining with mounting medium containing DAPI (Vector Labs.). Following the staining protocol, the samples were imaged as described in **section 4.12**.

4.7 Western blotting

All solutions and reagents were purchased from Sigma Aldrich unless otherwise stated.

4.7.1 Western blotting reagents

4.7.1.1 Lysis buffer

The lysis buffer is composed of 9 M urea (used to denature protein and increase its solubility), 75 mM Tris-HCL at a pH of 7.5 (used to regulate the acidity and osmolarity of the lysate), and 0.15 M of 2-mercaptoethanol (denatures the proteins).

4.7.1.2 Laemmli buffer (2X)

Solution contains 4% Sodium dodecyl sulfate (SDS), 20% glycerol, 10% 2-mercaptoethanol, 0.004% bromophenol blue and 0.125 M Tris HCl, at a pH of 6.8.

4.7.1.3 Tris-Glycine-SDS running buffer (10X)

This solution was prepared by dissolving 30.2 g of TRIZMA base and 144 g of glycine in 950 ml of dH_2O. SDS was also added at a final concentration of 10% from a 20% stock solution. The solution used during electrophoresis was diluted 10 fold with dH_2O from the 10X stock solution.

4.7.1.4 Tris-Glycine transfer buffer (10X)

This buffer was prepared by dissolving 30.2 g of TRIZMA base and 144 g of glycine in 1 litre of dH_2O. The solution used during the protein transfer step was diluted 10 fold in 700 ml of dH_2O and 200 ml of 100% methanol.

4.7.2 Sample preparation

A total of 750 x 10^3 cells were plated on 10 cm diameter dishes (Costar, Corning). After treatment, the samples were incubated at 37°C in 5% CO_2 humidified air for the designated

time depending on the experiment. The media was then removed from the dishes and the cells washed with ice cold PBS. The cells were then scraped in 1 ml of PBS and transferred to a 1.5 ml microcentrifuge tube. The samples were centrifuged at 16,400 x g (13,300 rpm) for 10 min using an Eppendorf 5415R centrifuge. Each sample was resuspended in 50 µl of lysis buffer, sonicated for 15 sec using a Digital Sonifier 450 (Branson, USA), and centrifuged at 16,400 x g (13,300 rpm) for 15 min. The supernatant was transferred to a new microcentrifuge tube. The protein concentration was measured using a NanoDrop ND-1000 at 280 nm. The samples to be loaded were prepared in a total volume of 30 µl by adding 50 µg of protein, 15 µl of 2X Laemmli buffer and dH_2O. The samples were denatured at 95°C for 5 min before loading.

4.7.3 Electrophoresis

All of the gels used during this project were purchased from Life Technologies with dimensions of 8 cm x 8 cm. When using Novex 4-20% Tris-glycine gels, the conditions used are described in **section 4.7.1.3**. When using NuPage 3-8% Tris-acetate gels, the running buffer was diluted 20 fold in dH_2O from a 20X stock solution purchased from Life Technologies. The gel cassettes were placed in a western blot kit Novex mini cell (Life Technologies) and 1X running buffer was added to fill the inner chamber, with an extra 200 ml of running buffer added to the outer chamber. On each gel, the molecular weight markers were loaded in the first lane. Depending on the molecular weight of the proteins, 5 µl of SeeBlue 2 marker (up to 250 kDa) or 10 µl of HiMark (up to 460 kDa) were loaded into the bottom of the first well. The samples were loaded into the bottom of separate wells. The Tris-glycine gels were run for 2 h at 125 V. On the other hand, Tris-acetate gels were run at 150 V for 2 h.

4.7.4 Western blotting

Western blot transfers were performed using a wet transfer XCell II Blot Module (Life Technologies). Nitrocellulose Hybond-ECL membrane (Amersham, GE Healthcare, UK) and blotting paper (Bio-Rad) were cut to the size of the gel. Gel, membrane, blotting paper and sponges were soaked in transfer buffer. Two pre-soaked sponges were placed on the cassette ensuring the removal of air bubbles. Two pieces of blotting paper were placed on the top of the sponges, with the gel being placed on top of the blotting paper. The membrane was then placed on the top of the gel followed by two more pieces of blotting paper. At this step it was important to guarantee no air bubbles were present between the membrane and the gel. If there were 2 gels to be transferred using the same cassette, one sponge was placed on the top of the blotting paper followed by a stack built similarly as for the first gel. Two more sponges were placed before the transfer cassette was closed and locked onto the western blot tank. The transfer cassette was filled up with transfer buffer, and the tank was filled with chilled dH_2O. The blot was run for 2 h and 35 min at 25 V, and 45 V for Tris-glycine and Tris-acetate gels respectively.

4.7.5 Blocking and antibody probing

The membranes were removed from the transfer cassette, and washed in PBS-T(1% Tween-20) for 5 min before being placed on blocking solution. When the membranes were developed by chemiluminescence, the blocking solution was composed of 5% milk powder (Morrisons, UK) in PBS-T. When the membranes were developed by detection of near-infrared fluorescence, the membranes were blocked in Li-Cor blocking solution (Li-Cor Biosciences, USA) diluted 1:1 in PBS-T. The membranes were blocked for 1 h at room temperature before the primary antibody was diluted in the blocking solution, and incubated overnight at 4°C. The details of all the primary antibodies used during this study

are described in detail in **table 4.3**. On the following day, the membranes were washed 3 times for 5 min in PBS-T. After the washes, the membranes were incubated for 1 h at room temperature with the secondary antibody solution. The secondary antibodies were diluted in the blocking solution depending on the developing method. The details of the horseradish peroxidase (HRP) conjugated and the near infrared secondary antibodies for fluorescence detection are described in **table 4.3**. Following incubation with the secondary antibody, the membranes were washed 2 times for 5 min in PBS-T and 1 time for 5 min in PBS. The membranes were kept in PBS at 4°C until development.

4.7.6 ECL detection and X-ray imaging

The excess of PBS was removed from the membranes and these were placed on Saran wrap (DOW chemical company, UK) on a flat surface. Enzymatic chemiluminescence (ECL) mixture (Amersham Biosciences, UK) was pipetted over the membranes and left for 5 min. The mixture was removed from the membranes and these were placed on a new piece of Saran wrap on a flat surface. The membranes were wrapped in the Saran wrap and taped into an X-ray cassette (Hypercassette, Amersham Biosciences). Under safe light conditions chemiluminescence X-ray film (Amersham Biosciences) was placed over the wrapped membranes. The length of time of exposure was dependent on the quality of the primary antibody and determined by the strength of the obtained signal. These exposures varied from experiment to experiment but normally the exposure times were between 30 sec and 5 min. The film was removed from the cassette and placed into the compact X4 X-ray developer (Xograph, UK). Once the film was developed, the molecular weights were marked on the film by placing it over the membrane and using the signal of the molecular weight marker.

4.7.7 Near-infrared imaging of membranes

The membranes were removed from PBS and placed onto an Odyssey CLX (Li-Cor Biosciences) infrared imaging system. The membranes were flattened onto the scanner to ensure there were no air bubbles present. The scanned area was determined depending on the size of the membrane, following development by exposing the membrane with 685 and/or 785 nm laser, depending on the secondary antibodies used. Once the scanning process finished, the exposure was modulated by changing the brightness and the contrast of the image depending on the quality of the primary antibodies used.

4.8 Fluorescence activated cell sorting (FACS)-cell cycle analysis

4.8.1 BrdU incorporation/7-Aminoactinomycin D (7-AAD) staining

Cells were plated unless otherwise stated at a density of 500 x 10^3 cells per T25 (25 cm^2 area) flask for FACS analysis. The cells were pulse-labelled with 10 μM of BrdU (marker for proliferating cells) for 30 min prior to harvesting, then washed with 1ml of PBS and trypsinised from the surface as described in **section 4.2.1**. The cells were transferred to a 15 ml tube and diluted in 6 ml of PBS before being centrifuged at 189 x g (1100 rpm) for 5 min to form a pellet using an Eppendorf 5702R centrifuge. The PBS supernatant was then aspirated and the cell pellet re-suspended in 1ml of ice cold 70% ethanol (used to fix the cells and permeabilize the membrane). The samples were then stored at 4°C until further processing. The samples were centrifuged at 735 x g (2000 rpm) for 10 min using a Jouan Centrifuge CR3i (Thermo Scientific). The cell pellet was re-suspended in 0.5ml of 0.1M HCl made in PBS and incubated at 37°C for 10 min in order to denature DNA and allow access by the BrdU antibody. The reaction was then stopped by adding 3 ml of PBS before centrifuging the sample for 10 min at 735 x g.

Antibody	Species	Cat. #	Supplier	Dilution	Mol. Weight (kDa)
pDNA-PKcs-Ser 2056	Rabbit	4215	Cell Signalling, USA	1:500	470
Total-DNA-PK	Rabbit	PC127-100UG	Calbiochem, Milipore, USA	1:200	470
P53BP1-Ser 1778	Rabbit	2675	Cell Signalling	1:500	450
Total-53BP1	Rabbit	4937	Cell Signalling	1:500	450
PARP-1	Mouse	551025	BD Pharmigen, USA	1:1,000	113, 89
PAR	Mouse	sc-56198	Santa Cruz Biotech, USA	1:200	150-250
pKap1-Ser 824	Rabbit	A300-767A	Bethyl Labs	1:10,000	100
Total-Kap1	Rabbit	A300-275A	Bethyl Labs	1:2,000	100
Total-Src	Mouse	2110	Cell Signalling	1:2,000	60
pSrc-Tyr 416	Rabbit	6943	Cell Signalling	1:1,000	60
Geminin	Mouse	ab104306	Abcam, UK	1:250	24
β-Actin	Rabbit	4970	Cell Signalling	1:2,000	45
IRDye 680	Rabbit	926-32221	Li-Cor Biosciences	1:10,000	N/A
DyLight 800	Mouse	A90-516D8	Bethyl Labs	1:10,000	N/A
Anti-Rabbit IgG HRP-linked	Rabbit	7074S	Cell Signalling	1:2,000	N/A
Anti-Mouse IgG HRP-linked	Mouse	7072S	Cell Signalling	1:2,000	N/A

Table 4.3 Details of the antibodies used for western blotting.

Cells were then incubated with 100 µl of the anti-BrdU solution (20 µl and-BrdU, 74 µl PBS, 5 µl 10% Tween-20, 1 µl FBS) at room temperature for 1 h, washed in 3 ml of PBS and centrifuged for 10 min at 735 x g. 100 µl of the anti-mouse APC Alexa Fluor 750 (Life Technologies) antibody solution (5 µl anti-mouse APC, 89 µl PBS, 5 µl 10% Tween-20, 1 µl FBS) were added to each sample and incubated at room temperature in the dark for 30 min. The cells were then washed in 3 ml of PBS and centrifuged at 735 x g for 10 min. The PBS was then removed and 1 ml of the 7-Aminoactinomycin D (7-AAD) (Sigma-Aldrich) staining solution was added (used to distinguish between viable and apoptotic cells, this agent binds to DNA which allowed different cell populations to be distinguished according to DNA content). This solution was made of 1 ml of PBS with 50 µg/ml of 7-AAD and 200 µg/ml of RNase A (Sigma-Aldrich) (catalyses the degradation of RNA into smaller components). The samples were then incubated at 37°C in the dark for 30 min prior to analysis. In order to obtain a cell cycle profile, the samples did not require BrdU incorporation and were incubated with the 7-AAD solution following fixation in ethanol and re-suspension in PBS.

4.8.2 FACS analysis

The measurements were taken at a rate of 150-300 events collection per sec. The G1 population peak was appropriately centred during acquisition at channel 200. 10,000 events were collected per sample. The histograms of the different populations and the distribution of these were obtained using ModFit LT software package (Verity Software House, USA). Using this software, fitting was performed to extrapolate the percentage of cells in each cell cycle stage (see **figure 4.2a**).

To determine S-phase duration and population doubling times (T_{pot}), the data analysis was performed using FlowJo (Tree Star Inc., USA) and using the method described by Begg *et*

al. (Begg *et al.*, 1985). In order to perform this analysis, it was necessary to isolate 4 populations on the plot of BrdU fluorescence as a function of DNA content (**figure 4.2b**). FG1 represents the mode of 7-AAD fluorescence of the BrdU negative cells gated for the G1 population. FG2M represents the mode of 7-AAD fluorescence of the BrdU negative cells gated for the G2M cells re-entering cell cycle. FL is the mode of 7-AAD fluorescence of the BrdU positive cells, which represent the S-G2 population. Labelling index (*Li*) represents the % of total BrdU positive cells. The S-phase duration and the potential doubling times were calculated as in **equations 4.1-4.3**.

The system used for data acquisition was the Becton Dickinson FACSCalibur (BD, USA).

RM: *relative movement of BrdU labelled cells towards G2M*	$RM = \frac{FL - FG1}{FG2M - FG1}$	**4.1**
T_s***:*** *S-phase duration (h)* ***t:*** *time of incubation (h)*	$T_s = \frac{0.5 \times t}{RM - 0.5}$	**4.2**
T_{pot}***:*** *doubling time (h)*	$T_{pot} = \frac{Ts}{Li}$	**4.3**

4.9 Clonogenic survival assay

Clonogenic survival assays were performed using HT1080-*wt*, 53BP1-YFP and Geminin-mCherry cells, to assess survival following low-LET γ-radiation. Cells were plated 16 h prior to irradiation in triplicate on 10 cm diameter dishes in 10 ml of medium at different cell densities per dose as described in **table 4.4**. Following irradiation, the cells were incubated at 37°C in 5% CO_2 humidified air for 10 days. The plates were then removed from the incubator and the medium removed before 2 ml of crystal violet staining solution (Sigma-Aldrich) (0.5% in ethanol) was added to each plate.

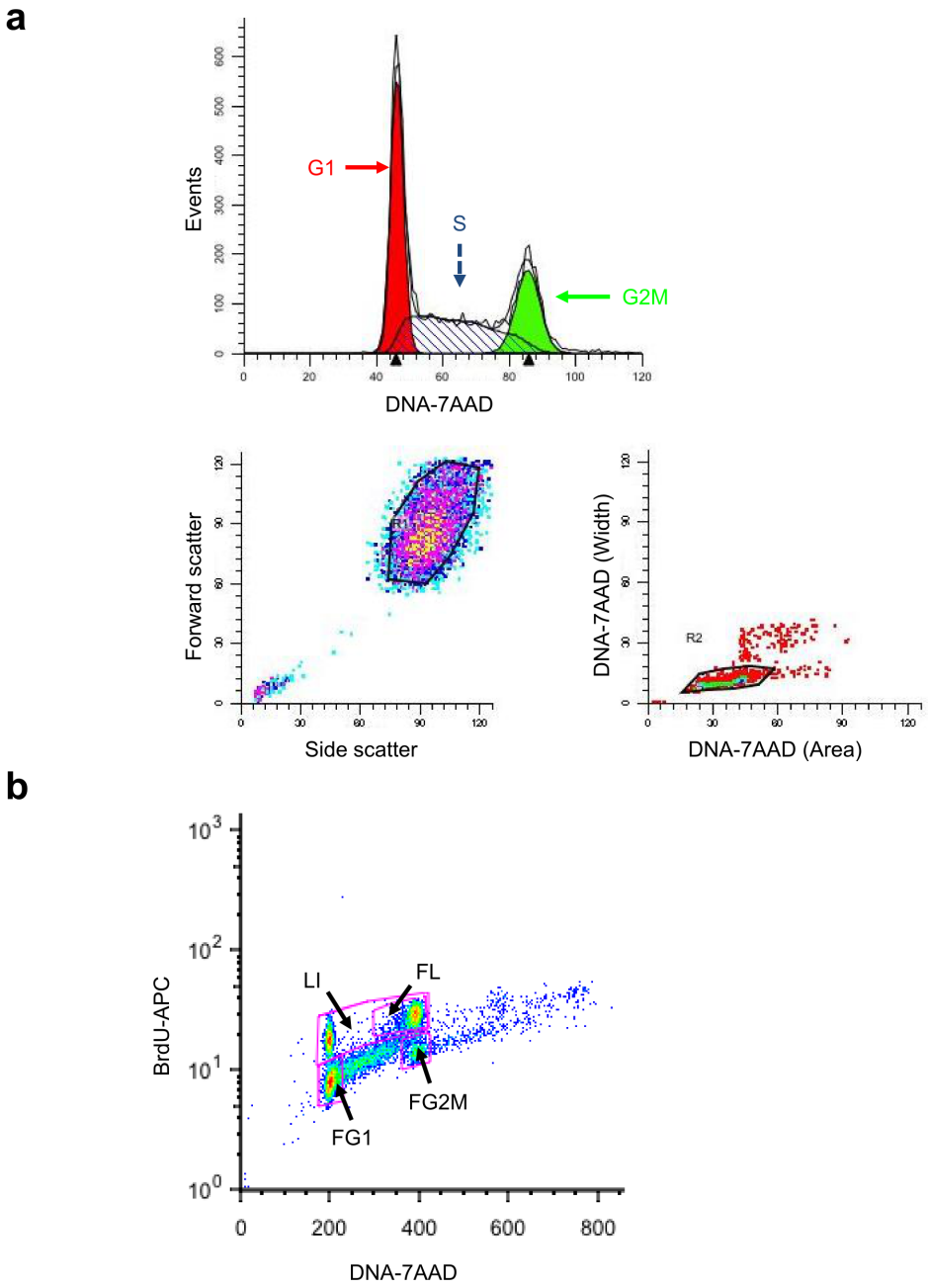


Figure 4.2 Cell cycle analyses by flow cytometry using ModFit, and FlowJo. a) ModFit obtained histogram based on the population isolated by size, and DNA content as measured by 7-AAD. **b)** FlowJo obtained cell cycle distribution based on BrdU fluorescence as a function of DNA content. The isolated populations used for the S-phase duration and T_{pot} calculations are indicated.

The samples were placed on a shaking platform for 30 min before the staining solution was removed and the plates washed in dH_2O and left to dry overnight.

The colonies were identified and counted using a colony counter (Gallenkamp, Germany). The plating efficiency (*PE*) and survival fraction (*SF*) was calculated for each cell line using **equation 4.4** and **equation 4.5** respectively. The survival data were plotted as the logarithm of the surviving fraction as a function of radiation dose.

***PE:** plating efficiency*

$$PE = \frac{\#\ of\ colonies\ counted}{\#\ of\ cells\ plated} \times 100 \qquad \textbf{4.4}$$

***SF:** surviving fraction*

$$SF = \frac{\#of\ colonies\ counted}{\left(\#\ of\ cells\ plated \times \frac{PE}{100}\right)} \qquad \textbf{4.5}$$

4.10 Scratch-wound assay

This assay was performed using HT1080-53B1-YFP cells, in order to assess the invasive phenotype and cell motility in response to Src inhibition. This is achieved by letting cells grow to confluency and then introducing a wound, and monitoring how quickly the wound area is repopulated. For this purpose, cells were plated at a density of 7,500 cells per well on an Essen BioScience 96-well plate (Essen BioScience, USA) 24 h before the wound was made using a Woundmaker (Essen BioScience). The 2 control columns were seeded with the equivalent DMSO volume to that of the highest Saracatinib concentration used. Each plate was placed in an Incucyte Zoom imaging system (Essen BioScience) at 37°C and 5% CO_2 humidified air. The wound on each well was imaged by phase contrast every 2 h for 24 h. The images were collected and processed per well using the Incucyte Zoom software (Essen BioScience). The invasiveness/motility per time point was measured as the relative wound density (RWD). This metric relies on measuring the spatial cell density in the wound area relative to the spatial cell density outside the wound area.

Dose (Gy)	Cell numbers plated
0	1000
2	2000
4	4000
6	6000
8	8000

Table 4.4 Seeding densities per radiation dose used in the clonogenic survival assay. Cell numbers were chosen to give a suitable number of colonies to count (>100 colonies) per dose point. Each density per dose point was repeated in triplicate per experiment.

This metric is designed to be 0% at time zero when the wound was made, and 100% when the spatial cell density in the wound area is the same as the density outside this area, making it a self-normalising metric. The RWD was averaged across all of the wells treated with the same Saracatinib concentration. The data were plotted as the RWD (%) per time point. Examples of the processed images are shown in **figure 4.3**.

4.11 Cell proliferation assay

This assay was performed using HT1080-53BP1-YFP cells, to measure the effect in cell proliferation of increasing Saracatinib concentrations. For this assay, cells were plated at a density of 2,500 cells per well on a 96-well plate (Costar, Corning) 24 h before starting to image the samples. Different concentrations of Saracatinib were added to the medium 10 min before the first image was taken, having 2 columns on each plate per concentration. The 2 control columns were seeded with the equivalent DMSO volume to that of the highest Saracatinib concentration used. The samples were put in an Incucyte Zoom imaging system (Essen BioScience) and imaged by phase contrast every 4 h for 24 h. 4 different fields of view were followed per well and monitored for the % of confluence using the Incucyte Zoom software (Essen BioScience). This metric determines the percentage of the image that is occupied by the cells. The % confluence was averaged over the 4 fields of view per well, and across all of the wells treated with the same concentrations of Saracatinib. The data were plotted as the % confluence over time. Examples of the processed images are shown in **figure 4.4**.

4.12 Fluorescence microscopy

The samples processed as described in **section 4.6** were imaged using a laser-scanning microscope LSM 780 (Zeiss, Germany). This system was equipped with a 405 nm laser used to visualise DAPI stained DNA. An Argon ion laser operating at 514 nm was used to

excite 53BP1-YFP. Geminin-mCherry was excited using a 561 nm diode-pumped solid-state (DPSS) laser. Alexa Fluor 647 labelled proteins, were excited with a 633 nm HeNe laser. The power, the gain and the pinhole were optimised to prevent saturation of the pixels, photobleaching of each fluorophore, and bleed through between channels.

4.12.1 Imaging of γ-H2AX/RAD51 and 53BP1 labelled samples

Samples stained for γ-H2AX or RAD51 were imaged using an EC Plan Neoflur 40×/1.3 (numerical aperture) oil objective (Zeiss). The output was digitised to 12 bits with a pixel size of 512 x 512 pixels, corresponding to a field of 212.5 μm x 212.5 μm with a pixel size of 0.415 μm x 0.415 μm. All images were averaged over 16 frames to reduce the Poisson distributed noise by a factor of 4. 53BP1-stained samples were imaged with the microscope system described in **section 2.5** using a Cy5 dichromatic cube.

4.12.2 Imaging of Cyclin A/EdU labelled samples

Samples stained for Cyclin A or EdU labelled were imaged using a Plan 20×/0.8 (numerical aperture) air objective (Zeiss). The output was digitised to 12 bits with a pixel size of 512 x 512 pixels, corresponding to a field of 425 μm x 425 μm with a pixel size of 0.83 μm x 0.83 μm. All images were averaged over 16 frames to reduce the Poisson distributed noise by a factor of 4. With either objective, data from 3 to 4 areas were acquired per sample in order to image 100-300 (cell cycle profile studies) cells to increase statistical significance. The images were analysed as described in **section 4.12.3**.

4.12.3 Image analysis

The number of foci per cell was manually determined using the ImageJ software package (Schneider *et al.*, 2012). The total number of foci was divided by the total number of cells in the image giving the average number of foci per cell.

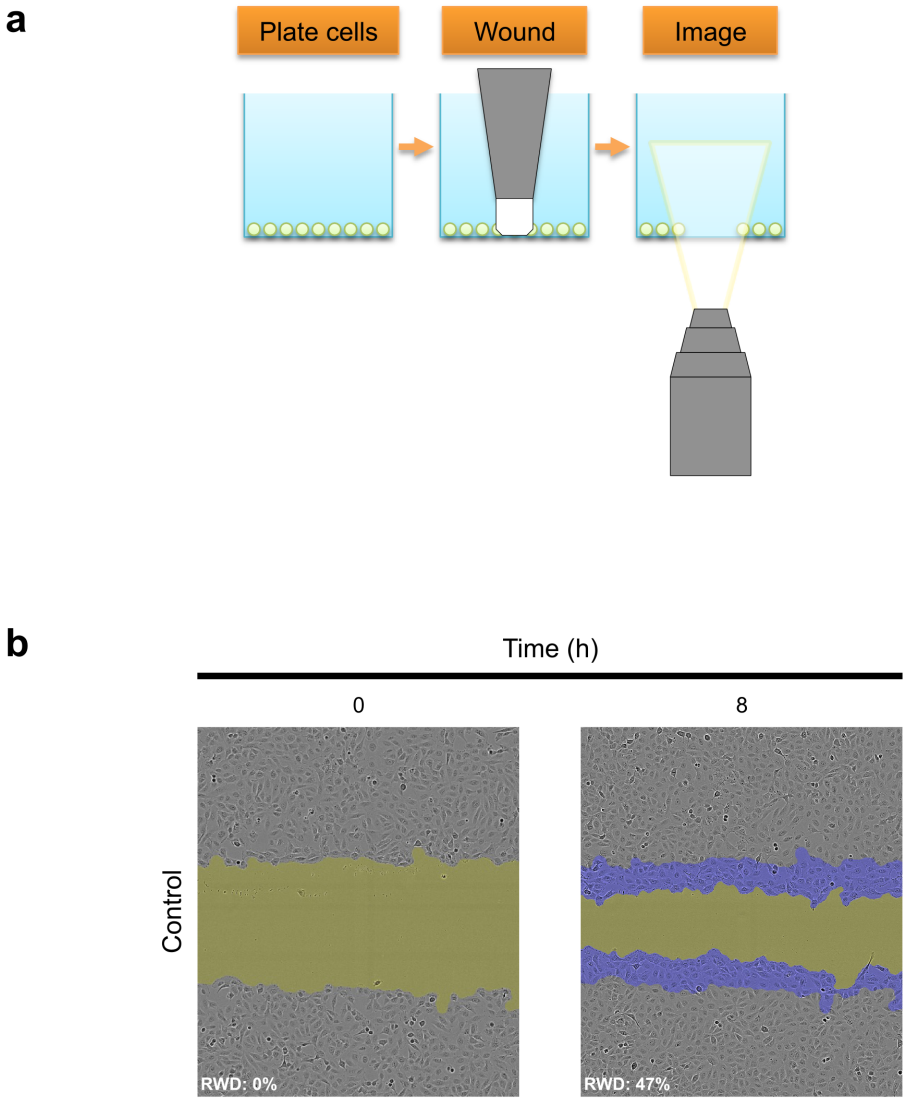


Figure 4.3 Scratch-wound assay description and analysis. a) Diagram of the protocol followed to perform the scratch-wound assay. The cells are plated 24 h before the experiment, wounded (layer of cells removed), and then imaged over time. **b)** Representative micrographs of the analysed control data. The green mask represents the wound region that is not populated. The blue mask illustrates the portion of the original wound region, which has become populated by cells. The relative wound density (RWD) percentages are indicated.

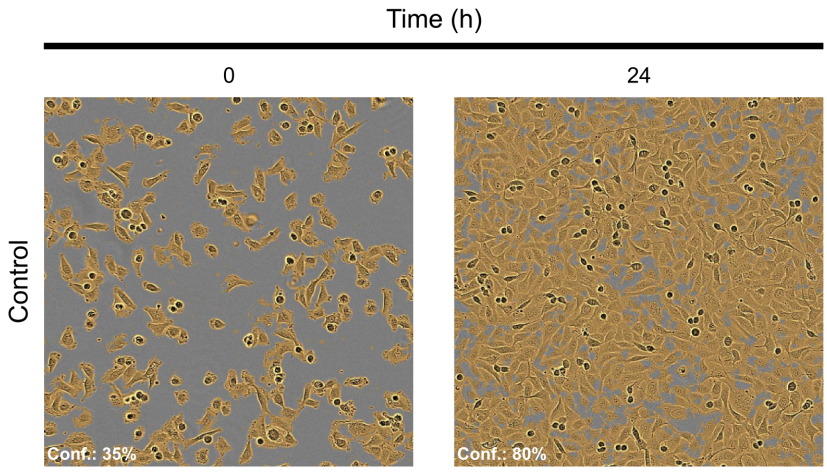


Figure 4.4 Cell proliferation assay analysis. Representative micrographs of the analysed control data. The Incucyte Zoom software (Essen BioScience) detects individual objects, and calculates the percentage of the total area that is occupied by the cells. The confluence percentages are indicated.

The images were merged with the nuclear staining image in order quantify only nuclear foci. The image display was adjusted to facilitate visibility of the dimmer cells, expanding the scale avoiding overexposure of the brightest cells. The number of foci per cell was also automatically determined using the TRI2 software package developed at the Gray Institute (Barber *et al.*, 2007). The use of this software is described in more detail in **Appendix A1**. The total number of cells positive for Cyclin A, Geminin-mCherry, EdU and DAPI stain, was obtained manually using ImageJ.

4.13 Statistical analysis

The data presented throughout this thesis were, unless otherwise stated, the result of an average over three individual experiments. The average was calculated using OriginPro (OriginLab, USA) software. The standard error of the mean (s.e.m.) was calculated using **equation 4.6**. The standard deviation used to calculate the standard errors was obtained with OriginPro software. When presented, the p-values were obtained using the One-way Anova statistical analysis tool provided by OriginPro software. The significance level was set at 0.05.

σ: *standard deviation*
n: *number of observations*

$$S.E.M. = \frac{\sigma}{\sqrt{n}} \qquad \textbf{4.6}$$

5. Dynamics of 53BP1-YFP recruitment to DNA damage sites at the single focus level

5.1 Introduction

The work presented in this chapter addresses the dynamics of recruitment and loss of 53BP1-YFP to radiation-induced DNA damage sites in real-time using living HT1080-53BP1-YFP cells and compares this with data obtained using fixed cells. The advantage of using the linac experimental approach is that individual foci may be followed in real-time in individual cells to give detailed information on prompt and delayed formation of foci post-irradiation. In order to perform such studies, it was necessary to optimise the image processing methodology. This optimisation was needed to minimise the out-of-field blurring characteristic of widefield microscopy. Cell segmentation and registration was tested to account for cell translational and rotational motion to assess the feasibility of automated data analysis, permitting time-resolved single-foci studies at the single-cell level. The stability of YFP to light exposure was also addressed to determine the impact of constant exposure on the observation of radiation-induced 53BP1 foci due to photobleaching. In addition, the invasive phenotype characteristic of HT1080 cells, in contrast to many other cell lines, confers greater mobility, which poses difficulties in following the same cells throughout the time sequence of a live-cell imaging experiment lasting up to several hours. Efforts were made in order to minimise cell motion and thus facilitate live-cell imaging experiments.

To study DNA repair kinetics, p53-binding protein 1 (53BP1) was used as the DNA damage signalling probe. In the majority of experiments on recruitment of 53BP1 to radiation-induced DSBs, immunocytochemistry methods have been used, with the cells generally irradiated at 4°C prior to their incubation at 37°C (Markova *et al.*, 2007; Rappold *et al.*, 2001; Wang *et al.*, 2002). The necessity to lower the temperature at which cells are irradiated is to minimise the DNA repair processes and as a consequence is reflected in the recruitment kinetics of proteins to DNA damage sites. In addition, immunocytochemistry approaches only provide a snapshot in time of the repair processes, without prior knowledge of the damage present at time of irradiation, especially when using micro-irradiation (Reynolds *et al.*, 2013). The recruitment kinetics of 53BP1-YFP to DNA damage sites has previously been characterised using living HT1080-53BP1-YFP cells (Asaithamby and Chen, 2009; Asaithamby *et al.*, 2011), where the maximum number of foci per cell was observed 30 min after irradiation. The number of foci subsequently returned to background levels ~8 h post-irradiation following a dose of 0.5 and 1 Gy.

Cells were therefore irradiated with the linear accelerator at 37°C in 5% CO_2 humidified air in order to explore the dynamics of recruitment of 53BP1-YFP in real-time, under physiological conditions. The formation and loss of 53BP1 foci with time were assessed and monitored at the single-focus level within single cells following irradiation with 0.5 Gy, highlighting the potential of this type of analysis in the study of individual prompt DSBs and late developing DSBs, detected through the recruitment of 53BP1-YFP in real-time to radiation-induced sites of DNA damage.

5.2 Results

5.2.1 Optimisation of image processing

As mentioned in **section 2.5**, the imaging part of the linac experiment system is a camera-based widefield imaging system. Since widefield imaging is contaminated by out-of-focus blurring (Pawley, 2006), image deconvolution was used to minimise the consequences of this effect. Blind image deconvolution (Holmes and O'Connor, 2000) was implemented in the AutoQuant X3 software package (Biggs, 2004). Since foci can be formed in any 'z' plane within the nucleus, low step-size z-scanning is required, followed by collapse of the z-stack. Multiple z-slices are acquired per FOV and per time point. Autoquant X3 software package estimates the system point spread function and uses this to predict the light dispersion above and below the focal plane. This process results in a collapsed image with minimal out-of-field blurring. Although this process is ideally performed with a large number of closely-spaced slices, cumulative photobleaching allowed only 21 slices to be collected. Each slice was collected with an exposure of 115 ms, at each FOV (covering the whole cell thickness), at a 'z' spacing of 350 nm. The resulting following deconvolution is an image stack, (for every time point and every field of view), which is collapsed to represent the total intensity for each cell nucleus. In **figure 5.1**, an example of a FOV is shown before and after deconvolution. The mean intensity within the rectangular region of interest (ROI) representing the background was decreased by a factor of 2 following deconvolution. On the other hand, the mean intensity of the focus highlighted within the circular ROI increases by a factor of 2 after de-convolution. In general, the minimum intensity observed in the deconvolved image set is reduced by a factor of 6 when compared to the original image set. These data highlight the increase in signal-to-background fluorescence ratio.

During live-cell imaging experiments, the cell translational or rotational motion causes problems for automated analysis. One way to correct for cell movement is to perform automated cell segmentation and registration. This was achieved by using previously published cell segmentation software package (Dzyubachyk *et al.*, 2010a; Dzyubachyk *et al.*, 2010b). Once the segmentation is concluded, it also corrects for the rotational motion of the nucleus. This approach has the great advantage of allowing single-cell studies, making it possible to follow the history of an independent focus (which would be complicated if per time point the focus coordinates were changing). In **figure 5.2a** an example is shown of a segmented FOV per time point. In **figure 5.2b** examples of two cells are shown, highlighting the correction of the rotational motion following segmentation. As a 'proof-of-principle', this software package was used to segment the cells presented in **sections 5.2.2** and **5.2.5**. A plethora of YFP intensities characteristic of this particular cell line poses difficulties to cell segmentation and automated foci analysis of multiple cells within the same FOV.

5.2.2 Stability of YFP to light exposure

Photobleaching is the photochemical destruction of a fluorophore due to excitation, and the extent of photobleaching increases with exposure time. Photobleaching is particularly hard to avoid during time-lapse live-cell imaging.

To assess the photobleaching kinetics of 53BP1-YFP during a conventional time-lapse experiment using the linac experiment system, HT1080-53BP1-YFP cells were plated in the cell dishes described in **section 2.3**. The samples were then placed within the environmental enclosure of the linac experiment system at 37°C and 5% CO_2 humidified air. 21-slice z-stacks were acquired per FOV. Each FOV was imaged 15 times to give a total of 315 frames (**figure 5.3a**). For comparison, the samples were imaged 15 times using

a standard sequence (6 times at 1 min intervals up to 5 min, 5 min intervals up to 15 min and finally every 15 min up to 2 h), 15 min intervals, and 1 min intervals. The data were processed as described in **section 5.2.1**. The mean intensities of 30 nuclei per condition per individual experiment were recorded and normalised to the maximum intensity observed in the first acquisition. The normalised intensity decreases in a linear fashion for the samples imaged once every minute, eventually reaching approximately 65% of the maximum intensity (**figures 5.3b** and **5.3c**). The cells imaged every 15 min (purple line in **figure 5.3c**) show an approximately linear decay in fluorescence intensity but at a lower rate when compared to the samples imaged every 60 sec (**figure 5.3c**). After 315 frames, the normalised intensity was approximately 80% of the maximum. When the samples were imaged using a standard time-lapse sequence, the decay in intensity followed that observed by the samples imaged every min up until the 6^{th} acquisition. After 126 collected frames, recovery in fluorescence intensity was observed due to the increase in time between acquisitions. The intensity decay followed that observed by the samples imaged every 15 min after 231 collected frames, reaching approximately 80% of the maximum intensity after 315 frames (**figures 5.3b** and **5.3c**). These data showed that the detrimental effects of the faster imaging at an early stage are counterbalanced by an increase in time between acquisitions as the experiment progressed. These findings confirmed the possibility of faster imaging at early times should this be required.

5.2.3 Cell mobility minimisation: Src-inhibition

HT1080 cells are known for being extremely invasive and motile (Niggli *et al.*, 2009). This poses difficulties during live-cell imaging experiments, due to the impediment of following the same cells throughout the experiment.

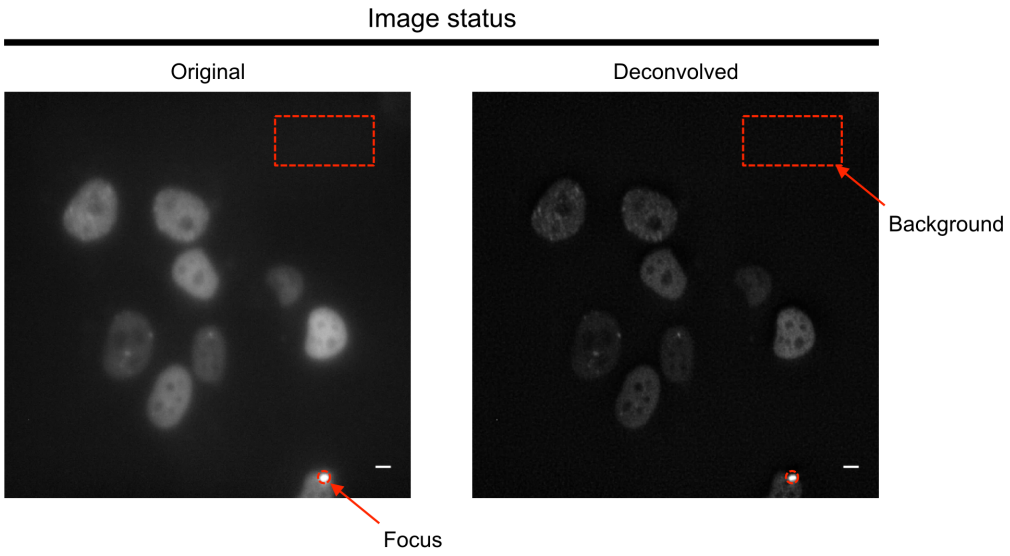


Figure 5.1 Image processing: blind deconvolution. Micrographs representing an example of a deconvolved dataset using AutoQuant X3. 21 z-slices were acquired with a 'z' spacing of 0.35 µm. The z-stack was deconvolved using AutoQuant X3. The z-stack was collapsed as the sum intensity projection. Scale bar = 5 µm.

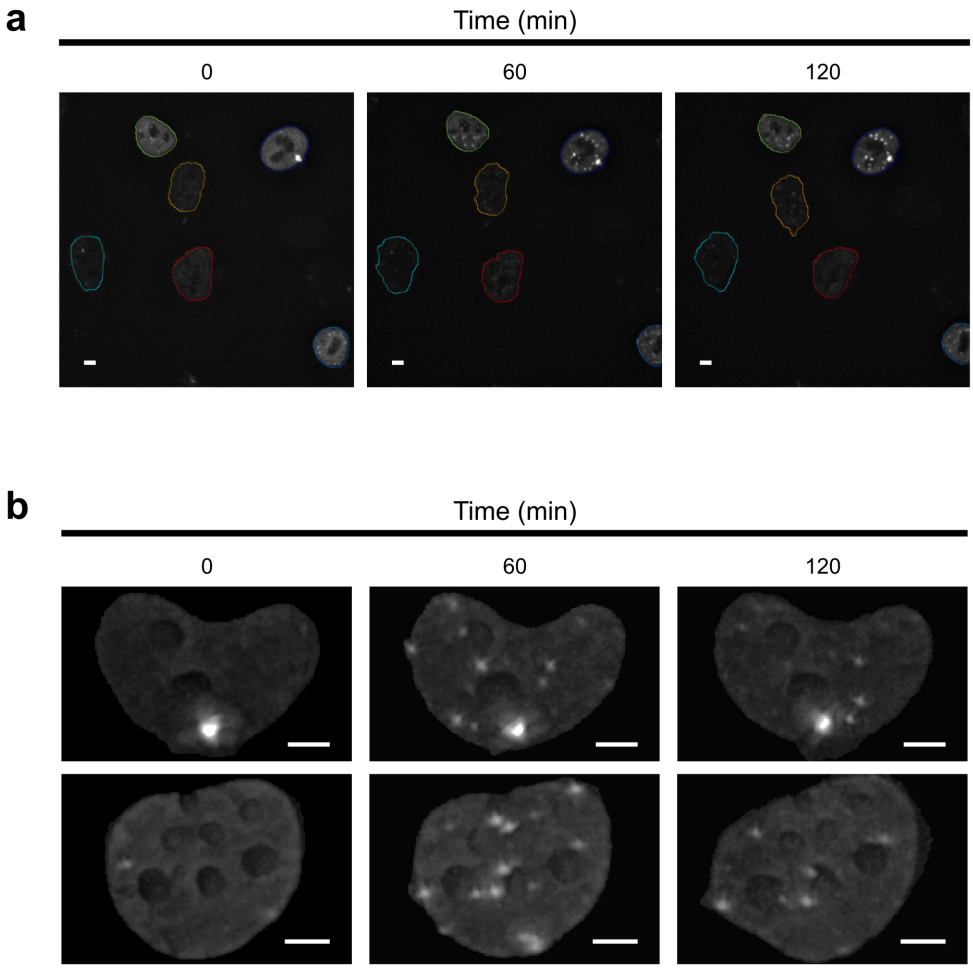


Figure 5.2 Image processing: cell segmentation and registration. a) Micrographs representing an example of a segmented FOV per time point. The images represent the deconvolved sum intensity projections per time point. **b)** Micrographs representing examples of two registered cells per time point post-segmentation. Scale bar = 5 µm.

In an attempt to reduce cell movement, the coverslips (part of the dishes described in **section 2.3**) were coated with poly-l-lysine (Sigma Aldrich) in order to enhance the adherence of the cells. Cells were plated as described in **section 4.5** and imaged every 15 min for 2 h using the imaging system described in **section 2.5**. This procedure does not have an effect on the translational movement capacity of the cells. Alternatively, the coverslips were coated with Cell-Tak (BD Biosciences) to enhance cell adhesion. This compound similarly to poly-l-lysine, did not impact on the movement capacity of HT1080-53BP1-YFP cells.

Src oncogene is part of the non-receptor tyrosine kinases, and it plays a role in processes such as cell migration, adhesion, invasion, survival and proliferation, both in normal and in cancer cells (Parsons and Parsons, 2004; Purnell *et al.*, 2009). Saracatinib, a known Src kinase inhibitor, has been shown to reduce the invasive potential of multiple cell lines, including HT1080 cells (Green *et al.*, 2009; Purnell *et al.*, 2009). The reduction of Src activity can be monitored by a decrease in the levels of Src phosphorylation at the Tyr-416 (Y416) residue (Arcaroli *et al.*, 2010). The reduction in cell motility imposed by Saracatinib could in principle facilitate DNA repair kinetics studies using HT1080-53BP1-YFP cells as a model system. The effect on cell movement was assessed by scratch-wound assays and observed in live cells using the system described in **section 2.5**. The effect of this compound on cell proliferation, and 53BP1-YFP recruitment kinetics to sites of damage was also analysed.

5.2.3.1 Saracatinib inhibitory effect

Saracatinib (LC Labs) was used to achieve Src inhibition (described in **table 4.1**). In order to test the inhibitory effect of Saracatinib on the inhibition of Src-Y416 phosphorylation 24 h before harvesting, HT1080-53BP1-YFP cells were plated for western blotting as

described in **section 4.7** with increasing Saracatinib concentrations ranging from 250 nM to 5 μM. In order to detect Src-Y416 phosphorylation as shown in **figure 5.4a**, it was necessary to load 150 μg of the whole cell extract (WCE) as determined by a protein concentration titration. All of the Saracatinib concentrations tested were shown to inhibit efficiently Src-Y416 phosphorylation (**figure 5.4b**) when compared to the levels in the control lane (addition of DMSO equivalent of the highest Saracatinib concentration). Concentrations higher than 5 μM were toxic to the cells.

5.2.3.2 Saracatinib effect on cell migration

As shown in **figure 5.4b**, Saracatinib is very effective in inhibiting Src-Y416 phosphorylation at low concentrations. However, it was necessary to assess the impact of increasing Saracatinib concentrations on cell migration. To assess cell migration, HT1080-53BP1-YFP cells were plated on a 96-well plate and processed using the scratch-wound assay as described in **section 4.10**. The inhibitor was added 10 min before introducing the wound. All wells were imaged every 2 h for 24 h after the wound had been introduced and the data were subsequently processed using the Incucyte Zoom software. The invasiveness/motility per time was measured as a relative wound density (RWD), which is based on the spatial cell density in the wound area relative to the spatial cell density outside the wound area. The RWDs were averaged over all the wells exposed to the same Saracatinib concentration per time point. As shown in **figure 5.5**, the wound area more readily repopulates under control conditions and at lower Saracatinib concentrations. The quantified data, shown in **figure 5.6a**, show the lowest RWD (30%) 24 h after wound induction for 5 μM Saracatinib. The effect on cell motility was confirmed by imaging live HT1080-53BP1-YFP cells in the presence or absence of 5 μM of Saracatinib (added at time of cell plating and 24 h before imaging).

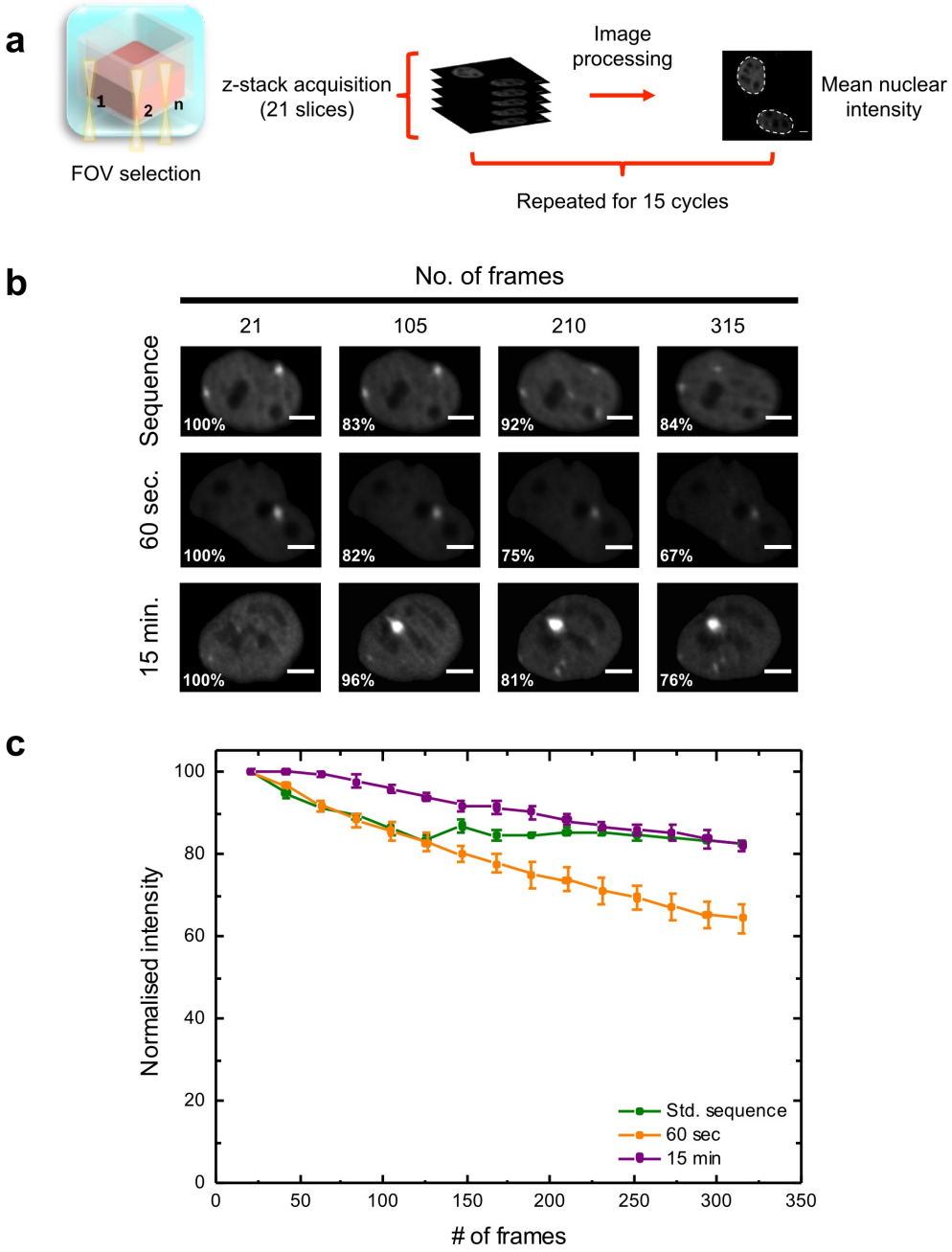


Figure 5.3 53BP1-YFP photobleaching kinetics. a) Experimental design. 15 z-stacks of 21 z-slices were obtained per FOV. The mean nuclei intensity was recorded per imaging cycle. Images were acquired with a standard imaging sequence (6 times at 1 min intervals up to 5 min, 5 min intervals up to 15 min and finally every 15 min up to 2 h), and 15 or 1 min intervals between imaging cycles. **b)** Representative micrographs. Intensity was normalised to the maximum mean intensity. Scale bar = 5 µm. **c)** Normalised intensity as a function of the number of frames. The error bars represent the s.e.m. (n = 3 independent experiments).

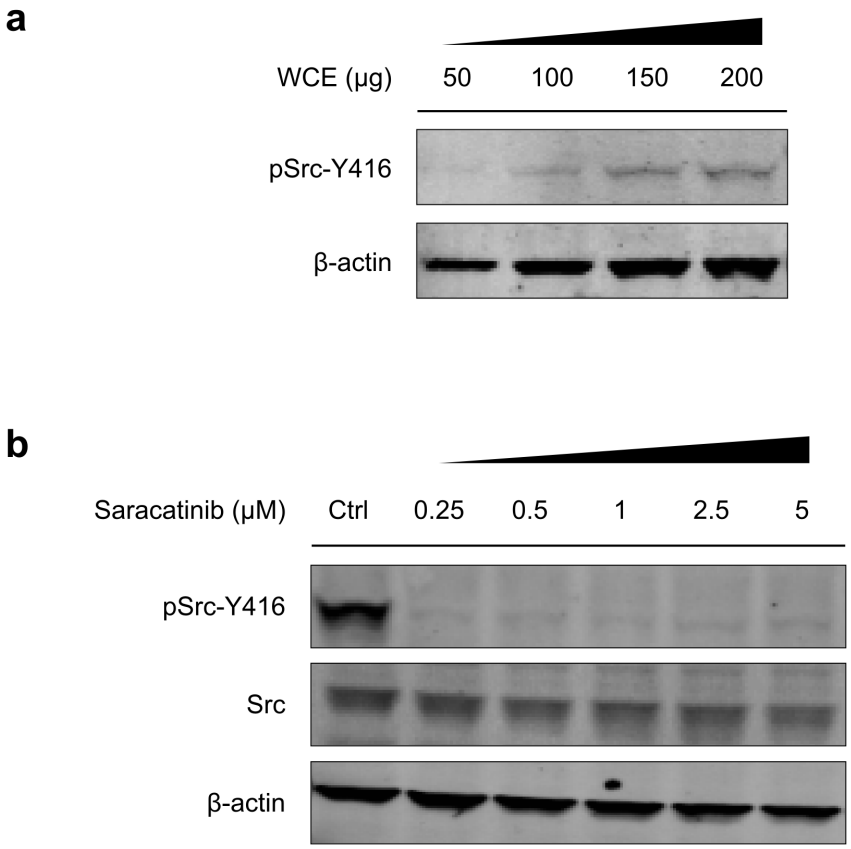


Figure 5.4 Saracatinib concentration titration. a) Optimisation of the concentration titration of HT1080-53BP1-YFP WCE necessary to observe pSrc-Y416. **b)** Representative western blots from concentration titration of Saracatinib. HT1080-53BP1-YFP cells were treated with increasing concentrations of Saracatinib for 24 h before harvesting. Saracatinib activity was monitored by pSrc-Y416 signal. Total-Src protein content and β-actin were probed as controls.

The displacement was measured using ImageJ by recording the position of the centre of the cell of interest at different time points. By analysing **figure 5.6b**, it is possible to observe 40 min after the first image was acquired under control conditions, that the translational movement of control cells is more evident than that observed after 2 h in cells exposed to 5 μM of Saracatinib.

5.2.3.3 Saracatinib effect on cell proliferation

The effect of Saracatinib on cell proliferation was assessed in order to exclude the possibility that the RWDs observed at increasing Saracatinib concentrations were related to proliferative impairment. To test this proposal, HT1080-53BP1-YFP cells were plated in a 96-well plate, and processed for a cell proliferation assay as described in **section 4.11**. The inhibitor was added 10 min before image acquisition. Four FOVs were imaged per well every 4 h for 24 h. The percent confluence was averaged over the four FOVs per well for all wells exposed to the same concentrations of Saracatinib. As shown in **figure 5.7**, cell proliferation is not affected by exposure to Saracatinib, as the observed percentage confluence is similar at the different concentrations of Saracatinib and control conditions, at the various time points measured. The quantified data, shown in **figure 5.8**, show a similar increase in the percent confluence for all the tested conditions; reaching approximately 80% confluence per well 24 h after the imaging process had been initiated.

5.2.3.4 Saracatinib effect on 53BP1 recruitment to sites of damage following irradiation

It was of course necessary to assess whether Saracatinib affects recruitment of 53BP1 to sites of damage in response to radiation treatment, in order to ensure that DNA repair kinetics are not modified.

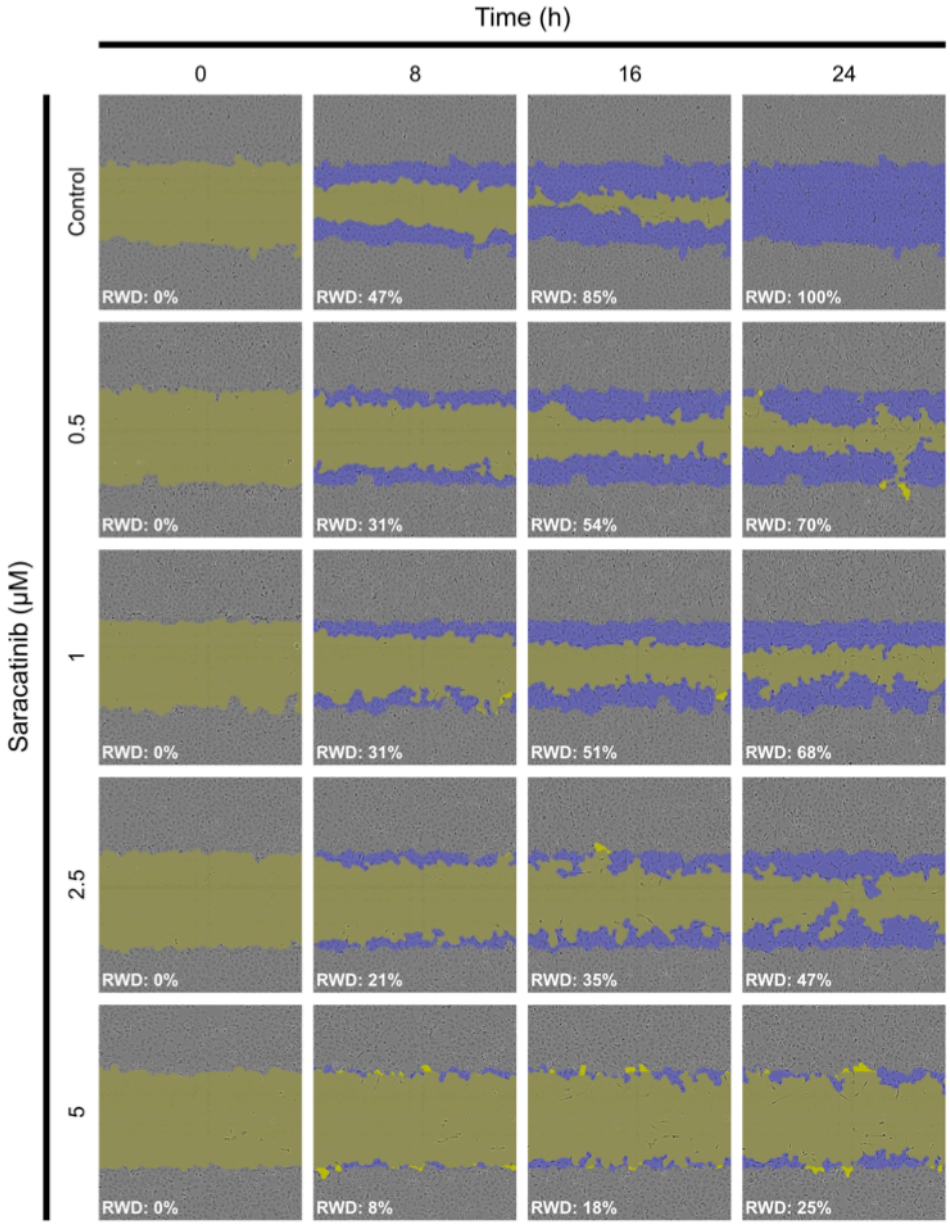


Figure 5.5 Scratch-wound assay in response to Saracatinib treatment. HT1080-53BP1-YFP cells were incubated with increasing concentrations of Saracatinib, ranging from 250 nM to 5 µM, added 10 min before the wound was introduced. Images of the wound region were acquired every 2 h for a period of 24 h. Representative micrographs of the analysed data are shown per concentration and time point. The green mask represents the wound region that is not populated. The blue mask illustrates the portion of the original wound region, which has become populated with cells. The relative wound density (RWD) percentages are indicated.

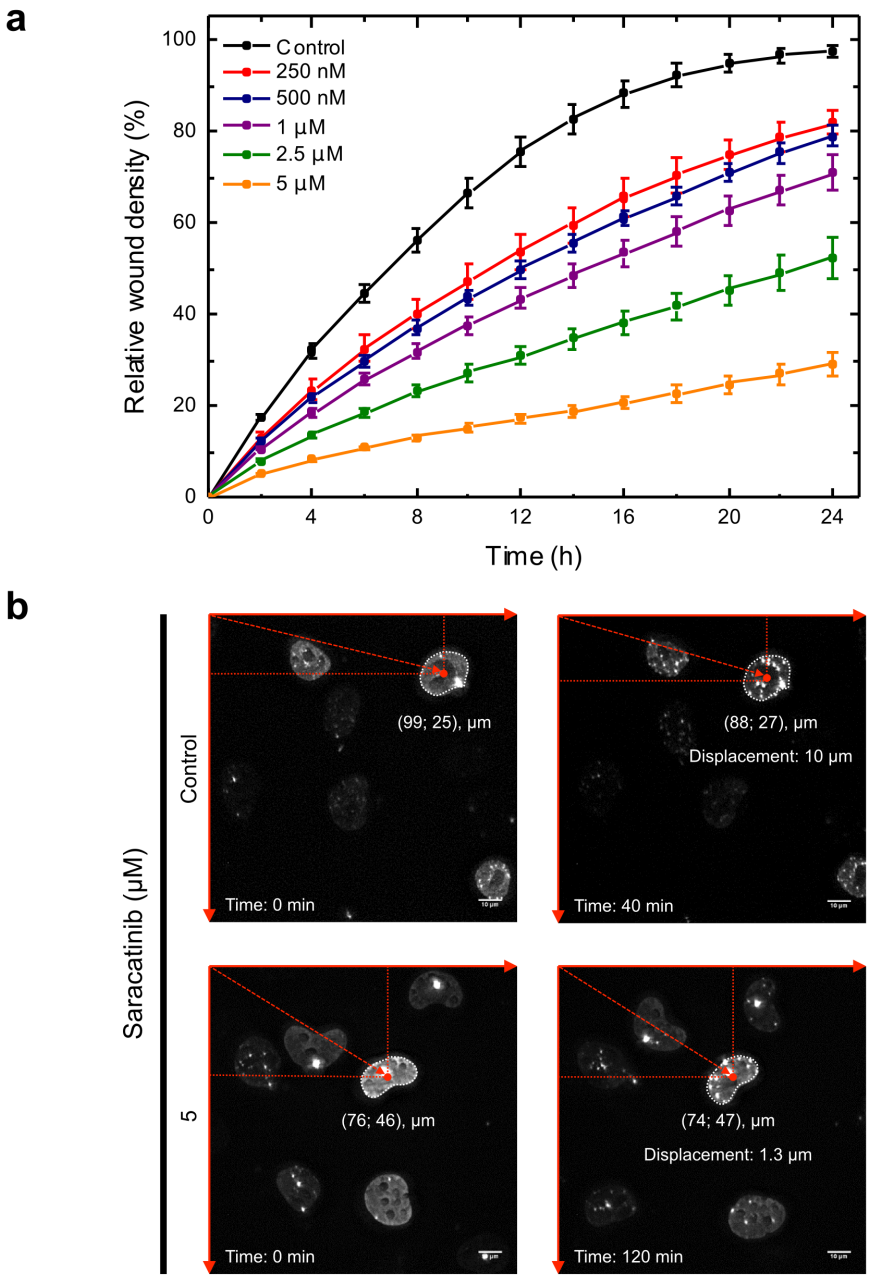


Figure 5.6 Saracatinib-induced reduction in cell motility. a) RWD as a function of time on the concentration of Saracatinib. The error bars represent the s.e.m. (n = 3 independent experiments). **b)** Micrographs representing live HT1080-53BP1-YFP cells imaged over time in the presence or absence of 5 µM Saracatinib treatment for 24 h. Displacement indicated measured by determining coordinates of the indicated cells using ImageJ. Scale bar = 10 µm.

In order to test this, HT1080-53BP1-YFP cells were plated on 10 cm diameter dishes for western blotting as described in **section 4.7**, in the presence or absence of 5 μM Saracatinib. The dishes were irradiated with 6 Gy using a ^{137}Cs source and placed at 37°C to allow repair processes to occur. The samples were harvested at 30, 90 and 180 min after irradiation. The samples were blotted for phosphorylated 53BP1 at Ser-1778 (S1778), to assess damage formation and repair over time. Phosphorylated Src-Y416 was monitored to ensure the Saracatinib inhibitory effect occurs. As shown in **figure 5.9a**, phosphorylated 53BP1 levels are comparable at all time points after irradiation irrespectively of Src-inhibition.

To investigate further the potential effects of Saracatinib on 53BP1 recruitment to sites of radiation-induced damage, HT1080-53BP1-YFP cells in the presence or absence of 5 μM Saracatinib were irradiated with the linac. Four FOVs were imaged per condition, twice before irradiation, one immediately after irradiation, then at 5 and 15 min, and finally every 15 min up to 2 h after irradiation. The captured z-stacks were deconvolved and the sum intensity projection obtained per time point per FOV. The number of 53BP1 foci formed were then manually counted using ImageJ. The average number of radiation-induced foci per cell was plotted as a function of time, as shown in **figure 5.9b**. The maximum number of foci/cell of 12 was detected 15 min after irradiation with 0.5 Gy with and without Src-inhibition. The number of foci/cell subsequently decreases approximately to half the level by 2 h after IR. These data confirm Saracatinib does not induce significant effects on the formation and loss kinetics of 53BP1-YFP in response to radiation damage.

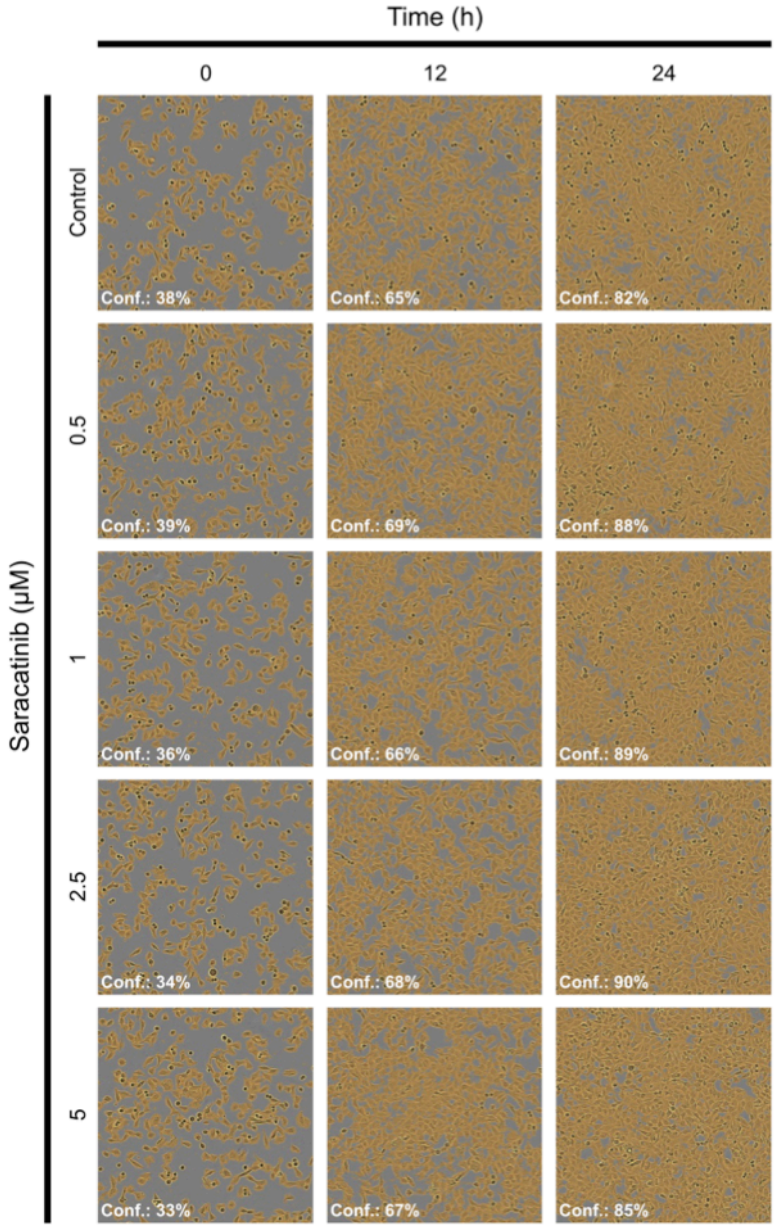


Figure 5.7 Proliferation assay in response to Saracatinib treatment. HT1080-53BP1-YFP cells were incubated with increasing concentrations of Saracatinib ranging from 250 nM to 5 µM, added 10 min before initiation of the imaging routine. Four FOVs were imaged per well on a 96-well plate every 4 h for a period of 24 h. Representative micrographs of the analysed data are displayed per concentration and time point. The orange mask illustrates the individual objects detected used to calculate the percentage of the total area that is occupied by the cells. The confluence percentages are indicated.

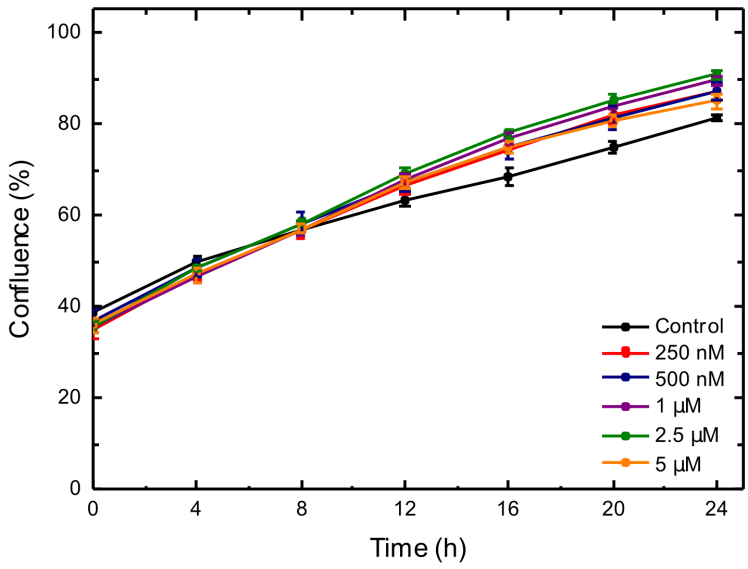


Figure 5.8 The effect of Saracatinib on cell proliferation. The confluence percentage is displayed as a function of time on the concentration of Saracatinib. The error bars represent the s.e.m. (n = 3 independent experiments).

5.2.4 53BP1-YFP recruitment kinetics to radiation-induced DNA damage in real-time

Live HT1080-53BP1-YFP tagged cells, which had been previously established and characterised (Asaithamby and Chen, 2009; Asaithamby *et al.*, 2011), were used to assess the kinetics of recruitment and loss of 53BP1 foci at sites of DNA damage for up to 2 h following pulsed electron irradiation at a dose of 0.5 Gy. Based on the photobleaching timescales described in **section 5.2.2**, the cells were imaged within 2 sec post-IR then at 1 min intervals up to 5 min, 5 min intervals up to 15 min and finally every 15 min up to 2 h. As a 'proof-of-principle', 25 cells (over three independent experiments) were manually segmented for all the time points and radiation-induced foci numbers/cell determined using an in-house developed software package, TRI2 (Barber *et al.*, 2007). Details of the testing of this software package are described in **Appendix A1**. 53BP1 foci, as biomarkers of DNA damage, were detected as early as 60 sec post-IR (**figure 5.10a**) with the maximum number of foci detected at 15 min post-IR (**figure 5.10b**). To confirm the live-cell imaging data, HT1080-53BP1-YFP cells were irradiated with the linac at 37°C and 5% CO_2 humidified air environment (**figure 5.10a**), followed by fixation at different time points up to 2 h post-IR (see **section 4.6**). The number of foci as a function of the time post IR is shown in **figure 5.10b**. From comparison of live versus fixed electron-irradiated cell data, the recruitment and loss of 53BP1 foci follow similar kinetics with ~35% of the radiation-induced foci disappearing within 2 h post-IR (**figure 5.10b inset**). However, if HT1080-53BP1-YFP cells are placed on ice for 10 min prior to irradiation, pre-cooling results in a delay in the formation of 53BP1 foci (**figure 5.10b**), with the maximum foci number seen at 30 min consistent with previous findings by others (Anderson *et al.*, 2010; Asaithamby and Chen, 2009; Schultz *et al.*, 2000).

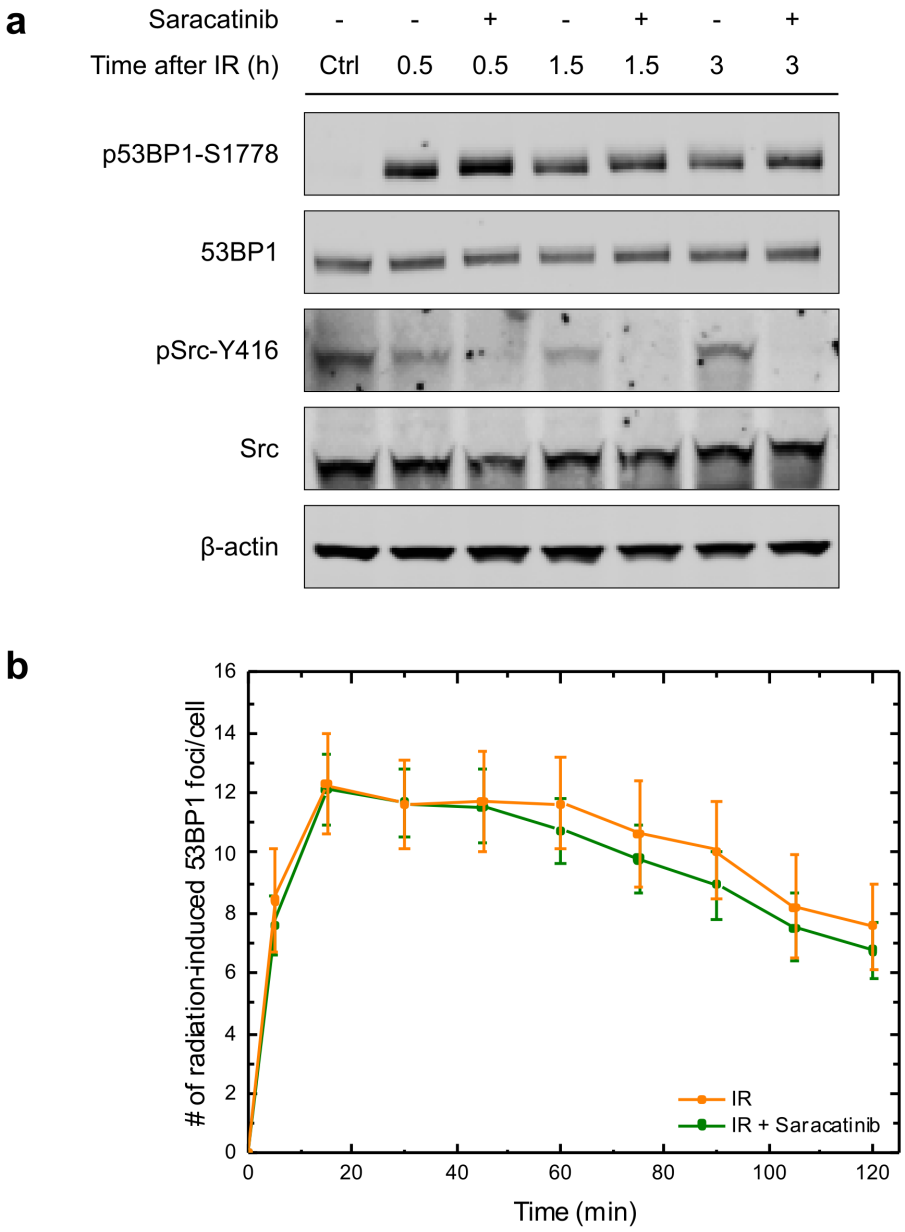


Figure 5.9 Saracatinib effect on 53BP1 following IR treatment. a) Representative western blots on time following radiation treatment with 6 Gy in the presence or absence of 5 µM Saracatinib. HT1080-53BP1-YFP cell lysates were blotted for p53BP1-S1778 to monitor damage, and pSrc-Y416 to monitor Saracatinib activity. Total-53BP1 and total-Src were blotted as controls. β-Actin was blotted as the loading control. **b)** Four FOVs were imaged per condition twice before irradiation following an acquisition immediately after irradiation, then 5 and 15 min, and subsequently every 15 min up to 2 h. The number of radiation-induced 53BP1 foci per cell was determined as a function of time after irradiation with 0.5 Gy using the linac experiment system with and without 5 µM Saracatinib. Background levels of 53BP1 foci/cell were determined based on images acquired prior to irradiation. This value was subtracted from the total number of observed foci. The error bars represent the s.e.m. (n = 3 individual experiments).

5.2.5 53BP1 single-foci mapping to sites of damage in individual cells following irradiation

Almost exclusively, the time courses of recruitment and loss of 53BP1 at radiation-induced damage sites have been based on mean foci numbers per cell, derived from analysing several tens of cells and using either immunocytochemical detection or tagged proteins. However, when using the linac/imaging system, the question arose whether the individual foci could be followed to assess if any foci appeared at later times. If so, this approach would be radically new, since 'latently' appearing foci cannot be detected by either immunocytochemistry, as each time point is a separate experiment, nor with laser micro-irradiation. This novel approach would address whether any 53BP1 foci develop at later times, when many of the DSB have been repaired. This approach would then allow a qualitative evaluation of the different observed foci, characterising each focus in terms of intensity over a given time course, allowing determination of the appearance and disappearance time of the individual foci.

To explore changes at shorter times in detail, imaging was performed immediately post-0.5 Gy IR (with <2 sec delay) of 53BP1-YFP cells and every 40 sec for up to 4 min, then at different time intervals up to 2 h. In this instance pre-irradiation imaging was performed every 20 min for 2 h (**figure 5.11c**). The data were treated as described in **section 5.2.1**. In **figure 5.11a**, an example of a single cell followed over time is shown, highlighting the presence of various foci, which have appeared at different times post-irradiation. This approach allows different type of information to be extracted, relevant to the history of the individual foci in a single cell. For instance, newly appearing foci (**figure 5.11a** turquoise circles) are initially seen at very early times, within 2 min post IR and, once developed, show a reduction in fluorescence intensity with time. Later developing foci were also

observed to be resolved either within ~1 h (pink triangles) or to increase in brightness with time (purple triangles and orange circles).

It is informative to determine the minimum detectable number of molecules present in a focus (Hinterdorfer and Van Oijen, 2009; Pawley, 2006). The calibration factors described in **Appendix A1** can be used to determine this value. The imaging system sensitivity is 25.5 counts per molecule, corresponding to 24.24 photons per molecule. The analysis of an easily detectable focus from the original image is as follows. An ROI was drawn around the focus and the total intensity was recorded. An ROI with the same area was used to determine the total nuclear background intensity, which was subtracted from the focus intensity. The total number of photons emitted from the focus ROI was determined to be 50,941 ± 226 (using photons/ADU from **Appendix A1**). The total number of photons emitted from the nuclear background ROI was 39,168 ± 198. The difference in the number photons was calculated to be 11,773 ± 109 which represents the total number of photons from the focus alone. Knowing that each molecule emits 24.24 photons for the used imaging conditions, the total number of molecules present in the focus was estimated to be 486.

The minimum detectable number of molecules per focus can also be estimated from a dim focus only visible in the deconvolved image. Using knowledge of the focus location in the deconvolved image, the total intensity from the original image was recorded by drawing an ROI in the same location. For this particular focus and background ROIs the total numbers of photons emitted were 17,054 ± 131 and 15,474 ± 124 respectively. The difference in the number of photons was determined to be 1,580 ± 40, indicating a minimum detectable number of molecules in the region of 65. By repeating this exercise with more foci, it would be possible to more accurately determine the limit of detectability of this system.

The variation in intensity (spatially averaged) for each focus over the pre- and post-irradiation time course is shown in **figure 5.11b**. This indicates the appearance and disappearance of each focus during recruitment and loss of 53BP1-YFP at sites of radiation-induced DNA damage. The intensities of any pre-existing foci, as determined pre-irradiation, were seen to decrease with time, reflecting the repair of non-IR damage (**figure 5.11a, 5.11b**).

5.3 Discussion

This chapter addressed data handling and optimisation of the images for 'proof-of-principle' experiments to validate the use of the linac experimental system, using recruitment and loss of 53BP1-YFP to radiation-induced DNA damage. Blind deconvolution of the acquired data was used as the method to circumvent the poorer z-resolution obtained when comparing epifluorescence with confocal microscopy.

Cell segmentation and registration were tested in order to study the feasibility of automated data handling for studies at the single-cell level.

These results show promise, revealing however that HT1080-53BP1-YFP cells are mobile compared to some other cell lines. This should be a consideration for future experiments using this type of analysis. The difference in expression levels of 53BP1-YFP among the cell population contributes to a variation of fluorescence intensities from cell to cell, posing difficulties in segmenting cells and undertaking automated foci counting using the TRI2 software package. Photobleaching kinetics of 53BP1-YFP were assessed, and showed faster decrease in normalised intensity when consecutive acquisitions are acquired quickly. For longer acquisition intervals of several minutes, the decay in intensity dropped to ~80% of the maximum after a total of 315 collected frames.

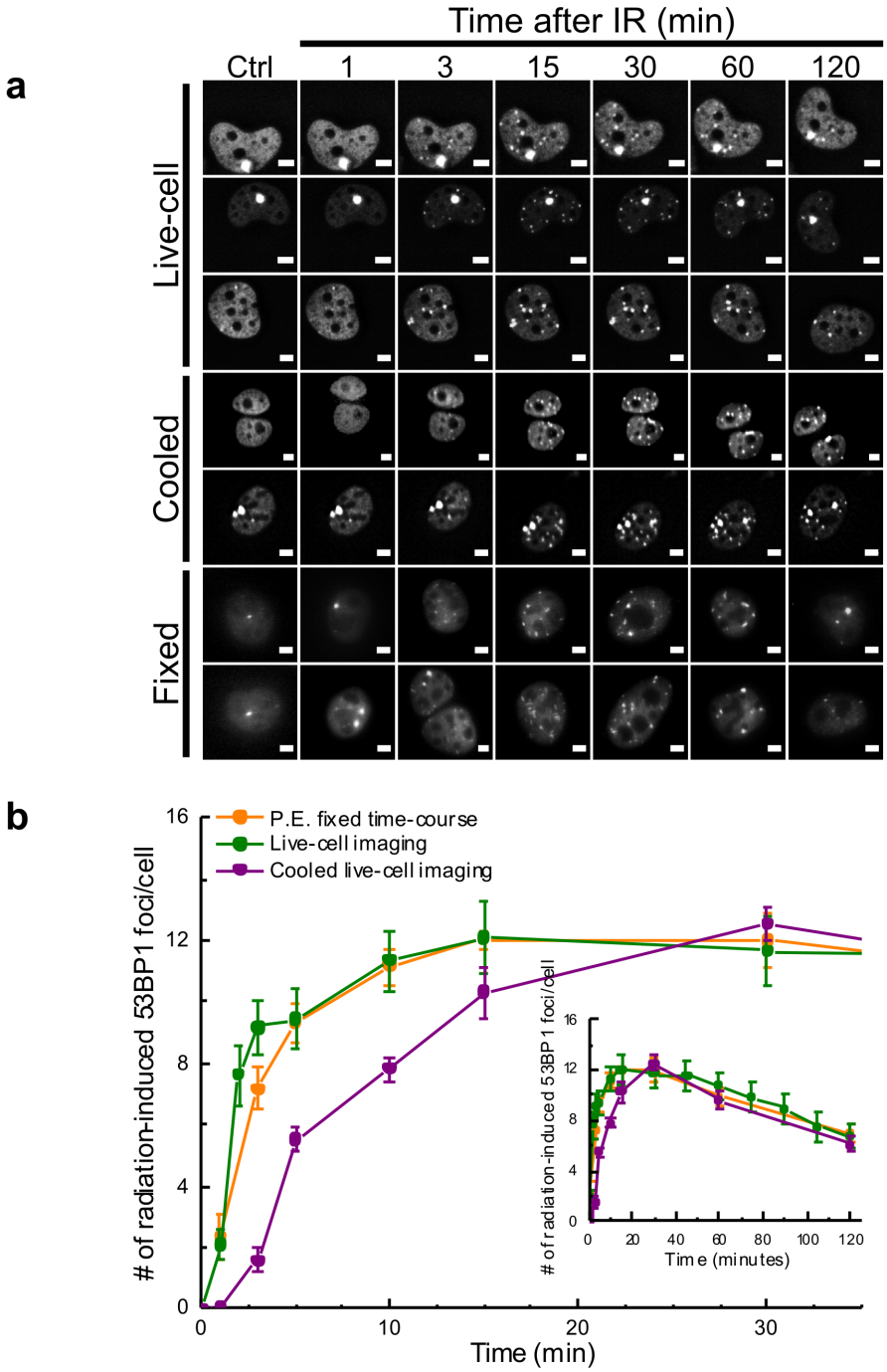


Figure 5.10 53BP1-YFP kinetics in response to 0.5 Gy. a) Micrographs representing 53BP1 foci formation and disappearance with time, and **b)** 53BP1 foci numbers as a function of time. Comparison between live-cell imaging (■) at 37°C, pre-cooled samples at 4°C subsequently restored to 37°C (■), and fixed samples which were irradiated under physiological conditions (■). Scale bar = 5 µm. Background levels of 53BP1 foci/cell were determined based on the obtained images prior to irradiation when using live-cell imaging, or based on control samples when immunocytochemistry was used. This value was subtracted from the total number of observed foci. Error bars represent the s.e.m. (n = 3 independent experiments).

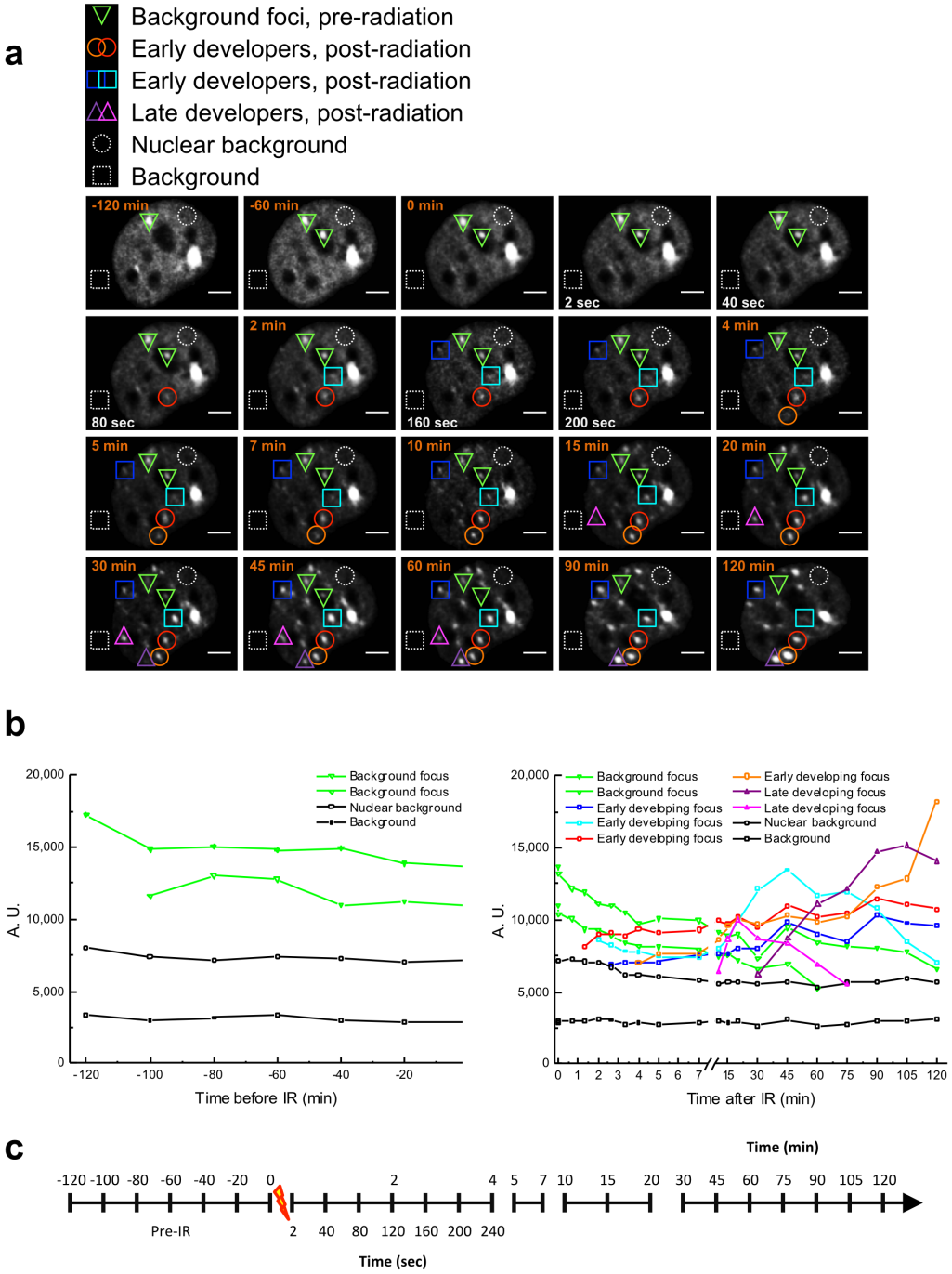


Figure 5.11 53BP1 single-foci mapping following irradiation. a) Micrographs per time point representing an HT1080-53BP1-YFP cell irradiated with 0.5 Gy using the linac experiment system. The obtained images were deconvolved and collapsed as the sum intensity projection, following segmentation and registration as described in **section 5.2.1**. Background regions and multiple foci are highlighted. Scale bar = 5 µm. **b)** Average A. U. per focus per time point of the foci highlighted. **c)** Diagram of the time-lapse imaging sequence.

A recovery of the mean nuclear intensity was observed if the time between acquisitions was increased during the experiment. However, the extent of photobleaching caused by constant exposure during live-cell imaging experiments with the real-time sequence used does not limit foci detection when compared with fixed samples. For example, the recruitment kinetics for formation and loss of 53BP1 foci obtained under equivalent radiation conditions are similar in both fixed- and live-cell imaging experiments (**figure 5.10b**).

Cell motility also needs to be considered in following the same cells throughout the time sequence in the absence of cell tracking. Motility was reduced in response to Src inhibition as observed in **figures 5.5** and **5.6**. This effect was obtained without impairing cell proliferation (**figures 5.7** and **5.8**), nor the DNA damage response, as measured by the recruitment and loss of 53BP1 to radiation-induced DNA damage sites (**figure 5.9**).

The recruitment of 53BP1 to radiation-induced DNA damage was studied with living HT1080-53BP1-YFP cells using the linac experiment system. The kinetics of recruitment and loss of 53BP1 are generally assessed as the average number of foci/cell at different time points following irradiation (**figure 5.10b**) (Asaithamby and Chen, 2009; Asaithamby *et al.*, 2011). The average numbers are obtained by evaluating several tens of cells to provide quantitative information on the average number of foci induced within the cell population. When utilising an average foci/cell type of analysis, it is not possible to comment on late appearing foci, which may or may not be present at the time of irradiation but, if present, represent new breaks being developed at later times. Single focus approaches, at the single cell level, can provide qualitative information about each focus, as some latent damage formed may be substrates, which lead to the recruitment of 53BP1 to such sites. These observations permit a more detailed overview of the different nature of

the breaks with time, which can arise in response to radiation damage (**figure 5.11**). IR can induce prompt DSBs but it is also known to generate clustered damage (Gulston *et al.*, 2002; Sutherland *et al.*, 2000; Sutherland *et al.*, 2002). The clustered damage sites are also known to be repaired slowly, when induced by IR to mammalian cells (Magnander *et al.*, 2010). Biochemical studies have shown that clustered damage sites induced by radiation are less efficiently repaired by BER than the individual lesions (Eccles *et al.*, 2011; Georgakilas *et al.*, 2013; Sage and Harrison, 2011) and as a consequence they may lead to replication-induced DSBs in S-phase cells. It was also shown that replication-induced DSBs are induced in irradiated and hydrogen peroxide treated cells, leading to the proposal of clustered damage sites, on encountering a replication fork, lead to replication DSBs which would recruit 53BP1 (Harper *et al.*, 2010; Saleh-Gohari *et al.*, 2005). There is therefore significant evidence that clustered damage sites induced by IR can be converted into replication DSBs, signalled by later-forming 53BP1 foci. It is proposed that some of the late forming 53BP1 foci in **figure 5.11** represent the conversion of clustered damage sites into replication-induced DSBs. These replication breaks are of different nature to promptly induced DSBs, and specifically require the HR repair machinery to be successfully repaired. These lesions would in principle be developed at much later times following damage induction.

Additionally, some clustered damage sites during processing by the BER machinery can potentially be converted into DSBs. Gulston *et al.* (2004) used pulsed-field gel electrophoresis (PFGE) as a method to assess DSB repair kinetics, and reported a rapid induction of DSBs within 15 min in V79-4 cells following irradiation at 37°C using a linear accelerator, consistent with the formation of DSBs (Gulston *et al.*, 2004).

The data presented in **figure 5.12** (selected foci from **figure 5.11**) highlight damage formation at later times (orange circles, blue squares and purple triangles), as displayed through the increasing intensities with time. These later forming foci could in principle reflect the conversion of clustered damage into replication DSBs. The purple triangles could also reflect the conversion of clustered damage sites into DSBs by BER processing, as detailed by Harper *et al.* 2010 (Harper *et al.*, 2010). Such novel approaches can in principle be applied to large numbers of cells to provide more quantitative information of the different ways in which breaks are formed at different times in response to radiation damage and signalled by 53BP1.

It is interesting that the majority of the DSBs (~60%) are resolved within 30 min, with only 20% of the breaks persisting for longer times, when determined by PFGE (**figure 5.13**). In order to compare 53BP1 recruitment kinetics to the DSB repair kinetics reported by Gulston *et al.* (2004) using PFGE, the number of foci found in the live-cell imaging data in **figure 5.10b** was multiplied by a factor of 2 assuming a dose of 1 Gy. If a maximum of 40 DSBs are assumed for a dose of 1 Gy, the PFGE data reported by Gulston *et al.* (2004) can be compared to 53BP1 recruitment and loss with time following irradiation (**figure 5.13**). The differences observed between the two methods in the number of breaks highlight the higher sensitivity of PFGE at early times for the detection of DSBs. The delay in the formation of 53BP1 foci is thought to be associated with the timing required for the signalling of DNA damage. Additionally, it is important to consider that the simple DSBs are more rapidly resolved, which may in principle lead to few 53BP1 molecules being recruited at the break site so they may not be microscopically visualised as a focus. At later times however, there is a higher level of persistence of 53BP1 foci when compared to the number of breaks detected by PFGE. The higher level of breaks present at later times could

in principle represent replication-induced DSBs forming at later times following irradiation (as shown in **figure 5.12**), which would not be detected by PFGE, consistent with this difference in part reflecting late appearing foci relative to those for prompt DSBs (**figure 5.13**). In addition, the higher level of breaks as reported by the number of 53BP1 could also be associated with a delay in the timing required for 53BP1 to dissociate from the damage site following repair, leading to focus dissolution, although this should also have applied to all the foci at the simple DSB, which repair more rapidly.

These preliminary data give, for the first time, an overview of the dynamics of foci formation from promptly-formed and late-appearing DNA damage, as signalled by 53BPP1. These data impact on the general interpretation of DSB repair kinetics and suggests caution in the interpretation of repair kinetics when using 53BP1 and phosphorylation of histone H2AX (γ-H2AX).

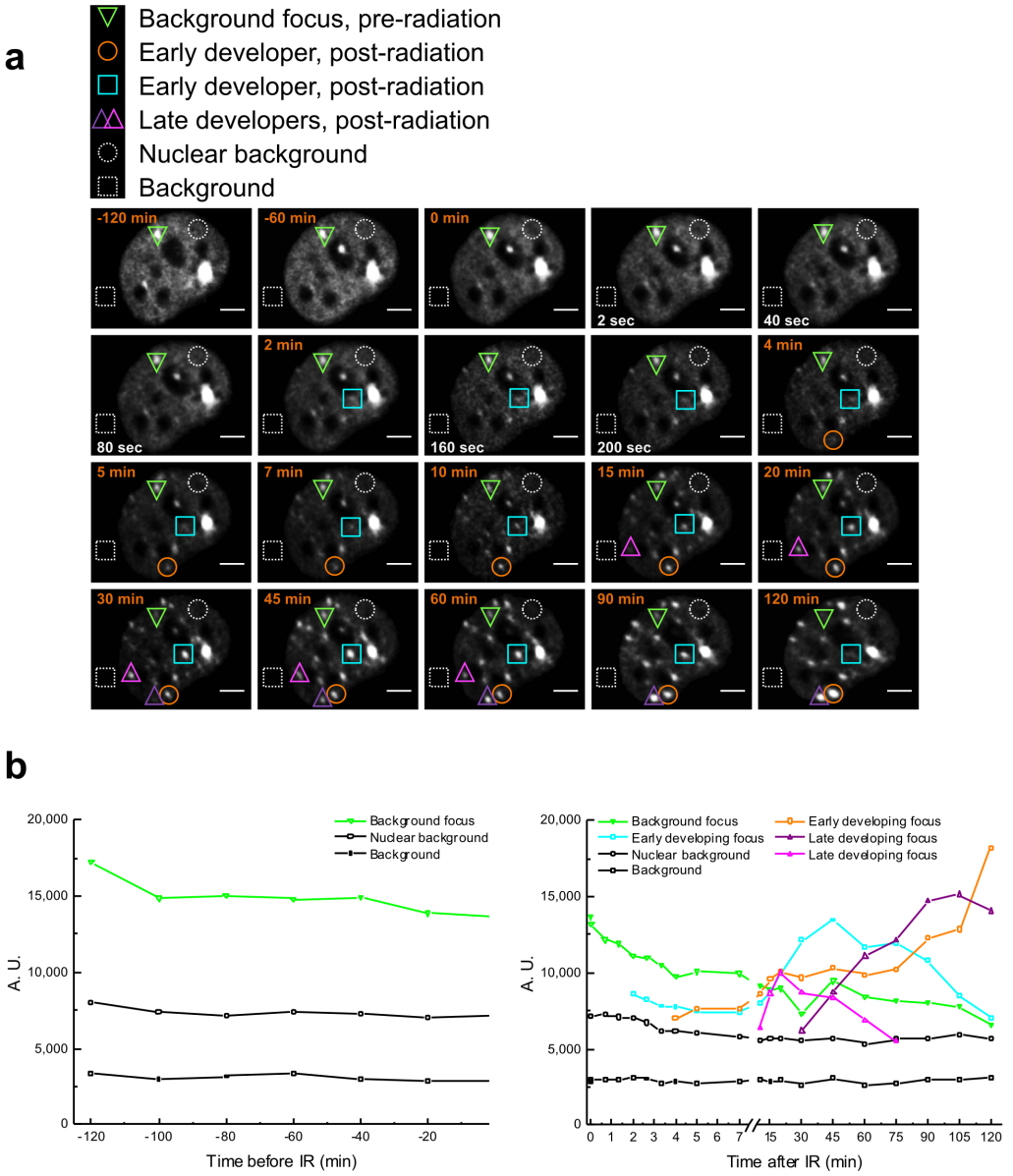


Figure 5.12 53BP1 single-foci mapping following irradiation (selected foci from figure 5.11). a) Micrographs per time point representing an HT1080-53BP1-YFP cell irradiated with 0.5 Gy using the linac experiment system. The obtained images were deconvolved and collapsed as the sum intensity projection, following segmentation and registration as described in **section 5.2.1**. Background regions and multiple foci are highlighted. Scale bar = 5 μm. **b)** Average A. U. per focus per time point of the foci highlighted.

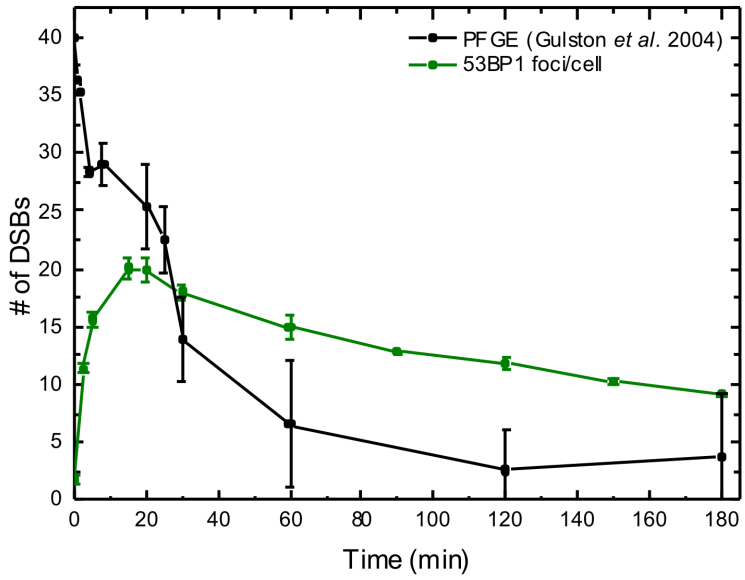


Figure 5.13 DSB repair kinetics following radiation treatment. The black line represents PFGE published data by Gulston *et al.* obtained from V79-4 cells irradiated at 37°C using a linear accelerator (Gulston *et al.*, 2004). The data was plotted assuming a maximum of 40 breaks per 1 Gy of low-LET radiation dose. The green line represents the number of foci found in the live-cell imaging data in figure **5.10b** multiplied by a factor of 2 mimicking the kinetics of 53BP1 recruitment and loss to damage sites in response to a dose of 1 Gy.

6. Specificity of DNA repair kinetics on phase of the cell cycle

6.1 Introduction

This chapter addresses the cell cycle phase dependence of recruitment and loss of 53BP1-YFP at sites of radiation-induced DNA damage. The aim is to better understand the interplay between different repair mechanisms, and to characterise any cell cycle specificity of late developing foci in response to radiation damage. As discussed in **chapter 5**, live-cell imaging combined with linac irradiation provides a novel approach to examine the repair processes involved in the resolution of radiation-induced lesions compared to more conventional immunocytochemistry approaches (Markova *et al.*, 2007; Rappold *et al.*, 2001; Wang *et al.*, 2002). Immunocytochemistry methods provide only a snapshot of the damage at a given time, with each time point representing an individual experiment, without any prior knowledge of the sites of damage, detected as foci, present at the time of irradiation. Such approaches do not allow the possibility of studying the evolution of damage formation and repair at a single-cell level. The data presented in **chapter 5** highlighted the possibility of radiation-induced clustered damage developing at later times following radiation treatment (**figure 5.11**) into replication-induced DSBs and potentially being one of the causes of late developing foci (Eccles *et al.*, 2011; Gulston *et al.*, 2004; Harper *et al.*, 2010; Sage and Harrison, 2011). To study such processes and their dependence on cell cycle, it is important to distinguish between G1 and S/G2 cells in order to identify those cells undergoing replication. S-phase cells can normally be distinguished

using BrdU or EdU labelling. Both BrdU and EdU are thymidine analogues, which are incorporated into replicating DNA, and can be detected immunocytochemically (Buck *et al.*, 2008; Harper *et al.*, 2010; Miltenburger *et al.*, 1986). However, with this approach, cells have to be fixed, making live-cell imaging impossible. Other researchers have also used Cyclin A staining as a method to discern between G1 and S/G2/M cells; this process also involves cell fixation (Escribano-Diaz *et al.*, 2013; Juan *et al.*, 1997). An approach which allows live-cell imaging studies involves proliferating cell nuclear antigen (PCNA), a key factor in DNA replication and repair, and its fusion to fluorescent proteins. This method has been used to distinguish G1 from S/G2/M cells during live-cell imaging experiments (Essers *et al.*, 2005).

Another method is based on Cdt1 and Geminin, two proteins involved in cell cycle regulation, with Geminin-mediated inhibition of Cdt1 being important in preventing replication (Saxena and Dutta, 2005). Cdt1 expression is maximal in G1, and degraded after the transition to S-phase. Conversely, Geminin is increasingly expressed from S-phase onwards and degraded rapidly after mitosis (McGarry and Kirschner, 1998). Sakaue-Sawano *et al.* (2008) have demonstrated the feasibility of using fluorescently labelled Cdt1 and Geminin to observe the dynamics of cell cycle progression in living cells (Sakaue-Sawano *et al.*, 2008). From a clinical standpoint, since Geminin is not present in all phases of the cell cycle, it can be used as a more selective predictor of tumour proliferative potential when compared to Ki67 (Rajan *et al.*, 2014). Geminin-associated fluorescence alone can be used to discern between G1 and both S and G2/M cells, as G1 cells should not show any Geminin-associated fluorescence. Therefore, the Geminin signal should allow monitoring of damage formation and resolution in living 53BP1-YFP cells, to give knowledge of whether cells are in G1 phase or S/G2 phases of the cell cycle. This biological system can be an important tool in studying DNA DSB repair kinetics in real-

time when using cells containing fluorescently tagged proteins, to give insights into the main pathways used for repair of DSBs depending on the phase of the cell cycle (Hinz *et al.*, 2005; Mladenov and Iliakis, 2011; Nagasawa *et al.*, 2010; Rothkamm *et al.*, 2003; Wilson *et al.*, 2010).

Coordination of repair and checkpoint functions in response to DNA damage induction involves several molecules, where ATM is one of the main signalling proteins (Lavin and Kozlov, 2007). ATM is involved in mediating the G1 checkpoint (Deckbar *et al.*, 2010) and acts together with ATR during S and G2 phases to control further cell cycle progression (Lukas *et al.*, 2004). In response to DSBs, ATM is initially activated by the MRN complex, and is involved in the phosphorylation of several proteins including histone H2AX and 53BP1 (Jowsey *et al.*, 2007; Matsuoka *et al.*, 2007; Ward *et al.*, 2003) and subsequent recruitment of multiple factors involved in DSB repair signalling, leading to lesion repair (Marechal and Zou, 2013; Stucki and Jackson, 2006).

As described in **chapter 1**, HR is an error-free repair pathway. It involves resection and sister chromatid strand invasion, and therefore it only occurs during S and G2 phases of the cell cycle (Hinz *et al.*, 2005; Mladenov and Iliakis, 2011; Wilson *et al.*, 2010). Lesions repaired by HR occur at a slower rate (Haaf *et al.*, 1995; Harper *et al.*, 2010; Shibata *et al.*, 2011; Yuan *et al.*, 1999), whereas NHEJ can occur during all stages of the cell cycle and it consists of several sub-pathways, which rapidly and efficiently resolve radiation-induced DSBs. In this context, NHEJ is normally assumed as the main repair pathway used by mammalian cells to cope with radiation-induced DSBs (Lieber, 2010; Lieber *et al.*, 2010; Mahaney *et al.*, 2009). As DNA-PKcs is one of the key molecules involved in the repair of DSBs via NHEJ (Mladenov and Iliakis, 2011; Smith and Jackson, 1999; van Gent and van der Burg, 2007), assessing the repair efficiency of radiation-induced DSBs, as monitored by 53BP1 foci in living cells, in response to DNA-PKcs inhibition, can help to unveil the

involvement of this molecule in the repair of frank and late developing DSBs in a cell cycle-dependent fashion. Repair activity of DNA-PKcs requires autophosphorylation at the S2023-2056, and Thr-2609-2647 clusters (Block *et al.*, 2004; Cui *et al.*, 2005). These phosphorylations are thought to play a role in resistance to radiation-induced damage (Nagasawa *et al.*, 2011). Phosphorylation of the T2609 cluster by ATM has also been reported (Chen *et al.*, 2007). Inhibition of these phosphorylation events is thought to pose obstacles to a fully functional NHEJ repair pathway (Ciszewski *et al.*, 2014; Tavecchio *et al.*, 2012; Zhao *et al.*, 2006). Inhibition of DNA-PKcs kinase activity leads to a deficiency in the repair processes in response to damage, consequently resulting in persistence of unrepaired breaks as observed by the prevalence of γ-H2AX foci from 1 h onwards after DNA damage induction (Mahaney *et al.*, 2009; Zhao *et al.*, 2006). Recently it was shown that DNA-PKcs is recruited mainly to complex DSBs but not simple DSBs (Reynolds *et al.*, 2012). Additionally, the persistence of DNA-PKcs at sites of complex DSBs is modulated by the presence of active ATM but independent of PARP inhibition (Chen *et al.*, 2007; Hammel *et al.*, 2010; Reynolds *et al.*, 2012).

Alternative NHEJ or B-NHEJ repair can occur independently of DNA-PKcs activity, when Ku70/80 heterodimer is not present, where PARP-1 functions as the main sensing molecule in this repair pathway (Mladenov and Iliakis, 2011). Since HT1080-53BP1-YFP cells have functional Ku available, it is therefore more likely that PARP-1 inhibition would be associated with its accumulation at unrepaired SSBs, which, in cycling cells, can be converted into replication-DSBs via replication fork collapse (Saleh-Gohari *et al.*, 2005). Additionally it is known that radiation induces clustered DNA damage (Eccles *et al.*, 2011; Sage and Harrison, 2011), which may lead to mutations, if they encounter a replication fork. Assessing the effect of PARP-1 inhibition in living cells in a cell cycle-phase specific

fashion may provide further insights on how cells in S-phase convert damage into replication DSB, which may also contribute to the late developing foci.

The overall aim of the investigations in this chapter is to provide preliminary insights, through monitoring of 53BP1 foci formation and disappearance in living cells in different phases of the cell cycle, on whether mammalian cells establish a balance between the different repair pathways throughout the cell cycle to repair radiation-induced damage and whether late developing foci depend in part on the phase of the cell cycle. These studies were also performed using the linac technology developed.

6.2 Results

6.2.1 HT1080-53BP1-YFP-Geminin-mCherry cell line establishment

To establish cell lines with Geminin-mCherry together with 53BP1-YFP, the HT1080-53BP1-YFP cells were transfected with Geminin-mCherry as described in **section 4.4**. Following transfection, individual clones were grown from colonies derived from single cells, and clonal selection was performed, as described in **section 4.4**. As mentioned in **section 6.1**, Geminin is increasingly expressed from S-phase onwards and degraded after mitosis (**figure 6.1b**). By imaging 53BP1-YFP cells transfected with Geminin-mCherry, it is possible to separate G1 and S/G2/M populations based on 53BP1 and Geminin-associated fluorescence. G1 cells only display 53BP1-YFP-associated fluorescence (**figure 6.1a**). On the other hand, S/G2/M cells emit both 53BP1-YFP and Geminin-mCherry-associated fluorescence.

6.2.1.1 Impact of Geminin-mCherry on cell cycle progression

Replication initiation is promoted by Cdt1, which is expressed during G1 and degraded during S-phase (Saxena and Dutta, 2005). Replication re-initiation is prevented by the expression of Geminin, a potent Cdt1 inhibitor until the next G1 phase. It was thought the

insertion of Geminin-mCherry could contribute to an unbalanced cell cycle progression. To assess this, the cell population for each cell cycle phase was compared between HT1080-53BP1-YFP and HT1080-53BP1-YFP-Geminin-mCherry cell lines. Cells were plated as described in **section 4.8.1** and allowed to grow overnight. Two samples per cell line were fixed as described in **section 4.8.1** with 6 h interval in between. The data were acquired and processed, as described in **section 4.8.2**. For the first time point, both cell lines have approximately 44-47% of the population in G1, 33% of the cells in S-phase, and 20-23% in G2. 6 h later the population distribution was similar, with a small decrease in the G1 population of the cells transfected with Geminin-mCherry (**figure 6.2**). These data highlighted that the distribution of the cells per cell cycle stage are not affected by the transfection with Geminin-mCherry.

6.2.1.2 S-phase duration measurements: BrdU incorporation

To assess cell cycle progression in more detail, HT1080-*wt*, 53BP1-YFP and Geminin-mCherry cells were plated as described in **section 4.8.1** and allowed to grow overnight. BrdU incorporation was performed for 30 min before the cells were harvested. Samples were fixed every 2 h for a period of 8 h. Data were collected and analysed for S-phase duration as described in **section 4.8.2** (**figure 6.3a**). S-phase durations ranged from 6.6 h (HT1080-*wt* cell line) to 7.1 h (Geminin-mCherry cell line) (**figure 6.3b**). The potential doubling times ranged from 16.6 h (HT1080-*wt* cell line) to 17.1 h (Geminin-mCherry cell line). Both S-phase duration and potential doubling time estimations were found to be similar for all the different cell lines, thus highlighting that the transfection with Geminin-mCherry does not result in impairment of cell cycle progression. 53BP1 and Geminin protein levels were also compared to the *wild-type* cells by western blotting (**figure 6.3c**). The data displayed in **figure 6.3c** show two bands when 53BP1 is probed in both 53BP1-

YFP and Geminin-mCherry cell lines, due to the presence of 53BP1-YFP in the cells when compared to *wild-type*, which only possess the endogenous 53BP1 form. Both Geminin and 53BP1 expression levels were similar for all the cell lines when the signal was normalised to the loading control β-Actin (to control for non-homogenous loading between the different lanes).

6.2.1.3 Geminin co-localisation with S/G2/M marker: Cyclin A

As described in **section 6.2.1**, Geminin-mCherry associated fluorescence should be specific to cells present in S and G2/M phases of the cell cycle. To assess the feasibility of using Geminin as a predictive S/G2/M marker, cells were co-stained for Cyclin A, a known S/G2/M marker (Murray, 2004). The samples were imaged using confocal microscopy, described in **section 4.12**. The total number of cells per FOV was determined by manually counting the nuclei stained with DAPI. The fraction of cells positive for 53BP1-YFP-associated fluorescence was determined to be approximately 95%. The S/G2/M population was determined by counting the cells positive for Geminin-mCherry and Cyclin A staining (**figure 6.4a**). The G1 population was determined by subtracting the fraction of cells positive for either Geminin-mCherry or Cyclin A to the fraction of cells stained with DAPI. The G1 population was determined to be approximately 60% and the S/G2/M population approximately 40% when determined based on Geminin-mCherry fluorescence or Cyclin A staining (**figure 6.4b**). These data highlighted the feasibility of using Geminin-mCherry-associated fluorescence to distinguish cells in S/G2/M within a cell population.

6.2.1.4 Cell cycle profile determination using EdU and Geminin-mCherry

Despite the correlation observed between Geminin-mCherry and Cyclin A staining, it was important to assess the population distribution by immunofluorescence and simultaneously by flow cytometry.

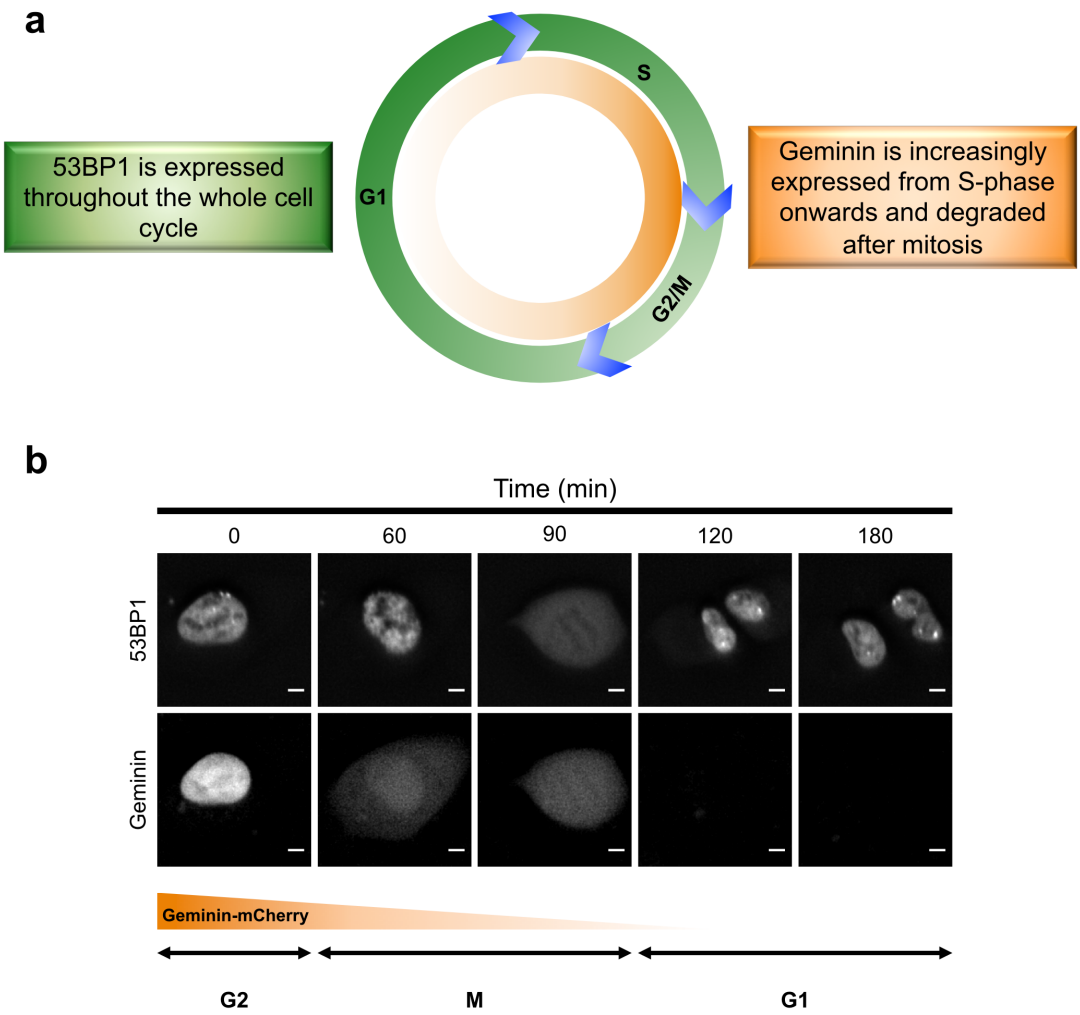


Figure 6.1 Geminin-mCherry expression throughout the cell cycle. a) Diagram representing 53BP1-YFP and Geminin-mCherry expression during the different stages of the cell cycle. **b)** Micrographs displaying HT1080-53BP1-YFP cells transfected with Geminin-mCherry undergoing mitosis. Geminin-mCherry fluorescence is degraded after mitosis. 53BP1-YFP and Geminin-mCherry were imaged with the different filter sets described in **section 2.5**. Scale bar = 5 µm.

Cells were plated as described in **section 4.2** in 3 cm diameter glass-walled dishes for immunofluorescence and 10 cm diameter dishes for flow cytometry (**section 4.8.1**). In order to guarantee a similar cell growth between the populations plated for immunofluorescence and flow cytometry, a surface area ratio between the different vessels used was determined to obtain the total number of cells to plate per vessel, ensuring a similar growth rate. The samples to be imaged were labelled with EdU (**section 4.6.3**) to isolate the S-phase population. Flow cytometry samples were stained with 7-AAD and processed as described in **section 4.8**. The cell cycle profiles (**figure 6.5a**) were determined using ModFit LT Software (Verity Software House) (**section 4.8.2**). The cell cycle profile was determined by immunofluorescence assessing the fraction of positive cells for DAPI, EdU, and Geminin-mCherry. The S-phase population was taken as the fraction of cells positive for EdU. The G2/M population was determined by subtracting the EdU positive population from that displaying Geminin-mCherry-associated fluorescence (**figures 6.5b** and **6.5c**). The G1 population was determined by subtracting the fraction of cells positive for Geminin-mCherry from the total number of cells as determined by DAPI staining. The data shown in **figure 6.5d** represent the different profiles obtained by both methods. The obtained cell cycle profiles were similar with a G1 population determined to be approximately 50%, 30% of the cells in S-phase, and the remaining 20% in G2/M. These data highlighted the capacity to specifically identify the S/G2/M population according to Geminin-mCherry-associated fluorescence.

6.2.1.5 Radiation resistance: clonogenic cell survival

Since the primary goal was to perform DNA repair kinetics using the established cell line, it was important to assess whether a stable transfection with Geminin-mCherry exerted any impact in terms of radiation sensitivity.

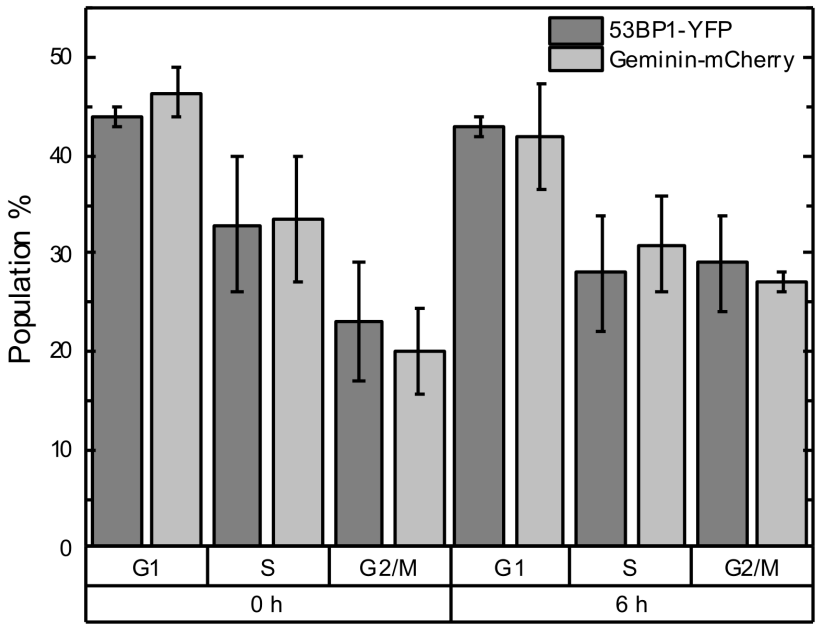
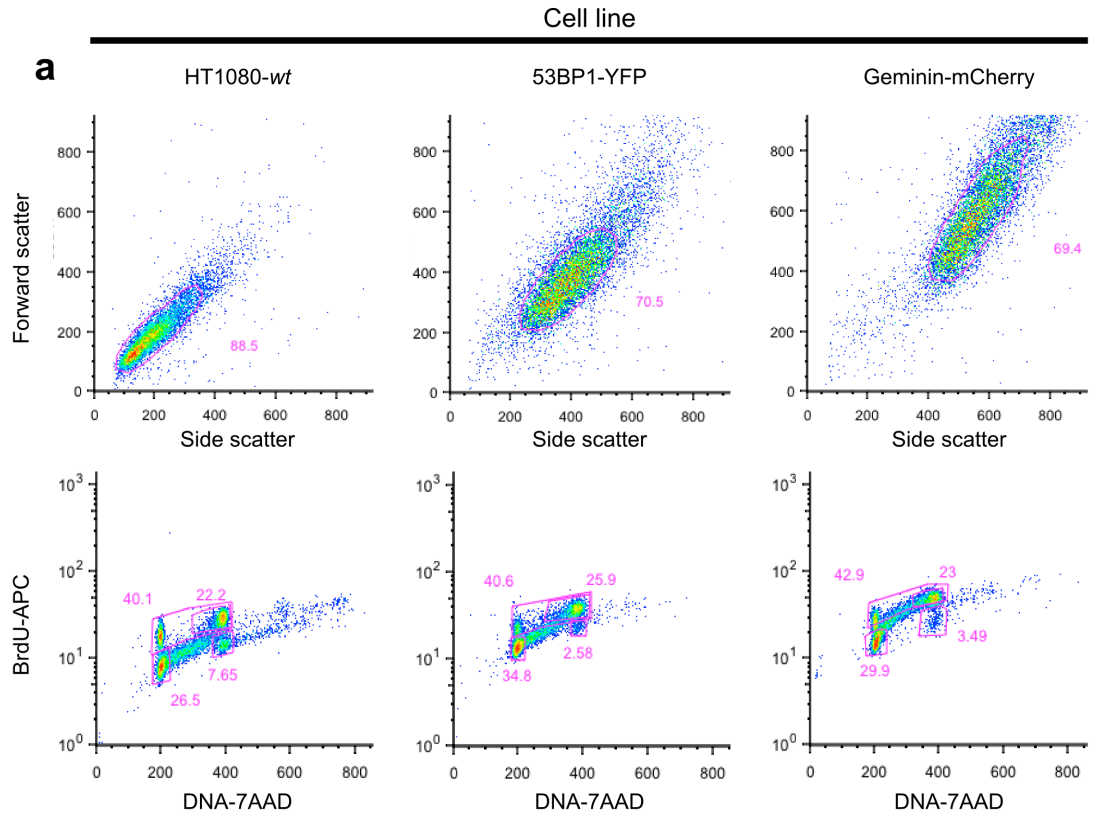


Figure 6.2 Cell cycle profile comparison between 53BP1-YFP and Geminin-mCherry cells. HT1080-53BP1-YFP and Geminin-mCherry cells were plated for cell cycle profile determination via 7-AAD staining using flow cytometry. Two time points were acquired per cell line with 6 h in between. Cell cycle profile determination was performed as described in **section 4.8.2**. The error bars represent the s.e.m. (n = 3 independent experiments).



b

HT1080 cell line	T_s ± s.d. (h)	T_{pot} ± s.d. (h)
wild-type	6.6 ± 1.1	16.6 ± 1.6
53BP1-YFP	7.0 ± 1.0	16.8 ± 1.6
53BP1-YFP-Geminin-mCherry	7.1 ± 0.8	17.1 ± 2.0

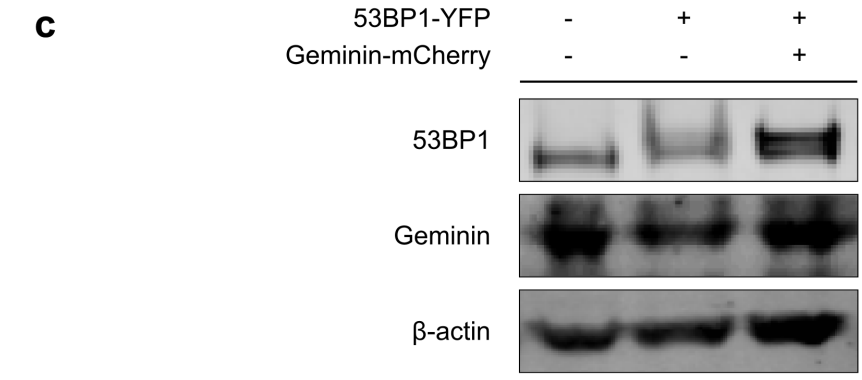


Figure 6.3 S-phase duration and 53BP1/Geminin expression levels. (a,b) Representative dot-plots of S-phase duration and T_{pot} determination based on BrdU labelling for HT1080-*wt*, 53BP1-YFP, and Geminin-mCherry cells. The errors represent the standard deviation of 2 independent experiments. **c)** Representative western blot of 53BP1 and Geminin protein levels compared to HT1080-*wt* cells.

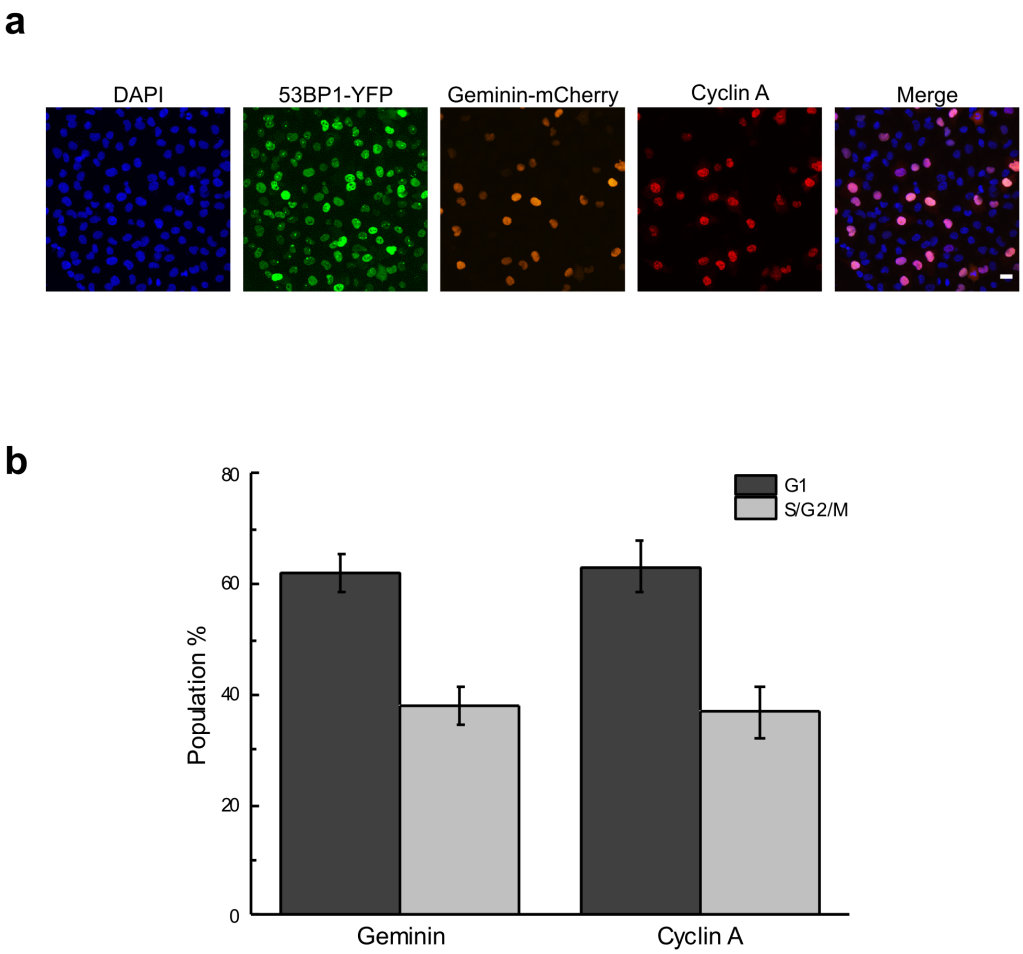


Figure 6.4 Geminin co-localisation with Cyclin A. a) Micrographs representing co-localisation between Geminin-mCherry and Cyclin A for S/G2/M population determination. Merged image is composed of DAPI, Geminin-mCherry and Cyclin A. Scale bar = 10 μm. **b)** Quantification of the number of cells positive for Geminin and Cyclin A. G1 population determined by subtracting the number of Geminin/Cyclin A positive cells to the total number of cells as determined by DAPI staining. The error bars represented the s.e.m. (n = 3 independent experiments).

To assess sensitivity to radiation, HT1080-*wt*, 53BP1-YFP and Geminin-mCherry cells were plated for clonogenic survival as described in **section 4.9**, with increasing cell numbers with dose (**table 4.4**). The samples were irradiated with doses ranging from 0 to 8 Gy using a ^{137}Cs source. The samples were placed at 37°C and 5% CO_2 humidified air, allowing the colonies to grow for 10 days. The colonies were fixed and stained, and the surviving fraction determined as described in **section 4.9**. The surviving fraction decreased with radiation dose, with 10% of the cells surviving to a dose of 8 Gy for all cell lines (**figure 6.6**). The p-values were calculated per dose point, indicating no significant difference, and thus confirming a similar radiation sensitivity phenotype, independently of the transfected vectors when compared to *wild-type* cells.

6.2.2 53BP1-YFP recruitment kinetics following irradiation: G1 vs. S/G2

As showed in **sections 6.2.1.3** and **6.2.1.4**, Geminin-mCherry fluorescence can be used in combination with 53BP1-YFP-associated fluorescence, to identify G1 cells from those in S/G2/M. With such model system it is possible to follow 53BP1-YFP recruitment dynamics to linac radiation-induced DNA damage in living cells during different phases of the cell cycle. To assess 53BP1 recruitment dynamics to damage sites, Geminin-mCherry cells were plated on the sample dishes described in **section 2.3** to be irradiated, and imaged using the linac experiment system. The cells were imaged for 53BP1-YFP twice before irradiation. Following irradiation with 0.5 Gy, the cells were imaged within 2 sec post-IR then at 2.5 min intervals up to 5 min, at min 15, 20 and 30, and finally every 30 min up to 4 h. Geminin-mCherry was imaged once before irradiation, and at every time point from 30 min onwards. A total of 21 ‘z’-slices were collected for each FOV per fluorophore, with exposures of 115 ms using the filter sets described in **section 2.5**. The data were deconvolved as described in **section 5.2.1**. For each FOV, the G1 population was identified

from the total population based on Geminin-mCherry fluorescence (**figure 6.7a**). The number of radiation-induced foci per cell was manually determined per time point for two independent cell populations, depending on the expression of Geminin-mCherry. Mitotic cells were not counted during these experiments since no foci were observed, due to the morphological changes that are undergoing during this cell cycle stage. The number of radiation-induced foci was determined by subtracting the background levels of 53BP1 foci, as determined from the time points taken prior to irradiation. The number of 53BP1 foci was plotted as a function of time per cell population (**figure 6.7b**). Similarly to the data shown in **figure 5.10**, the number of 53BP1 foci increases rapidly following irradiation, reaching approximately 8 foci/cell 5 min after irradiation, for both populations. The maximum number of foci/cell was determined to be approximately 11 for both G1 and S/G2 cells, observed 15 min post-IR. After 15 min the number of 53BP1 foci reduced for both populations. For the G1 population, the number of foci reduces more readily, with an average of 3 foci/cell present 4 h after irradiation. For the S/G2 population, the decay is similar over the initial 60-90 min time after which more foci persist than seen in G1 cells with, on average of 6 foci/cell at 4 h post-IR (**figure 6.7b**). These data highlight a clear difference in the recruitment and loss of 53BP1, particularly at later times, on the phase of the cell cycle. Such detailed information has not been obtained in the past by any studies.

6.2.3 Dependence of 53BP1 kinetics at sites of radiation-induced DNA damage in response to DNA-PKcs inhibition

DNA-PKcs is a major player in the repair of DSBs by the classical NHEJ or normally referred to as DNA-PKcs-dependent NHEJ repair pathway (Mladenov and Iliakis, 2011; van Gent and van der Burg, 2007) and is involved in repairing a sub-class of DSB, namely complex DSB (Reynolds *et al.*, 2012; Riballo *et al.*, 2004).

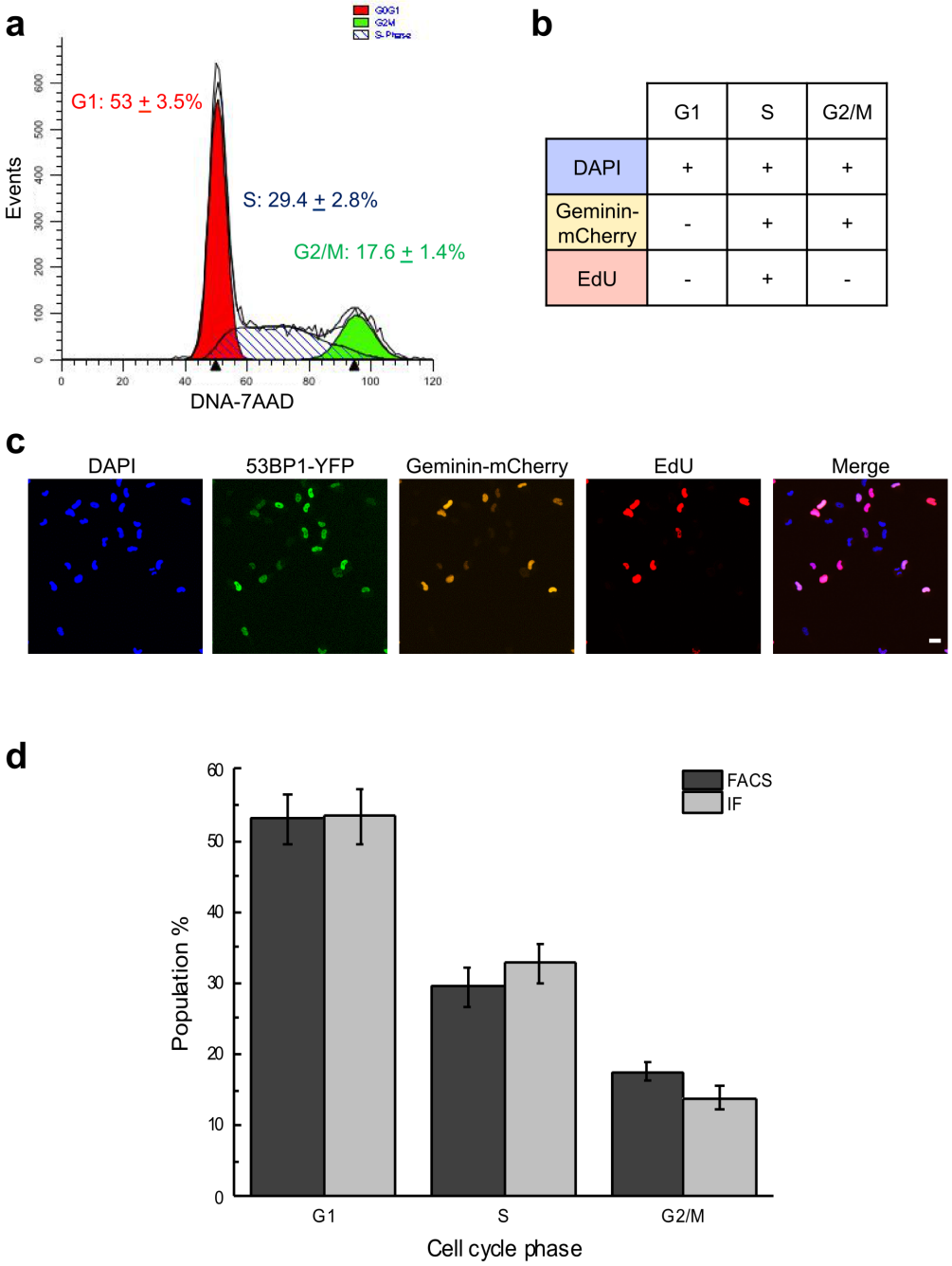


Figure 6.5 Cell cycle profile determination via immunofluorescence and flow cytometry. a) Representative cell cycle profile as determined by 7-AAD staining for HT1080 cells containing 53BP1-YFP and Geminin-mCherry. **b)** Cell populations based on EdU, Geminin-mCherry and DAPI. **c)** Representative micrographs of the different probes used to determine the cell cycle profile via immunofluorescence. Merged image is composed of DAPI, Geminin-mCherry and EdU. Scale bar = 10 µm. **d)** Comparison of the cell cycle profiles obtained by FACS and population isolation via immunofluorescence staining. The error bars represent the s.e.m. (n = 3 independent experiments).

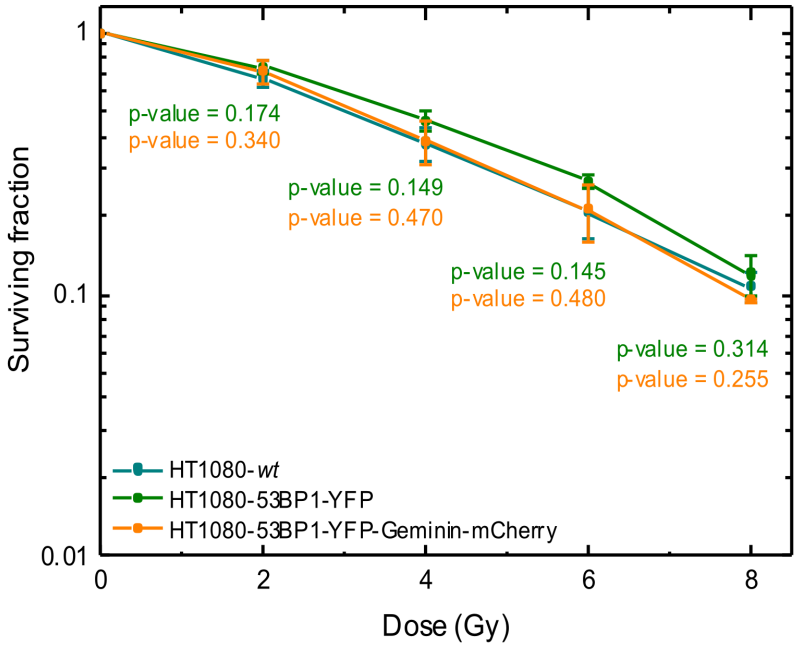


Figure 6.6 Radiation resistance determination of HT1080-*wt*, 53BP1-YFP, and Geminin-mCherry cells. All cell lines were plated for irradiation with increasing doses using a ^{137}Cs source. Cells were plated at different densities according to radiation dose as described in **table 4.4**. Colonies were allowed to grow for 10 days before staining. The p-values were obtained using One-way Anova between the *wt* cells and the fluorophore-labelled cell lines. The error bars represent the s.e.m. (n = 3 independent experiments).

DNA-PKcs is recruited to DSB sites by the Ku70/80 heterodimer, mediated through phosphorylation of the N-terminal region of DNA-PKcs (Davis *et al.*, 2013). This phosphorylation of DNA-PKcs regulates its dynamics at DSB (Uematsu *et al.*, 2007) and activation of its kinase activity, which also leads to its autophosphorylation (Davis and Chen, 2013). The effect of an inhibitor of phosphorylation of DNA-PKcs on the recruitment and loss of DNA-PKcs on cell cycle was investigated based on the dynamics of 53BP1 at sites of DNA damage using HT1080 cells tagged with Geminin-mCherry and 53BP1-YFP. Prior to live-cell imaging experiments, a titration was performed to optimise the concentration of the DNA-PKcs inhibitor (DNA-PKcsi) to use in subsequent experiments. DNA-PKcsi was added to the samples 1 h prior to irradiation at concentrations ranging from 0.5 to 5 μM. When used at concentrations higher than 1 μM, NU7441 has been reported to increasingly inhibit AKT phosphorylation (Tavecchio *et al.*, 2012). To assess the efficiency of the inhibitor, phosphorylation of DNA-PKcs at S2056 was monitored by western blotting in samples irradiated with 6 Gy and harvested 1 h after irradiation (**figure 6.8a**). For a concentration of ≥1 μM the phosphorylation signal was seen to decrease to similar levels, when compared to samples treated with radiation alone. The phosphorylation of 53BP1 at S1778 was monitored in the presence of increasing concentrations of DNA-PKcsi. This phosphorylation signal is higher for cells treated with radiation in combination with different concentrations of DNA-PKcsi (**figure 6.8a**) under the same conditions described above. A concentration of 1 μM DNA-PKcsi was therefore used in further experiments. Western blotting analysis was also performed to assess the dependence of the levels of 53BP1 phosphorylation at S1778 on time in response to radiation alone or in combination with DNA-PKcsi. Cells were exposed to 6 Gy using a ^{137}Cs source, in the presence and absence of 1 μM DNA-PKcsi.

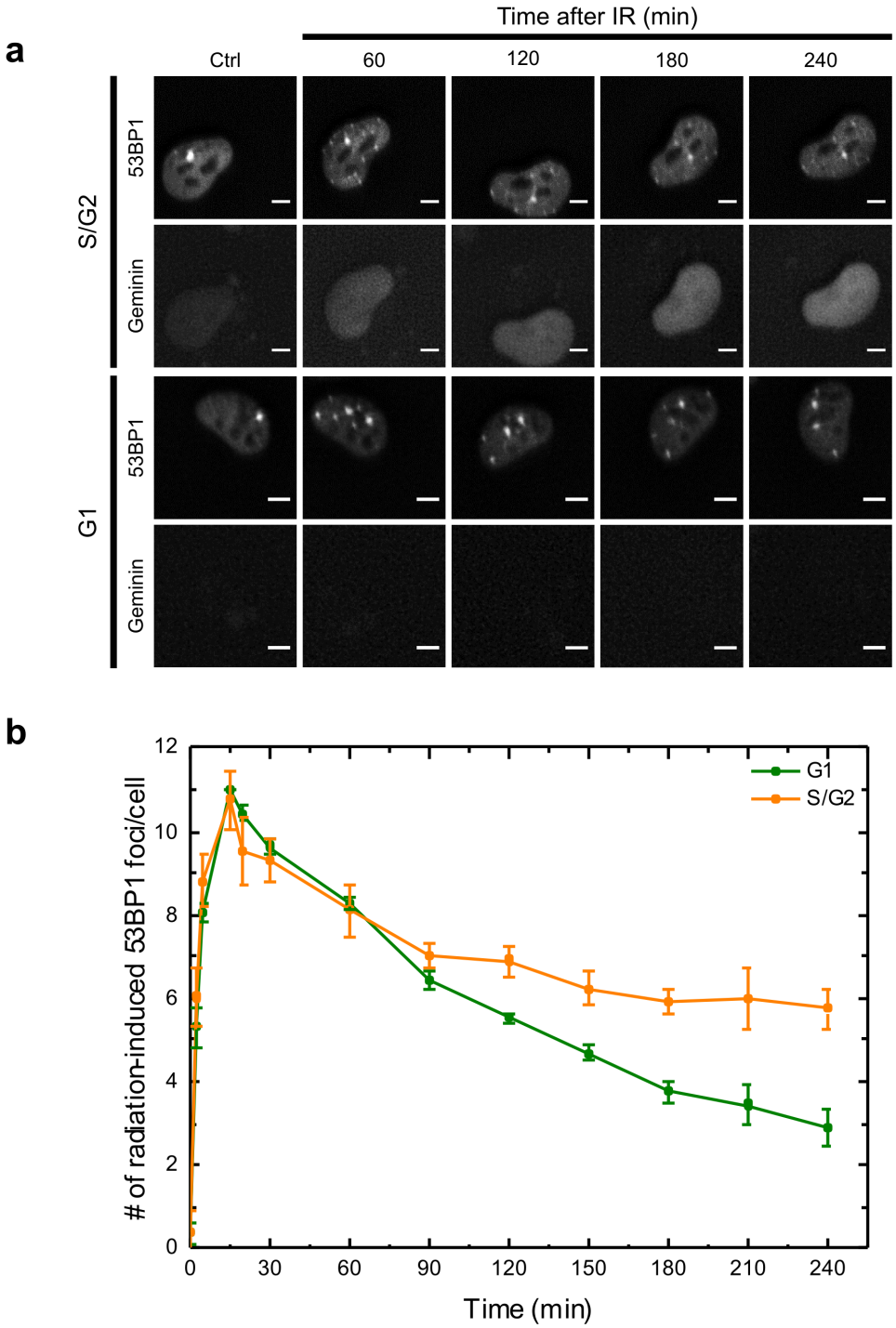


Figure 6.7 Cell cycle phase-specific 53BP1-YFP kinetics in response to radiation. HT1080 cells containing 53BP1-YFP and Geminin-mCherry were irradiated with 0.5 Gy and monitored for 53BP1 foci formation and disappearance using the linac experiment system for 4 h. **a)** Micrographs representing 53BP1-YFP and Geminin-mCherry fluorescence with time after irradiation. G1 and S/G2 cells isolated based on Geminin-mCherry fluorescence. Scale bar = 5 µm. **b)** Quantification of the number of radiation-induced 53BP1 foci with time after irradiation per cell fraction. Background levels of 53BP1 foci/cell were subtracted from images obtained prior to irradiation. At least 70 cells were analysed per cell fraction. The error bars represent the s.e.m. (n = 3 independent experiments).

The samples were harvested at 30 min, 90 min, and 3 h after irradiation. DNA-PKcsi activity was monitored by phosphorylation of DNA-PKcs at S2056. The irradiated cells, when in combination with DNA-PKcsi, displayed similar levels of phosphorylation of 53BP1-S1778. The persistent 53BP1-S1778 signal compared to that displayed when the cells were treated with radiation alone (**figure 6.8b**) is similar. Whether this similarity reflects repair efficiencies of DNA damage or some other process was investigated further by characterising the recruitment and loss kinetics of 53BP1 to DNA damage sites. HT1080-53BP1-YFP cells were irradiated with 0.5 Gy using the linac experiment system in the presence and absence of DNA-PKcsi. The cells were imaged within 2 sec post-IR then at 2.5 min intervals up to 5 min, at min 15, 20 and 30, and finally every 30 min up to 3 h. The data were processed as described in **section 5.2.1**, and the foci manually counted as described in **section 4.12.3**. DNA-PKcs inhibition resulted in similar kinetics for formation of 53BP1-YFP foci within 20 min post-IR to that displayed by the cells exposed to radiation alone. At longer times in the presence of the inhibitor, the number of foci/cell only reaches a maximum 60 min post IR (**figure 6.9**). The number of foci/cell decreases at a slower rate to that observed in cells treated with radiation alone. The number of foci/cell 3 h post-IR was determined to be approximately 9 in the presence of DNA-PKcsi, in contrast to only 5 foci in the irradiated control (**figure 6.9b**). DNA-PKcs inhibition results in persistence of some of the 53BP1 foci, reflecting repair impairment, and reduced rate of its dephosphorylation or as yet other unknown factors such as phase of the cell cycle.

6.2.3.1 Dependence of 53BP1 kinetics at sites of DNA damage in response to DNA-PKcs inhibition: effects of cell cycle

Prompt-DSBs and replication breaks, induced by ionising radiation in different phases of the cell cycle, were assessed by time-dependent recruitment of 53BP1-YFP to sites of cell

damage, highlighting the impact of DNA-PKcs kinase activity inhibition on the repair of DSBs following irradiation with the linac experiment system. Cells containing 53BP1-YFP and Geminin-mCherry were plated as described in **section 4.5** and allowed to grow overnight. The DNA-PKcs inhibitor, NU7441 was added at a concentration of 1 μM 1 h before irradiation with 0.5 Gy (solid lines in **figure 6.10b**). Control samples treated with the equivalent DMSO volume were also irradiated with 0.5 Gy (dashed lines in **figure 6.10b**). The samples were imaged up to 4 h after irradiation for both 53BP1-YFP and Geminin-mCherry as described in **section 6.2.2**. The number of radiation-induced 53BP1 foci/cell was plotted as a function of time for different phases of the cell cycle as determined by Geminin-mCherry-associated fluorescence (**figure 6.10a**). Similarly to the data shown in **figure 6.9b**, there is a delay in the formation of 53BP1 foci followed by a persistence of foci in both G1 and S/G2 cells following irradiation, when the cells had been exposed to DNA-PKcs inhibitor. As previously indicated, in the absence of the inhibitor, the number of 53BP1 foci persisting at longer times is greater in S/G2 phase cells. The maximum number of foci/cell was determined to be approximately 12 at 1 h after irradiation and independent of the phase of the cell cycle (**figure 6.10b**). The initial rate at which 53BP1 foci disappeared is similar for G1 and S/G2 cells in the presence of the inhibitor, and slower than that displayed by cells treated with radiation alone. The number of foci/cell reached approximately 8 for G1 cells and 8.5 for S/G2 cells at 4 h when DNA-PKcs kinase activity was compromised. These data highlight a cell cycle independent effect of DNA-PKcs inhibition on the persistence of 53BP1 foci in contrast to that seen with radiation treatment alone. To corroborate these findings, the 53BP1-YFP cells were plated for γ-H2AX staining following irradiation with 0.5 Gy using a ^{137}Cs source in the presence and absence of 1 μM DNA-PKcsi.

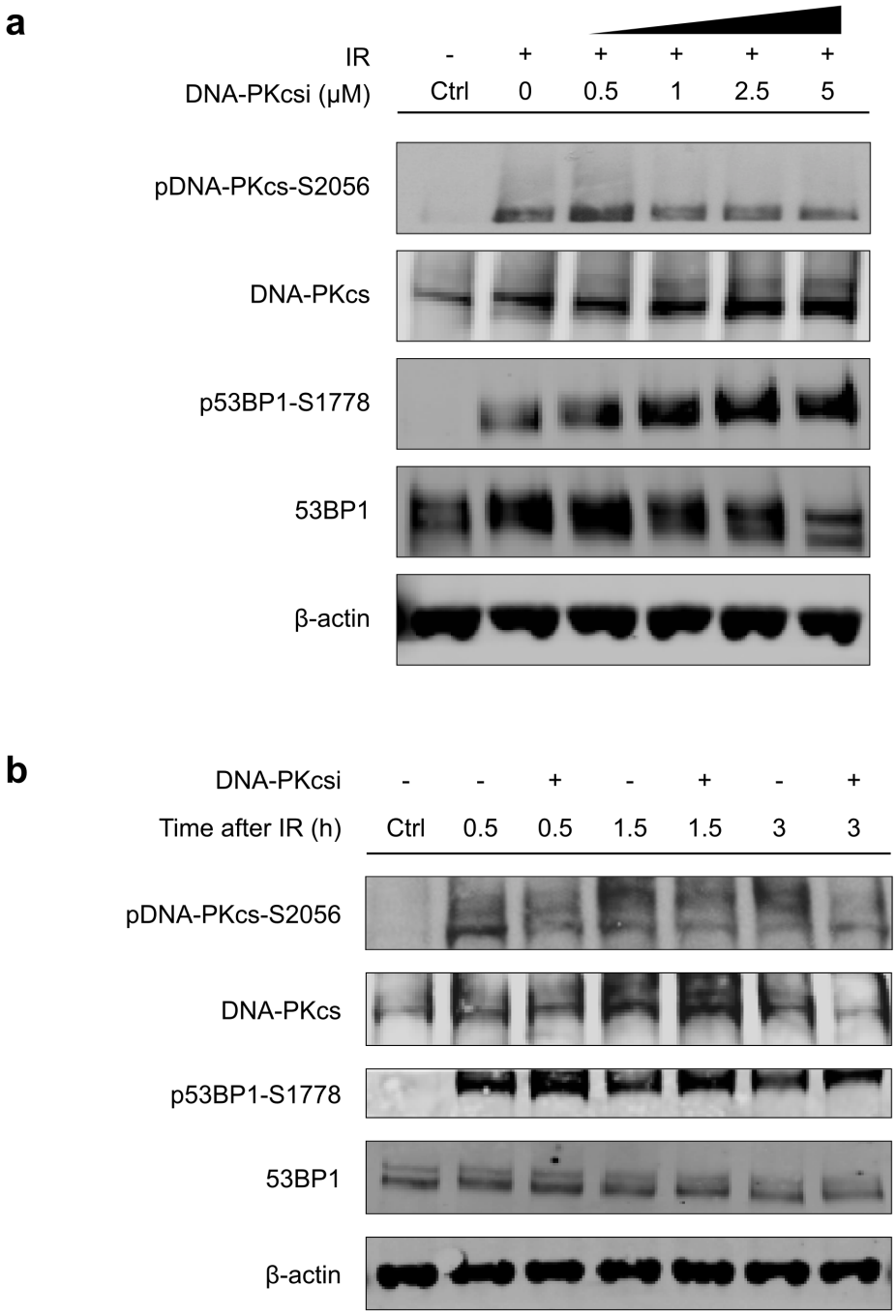


Figure 6.8 DNA-PKcsi titration and time course in response to radiation treatment. a) HT1080-53BP1-YFP cells were treated with increasing concentrations of DNA-PKcsi for 1 h before irradiation with 6 Gy using a ^{137}Cs source, and allowed to repair for 1 h. p53BP1-S1778 was blotted as a marker of damage and total-53BP1 as a control. DNA-PKcs phosphorylation at S2056 was blotted to monitor DNA-PKcsi activity, and total-DNA-PKcs as a control. β-Actin was blotted as the loading control. **b)** Representative western blots from time course up to 3 h following radiation treatment with 6 Gy in the presence and absence of 1 μM of DNA-PKcsi. Lysates were prepared from HT1080 cells containing 53BP1-YFP and blotted for p53BP1-S1778 to monitor damage, and pDNA-PKcs-S2056 to monitor DNA-PKcsi activity. Total-53BP1 and total-DNA-PKcs were blotted as controls. β-Actin was blotted as the loading control.

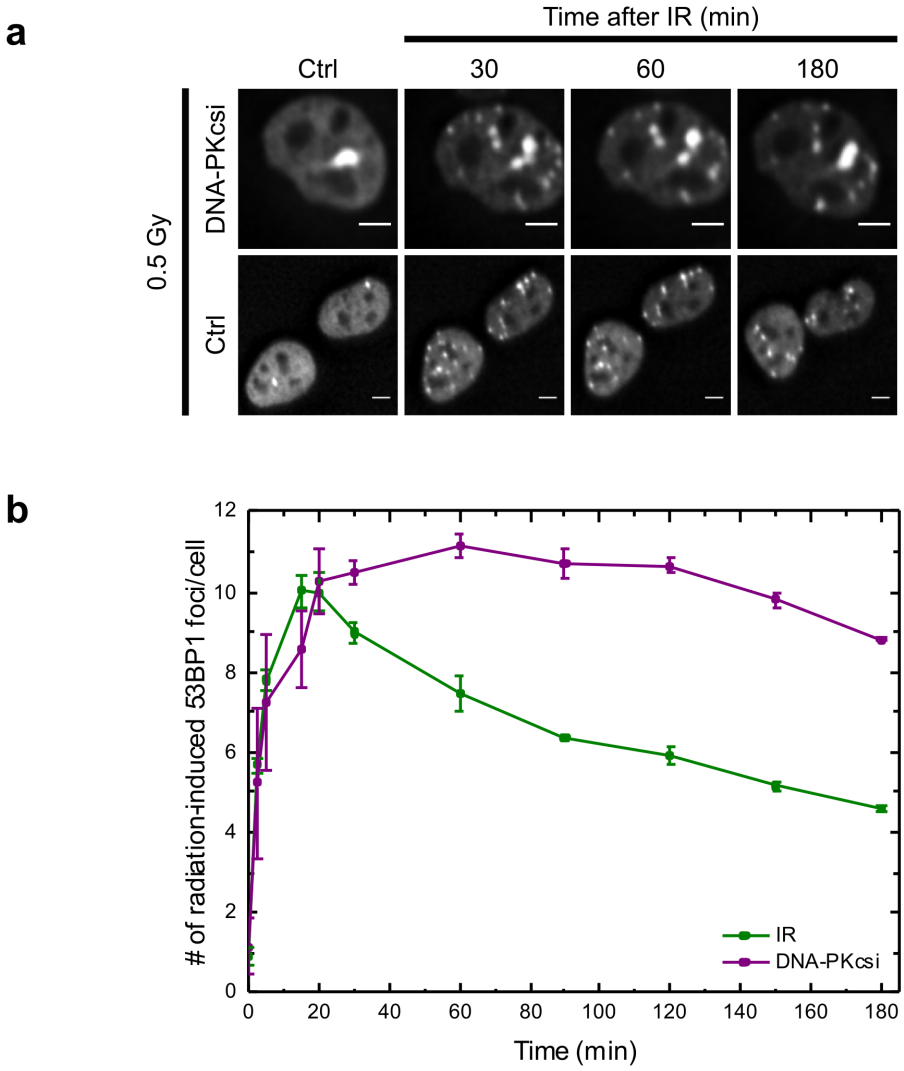


Figure 6.9 53BP1-YFP kinetics in response to 0.5 Gy in combination with DNA-PKcsi. a) Micrographs representing 53BP1 foci formation and disappearance in HT1080-53BP1-YFP living cells with time in response to 0.5 Gy alone, and in combination with DNA-PKcsi added 1 h before irradiation at a concentration of 1 µM. Scale bar = 5 µm. **b)** 53BP1 foci numbers as a function of time. Background levels of 53BP1 foci/cell were determined based on images obtained prior to irradiation and subtracted to the total number of observed foci. Error bars represent the s.e.m. (n = 3 independent experiments).

The exponentially growing cells were allowed to repair the radiation-induced damage for different times, 30 min, 2 h and 4 h after irradiation (**figure 6.11a**). The number of foci/cell was manually determined using ImageJ, and plotted as a function of time (**figure 6.11b**). The cells exposed to radiation treatment in combination with DNA-PKcs inhibition, have approximately 11 foci/cell 4 h after radiation treatment. The number observed is ~2-fold higher than that displayed by cells treated with 0.5 Gy alone. Taking the data on 53BP1 and γ-H2AX foci together, these findings indicate that the reduced repair efficiency of the NHEJ pathway through DNA-PKcs inhibition may lead to persistence of DSB produced promptly or as late developing DSB post-IR, but involving processes which may overshadow any processes which are dependent on the phase of the cell cycle (**figures 6.10b** and **6.11b**).

6.2.4 ATM kinase activity inhibition results in 53BP1 foci formation delay

ATM kinase is a key player in DSB repair and cell cycle checkpoint coordination (Lavin and Kozlov, 2007). ATM is responsible for phosphorylating multiple factors in response to DNA damage, such as histone H2AX at Ser-139 (resulting in γ-H2AX), and MDC1 (mediator of DNA damage checkpoint protein 1). MDC1 and γ-H2AX form a complex, which is responsible for a cascade of events that lead to the recruitment of multiple factors to damage sites, including the tumour suppressor molecule 53BP1 (FitzGerald *et al.*, 2009). In response to ionising radiation, ATM also phosphorylates 53BP1 at multiple serine residues including S1778 (Lee *et al.*, 2009; Stewart, 2009). To assess the importance of ATM kinase activity in the recruitment of 53BP1 recruitment to radiation-induced damage sites and its significance in the resolution of such damage, the formation and loss of 53BP1 foci following IR using the linac irradiation facility was monitored in response to 0.5 Gy in the presence and absence of ATM inhibition.

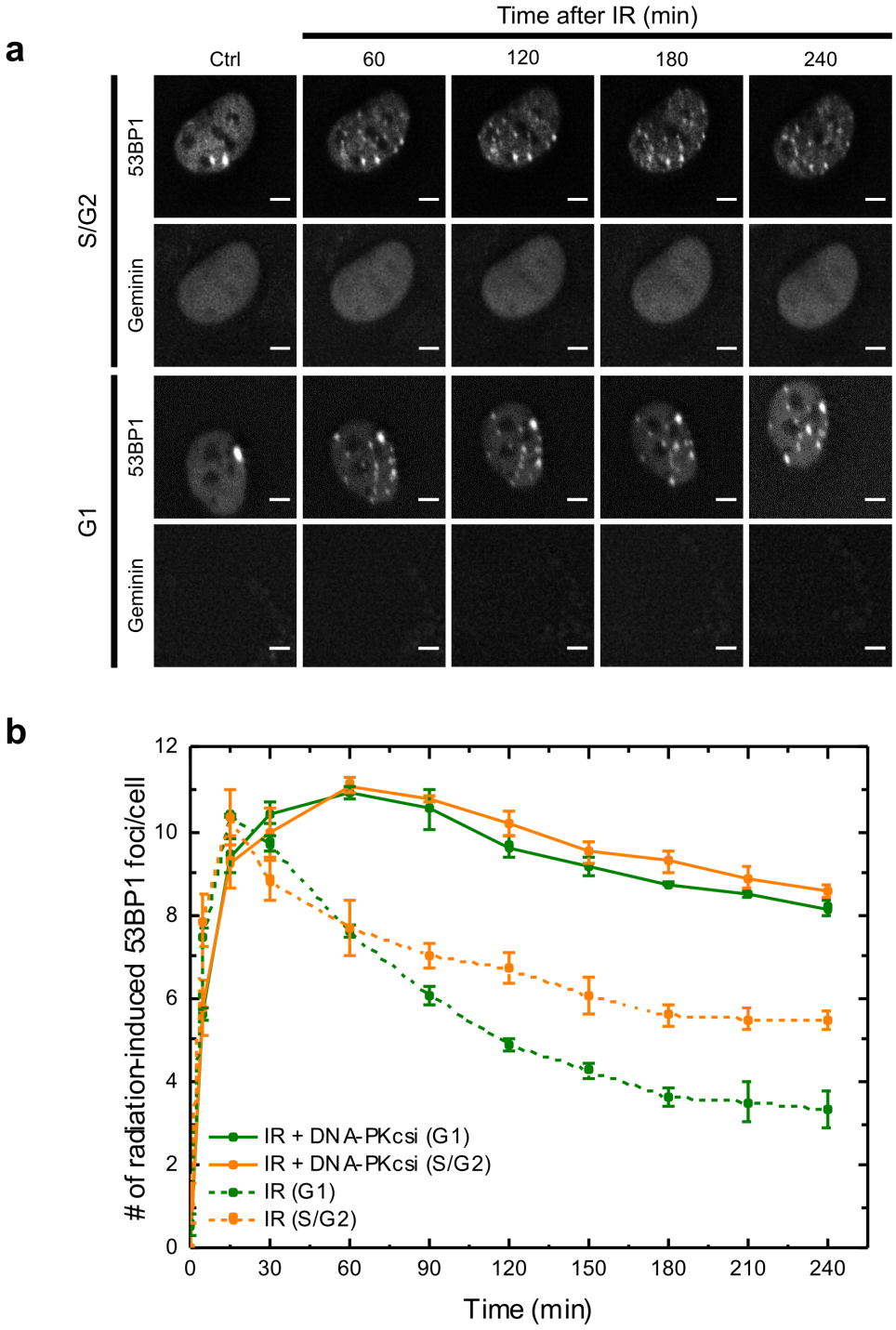


Figure 6.10 DNA-PKcsi induces 53BP1 foci persistence following radiation damage. a) Micrographs representing 53BP1 foci formation and disappearance with time in response to 1 µM of DNA-PKcsi added 1 h before irradiation with 0.5 Gy. Geminin-mCherry fluorescence was monitored for cell cycle stage determination. Scale bar = 5 µm. **b)** 53BP1 radiation-induced foci numbers as a function of time per cell fraction. Background levels of 53BP1 foci/cell were subtracted based on the average numbers observed prior to irradiation. Solid lines represent irradiation in combination with DNA-PKcsi. Dashed lines represent irradiation alone with DMSO equivalent volume. At least 70 cells were analysed per cell fraction. The error bars represent the s.e.m. (n = 3 independent experiments).

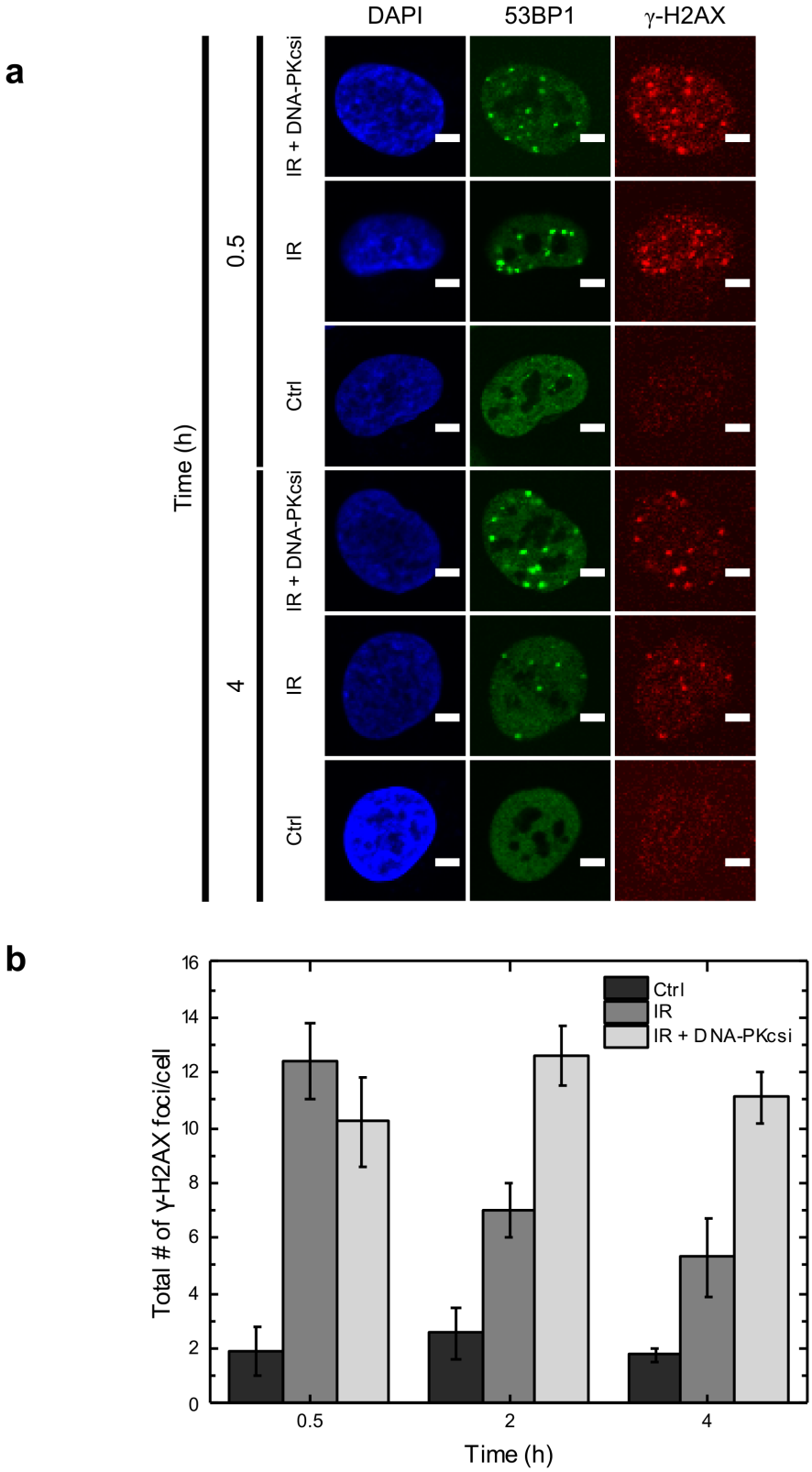


Figure 6.11 DNA-PKcsi induces γ-H2AX foci persistence following radiation damage. a) Micrographs representing γ-H2AX and 53BP1 foci in response to radiation treatment with 0.5 Gy using a ^{137}Cs source, in the presence and absence of 1 μM DNA-PKcsi. Samples were fixed at the indicated time points. Scale bar = 5 μm. **b)** Quantification of the number of γ-H2AX foci/cell as a function of time. The error bars represent the s.e.m. (n = 3 independent experiments).

Prior to live-cell experiments, a titration experiment was performed using HT1080-53BP1-YFP cells, to optimise the concentration necessary to inhibit ATM activity. The ATM inhibitor (ATMi) was added to the samples 1 h prior to irradiation, at concentrations ranging from 1 to 10 μM. The samples were irradiated with 6 Gy using a ^{137}Cs source, and allowed to repair for 1 h. The activity of the ATMi was monitored by western blotting as described in **section 4.7**, both through 53BP1 phosphorylation at S1778, and KAP1 phosphorylation at S824 as a surrogate marker for ATM kinase activity (Noon *et al.*, 2010) (**figure 6.12a**). Phosphorylation of both 53BP1 and KAP1 was impaired in response to 6 Gy IR in combination with 10 μM of ATMi. A concentration of 10 μM ATMi was used for further experiments.

Western blotting analysis was performed to assess the timescale of 53BP1 phosphorylation at S1778 and KAP1 at S824 (Noon *et al.*, 2010) in response to radiation damage alone or in combination with ATMi. Cells were irradiated with 6 Gy in the presence and absence of ATMi, and harvested at 30 min, 90 min, and 3 h after irradiation. 53BP1 phosphorylation at S1778 residue by ATM in response to radiation damage was abrogated in the presence of ATMi, highlighting a deficiency in DNA damage signalling (**figure 6.12b**). The control samples in the absence of ATMi display similar levels of phosphorylation of 53BP1-S1778 levels with time after irradiation. Total-53BP1 levels were similar for all the samples when normalised to the loading control (β-Actin). KAP1 phosphorylation was also abrogated in response to damage, confirming ATM kinase activity inhibition.

To characterise the effects of ATMi on the recruitment and loss of 53BP1 at DNA damage sites, HT1080-53BP1-YFP cells in exponential growth were irradiated with 0.5 Gy using the linac experiment system in the presence and absence of ATMi. The cells were imaged within 2 sec post-IR then at 2.5 min intervals up to 5 min, at 15, 20 and 30, and finally every 30 min up to 3 h. The data were processed as described in **section 5.2.1**, and the foci

manually counted as described in **section 4.12.3**. ATM inhibition impairs the recruitment of 53BP1-YFP to damage sites, resulting in fewer foci per cell being formed in response to radiation damage when compared to cells treated with 0.5 Gy only (**figure 6.13a**). In the presence of ATMi, the number of radiation-induced foci was determined to be 3 per cell 30 min post-IR and this level remains constant up to 3 h (**figure 6.13b**). This level of foci contrasts with the level of ~10 foci/cell at 30 min, followed by a loss of foci with time (**figure 6.13b**). This reduction may reflect the reduced levels of phosphorylation of 53BP1 required for efficient recruitment to damage sites.

6.2.4.1 ATM kinase inhibition: effects of cell cycle

To assess the importance of ATM kinase activity in the recruitment of 53BP1 to radiation-induced DSBs on the phase of the cell cycle, 53BP1 recruitment and loss at damage sites was monitored using cells containing 53BP1-YFP and Geminin-mCherry. Cells were plated and allowed to grow overnight. The ATM inhibitor (KU55933) was added at a concentration of 10 μM 1 h before irradiation with 0.5 Gy using the linac experiment system. Control samples treated with the equivalent DMSO volume were irradiated with 0.5 Gy for comparison. Similar to the procedure described in **section 6.2.2**, the samples were imaged up to 4 h after irradiation for both 53BP1-YFP and Geminin-mCherry. The number of radiation-induced 53BP1 foci per cell was determined as a function of time, with G1 and S/G2 cells distinguished based on Geminin-mCherry-associated fluorescence (**figure 6.14a**). As evidenced in **figure 6.14b**, both G1 and S/G2 populations exhibit a delay in the formation of radiation-induced 53BP1 foci with ATM inhibition. In response to ATM inhibition, both G1 and S/G2 populations displayed a 4-fold lower number of foci/cell compared to control 15 min after irradiation (**figure 6.14b**). The number of foci was seen to slowly increase with time for the S/G2 population, reaching 6 foci/cell 4 h

after radiation treatment, whereas the G1 population reaches a maximum number of 4 foci/cell 90 min after irradiation, with only 2 foci/cell seen 4 h after irradiation. The foci numbers observed for both G1 and S/G2 populations 4 h after radiation treatment are comparable to those displayed in the control samples. These data highlight a compromised efficiency in the signalling of radiation-induced DSBs independently of the cell cycle phase caused by ATM kinase activity inhibition, as evidenced by the initial delay in the formation of 53BP1 foci in response to radiation treatment (**figures 6.13b** and **6.14b**). This reduction may relate to the lower levels of phosphorylation of 53BP1 (see **figure 6.12**). The increasing number of 53BP1 foci observed in S/G2 cells may be irrespective of ATM inhibition and could be associated with the development of later developing foci arising from replication-induced DSB.

6.2.5 PARP inhibition induces collapsed replication forks

Poly (ADP-ribose) polymerase-1 (PARP-1) is a key player in the repair of SSBs spontaneously or endogenously generated to the genomic DNA, being recruited to such lesions prior to their repair via BER (Fisher *et al.*, 2007). PARP-1 binds to the SSBs promoting its own PARylation, leading to the recruitment of molecules involved in BER such as XRCC1, and subsequent release of PARP-1 from the damage site (El-Khamisy *et al.*, 2003). SSBs are a type of lesion, which may not pose a direct cytotoxic effect, but they can give rise to DSBs during DNA replication via collapsed replication forks requiring HR repair (Harper *et al.*, 2010; Saleh-Gohari *et al.*, 2005). PARP-1 has also been reported to possess a role as a DSB sensor molecule of lesions to be repaired via the B-NHEJ or MMEJ repair pathway (Mladenov and Iliakis, 2011).

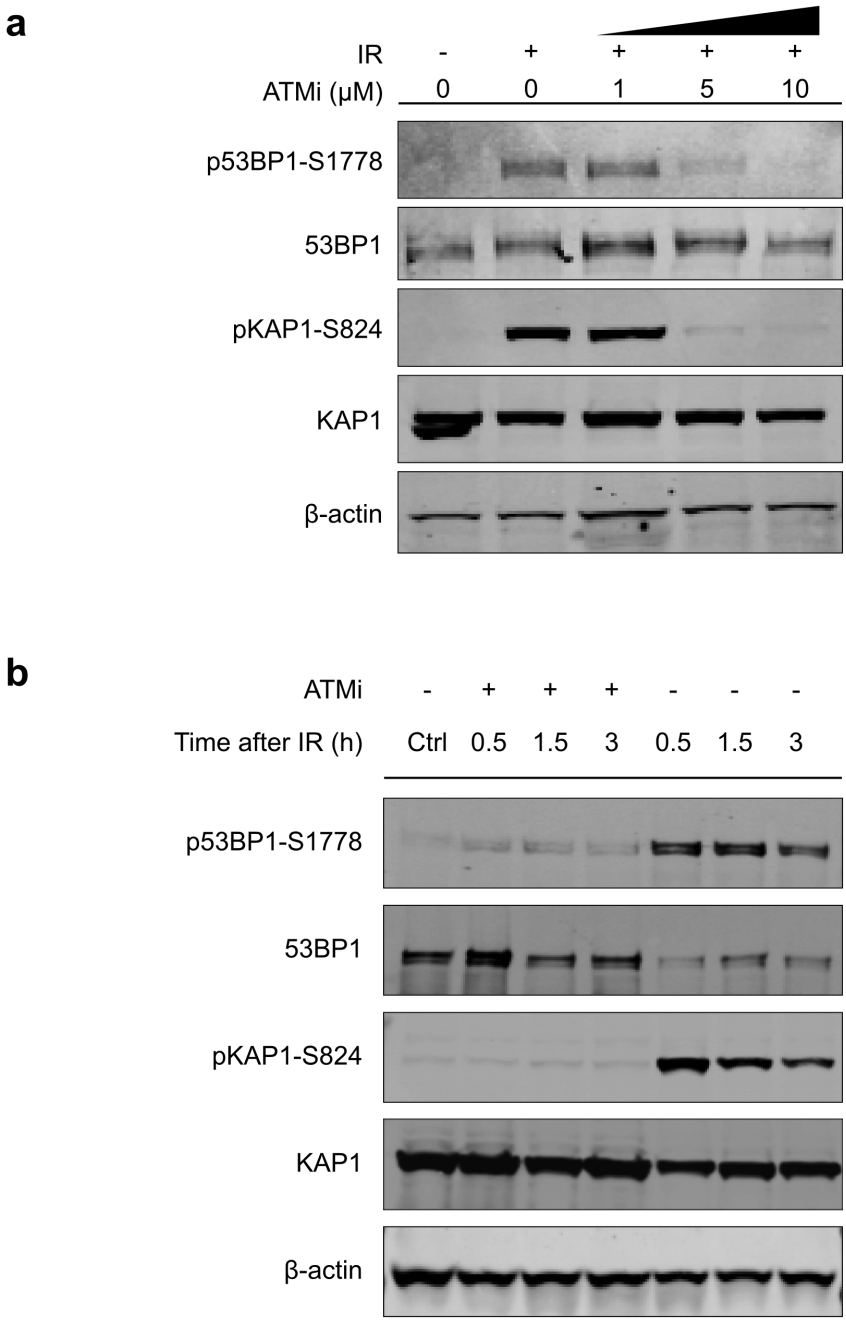


Figure 6.12 ATMi titration and time course in response to radiation treatment. a) HT1080-53BP1-YFP cells were treated with increasing concentrations of ATMi for 1 h before irradiation with 6 Gy using a ^{137}Cs source, and allowed to repair for 1 h. p53BP1-S1778 was blotted as a marker of damage and total-53BP1 as a control. KAP1 phosphorylation at S824 was blotted to monitor ATMi activity, and total-KAP1 as a control. β-Actin was blotted as the loading control. **b)** Representative western blots from time course up to 3 h following radiation treatment with 6 Gy in the presence and absence of 10 μM of ATMi. Lysates were prepared from HT1080 cells containing 53BP1-YFP and blotted for p53BP1-S1778 to monitor damage, and pKAP1-S824 to monitor ATMi activity. Total-53BP1 and total-KAP1 were blotted as controls. β-Actin was blotted as the loading control.

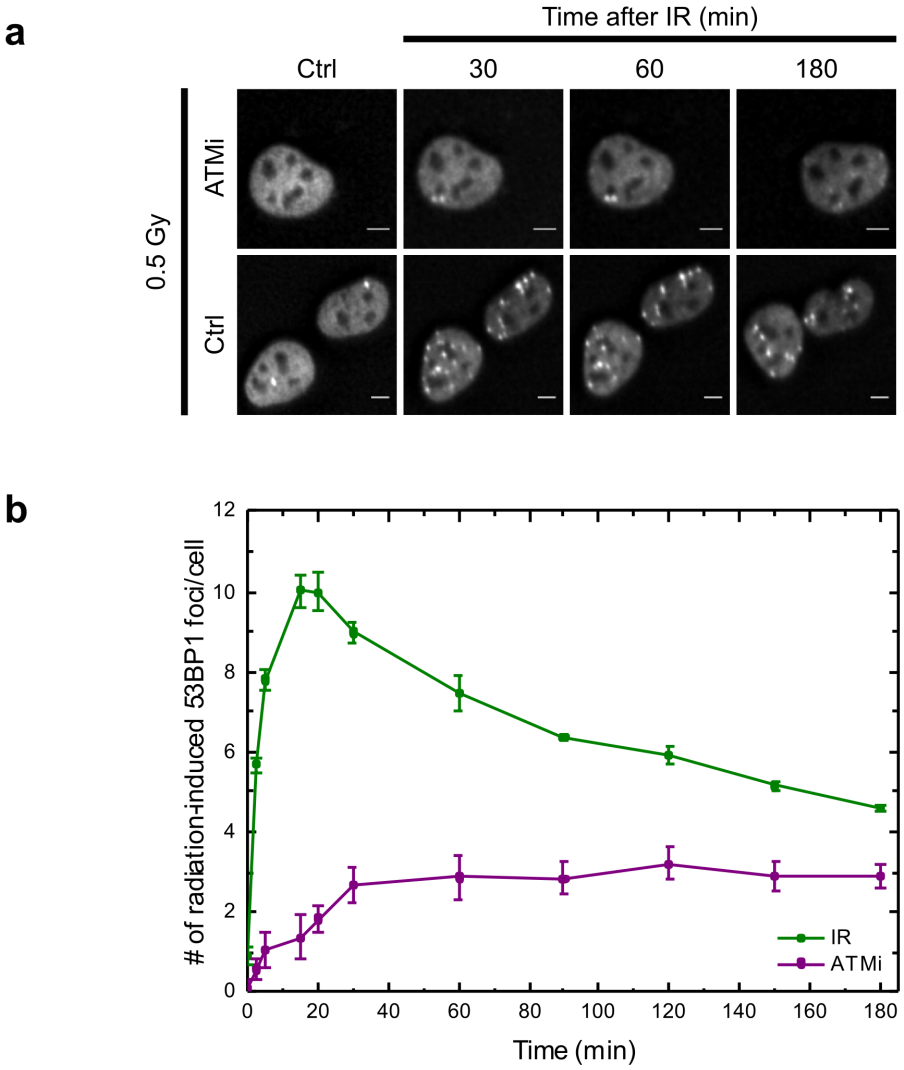


Figure 6.13 53BP1-YFP kinetics in response to 0.5 Gy in combination with ATMi. **a)** Micrographs representing 53BP1 foci formation and disappearance in HT1080-53BP1-YFP living cells with time in response to 0.5 Gy alone, and in combination with ATMi added 1 h before irradiation at a concentration of 10 µM. Scale bar = 5 µm. **b)** 53BP1 foci numbers as a function of time. Background levels of 53BP1 foci/cell were determined based on the obtained images prior to irradiation and subtracted to the total number of observed foci. Error bars represent the s.e.m. (n = 3 independent experiments).

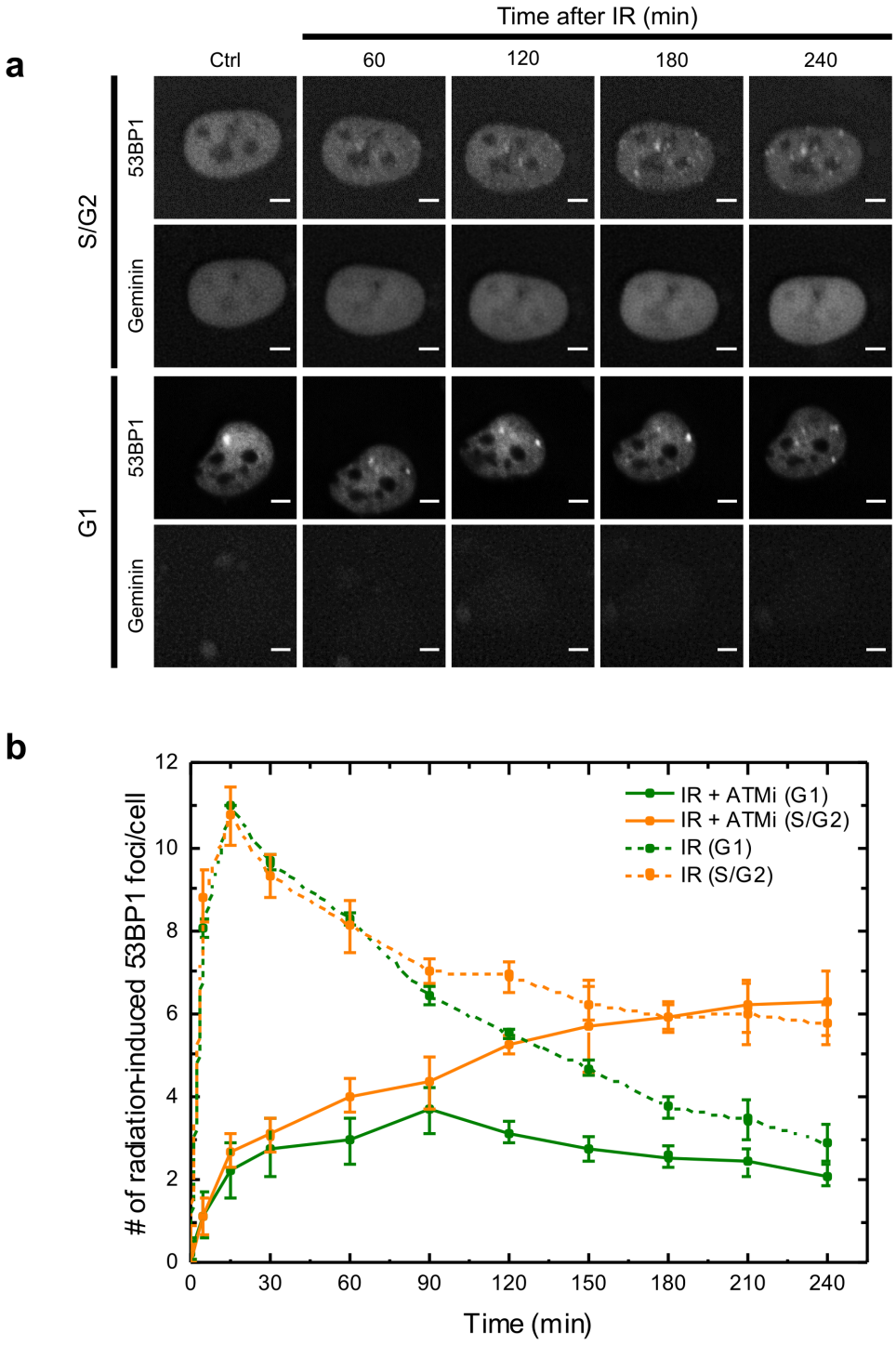


Figure 6.14 ATMi results in 53BP1 foci formation delay in response to radiation treatment. a) Micrographs representing 53BP1 foci formation and disappearance with time in response to 10 µM of ATMi added 1 h before irradiation with 0.5 Gy. Geminin-mCherry fluorescence was monitored for cell cycle stage determination. Scale bar = 5 µm. **b)** 53BP1 radiation-induced foci numbers as a function of time per cell fraction. Background levels of 53BP1 foci/cell were subtracted based on the average numbers observed prior to irradiation. Solid lines represent irradiation in combination with ATMi. Dashed lines represent irradiation alone with DMSO equivalent volume. At least 70 cells were analysed per cell fraction. The error bars represent the s.e.m. (n = 3 independent experiments).

53BP1 recruitment and loss at radiation-induced damage sites was monitored in living cells in response to chemical inhibition of PARP, in order to assess the effect of PARP-1 activity in the generation of collapsed replication forks and repair of DNA DSBs throughout the cell cycle. To determine the optimal concentration of PARP inhibitor (AZD2281) to use, a titration experiment was performed using HT1080 cells containing 53BP1-YFP and Geminin-mCherry. PARPi was added to the samples 2 h prior to irradiation, at concentrations ranging from 1 to 10 μM. The samples were irradiated with 6 Gy using a ^{137}Cs source, and allowed to repair for 1 h. The efficacy of PARP inhibition was determined by western blotting as described in **section 4.7**, by monitoring PAR levels. PARylation was abrogated for all the tested concentrations, when compared to control and irradiated samples (**figure 6.15**). The high level of PAR in the control sample may be the result of endogenously induced damage. PARP-1 levels were similar between all samples. Cleaved PARP-1, a marker of apoptosis (McGowan *et al.*, 1996), was seen to increase with PARP inhibition. Phosphorylation of 53BP1 at S1778 displaying similar levels in the absence of and for all PARPi concentrations tested following IR. Based upon these results and previously reported data, PARPi was used at a concentration of 5 μM for further experiments.

To assess if any effect of PARP inhibition on the dynamics of recruitment of 53BP1 at sites of damage depends on the phase of the cell cycle, cells containing 53BP1 and Geminin-mCherry were plated and allowed to grow overnight. PARPi was added at a concentration of 5 μM 2 h before irradiation with 0.5 Gy, using the linac experiment system. Unirradiated control samples exposed to PARPi were used to assess the effect of PARP inhibitor on the background levels of 53BP1 foci (dashed lines in **figure 6.17**). The samples were imaged for up to 4 h, as described in **section 6.2.2**. The number of 53BP1 foci per cell was manually determined for both G1 and S/G2 cell populations identified

based on Geminin-mCherry fluorescence (**figure 6.16**). The total number of 53BP1 foci/cell was plotted as a function of time for all described populations. The G1 fraction of the unirradiated samples, displayed a baseline level of on average 1.5 foci/cell. The irradiated G1 fraction in the presence of PARPi displayed similar 53BP1 recruitment and loss kinetics to those observed for G1 cells in the absence of PARPi (**figure 6.7b** for comparison). The maximum number of foci/cell was determined to be 13 observed 15 min after irradiation, subsequently decreasing to on average 5 foci/cell 4 h after irradiation. These numbers are in agreement with G1 cells irradiated in the absence of PARP inhibition if the number of background 53BP1 foci is subtracted from the total. In contrast to G1 cells, the unirradiated S/G2 cells display an average of 13 foci/cell throughout the whole timescale followed. The S/G2 cells, which were exposed to 0.5 Gy in combination with PARPi, displayed an initial number of 14 foci/cell, increasing to a maximum of 20 observed 15 min after irradiation. Even at 4 h after irradiation, these cells displayed, on average, 18 foci/cell, when the majority of IR-induced foci have disappeared in G1 cells. The maximum number observed for this population could in principle be higher than 20 foci/cell since the number of foci posed difficulties to the manual counting due to some overlap. These data are consistent with the data from western blot analysis. For instance, cells were irradiated with 6 Gy using a ^{137}Cs source, in the presence and absence of PARPi, and harvested at 1 h, 2 h and 4 h after irradiation. PARylation is significantly reduced in the samples exposed to PARPi in contrast to those that had been exposed to radiation only (**figure 6.18**). Similarly to live-cell imaging data, the levels of phosphorylated 53BP1-S1778 remain higher for samples exposed to radiation in combination with PARPi and the higher levels of 53BP1 foci seen. PARP-1 levels were similar for all the samples with the exception of PARP-1 cleavage not being observed in the unirradiated control sample.

Total-53BP1 levels were similar for all the samples when normalised to the loading control (β-Actin).

To assess the suggestion that PARP inhibition enhances the lifetime of endogenously produced DNA damage and as a consequence increases the probability of collapsed replication forks which require repair by HR, cells were irradiated with 0.5 Gy using a ^{137}Cs source in the presence and absence of PARPi and immuno-stained for RAD51 as described in **section 4.6.2**. The cells were irradiated with 0.5 Gy and placed at 37°C and 5% CO_2 humidified air to allow repair. The cells were fixed at 30 min, 2 h and 4 h after irradiation. The samples were imaged as described in **section 4.12.1**. The number of RAD51 foci/cell was determined for the S/G2 population identified through Geminin-mCherry fluorescence (**figure 6.19a**). The number of RAD51 foci/cell was plotted as a function of time per condition. PARPi inhibition in combination with 0.5 Gy resulted in an increased number of RAD51 foci, with an observed maximum of approximately 6 foci/cell 2 h after irradiation (**figure 6.19b**). This number decreased to 5 foci/cell 4 h after irradiation. The maximum number observed was 2.4-fold higher than those displayed in the irradiated controls. The irradiated samples displayed an increase of the level of RAD51 foci with time after irradiation, with 2.5 foci/cell present 4 h after irradiation. The unirradiated controls had an average background level of 1.3 foci/cell.

The data presented in this section highlight an increase in the levels of damage with PARP inhibition, as observed by the number of 53BP1 foci in the absence of radiation in S/G2 cells and confirmed by the levels of phosphorylated 53BP1-S1778 (**figures 6.16-6.18**). These observations are consistent with PARP inhibition, causing the lifetime of endogenous damage to be extended and enhancing its probability of encountering a replication fork in S phase. The replication break would then be signalled through recruitment of 53BP1. Following IR, higher levels of 53BP1 foci were observed in S/G2

cells in the presence of the PARP inhibitor, and confirmed by the higher levels of RAD51 foci in S/G2 cells, supporting the suggestion that this type of damage requires HR for repair (**figures 6.17** and **6.19**).

6.3 Discussion

This chapter focused on preliminary experiments to explore the range of applications of the linac experiment system. In particular, this chapter addressed the possibility of using the linac experiment system to perform cell cycle phase-specific DNA repair kinetics studies with HT1080 cells containing 53BP1-YFP as a DSB marker, and Geminin-mCherry as a cell cycle phase indicator. These cells were shown not to have cell cycle progression impairments due to the introduction of Geminin-mCherry, nor added sensitivity or resistance to radiation (**figures 6.1-6.3** and **6.6**). Geminin-mCherry was found to co-localise with Cyclin A (S/G2/M marker), guaranteeing the specificity of Geminin-mCherry expression solely to cells present in S and G2/M phases (**figure 6.4**). EdU staining together with Geminin-mCherry fluorescence and DAPI staining allowed determination of the cell cycle profile by immunofluorescence. These results were corroborated by FACS analysis, providing further evidence of the specificity of Geminin-mCherry fluorescence to S and G2/M cells (**figure 6.5**).

6.3.1 53BP1-YFP recruitment kinetics following irradiation: effects of cell cycle

The recruitment of 53BP1 to sites of radiation-induced DNA damage was followed with the linac experiment system using Geminin-mCherry-associated fluorescence to discern G1 from S/G2 cells. In G1 cells, DSB repair is restricted to the NHEJ repair pathway, whereas in S/G2 cells both NHEJ and HR can operate to resolve DSB lesions (Mladenov and Iliakis, 2011). The data shown in **figure 6.7b** highlight a difference between G1 and S/G2 cells in the kinetics of 53BP1 foci disappearance.

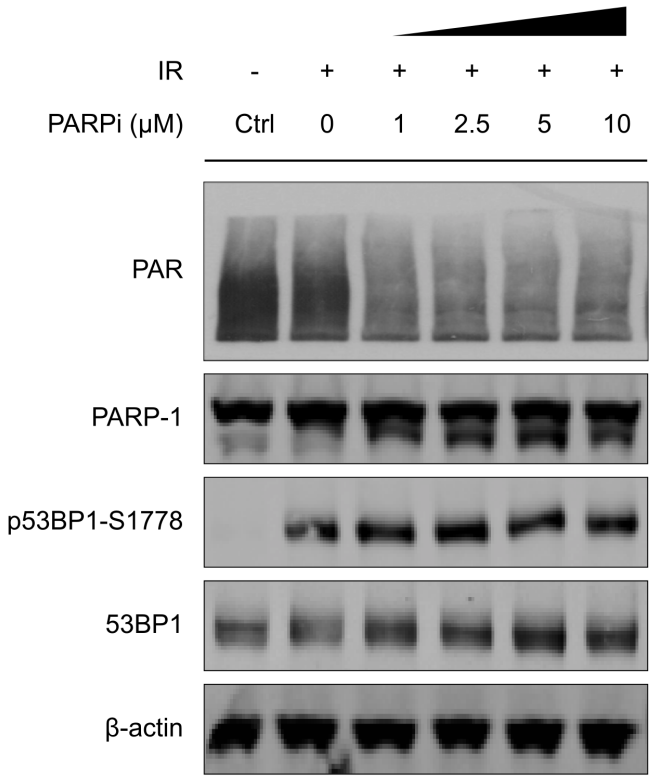


Figure 6.15 PARPi concentration titration. HT1080 cells containing 53BP1-YFP and Geminin-mCherry were treated with increasing concentrations of PARPi for 2 h before irradiation with 6 Gy using a ^{137}Cs source. p53BP1-S1778 was blotted as a marker of damage and total-53BP1 as a control. PAR levels were blotted to monitor PARPi activity, and PARP-1 as a control. β-Actin was blotted as the loading control.

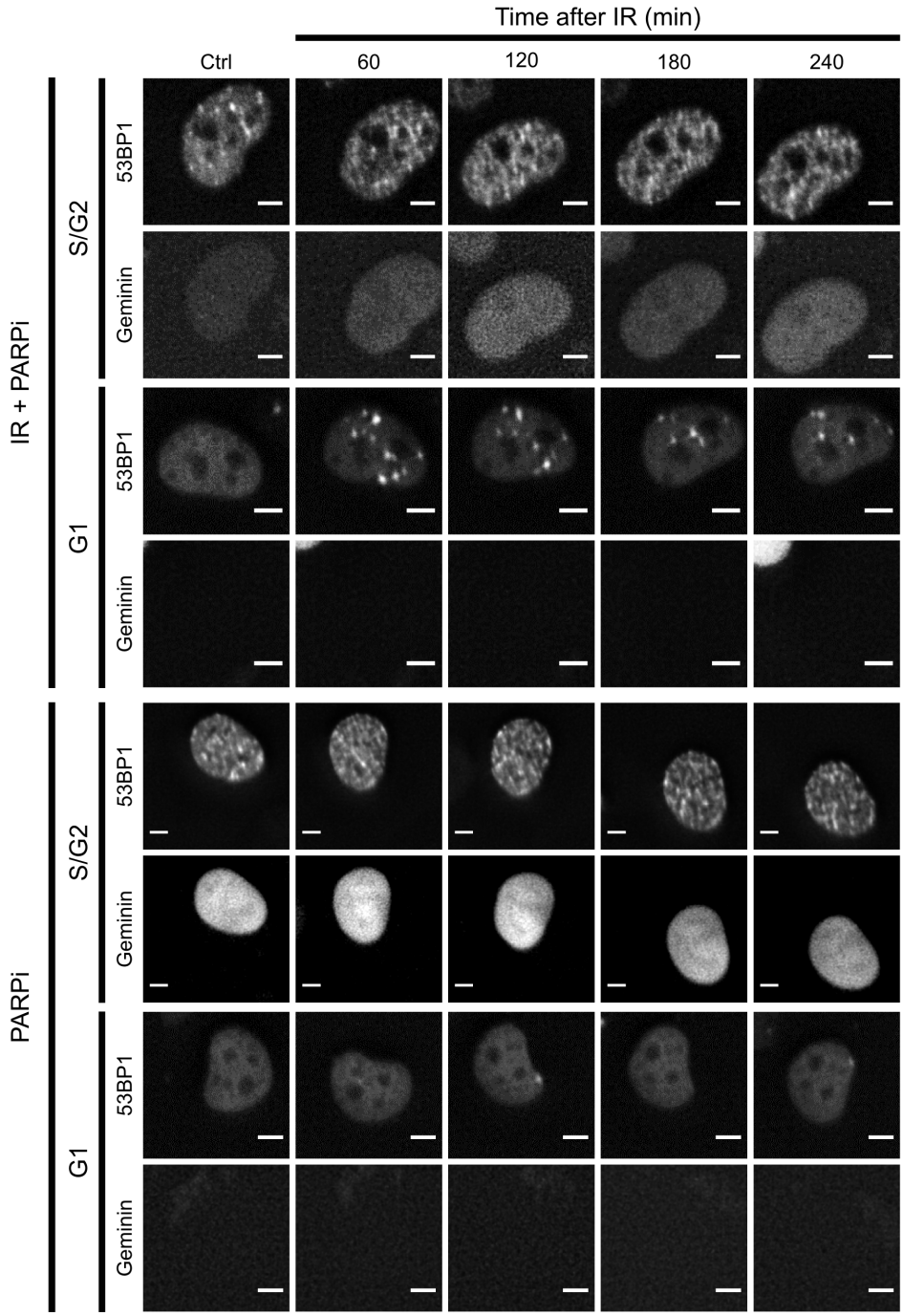


Figure 6.16 PARPi leads to increased levels of 53BP1 foci in S/G2 cells. Micrographs representing 53BP1 foci formation and disappearance with time in response to PARP inhibition alone and in combination with 0.5 Gy. PARPi was added at a concentration of 5 μM 2 h before initiating the imaging acquisition. Geminin-mCherry fluorescence was monitored for cell cycle stage determination. Scale bar = 5 μm.

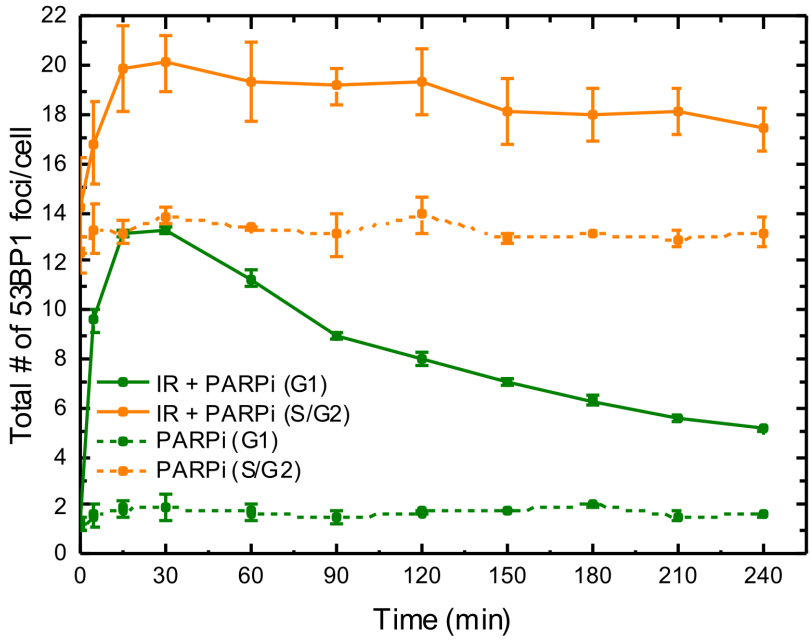


Figure 6.17 PARPi leads to increased levels of 53BP1 foci in S/G2 cells. 53BP1 radiation-induced foci numbers as a function of time per cell fraction. Solid lines represent irradiation with 0.5 Gy in combination with PARPi. Dashed lines represent PARPi used as a single agent. At least 70 cells were analysed per cell fraction. The error bars represent the s.e.m. (n = 3 independent experiments).

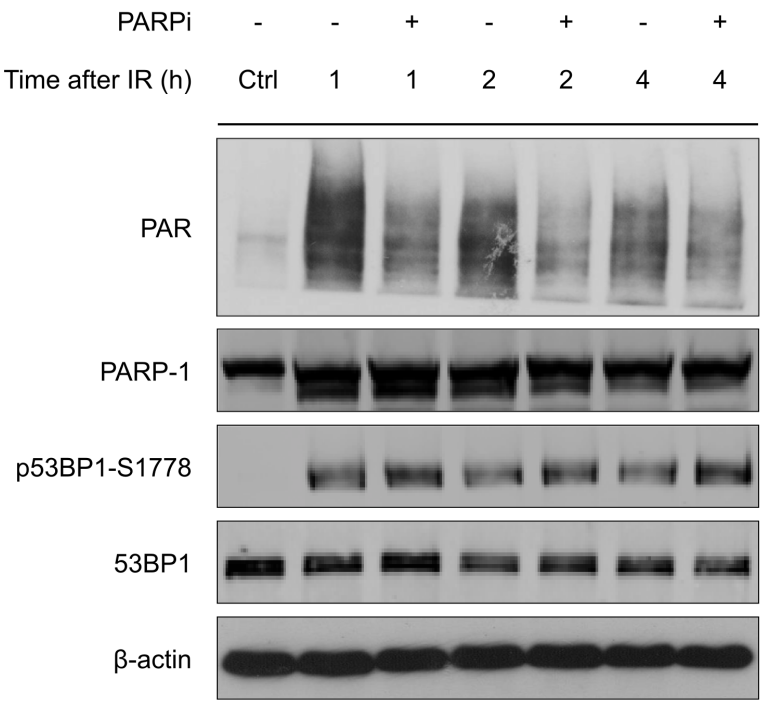


Figure 6.18 PARPi leads to p53BP1-S1778 accumulation following radiation damage. Representative western blots from time course up to 4 h following radiation treatment with 6 Gy using a ^{137}Cs source in the presence and absence of 5 μM of PARPi. Lysates were prepared from HT1080 cells containing 53BP1-YFP and Geminin-mCherry and blotted for p53BP1-S1778 to monitor damage, and PAR levels to monitor PARPi activity. Total-53BP1 and PARP-1 were blotted as controls. β-Actin was blotted as the loading control.

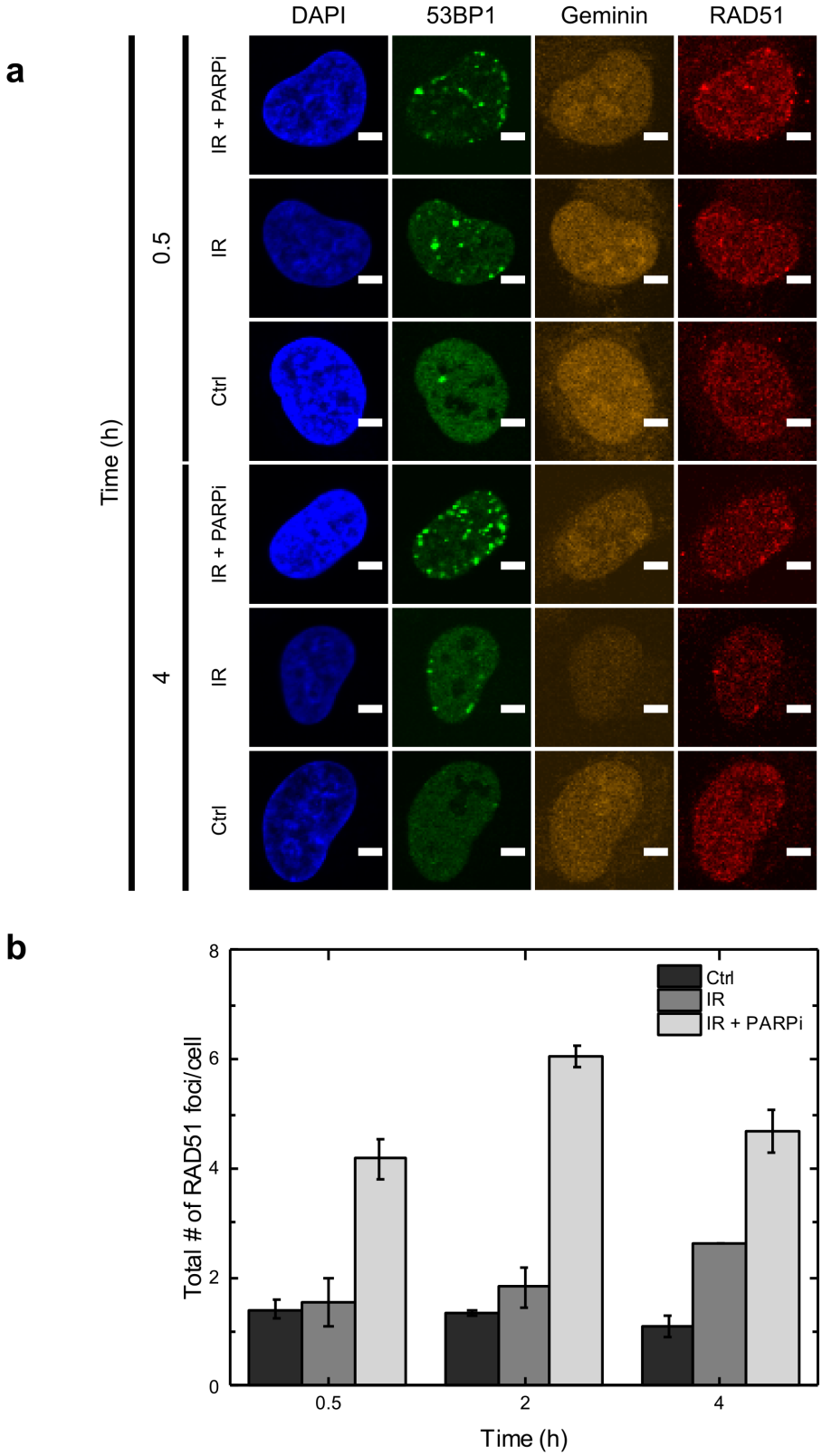


Figure 6.19 PARPi induces RAD51 foci in S/G2 cells following radiation damage. **a)** Micrographs representing RAD51 and 53BP1 foci in response to 0.5 Gy using a ^{137}Cs in the presence and absence of PARPi. Scale bar = 5 μm. **b)** Quantification of the number of RAD51 foci/cell as a function of time. The error bars represent the s.e.m. (n = 3 independent experiments).

The different kinetics observed between G1 and S/G2 populations may reflect the longer times required for appropriate damage resolution by the HR machinery (Shibata *et al.*, 2011).

Furthermore, given that 53BP1 has a specific role in G1 cells of preventing HR repair by impeding BRCA1 association during this cell cycle stage, it would be anticipated a higher number of 53BP1 foci should be observed in G1 cells (Escribano-Diaz *et al.*, 2013). The similar foci numbers observed between G1 and S/G2 cells, and the longer repair times specifically in S/G2 cells, could confer a role for 53BP1 to protect DNA ends in S/G2 cells given the complexity of the damage imposed by IR, which may dramatically challenge the cellular DNA repair machinery.

Additionally, 53BP1 has been reported to be involved in the signalling for repair of DNA DSBs in heterochromatic regions (which are predominantly repaired by HR), promoting chromatin decondensation, being further displaced by BRCA1 prior to HR repair. The prolonged repair times observed in S/G2 cells could in principle reflect the ongoing processing of heterochromatic DSBs (Goodarzi *et al.*, 2008; Kakarougkas *et al.*, 2013; Noon *et al.*, 2010).

The different kinetics observed between the two populations may also reflect the potential impact of the different types of DSBs that can be caused by radiation damage. Aside from promptly-induced DSBs, this type of lesion could also arise due to the conversion of clustered damage into DSBs by BER processing, as detailed by Harper *et al.* (Harper *et al.*, 2010), which are signalled at later times. Damage clusters have also been reported to be less efficiently repaired by BER (Eccles *et al.*, 2011; Georgakilas *et al.*, 2013; Sage and Harrison, 2011), and as a consequence they may encounter a replication fork leading to its collapse to form a replication-induced DSB, which would be signalled at later times following radiation treatment, specifically in S/G2 cells (**figure 6.20**). These lesions have

been reported to require HR repair to be resolved, leading to longer repair times (Saleh-Gohari *et al.*, 2005).

Previously reported data by Gulston *et al.* has shown by PFGE analysis that ~60% of the radiation-induced DSBs have been repaired by 15-30 min after IR, the time at which 53BP1 levels are maximum (Gulston *et al.*, 2004). These findings point to the fact that the majority of the frank radiation-induced DSBs are repaired promptly after damage induction, where the number of 53BP1 molecules recruited to such breaks is potentially not sufficient to allow observation of such lesions by fluorescence microscopy at short times following irradiation. 53BP1 foci could in principle signal complex breaks when compared to the differences in time required to repair simple breaks after irradiation as observed by PFGE (Gulston *et al.*, 2004). Single-foci studies discussed in **chapter 5**, and illustrated in **figures 5.11** and **5.12**, can in principle become an asset to better understand the differences observed between G1 and S/G2 cells in the repair kinetics of radiation-induced lesions, which may be related with the nature of different types of breaks induced.

6.3.2 DNA-PKcs inhibition leads to compromised repair efficiency

Several reports have highlighted a more prominent requirement for DNA-PKcs involvement in the resolution of DSBs of complex nature (Anderson *et al.*, 2010; Reynolds *et al.*, 2012; Riballo *et al.*, 2004). MO59J cells which are defective in DNA-PKcs only seem to display a compromised repair efficiency in the resolution of higher complexity breaks as evidenced by the persistence of breaks at late times post-irradiation with both high- and low-LET radiation (Anderson *et al.*, 2010). These findings suggest a non-essential role for DNA-PKcs in the rejoining of frank radiation-induced simple DSBs, and a requirement for DNA-PKcs in the resolution of complex damage. However, when chemically inhibited using NU7441, DNA-PKcs kinase activity abrogation results in a

compromised repair efficiency as evidenced by the persistence of γ-H2AX foci at late times post irradiation (Zhao *et al.*, 2006), although most of the simple breaks are repaired independent of DNK-PKcs prior to γ-H2AX signalling (Reynolds *et al.*, 2012). This complication is emphasised through the repair of slowly repairing DSB (unrepaired damage) as measured by neutral comet assay being modified by DNA-PKcs inhibition (Ciszewski *et al.*, 2014; Wang and Lees-Miller, 2013; Zhao *et al.*, 2006). Chemical inhibition of DNA-PKcs also leads to a reduction in the surviving fraction to increasing doses of ionising radiation, reflecting an increased radiosensitivity (Ciszewski *et al.*, 2014; Tavecchio *et al.*, 2012; Zhao *et al.*, 2006).

DNA-PKcs kinase activity was inhibited in order to assess the dependency on the classical NHEJ repair pathway to relieve the burden caused by radiation-induced DSBs. The data shown in **figure 6.9b** highlight a delay in the formation of 53BP1 foci when the kinase activity of DNA-PKcs is compromised. Additionally, 53BP1 was seen to persist at sites of damage when compared to cells treated with 0.5 Gy alone, reflecting a reduced repairability (supported by γ-H2AX foci persistence as shown in **figure 6.11**). This inhibition should be considered knowing that the majority of the radiation-induced breaks are repaired prior to the full development of the 53BP1 foci (Gulston *et al.*, 2004) and the lack of DNA-PKcs inhibition on the loss of simple DSB (Reynolds *et al.*, 2012). The observed delay in 53BP1 foci formation in the presence of DNA-PKcsi may highlight a combination of compromised repairability together with new potential breaks being formed through the processing of clustered lesions by the BER machinery at the later times. Replication DSBs contribute to the high levels of 53BP1 foci observed at later times following radiation treatment as discussed in **chapter 5**. To assess the potential contribution of replication-induced DSBs to the high levels of 53BP1 foci, the recruitment and loss of 53BP1 was monitored using Geminin-mCherry associated fluorescence to

identify G1 and S/G2 cells. A clear difference is observed (**figure 6.7b**) between G1 and S/G2 cells in the recruitment and loss of 53BP1 when cells are treated with 0.5 Gy alone, with higher levels of 53BP1 foci present in S/G2 cells up to 4 h after irradiation. The data shown in **figure 6.19b** show an increase in RAD51 foci formation with time after irradiation with 0.5 Gy, consistent with replication-induced DSBs. The data presented in **figure 6.10b**, however, show no clear difference between the G1 and S/G2 populations when DNA-PKcs kinase activity is inhibited, with both populations displaying a delay in the formation of 53BP1 foci, and a persistence of 53BP1 at the damage sites at later times. These data could highlight the formation of replication DSBs at later times post-radiation treatment, contributing to the high, persistent levels of 53BP1 foci observed, and as a consequence overshadow any loss of complex DSB at earlier times. Based on the observations with RAD51, it is predicted only ~3 additional foci through replication events would be seen (**figure 6.19**). Single-foci analysis could therefore become a valuable tool to better characterise the impact of DNA-PKcs inhibition on the formation and resolution of different types of DBSs.

Taken together, these findings suggest a delay in the recruitment of 53BP1 and an impairment of the NHEJ repair pathway, which is also reflected by a prominence of 53BP1 foci at later times, suggesting a compromised repair capacity (Tavecchio *et al.*, 2012; Zhao *et al.*, 2006) (summarised in **figure 6.21**). Several reports suggest this effect is due to DNA-PKcs remaining bound to DSBs as the persistence of DNA-PKcs at DSB sites depends on the phosphorylation/autophosphorylation status of DNA-PKcs, since Uematsu *et al*. (Uematsu *et al.*, 2007) showed that the rate of release of DNA-PKcs from DSBs is also retarded when the autophosphorylation sites are mutated. Phosphorylation of DNA-PKcs induces a conformational change, facilitating the release of DNA-PKcs from DNA ends (Hammel *et al.*, 2010).

6.3.3 ATM kinase activity inhibition impairs 53BP1 recruitment to prompt radiation-induced DSBs

ATM inhibition results in a delay in 53BP1 foci formation in response to radiation damage with a maximum number of foci/cell of ~60% less than that displayed by cells treated with radiation alone (**figure 6.13b**). These data are in agreement with reports describing a decrease in the number of 53BP1 foci following radiation or camptothecin treatment using ATM inhibition and ATM null cells (Harding and Bristow, 2012; Rappold *et al.*, 2001; Sordet *et al.*, 2009). The lack of 53BP1 phosphorylation by ATM in response to radiation damage correlates with the delay in 53BP1 foci formation when ATM kinase activity is compromised (Jowsey *et al.*, 2007; Matsuoka *et al.*, 2007; Ward *et al.*, 2003). The small number of 53BP1 foci depicted in **figure 6.13b** correlates with the low levels of 53BP1 phosphorylation on Ser-1778 in response to radiation damage in combination with ATMi shown in **figure 6.12b**.

HT1080-53BP1-YFP cells containing Geminin-mCherry were used to assess if 53BP1 foci formation in response to radiation-induced damage in combination with ATM inhibition is cell cycle-dependent. ATMi in combination with 0.5 Gy resulted in low levels of 53BP1 foci in G1 cells, contrastingly to S/G2 cells, which displayed increasing levels of 53BP1 foci with time after irradiation (**figure 6.14**). These slow-forming 53BP1 foci specific to S/G2 cells are suggested to be associated with the development of replication DSBs leading to 53BP1 accumulation at damage sites. Replication breaks are generally sensed by RPA leading to the activation of ATR (Ciccia and Elledge, 2010; Marechal and Zou, 2013). Jowsey *et al.* have reported ATR is capable of phosphorylating 53BP1 in response to UV damage, in an ATM-independent manner. 53BP1 phosphorylation by ATR is not abrogated when UV damage is induced in combination with ATMi, confirming ATM-

independent phosphorylation of 53BP1 in response to UV damage (Jowsey *et al.*, 2007). Hickson *et al.* characterised the ATMi KU55399, and reported no effects on ATR activity in response to ATM inhibition (Hickson *et al.*, 2004). ATR has also been shown to promote γ-H2AX accumulation in response to hydroxyurea (HU) treatment independently of ATM activity, which would justify the signalling of these lesions in contrast to DNA DSBs promptly induced, which are preferentially signalled via ATM (Gamper *et al.*, 2013; Marechal and Zou, 2013; Shiotani and Zou, 2009; Stiff *et al.*, 2006; Ward and Chen, 2001; Zou and Elledge, 2003). Taken together, these findings point towards a potential role for ATR in recruiting 53BP1 to damage sites independent of ATM, and specifically in S/G2 cells, consistent with the proposed late developing replication DSBs (**figures 6.20** and **6.23**) as also discussed in **chapter 5**.

A switch from ATM to ATR signalling associated with damage complexity as evidenced by comparing low- and high-LET irradiations has also been reported (Saha *et al.*, 2013). All these facts support a more important role for ATR in the signalling of replicative DSBs (**figure 6.23**).

6.3.4 PARP inhibition leads to damage accumulation in S/G2 cells

PARP inhibition is associated with a persistence of unrepaired clusters and DNA damage which are converted into DSBs due to the collapsing of stalled replication forks (Saleh-Gohari *et al.*, 2005). Several reports have shown the induction of γ-H2AX in response to PARPi alone, highlighting damage accumulation due to abrogation of PARP activity (Bryant *et al.*, 2005; Harper *et al.*, 2010). Using HT1080-53BP1-YFP cells containing Geminin-mCherry to distinguish G1 and S/G2 cells, PARPi was seen to have a substantial effect in the number of 53BP1 foci formed specifically in S/G2 cells. G1 cells presented no 53BP1 foci formation due to PARP inhibition (**figures 6.16** and **6.17**).

When PARPi was used in combination with radiation treatment, G1 cells displayed similar 53BP1 recruitment and loss kinetics to that displayed by G1 cells treated with radiation alone (see **figures 6.7b** and **6.17**). These findings are in agreement with observations reported by Reynolds *et al.* where PARP inhibition did not affect NHEJ-mediated repair (Reynolds *et al.*, 2012). Additionally, S/G2 cells presented a higher number of 53BP1 foci/cell due to the additional damage caused by radiation when compared to S/G2 cells treated with PARPi alone (**figure 6.17**). The disappearance kinetics of 53BP1 foci observed from 2.5 h onwards, were similar to that displayed by S/G2 cells exposed to PARPi alone, with the total numbers differing by 4 foci/cell. Interestingly, the disappearance kinetics of 53BP1 foci is also similar to that displayed by S/G2 cells at later times, which have only been exposed to radiation damage (**figure 6.7b**). The difference in the number of 53BP1 foci between irradiated G1 and S/G2 cells is ~3-4 foci/cell, suggesting a potential induction of DSBs which were originated from collapsed replication forks, and therefore specific to the S/G2 population. These findings correlate with the induction of RAD51 foci in response to 0.5 Gy alone or in combination with PARPi (**figure 6.19**). Cells exposed to PARPi displayed higher levels of RAD51 foci/cell when compared to irradiated and unirradiated controls, suggesting the necessity for HR repair in response to the induction of collapsed replication forks (Saleh-Gohari *et al.*, 2005). The cells exposed to radiation alone, presented increasing levels of RAD51 foci with time after irradiation, suggesting development of damage requiring the HR machinery for complete resolution, consistent with the proposed formation of radiation-induced replication DSBs (**figure 6.19**, findings summarised in **figure 6.21**).

6.3.5 Summary

In summary, all of the presented data suggests the main repair pathway used to solve DSBs is the classical NHEJ repair pathway, as evidenced by persistent 53BP1 and γ-H2AX foci observed in both G1 and S/G2 cells, in response to 0.5 Gy in combination with DNA-PKcsi. Moreover, ATM is one of the main molecules responsible for the signalling of DSBs in response to radiation damage, as shown by the reduction in the number of 53BP1 foci following irradiation in combination with ATM inhibition. The increase in the number of 53BP1 foci in S/G2 cells at later times, is consistent with the observations that radiation induces replicative-induced DSBs (Harper *et al.*, 2010; Saleh-Gohari *et al.*, 2005) in part as a consequence of clustered damage sites encountering replication forks. These replication DSBs are signalled via ATR therefore circumventing ATM inhibition, which is consistent with the increasing levels of RAD51 foci at later times following radiation treatment (**figures 6.19** and **6.23**).

PARP inhibition leads to the persistence of unrepaired clusters plus DNA damage, which are converted into DSBs as cells undergo replication. These lesions are of complex nature and require HR repair pathway to be resolved (Saleh-Gohari *et al.*, 2005). The observed levels of RAD51 foci support the induction of replicative DSBs due to PARP inhibition (**figure 6.19**), in agreement with an increase in the numbers of RAD51 and γ-H2AX when radiation treatment was combined with PARP inhibition (Harper *et al.*, 2010). γ-H2AX is abrogated in response to replication fork stalling induced by hydroxyurea (HU) in ATR-mutated cells but not in response to ATM inhibition or in ATM mutated cells (Stiff *et al.*, 2006). These findings are consistent with the data presented in this chapter addressing the potential induction of replication DSBs arising from collapsed replication forks due to radiation damage (**figures 6.7**, **6.14**, **6.16**, **6.17**, **6.19** and **6.23**).

Preliminary single-foci analysis of HT1080-53BP1-YFP cells containing Geminin-mCherry following irradiation with 0.5 Gy (**figure 6.22**) point towards late developing foci in both G1 and S/G2 cells although those in S/G2 cells may persist longer, although more experiments are necessary for definitive proof. It is hypothesized these foci could represent replication-induced DSBs originated from clustered damage encountering a replication fork (red and orange circles in **figure 6.22**, orange circles and purple triangles in **figure 5.12**) in S/G2 cells. Foci appearing at later times in G1 cells could represent clusters processed by BER enzymes into DSB at earlier times (Harper *et al.*, 2010) which are more readily resolved than replication-induced DSBs (blue circle in **figure 6.22**, pink triangles and blue squares in **figure 5.12**). Single-foci analysis in large numbers of living cells in a cell cycle-specific fashion could provide further evidence regarding the nature of the various DSBs signalled by 53BP1 accumulation.

Collectively, these data could provide supporting evidence for the potential induction of replicative DSBs following radiation treatment, and a switch from ATM to ATR in the signalling for repair via HR of such deleterious lesions (**figure 6.23**).

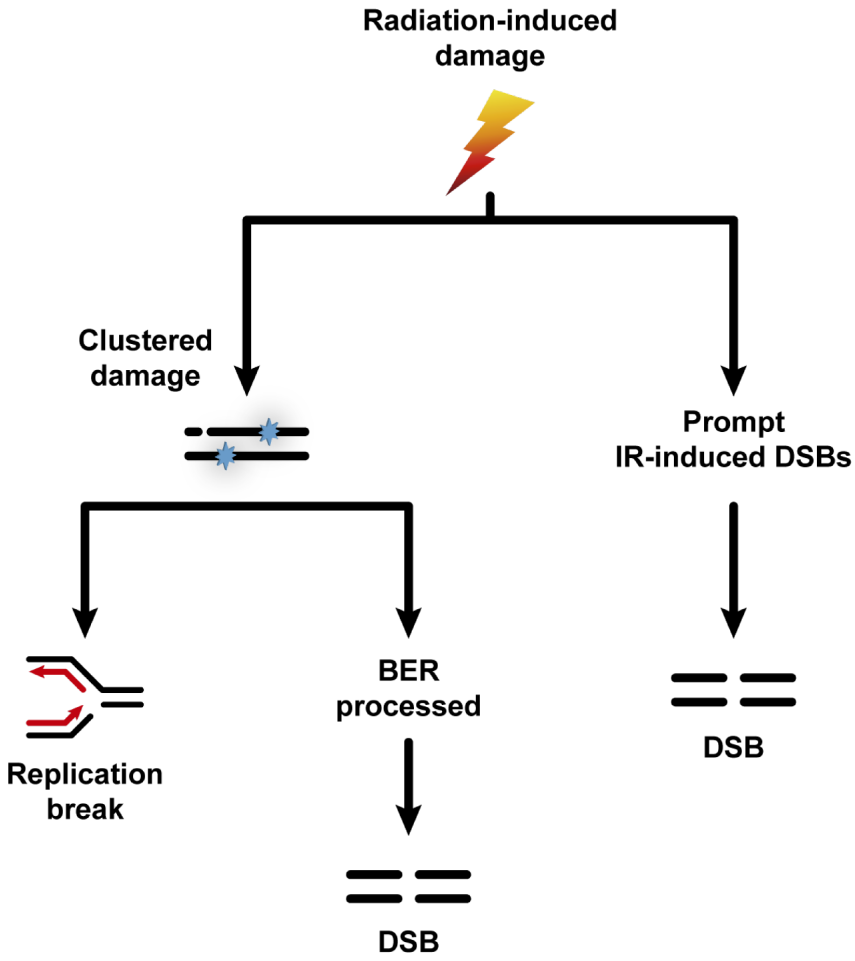


Figure 6.20 Different classes of DSBs caused by radiation-induced DNA damage. Diagram representing the variety of DSBs caused by radiation, which can be promptly induced, or arise due to the processing of clusters by BER enzymes. Replication-induced DBSs originate if unrepaired clusters encounter a replication fork.

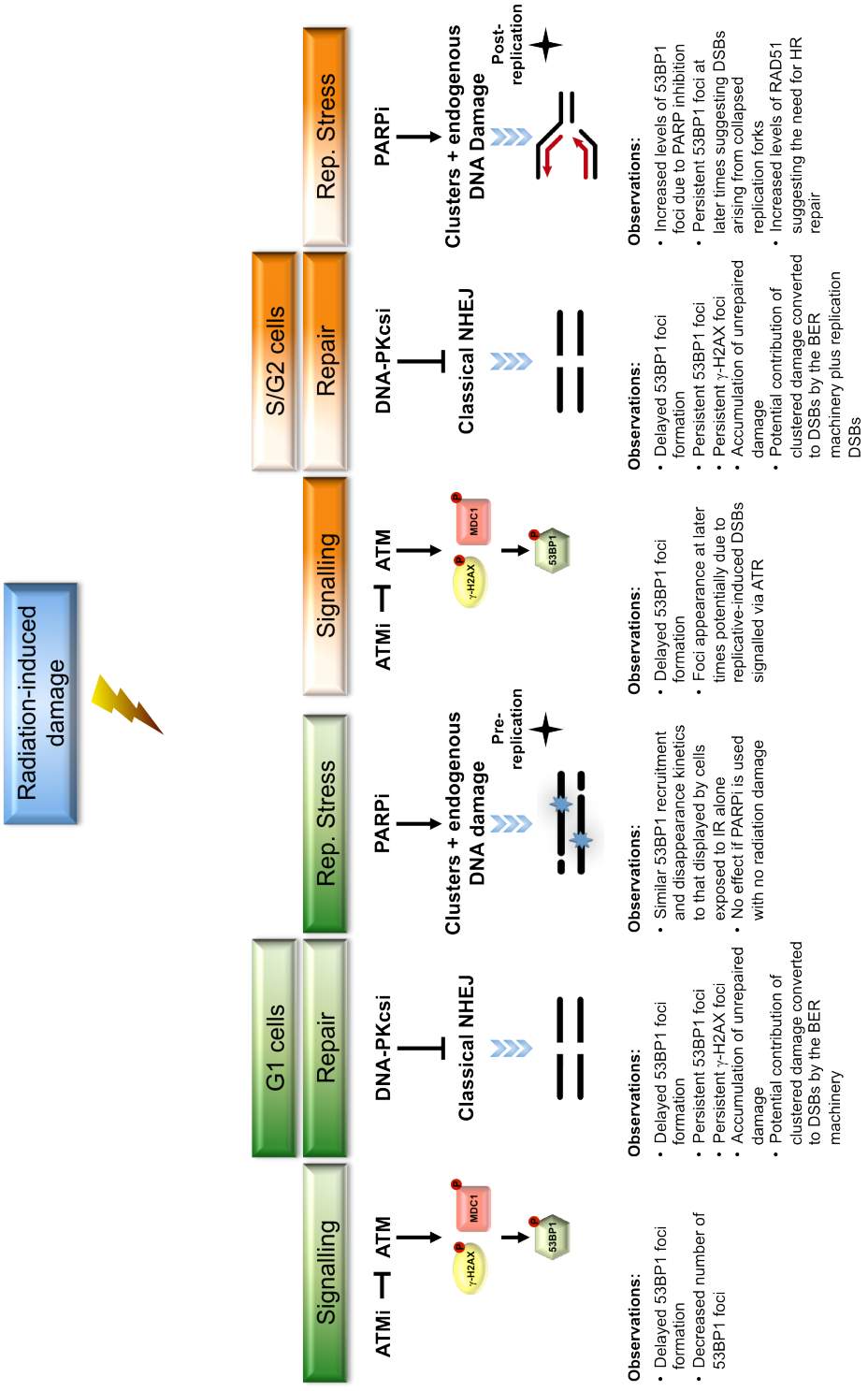

Radiation-induced damage
G1 cells
S/G2 cells
Signalling
Repair
Rep. Stress
ATMi ⊣ ATM
DNA-PKcsi ⊥
PARPi →
γ-H2AX
MDC1
53BP1
Classical NHEJ
Clusters + endogenous DNA damage
Pre-replication
Post-replication
Observations:
• Delayed 53BP1 foci formation
• Decreased number of 53BP1 foci
Observations:
• Delayed 53BP1 foci formation
• Persistent 53BP1 foci
• Persistent γ-H2AX foci
• Accumulation of unrepaired damage
• Potential contribution of clustered damage converted to DSBs by the BER machinery
Observations:
• Similar 53BP1 recruitment and disappearance kinetics to that displayed by cells exposed to IR alone
• No effect if PARPi is used with no radiation damage
Observations:
• Delayed 53BP1 foci formation
• Foci appearance at later times potentially due to replicative-induced DSBs signalled via ATR
Observations:
• Delayed 53BP1 foci formation
• Persistent 53BP1 foci
• Persistent γ-H2AX foci
• Accumulation of unrepaired damage
• Potential contribution of clustered damage converted to DSBs by the BER machinery plus replication DSBs
Observations:
• Increased levels of 53BP1 foci due to PARP inhibition
• Persistent 53BP1 foci at later times suggesting DSBs arising from collapsed replication forks
• Increased levels of RAD51 suggesting the need for HR repair

Figure 6.21 DNA damage response in G1 and S/G2 cells following radiation treatment in combination with ATMi, DNA-PKcsi, and PARPi. Diagram representing the cascade of events, which potentially lead to the observations, noted in G1 and S/G2 cells, in response to radiation treatment in combination with the various used inhibitors.

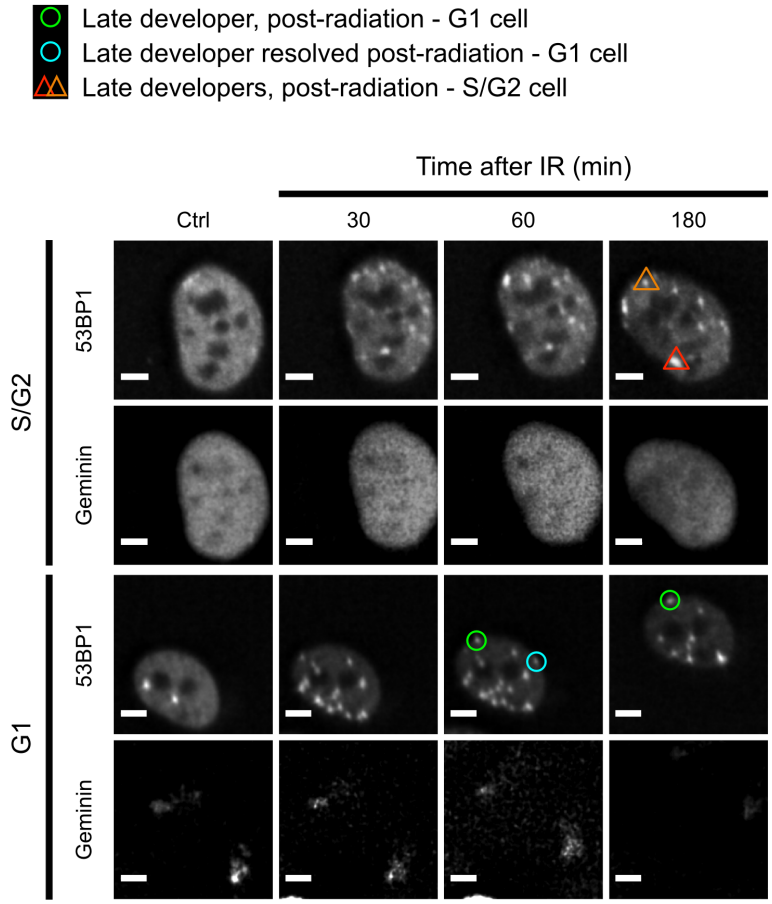


Figure 6.22 53BP1 single-foci mapping following irradiation: effects of cell cycle. Micrographs per time point representing HT1080-53BP1-YFP cells containing Geminin-mCherry, irradiated with 0.5 Gy using the linac experiment system. Late appearing foci are highlighted in both G1 and S/G2 cells. The red and orange triangles represent late developing foci in a Geminin-mCherry positive cell. The green and blue circles represent late developing foci in a G1 cell (Geminin-mCherry negative). Scale bar = 5 μm.

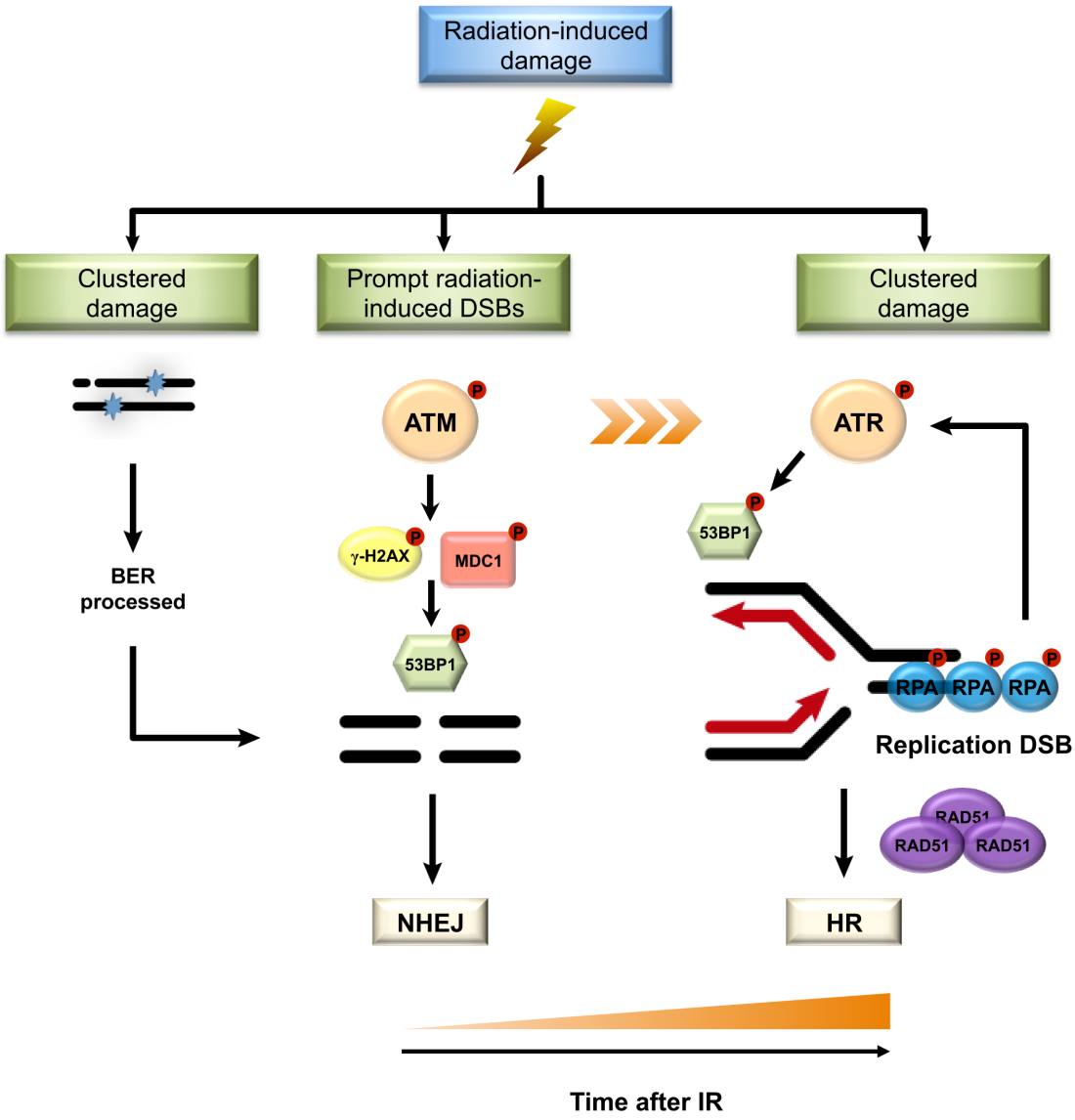


Figure 6.23 Proposed model for the signalling and repair of different types of DSBs that can arise with radiation damage. Processing of clusters by BER enzymes can lead to the formation of DSBs that can be repaired via NHEJ or possibly HR. Prompt DSBs are mainly signalled via ATM leading to a cascade of events, which lead to the recruitment of 53BP1 to DSBs. These breaks can be repaired via NHEJ or possibly HR. At later times following radiation treatment, clusters may cause collapsed replication forks, which are sensed by RPA leading to activation of ATR and subsequent recruitment of 53BP1. These breaks require HR repair to be resolved.

7. General discussion

The work presented in this thesis describes a novel system capable of delivering well-defined doses of low-LET radiation (electrons) in a short time (sub-μs) to mammalian cells, maintained within a physiological environment, and exploiting a co-located microscopy imaging system for time-lapse imaging before and after damage induction (**chapter 2**). The described experimental setup overcomes many of the problems with laser microbeams (Kong *et al.*, 2009; Reynolds *et al.*, 2013) in generating quantifiable levels of damage based on accurate dosimetry. The capacity to irradiate cells within a controlled environment allows biological processes to take place with minimal disturbance in comparison to immuno-staining techniques, generally used where each time point is a separate cell population and tend to be irradiated at lower temperatures, generally around 4°C (Markova *et al.*, 2007; Rappold *et al.*, 2001; Wang *et al.*, 2002).

Real-time dynamic studies of biochemical events in cells is additionally enhanced by allowing up to nine samples to be investigated in parallel over time with plans to extend to a 96-well plate system for medium throughput studies using various microarray libraries. This advance emphasizes the flexibility of the system to explore other biological processes using shRNA technology or to study the effects of small molecule inhibitors on cell pathways, which are perturbed by IR.

As highlighted in **chapter 3**, the capacity to predict and manipulate the dose distribution across the sample opens up opportunities to explore processes and their associated radiation dose dependence within the same population of cells. For instance, by using highly collimated beams, it is possible to concentrate the dose delivery in a specific area of

the sample, and have access to non-irradiated areas within the same sample, which can be used as control (**figures 3.7** and **3.8**).

7.1 Single-foci studies as a qualitative measure of DNA DSBs

This novel experimental setup has allowed for the first time observations of the appearance and disappearance of radiation-induced foci (**figures 5.10** and **5.11**) in the same cell population at very early times prior to and following irradiation with sparsely ionising radiation, in HT1080 cells which constitutively express YFP-labelled 53BP1 as a damage biomarker. The advantage of using the described linac experimental approach is that individual foci may be followed in time, in individual cells to give detailed information on prompt and delayed formation of foci post-irradiation. This approach contrasts with the general assessment of the average number of foci/cell at different time points following damage induction, where it is not possible to comment on late appearing foci which may or not be present at the time of irradiation. As depicted in **figures 5.11** and **5.12**, single-foci studies can provide qualitative information about each focus regarding the different nature of breaks, which can arise in response to radiation damage. The data presented in **figure 5.12** highlight damage formation at later times, where these later forming foci could in principle reflect the conversion of radiation-induced clustered damage into replication DSBs. Some of the highlighted foci may also reflect the conversion of clustered damage sites into DSBs by BER processing, as previously reported by Harper *et al.* (Gulston *et al.*, 2004; Harper *et al.*, 2010) (**figure 6.20**). These data are unique in providing the first overview of the dynamics of foci formation from promptly formed and late appearing DNA damage, signalled by 53BP1. Such results impact on the general understanding of DSB repair kinetics and question the generalised interpretations of repair kinetics as

measured by 53BP1 recruitment and phosphorylation of histone H2AX (γ-H2AX), generally detected by immuno-staining.

To characterise better the nature of late developing foci, single-foci studies could be carried out in large numbers of cells potentially using a different cell line overcoming the difficulties posed by the invasive and motile phenotypes characteristic of HT1080 cells (Niggli *et al.*, 2009). A more homogenous distribution of 53BP1-associated fluorescence amongst the cell population would facilitate automated forms of analysis contributing to larger scale single-foci studies.

Collectively, the data presented in **chapters 2, 3** and **5** were used to develop a draft manuscript to be submitted (CD Martins *et al.*) in which this novel system is described.

7.2 Radiation-induced ATM to ATR switch?

Studies were made to show the flexibility of the irradiation and imaging system developed by observation of late developing foci in response to radiation damage by using HT1080-53BP1-YFP cells containing Geminin-mCherry, the latter used as a cell cycle phase indicator, (**figures 6.1**, **6.4** and **6.5**) and in the presence or absence of small molecule inhibitors of proteins involved in the major DNA damage repair pathways. Using this biological system, DNA-PKcs inhibition in combination was shown to lead to 53BP1 and accumulation at radiation-induced DNA damage sites independent of the cell cycle phase, reflecting that the repair capacity is compromised (**figures 6.9-6.11**). These observations were also verified through observation of γ-H2AX foci in immuno-stained cells. A persistence of higher levels of 53BP1 foci was noted specifically in S/G2 cells up to 4 h following pulsed irradiation (**figures 6.7** and **6.11**). Additionally, ATM inhibition led to a reduction in the number of 53BP1 foci following pulsed irradiation, identifying ATM as one of the main molecules responsible for the signalling of radiation-induced DSBs.

Interestingly, the number of 53BP1 foci increases at later times specifically in S/G2 cells, indicative that radiation damage is converted into replication-induced DSBs. Replication-induced DSBs, which are signalled via ATR, therefore circumvent ATM inhibition (Ciccia and Elledge, 2010; Marechal and Zou, 2013), consistent with the increased levels of RAD51 foci seen at later times following pulsed irradiation (**figures 6.19**).

PARP inhibition leads to the persistence of endogenous DNA damage, which is converted into replication-induced DSB as cells undergo replication in the absence of radiation (**figure 6.20**). The replicative DSBs are of complex nature and require HR repair pathway to be resolved (Saleh-Gohari *et al.*, 2005) and their formation reflects the role of PARP inhibition in synthetic lethality (Bryant *et al.*, 2005). The increase in the levels of 53BP1 foci in response to PARP inhibition specifically in S/G2 cells, confirm 53BP1 signalling of replication-induced DSBs (**figures 6.16** and **6.17**). Interestingly, the difference in the levels of 53BP1 foci in S/G2 cells treated with PARPi ± pulse irradiation with 0.5 Gy are consistent with the difference observed between irradiated G1 and S/G2 cells, potentially reflecting an additive effect of replication-induced DSBs caused by radiation damage at later times. The later development of such breaks is consistent with the late formation of RAD51 foci seen 4 h after pulsed irradiation (**figure 6.19**).

The levels of breaks, as determined from the number of 53BP1 foci are observed up to 3 h following pulsed irradiation, and are also higher when compared to the levels of DSB detected at these later times reported by Gulston *et al.* using PFGE (**figure 5.13**) (Gulston *et al.*, 2004). This difference at later times is proposed to reflect the lack of detection of replication-induced DSBs by PFGE, whereas 53BP1 is known to signal this type of break.

7.3 Future work

Based on the data discussed in **chapters 5** and **6**, evidence was presented suggesting that a fraction of 53BP1 foci are signalled in response to DNA damage at late times following irradiation, supporting the proposed development of replication-induced DSBs and/or DSB through processing of clustered damage at later times. This proposal is further supported by the persistence of higher levels of 53BP1 foci specifically in S/G2 cells in response to radiation treatment alone and in combination with ATM inhibition. As ATR is known to signal replication breaks (Marechal and Zou, 2013), further evidence for replication-induced DSBs following irradiation could be provided by addressing whether the formation of late developing radiation-induced 53BP1 foci in S/G2 cells are present if ATR is inhibited. It is known that the ATM inhibitor at the concentration used would not act as an ATR inhibitor. It is hypothesized that the levels of 53BP1 foci in S/G2 cells should decrease at a similar rate to that displayed by G1 cells if late developed replication-induced breaks are not signalled due to ATR inhibition. By inhibiting ATR kinase activity concomitantly with ATM inhibition, the levels of 53BP1 foci in S/G2 cells should become similar to background levels, abrogating the signalling of both prompt and late developing foci.

Based on the dynamics for formation of RAD51 in the presence of the ATM inhibitor, phosphorylation of RPA at Ser-4/8 residues, an earlier event than the recruitment of RAD51 in HR, should also be monitored to provide further evidence of the existence of ssDNA regions signalling replicative stress (Liu *et al.*, 2012). Additionally, the DNA fibre staining technique (Pires *et al.*, 2010) could be used to monitor the levels of nascent DNA in response to radiation treatment in combination with various inhibitors, providing further evidence for the induction of stalled forks in response to the inhibitor studies described.

The ‘proof-of-principle’ observation of late developing foci by single-foci analysis within individual cells throughout different phases of the cell cycle, should be extended to an evaluation of a large number of living cells to obtain statistically meaningful data, and provide further evidence on the nature of the various types of damage that signal through 53BP1 accumulation at times later than those for the promptly formed IR DSBs.

Collectively, these additional experiments could address whether the induction of replicative DSBs in response to ionising radiation, promotes a switch from ATM to ATR in the signalling for repair of such lesions.

For a general perspective, these preliminary findings using DNA damage repair provide a novel approach to evaluate the types of damage that signal through 53BP1 at later times in the presence and absence of DNA repair inhibitors, an approach that is not presently available using conventional immuno-staining techniques. The knowledge obtained may be used to identify potential biological targets coupled with drug discovery for translation into adjuncts for radiotherapy.

References

Almeida, K.H., and Sobol, R.W. (2007). A unified view of base excision repair: Lesion-dependent protein complexes regulated by post-translational modification. DNA Repair *6*, 695-711.

Anderson, C.W., and Carter, T.H. (1996). The DNA-activated protein kinase - DNA-PK. Molecular Analysis of DNA Rearrangements in the Immune System *217*, 91-111.

Anderson, J.A., Harper, J.V., Cucinotta, F.A., and O'Neill, P. (2010). Participation of DNA-PKcs in DSB Repair after Exposure to High- and Low-LET Radiation. Radiation Research *174*, 195-205.

Arcaroli, J.J., Touban, B.M., Tan, A.C., Varella-Garcia, M., Powell, R.W., Eckhardt, S.G., Elvin, P., Gao, D., and Messersmith, W.A. (2010). Gene array and fluorescence in situ hybridization biomarkers of activity of saracatinib (AZD0530), a Src inhibitor, in a preclinical model of colorectal cancer. Clinical Cancer Research *16*, 4165-4177.

Asaithamby, A., and Chen, D.J. (2009). Cellular responses to DNA double-strand breaks after low-dose gamma-irradiation. Nucleic Acids Research *37*, 3912-3923.

Asaithamby, A., Hu, B.R., and Chen, D.J. (2011). Unrepaired clustered DNA lesions induce chromosome breakage in human cells. Proceedings of the National Academy of Sciences of the United States of America *108*, 8293-8298.

Asaithamby, A., Uematsu, N., Chatterjee, A., Story, M.D., Burma, S., and Chen, D.J. (2008). Repair of HZE-Particle-induced DNA double-strand breaks in normal human fibroblasts. Radiation Research *169*, 437-446.

Auckley, D.H., Crowell, R.E., Heaphy, E.R., Stidley, C.A., Lechner, J.F., Gilliland, F.D., and Belinsky, S.A. (2001). Reduced DNA-dependent protein kinase activity is associated with lung cancer. Carcinogenesis *22*, 723-727.

Badie, S., Liao, C.Y., Thanasoula, M., Barber, P., Hill, M.A., and Tarsounas, M. (2009). RAD51C facilitates checkpoint signaling by promoting CHK2 phosphorylation. Journal of Cell Biology *185*, 587-600.

Bakkenist, C.J., and Kastan, M.B. (2003). DNA damage activates ATM through intermolecular autophosphorylation and dimer dissociation. Nature *421*, 499-506.

Barber, P.R., Locke, R.J., Pierce, G.P., Rothkamm, K., and Vojnovic, B. (2007). Gamma-H2AX Foci Counting: Image processing and control software for high-content screening - art. no. 64411M. Imaging, Manipulation, and Analysis of Biomolecules, Cells, and Tissues V *6441*, M4411-M4411.

Barber, P.R., Tullis, I.D., Pierce, G.P., Newman, R.G., Prentice, J., Rowley, M.I., Matthews, D.R., Ameer-Beg, S.M., and Vojnovic, B. (2013). The Gray Institute 'open' high-content, fluorescence lifetime microscopes. Journal of Microscopy *251*, 154-167.

Bartek, J., Lukas, J., and Bartkova, J. (2007). DNA damage response as an anti-cancer barrier - Damage threshold and the concept of 'conditional haploinsufficiency'. Cell Cycle *6*, 2344-2347.

Bartkova, J., Horejsi, Z., Koed, K., Kramer, A., Tort, F., Zieger, K., Guldberg, P., Sehested, M., Nesland, J.M., Lukas, C., Orntoft, T., Lukas, J., and Bartek, J. (2005). DNA damage response as a candidate anti-cancer barrier in early human tumorigenesis. Nature *434*, 864-870.

Batchelor, E., Loewer, A., and Lahav, G. (2009). The ups and downs of p53: understanding protein dynamics in single cells. Nature Reviews Cancer *9*, 371-377.

Battistoni, G., Cerutti, F., Fasso, A., Ferrari, A., Muraro, S., Ranft, J., Roesler, S., and Sala, P. (2007). The FLUKA code: Description and benchmarking. Paper presented at: AIP Conference Proceedings.

Begg, A.C., McNally, N.J., Shrieve, D.C., and Karcher, H. (1985). A method to measure the duration of DNA synthesis and the potential doubling time from a single sample. Cytometry *6*, 620-626.

Bekker-Jensen, S., Lukas, C., Kitagawa, R., Melander, F., Kastan, M.B., Bartek, J., and Lukas, J. (2006). Spatial organization of the mammalian genome surveillance machinery in response to DNA strand breaks. Journal of Cell Biology *173*, 195-206.

Bennett, P.V., Cintron, N.S., Gros, L., Laval, J., and Sutherland, B.M. (2004). Are endogenous clustered DNA damages induced in human cells? Free Radical Biology and Medicine *37*, 488-499.

Bennett, P.V., Cuomo, N.L., Paul, S., Tafrov, S.T., and Sutherland, B.M. (2005). Endogenous DNA damage clusters in human skin, 3-D model, and cultured skin cells. Free Radical Biology and Medicine *39*, 832-839.

Bétermier, M., Bertrand, P., and Lopez, B.S. (2014). Is non-homologous end-joining really an inherently error-prone process? PLoS Genetics *10*, e1004086.

Biggs, D. (2004). Clearing up deconvolution. Biophotonics International *11*, 32-37.

Bisby, R.H., Botchway, S.W., Dad, S., and Parker, A.W. (2006). Single- and multi-photon excited fluorescence from serotonin complexed with beta-cyclodextrin. Photochemical & Photobiological Sciences *5*, 122-125.

Blaikley, E.J., Tinline-Purvis, H., Kasparek, T.R., Marguerat, S., Sarkar, S., Hulme, L., Hussey, S., Wee, B.-Y., Deegan, R.S., and Walker, C.A. (2014). The DNA damage checkpoint pathway promotes extensive resection and nucleotide synthesis to facilitate homologous recombination repair and genome stability in fission yeast. Nucleic Acids Research, gku190.

Blier, P.R., Griffith, A.J., Craft, J., and Hardin, J.A. (1993). Binding of Ku Protein to DNA - Measurement of Affinity for Ends and Demonstration of Binding to Nicks. Journal of Biological Chemistry *268*, 7594-7601.

Block, W.D., Yu, Y.P., Merkle, D., Gifford, J.L., Ding, Q., Meek, K., and Lees-Miller, S.P. (2004). Autophosphorylation-dependent remodeling of the DNA-dependent protein kinase catalytic subunit regulates ligation of DNA ends. Nucleic Acids Research *32*, 4351-4357.

Bolderson, E., Tomimatsu, N., Richard, D.J., Boucher, D., Kumar, R., Pandita, T.K., Burma, S., and Khanna, K.K. (2010). Phosphorylation of Exo1 modulates homologous recombination repair of DNA double-strand breaks. Nucleic Acids Research *38*, 1821-1831.

Bonner, W.M., Redon, C.E., Dickey, J.S., Nakamura, A.J., Sedelnikova, O.A., Solier, S., and Pommier, Y. (2008). Opinion Gamma H2ax and Cancer. Nature Reviews Cancer *8*, 957-967.

Born, M., and Wolf, E. (1999). Principles of Optics (Cambridge, U.K.: Cambridge Univ. Press).

Botchway, S.W., Crisostomo, A.G., Parker, A.W., and Bisby, R.H. (2007). Near infrared multiphoton-induced generation and detection of hydroxyl radicals in a biochemical system. Archives of Biochemistry and Biophysics *464*, 314-321.

Botchway, S.W., Reynolds, P., Parker, A.W., and O'Neill, P. (2010). Use of near infrared femtosecond lasers as sub-micron radiation microbeam for cell DNA damage and repair studies. Mutation Research-Reviews in Mutation Research *704*, 38-44.

Botchway, S.W., Stevens, D.L., Hill, M.A., Jenner, T.J., and ONeill, P. (1997). Induction and rejoining of DNA double-strand breaks in Chinese hamster V79-4 cells irradiated with characteristic aluminum K and copper L ultrasoft X rays. Radiation Research *148*, 317-324.

Bouwman, P., Aly, A., Escandell, J.M., Pieterse, M., Bartkova, J., van der Gulden, H., Hiddingh, S., Thanasoula, M., Kulkarni, A., Yang, Q.F., Haffty, B.G., Tommiska, J., Blomqvist, C., Drapkin, R., Adams, D.J., Nevanlinna, H., Bartek, J., Tarsounas, M., Ganesan, S., and Jonkers, J. (2010). 53BP1 loss rescues BRCA1 deficiency and is associated with triple-negative and BRCA-mutated breast cancers. Nature Structural & Molecular Biology *17*, 688-U656.

Brown, E.J., and Baltimore, D. (2000). ATR disruption leads to chromosomal fragmentation and early embryonic lethality. Genes & Development *14*, 397-402.

Bryant, H.E., Schultz, N., Thomas, H.D., Parker, K.M., Flower, D., Lopez, E., Kyle, S., Meuth, M., Curtin, N.J., and Helleday, T. (2005). Specific killing of BRCA2-deficient tumours with inhibitors of poly(ADP-ribose) polymerase. Nature *434*, 913-917.

Buck, S.B., Bradford, J., Gee, K.R., Agnew, B.J., Clarke, S.T., and Salic, A. (2008). Detection of S-phase cell cycle progression using 5-ethynyl-2'-deoxyuridine incorporation

with click chemistry, an alternative to using 5-bromo-2'-deoxyuridine antibodies. Biotechniques *44*, 927-929.

Bunting, S.F., Callen, E., Wong, N., Chen, H.T., Polato, F., Gunn, A., Bothmer, A., Feldhahn, N., Fernandez-Capetillo, O., Cao, L., Xu, X.L., Deng, C.X., Finkel, T., Nussenzweig, M., Stark, J.M., and Nussenzweig, A. (2010). 53BP1 Inhibits Homologous Recombination in Brca1-Deficient Cells by Blocking Resection of DNA Breaks. Cell *141*, 243-254.

Burkhart, D.L., and Sage, J. (2008). Cellular mechanisms of tumour suppression by the retinoblastoma gene. Nature Reviews Cancer *8*, 671-682.

Burma, S., Chen, B.P.C., and Chen, D.J. (2006). Role of non-homologous end joining (NHEJ) in maintaining genomic integrity. DNA Repair *5*, 1042-1048.

Butterworth, K.T., McMahon, S.J., Currell, F.J., and Prise, K.M. (2012). Physical basis and biological mechanisms of gold nanoparticle radiosensitization. Nanoscale *4*, 4830-4838.

Byun, T.S., Pacek, M., Yee, M.C., Walter, J.C., and Cimprich, K.A. (2005). Functional uncoupling of MCM helicase and DNA polymerase activities activates the ATR-dependent checkpoint. Genes & Development *19*, 1040-1052.

Cadet, J., Douki, T., and Ravanat, J.L. (2008). Oxidatively generated damage to the guanine moiety of DNA: Mechanistic aspects and formation in cells. Accounts of Chemical Research *41*, 1075-1083.

Cadet, J., Ravanat, J.L., TavernaPorro, M., Menoni, H., and Angelov, D. (2012). Oxidatively generated complex DNA damage: Tandem and clustered lesions. Cancer Letters *327*, 5-15.

Caldecott, K.W. (2008). Single-strand break repair and genetic disease. Nature Reviews Genetics *9*, 619-631.

Cao, L., Xu, X.L., Bunting, S.F., Liu, J., Wang, R.H., Cao, L.Y.L., Wu, J.J., Peng, T.N., Chen, J.J., Nussenzweig, A., Deng, C.X., and Finkel, T. (2009). A Selective Requirement for 53BP1 in the Biological Response to Genomic Instability Induced by Brca1 Deficiency. Molecular Cell *35*, 534-541.

Casper, A.M., Nghiem, P., Arlt, M.F., and Glover, T.W. (2002). ATR regulates fragile site stability. Cell *111*, 779-789.

Cerenkov, P.A. (1937). Visible Radiation Produced by Electrons Moving in a Medium with Velocities Exceeding that of Light. Physical Review *52*, 378-379.

Chailleux, C., Tyteca, S., Papin, C., Boudsocq, F., Puget, N., Courilleau, C., Grigoriev, M., Canitrot, Y., and Trouche, D. (2010). Physical interaction between the histone acetyl transferase Tip60 and the DNA double-strand breaks sensor MRN complex. Biochemical Journal *426*, 365-371.

Chan, D.W., Chen, B.P.C., Prithivirajsingh, S., Kurimasa, A., Story, M.D., Qin, J., and Chen, D.J. (2002). Autophosphorylation of the DNA-dependent protein kinase catalytic subunit is required for rejoining of DNA double-strand breaks. Genes & Development *16*, 2333-2338.

Chapman, J.R., Barral, P., Vannier, J.B., Borel, V., Steger, M., Tomas-Loba, A., Sartori, A.A., Adams, I.R., Batista, F.D., and Boulton, S.J. (2013). RIF1 Is Essential for 53BP1-Dependent Nonhomologous End Joining and Suppression of DNA Double-Strand Break Resection. Molecular Cell *49*, 858-871.

Chapman, J.R., Sossick, A.J., Boulton, S.J., and Jackson, S.P. (2012). BRCA1-associated exclusion of 53BP1 from DNA damage sites underlies temporal control of DNA repair. Journal of Cell Science *125*, 3529-3534.

Chen, B.P.C., Chan, D.W., Kobayashi, J., Burma, S., Asaithamby, A., Morotomi-Yano, K., Botvinick, E., Qin, J., and Chen, D.J. (2005). Cell cycle dependence of DNA-dependent protein kinase phosphorylation in response to DNA double strand breaks. Journal of Biological Chemistry *280*, 14709-14715.

Chen, B.P.C., Uematsu, N., Kobayashi, J., Lerenthal, Y., Krempler, A., Yajima, H., Lobrich, M., Shiloh, Y., and Chen, D.J. (2007). Ataxia telangiectasia mutated (ATM) is essential for DNA-PKcs phosphorylations at the Thr-2609 cluster upon DNA double strand break. Journal of Biological Chemistry *282*, 6582-6587.

Chen, L.C., Nievera, C.J., Lee, A.Y.L., and Wu, X.H. (2008). Cell cycle-dependent complex formation of BRCA1.CtIP.MRN is important for DNA double-strand break repair. Journal of Biological Chemistry *283*, 7713-7720.

Chinnaiyan, P., Huang, S.M., Vallabhaneni, G., Armstrong, E., Varambally, S., Tomlins, S.A., Chinnaiyan, A.M., and Harari, P.M. (2005). Mechanisms of enhanced radiation response following epidermal growth factor receptor signaling inhibition by Erlotinib (Tarceva). Cancer Research *65*, 3328-3335.

Ciccia, A., and Elledge, S.J. (2010). The DNA damage response: making it safe to play with knives. Molecular Cell *40*, 179-204.

Cimprich, K.A., and Cortez, D. (2008). ATR: an essential regulator of genome integrity. Nature Reviews Molecular Cell Biology *9*, 616-627.

Ciszewski, W.M., Tavecchio, M., Dastych, J., and Curtin, N.J. (2014). DNA-PK inhibition by NU7441 sensitizes breast cancer cells to ionizing radiation and doxorubicin. Breast Cancer Research and Treatment *143*, 47-55.

Connell, T., Alexander, A., Evans, M., and Seuntjens, J. (2012). An experimental feasibility study on the use of scattering foil free beams for modulated electron radiotherapy. Physics in Medicine and Biology *57*, 3259.

Cortez, D., Guntuku, S., Qin, J., and Elledge, S.J. (2001). ATR and ATRIP: Partners in checkpoint signaling. Science *294*, 1713-1716.

Costes, S.V., Boissiere, A., Ravani, S., Romano, R., Parvin, B., and Barcellos-Hoff, M.H. (2006). Imaging features that discriminate between foci induced by high- and low-LET radiation in human fibroblasts. Radiation Research *165*, 505-515.

Costes, S.V., Chiolo, I., Pluth, J.M., Barcellos-Hoff, M.H., and Jakob, B. (2010). Spatiotemporal characterization of ionizing radiation induced DNA damage foci and their relation to chromatin organization. Mutation Research *704*, 78-87.

Cui, X.P., Yu, Y.P., Gupta, S., Cho, Y.M., Lees-Miller, S.P., and Meek, K. (2005). Autophosphorylation of DNA-dependent protein kinase regulates DNA end processing and may also alter double-strand break repair pathway choice. Molecular and Cellular Biology *25*, 10842-10852.

Curtin, N.J., and Szabo, C. (2013). Therapeutic applications of PARP inhibitors: Anticancer therapy and beyond. Molecular Aspects of Medicine *34*, 1217-1256.

Cygler, J., Li, X.A., Ding, G.X., and Lawrence, E. (1997). Practical approach to electron beam dosimetry at extended SSD. Physics in medicine & biology *42*, 1505-1514.

Datta, K., Jaruga, P., Dizdaroglu, M., Neumann, R.D., and Winters, T.A. (2006). Molecular analysis of base damage clustering associated with a site-specific radiation-induced DNA double-strand break. Radiation Research *166*, 767-781.

Datta, K., Neumann, R.D., and Winters, T.A. (2005a). Characterization of a complex 125I-induced DNA double-strand break: Implications for repair 1. International Journal of Radiation Biology *81*, 13-21.

Datta, K., Neumann, R.D., and Winters, T.A. (2005b). Characterization of complex apurinic/apyrimidinic-site clustering associated with an authentic site-specific radiation-induced DNA double-strand break. Proceedings of the National Academy of Sciences of the United States of America *102*, 10569-10574.

Datta, K., Weinfeld, M., Neumann, R.D., and Winters, T.A. (2007). Determination and analysis of site-specific 125I decay-induced DNA double-strand break end-group structures. Radiation Research *167*, 152-166.

Davis, A.J., and Chen, D.J. (2013). DNA double strand break repair via non-homologous end-joining. Translational Cancer Research *2*, 130-143.

Davis, A.J., Lee, K.J., and Chen, D.J. (2013). The N-terminal region of the DNA-dependent protein kinase catalytic subunit is required for its DNA double-stranded break-mediated activation (vol 288, pg 7037, 2013). Journal of Biological Chemistry *288*, 18776-18776.

de Angelis, A., Kolb, J.F., Zeni, L., and Schoenbach, K.H. (2008). Kilovolt Blumlein pulse generator with variable pulse duration and polarity. Review of Scientific Instruments *79*.

de Lara, C.M., Hill, M.A., Jenner, T.J., Papworth, D., and O'Neill, P. (2001). Dependence of the yield of DNA double-strand breaks in Chinese hamster V79-4 cells on the photon energy of ultrasoft X rays. Radiation Research *155*, 440-448.

de Murcia, J.M., Niedergang, C., Trucco, C., Ricoul, M., Dutrillaux, B., Mark, M., Oliver, F.J., Masson, M., Dierich, A., LeMeur, M., Walztinger, C., Chambon, P., and deMurcia, G. (1997). Requirement of poly(ADP-ribose) polymerase in recovery from DNA damage in mice and in cells. Proceedings of the National Academy of Sciences of the United States of America *94*, 7303-7307.

Deckbar, D., Stiff, T., Koch, B., Reis, C., Lobrich, M., and Jeggo, P.A. (2010). The limitations of the G1-S checkpoint. Cancer Research *70*, 4412-4421.

Delara, C.M., Jenner, T.J., Townsend, K.M.S., Marsden, S.J., and Oneill, P. (1995). The Effect of Dimethyl-Sulfoxide on the Induction of DNA Double-Strand Breaks in V79-4 Mammalian-Cells by Alpha-Particles. Radiation Research *144*, 43-49.

Dianov, G.L., and Hubscher, U. (2013). Mammalian base excision repair: the forgotten archangel. Nucleic Acids Research *41*, 3483-3490.

Dinant, C., de Jager, M., Essers, J., van Cappellen, W.A., Kanaar, R., Houtsmuller, A.B., and Vermeulen, W. (2007). Activation of multiple DNA repair pathways by subnuclear damage induction methods. Journal of Cell Science *120*, 2731-2740.

Ding, Q., Reddy, Y.V.R., Wang, W., Woods, T., Douglas, P., Ramsden, D.A., Lees-Miller, S.P., and Meek, K. (2003). Autophosphorylation of the catalytic subunit of the DNA-dependent protein kinase is required for efficient end processing during DNA double-strand break repair. Molecular and Cellular Biology *23*, 5836-5848.

DiTullio, R.A., Mochan, T.A., Venere, M., Bartkova, J., Sehested, M., Bartek, J., and Halazonetis, T.D. (2002). 53BP1 functions in an ATM-dependent checkpoint pathway that is constitutively activated in human cancer. Nature Cell Biology *4*, 998-1002.

Dobbs, T.A., Palmer, P., Maniou, Z., Lomax, M.E., and O'Neill, P. (2008). Interplay of two major repair pathways in the processing of complex double-strand DNA breaks. DNA Repair *7*, 1372-1383.

Douglas, P., Cui, X.P., Block, W.D., Yu, Y.P., Gupta, S., Ding, Q., Ye, R.Q., Morrice, N., Lees-Miller, S.P., and Meek, K. (2007). The DNA-dependent protein kinase catalytic subunit is phosphorylated in vivo on threonine 3950, a highly conserved amino acid in the protein kinase domain. Molecular and Cellular Biology *27*, 1581-1591.

Downey, M., and Durocher, D. (2006). gamma H2AX as a checkpoint maintenance signal. Cell Cycle *5*, 1376-1381.

Dzyubachyk, O., Essers, J., van Cappellen, W.A., Baldeyron, C., Inagaki, A., Niessen, W.J., and Meijering, E. (2010a). Automated analysis of time-lapse fluorescence microscopy images: from live cell images to intracellular foci. Bioinformatics *26*, 2424-2430.

Dzyubachyk, O., van Cappellen, W.A., Essers, J., Niessen, W.J., and Meijering, E. (2010b). Advanced Level-Set-Based Cell Tracking in Time-Lapse Fluorescence Microscopy. IEEE Transactions on Medical Imaging *29*, 852-867.

Eastman, A., and Barry, M.A. (1992). The origins of DNA breaks: a consequence of DNA damage, DNA repair, or apoptosis? Cancer Investigation *10*, 229-240.

Eccles, L.J., O'Neill, P., and Lomax, M.E. (2011). Delayed repair of radiation induced clustered DNA damage: Friend or foe? Mutation Research-Fundamental and Molecular Mechanisms of Mutagenesis *711*, 134-141.

El-Khamisy, S.F., Masutani, M., Suzuki, H., and Caldecott, K.W. (2003). A requirement for PARP-1 for the assembly or stability of XRCC1 nuclear foci at sites of oxidative DNA damage. Nucleic Acids Research *31*, 5526-5533.

Escribano-Diaz, C., Orthwein, A., Fradet-Turcotte, A., Xing, M.T., Young, J.T.F., Tkac, J., Cook, M.A., Rosebrock, A.P., Munro, M., Canny, M.D., Xu, D.Y., and Durocher, D. (2013). A Cell Cycle-Dependent Regulatory Circuit Composed of 53BP1-RIF1 and BRCA1-CtIP Controls DNA Repair Pathway Choice. Molecular Cell *49*, 872-883.

Essers, J., Theil, A.F., Baldeyron, C., van Cappellen, W.A., Houtsmuller, A.B., Kanaar, R., and Vermeulen, W. (2005). Nuclear dynamics of PCNA in DNA replication and repair. Molecular and Cellular Biology *25*, 9350-9359.

Fattah, F., Lee, E.H., Weisensel, N., Wang, Y.B., Lichter, N., and Hendrickson, E.A. (2010). Ku Regulates the Non-Homologous End Joining Pathway Choice of DNA Double-Strand Break Repair in Human Somatic Cells. PLoS Genetics *6*.

Feng, L., and Chen, J.J. (2012). The E3 ligase RNF8 regulates KU80 removal and NHEJ repair. Nature Structural & Molecular Biology *19*, 201-206.

Feng, Z.H., Scott, S.P., Bussen, W., Sharma, G.G., Guo, G.S., Pandita, T.K., and Powell, S.N. (2011). Rad52 inactivation is synthetically lethal with BRCA2 deficiency. Proceedings of the National Academy of Sciences of the United States of America *108*, 686-691.

Ferguson, D.O., Sekiguchi, J.M., Chang, S., Frank, K.M., Gao, Y.J., DePinho, R.A., and Alt, F.W. (2000). The nonhomologous end-joining pathway of DNA repair is required for genomic stability and the suppression of translocations. Proceedings of the National Academy of Sciences of the United States of America *97*, 6630-6633.

Fernandez-Capetillo, O., Chen, H.T., Celeste, A., Ward, I., Romanienko, P.J., Morales, J.C., Naka, K., Xia, Z.F., Camerini-Otero, R.D., Motoyama, N., Carpenter, P.B., Bonner, W.M., Chen, J.J., and Nussenzweig, A. (2002). DNA damage-induced G(2)-M checkpoint activation by histone H2AX and 53BP1. Nature Cell Biology *4*, 993-997.

Filippo, J.S., Sung, P., and Klein, H. (2008). Mechanism of eukaryotic homologous recombination. Annual Review of Biochemistry *77*, 229-257.

Fisher, A.E., Hochegger, H., Takeda, S., and Caldecott, K.W. (2007). Poly(ADP-ribose) polymerase 1 accelerates single-strand break repair in concert with poly(ADP-ribose) glycohydrolase. Molecular and Cellular Biology *27*, 5597-5605.

FitzGerald, J.E., Grenon, M., and Lowndes, N.F. (2009). 53BP1: function and mechanisms of focal recruitment. Biochemical Society Transactions *37*, 897-904.

Fortini, P., Pascucci, B., Parlanti, E., D'Errico, M., Simonelli, V., and Dogliotti, E. (2003). The base excision repair: mechanisms and its relevance for cancer susceptibility. Biochimie *85*, 1053-1071.

Frank, K.M., Sekiguchi, J.M., Seidl, K.J., Swat, W., Rathbun, G.A., Cheng, H.L., Davidson, L., Kangaloo, L., and Alt, F.W. (1998). Late embryonic lethality and impaired V(D)J recombination in mice lacking DNA ligase IV. Nature *396*, 173-177.

Frelin, A., Fontbonne, J., Ban, G., Colin, J., Labalme, M., Batalla, A., Isambert, A., Vela, A., and Leroux, T. (2005). Spectral discrimination of Čerenkov radiation in scintillating dosimeters. Medical Physics *32*, 3000.

Friedberg, E.C. (2001). How nucleotide excision repair protects against cancer. Nature Reviews Cancer *1*, 22-33.

Friedberg, E.C. (2003). DNA damage and repair. Nature *421*, 436-440.

Gamper, A.M., Rofougaran, R., Watkins, S.C., Greenberger, J.S., Beumer, J.H., and Bakkenist, C.J. (2013). ATR kinase activation in G1 phase facilitates the repair of ionizing radiation-induced DNA damage. Nucleic Acids Research *41*, 10334-10344.

Gao, Y.J., Sun, Y., Frank, K.M., Dikkes, P., Fujiwara, Y., Seidl, K.J., Sekiguchi, J.M., Rathbun, G.A., Swat, W., Wang, J.Y., Bronson, R.T., Malynn, B.A., Bryans, M., Zhu, C.M., Chaudhuri, J., Davidson, L., Ferrini, R., Stamato, T., Orkin, S.H., Greenberg, M.E., and Alt, F.W. (1998). A critical role for DNA end-joining proteins in both lymphogenesis and neurogenesis. Cell *95*, 891-902.

Gell, D., and Jackson, S.P. (1999). Mapping of protein-protein interactions within the DNA-dependent protein kinase complex. Nucleic Acids Research *27*, 3494-3502.

Georgakilas, A.G., O'Neill, P., and Stewart, R.D. (2013). Induction and Repair of Clustered DNA Lesions: What Do We Know So Far? Radiation Research *180*, 100-109.

Giglia-Mari, G., Zotter, A., and Vermeulen, W. (2011). DNA Damage Response. Cold Spring Harbor Perspectives in Biology *3*.

Gilchrist, S., and Vojnovic, B. (2011), A Software Control System for Robotic Sample Transfer http://users.ox.ac.uk/~atdgroup/radiation_linac.shtml, 27/01, 2014

Gilley, D., Tanaka, H., Hande, M.P., Kurimasa, A., Li, G.C., Oshimura, M., and Chen, D.J. (2001). DNA-PKcs is critical for telomere capping. Proceedings of the National Academy of Sciences of the United States of America *98*, 15084-15088.

Goodarzi, A.A., Noon, A.T., Deckbar, D., Ziv, Y., Shiloh, Y., Lobrich, M., and Jeggo, P.A. (2008). ATM signaling facilitates repair of DNA double-strand breaks associated with heterochromatin. Molecular Cell *31*, 167-177.

Goodhead, D.T. (1989). The Initial Physical Damage Produced by Ionizing-Radiations. International Journal of Radiation Biology *56*, 623-634.

Goodhead, D.T. (1994). Initial Events in the Cellular Effects of Ionizing Radiations: Clustered Damage in DNA. International Journal of Radiation Biology *65*, 7-17.

Gorgoulis, V.G., Vassiliou, L.V.F., Karakaidos, P., Zacharatos, P., Kotsinas, A., Liloglou, T., Venere, M., DiTullio, R.A., Kastrinakis, N.G., Levy, B., Kletsas, D., Yoneta, A., Herlyn, M., Kittas, C., and Halazonetis, T.D. (2005). Activation of the DNA damage checkpoint and genomic instability in human precancerous lesions. Nature *434*, 907-913.

Gottschalk, A.J., Timinszky, G., Kong, S.E., Jin, J.J., Cai, Y., Swanson, S.K., Washburn, M.P., Florens, L., Ladurner, A.G., Conaway, J.W., and Conaway, R.C. (2009). Poly(ADP-ribosyl)ation directs recruitment and activation of an ATP-dependent chromatin remodeler. Proceedings of the National Academy of Sciences of the United States of America *106*, 13770-13774.

Green, T.P., Fennell, M., Whittaker, R., Curwen, J., Jacobs, V., Allen, J., Logie, A., Hargreaves, J., Hickinson, D.M., Wilkinson, R.W., Elvin, P., Boyer, B., Carragher, N., Ple, P.A., Bermingham, A., Holdgate, G.A., Ward, W.H., Hennequin, L.F., Davies, B.R., and Costello, G.F. (2009). Preclinical anticancer activity of the potent, oral Src inhibitor AZD0530. Molecular Oncology *3*, 248-261.

Gu, J.F., Lu, H.H., Tsai, A.G., Schwarz, K., and Lieber, M.R. (2007). Single-stranded DNA ligation and XLF-stimulated incompatible DNA end ligation by the XRCC4-DNA ligase IV complex: influence of terminal DNA sequence. Nucleic Acids Research *35*, 5755-5762.

Gulston, M., de Lara, C., Jenner, T., Davis, E., and O'Neill, P. (2004). Processing of clustered DNA damage generates additional double-strand breaks in mammalian cells post-irradiation. Nucleic Acids Research *32*, 1602-1609.

Gulston, M., Fulford, J., Jenner, T., de Lara, C., and O'Neill, P. (2002). Clustered DNA damage induced by radiation in human fibroblasts (HF19), hamster (V79-4) cells and plasmid DNA is revealed as Fpg and Nth sensitive sites. Nucleic Acids Research *30*, 3464-3472.

Haaf, T., Golub, E.I., Reddy, G., Radding, C.M., and Ward, D.C. (1995). Nuclear Foci of Mammalian Rad51 Recombination Protein in Somatic-Cells after DNA-Damage and Its Localization in Synaptonemal Complexes. Proceedings of the National Academy of Sciences of the United States of America *92*, 2298-2302.

Hamada, N., Schettino, G., Kashino, G., Vaid, M., Suzuki, K., Kodama, S., Vojnovic, B., Folkard, M., Watanabe, M., Michael, B.D., and Prise, K.M. (2006). Histone H2AX phosphorylation in normal human cells irradiated with focused ultrasoft X rays: Evidence for chromatin movement during repair. Radiation Research *166*, 31-38.

Hammel, M., Yu, Y., Mahaney, B.L., Cai, B., Ye, R., Phipps, B.M., Rambo, R.P., Hura, G.L., Pelikan, M., and So, S. (2010). Ku and DNA-dependent protein kinase dynamic

conformations and assembly regulate DNA binding and the initial non-homologous end joining complex. Journal of Biological Chemistry *285*, 1414-1423.

Hanahan, D., and Weinberg, R.A. (2000). The hallmarks of cancer. Cell *100*, 57-70.

Hanahan, D., and Weinberg, R.A. (2011). Hallmarks of cancer: the next generation. Cell *144*, 646-674.

Harding, S.M., and Bristow, R.G. (2012). Discordance between phosphorylation and recruitment of 53BP1 in response to DNA double-strand breaks. Cell Cycle *11*, 1432-1444.

Harley, C.B., Kim, N.W., Prowse, K.R., Weinrich, S.L., Hirsch, K.S., West, M.D., Bacchetti, S., Hirte, H.W., Counter, C.M., Greider, C.W., and et al. (1994). Telomerase, cell immortality, and cancer. Cold Spring Harbor Symposia on Quantitative Biology *59*, 307-315.

Harper, J.V., Anderson, J.A., and O'Neill, P. (2010). Radiation induced DNA DSBs: Contribution from stalled replication forks? DNA Repair (Amst) *9*, 907-913.

Harper, J.V., Reynolds, P., Leatherbarrow, E.L., Botchway, S.W., Parker, A.W., and O'Neill, P. (2008). Induction of Persistent Double Strand Breaks Following Multiphoton Irradiation of Cycling and G(1)-arrested Mammalian Cells-Replication-induced Double Strand Breaks. Photochemistry and Photobiology *84*, 1506-1514.

Harper, J.W., and Elledge, S.J. (2007). The DNA damage response: Ten years after. Molecular Cell *28*, 739-745.

Harris, J.L., Jakob, B., Taucher-Scholz, G., Dianov, G.L., Becherel, O.J., and Lavin, M.F. (2009). Aprataxin, poly-ADP ribose polymerase 1 (PARP-1) and apurinic endonuclease 1 (APE1) function together to protect the genome against oxidative damage. Human Molecular Genetics *18*, 4102-4117.

Helleday, T. (2010). Homologous recombination in cancer development, treatment and development of drug resistance. Carcinogenesis *31*, 955-960.

Helleday, T. (2011). The underlying mechanism for the PARP and BRCA synthetic lethality: Clearing up the misunderstandings. Molecular Oncology *5*, 387-393.

Helleday, T., Petermann, E., Lundin, C., Hodgson, B., and Sharma, R.A. (2008). DNA repair pathways as targets for cancer therapy. Nature Reviews Cancer *8*, 193-204.

Heyer, W.D., Ehmsen, K.T., and Liu, J. (2010). Regulation of Homologous Recombination in Eukaryotes. Annual Review of Genetics, Vol 44 *44*, 113-139.

Hickson, I., Yan, Z., Richardson, C.J., Green, S.J., Martin, N.M.B., Orr, A.I., Reaper, P.M., Jackson, S.P., Curtin, N.J., and Smith, G.C.M. (2004). Identification and characterization of a novel and specific inhibitor of the ataxia-telangiectasia mutated kinase ATM. Cancer Research *64*, 9152-9159.

Hinterdorfer, P., and Van Oijen, A. (2009). Handbook of single-molecule biophysics (Dordrecht ; New York: Springer).

Hinz, J.M., Yamada, N.A., Salazar, E.P., Tebbs, R.S., and Thompson, L.H. (2005). Influence of double-strand-break repair pathways on radiosensitivity throughout the cell cycle in CHO cells. DNA Repair *4*, 782-792.

Hirayama, R., Ito, A., Noguchi, M., Matsumoto, Y., Uzawa, A., Kobashi, G., Okayasu, R., and Furusawa, Y. (2013). OH radicals from the indirect actions of X-rays induce cell lethality and mediate the majority of the oxygen enhancement effect. Radiation Research *180*, 514-523.

Holmes, T.J., and O'Connor, N.J. (2000). Blind deconvolution of 3D transmitted light brightfield micrographs. Journal of Microscopy-Oxford *200*, 114-127.

Hsu, H.L., Yannone, S.M., and Chen, D.J. (2002). Defining interactions between DNA-PK and ligase IV/XRCC4. DNA Repair *1*, 225-235.

Huyen, Y., Zgheib, O., Ditullio, R.A., Jr., Gorgoulis, V.G., Zacharatos, P., Petty, T.J., Sheston, E.A., Mellert, H.S., Stavridi, E.S., and Halazonetis, T.D. (2004). Methylated lysine 79 of histone H3 targets 53BP1 to DNA double-strand breaks. Nature *432*, 406-411.

Iftode, C., Daniely, Y., and Borowiec, J.A. (1999). Replication protein A (RPA): The eukaryotic SSB. Critical Reviews in Biochemistry and Molecular Biology *34*, 141-180.

Iliakis, G. (2009). Backup pathways of NHEJ in cells of higher eukaryotes: Cell cycle dependence. Radiotherapy and Oncology *92*, 310-315.

Ingraham, S.E., Lynch, R.A., Kathiresan, S., Buckler, A.J., and Menon, A.G. (1999). hREC2, a RAD51-like gene, is disrupted by t(12;14) (q15;q24.1) in a uterine leiomyoma. Cancer Genetics and Cytogenetics *115*, 56-61.

Iwabuchi, K., Bartel, P.L., Li, B., Marraccino, R., and Fields, S. (1994). 2 Cellular Proteins That Bind to Wild-Type but Not Mutant P53. Proceedings of the National Academy of Sciences of the United States of America *91*, 6098-6102.

Jackson, S.P., and Bartek, J. (2009). The DNA-damage response in human biology and disease. Nature *461*, 1071-1078.

Jain, S., Coulter, J.A., Butterworth, K.T., Hounsell, A.R., McMahon, S.J., Hyland, W.B., Muir, M.F., Dickson, G.R., Prise, K.M., and Currell, F.J. (2014). Gold nanoparticle cellular uptake, toxicity and radiosensitisation in hypoxic conditions. Radiotherapy and Oncology.

Jain, S., Coulter, J.A., Hounsell, A.R., Butterworth, K.T., McMahon, S.J., Hyland, W.B., Muir, M.F., Dickson, G.R., Prise, K.M., Currell, F.J., O'Sullivan, J.M., and Hirst, D.G. (2011). Cell-Specific Radiosensitization by Gold Nanoparticles at Megavoltage Radiation Energies. International Journal of Radiation Oncology Biology Physics *79*, 531-539.

Jakob, B., Splinter, J., Conrad, S., Voss, K.O., Zink, D., Durante, M., Lobrich, M., and Taucher-Scholz, G. (2011). DNA double-strand breaks in heterochromatin elicit fast repair

protein recruitment, histone H2AX phosphorylation and relocation to euchromatin. Nucleic Acids Research *39*, 6489-6499.

Jakob, B., Splinter, J., and Taucher-Scholz, G. (2009). Positional stability of damaged chromatin domains along radiation tracks in mammalian cells. Radiation Research *171*, 405-418.

James, N.D., Hussain, S.A., Hall, E., Jenkins, P., Tremlett, J., Rawlings, C., Crundwell, M., Sizer, B., Sreenivasan, T., Hendron, C., Lewis, R., Waters, R., Huddart, R.A., and Investigators, B. (2012). Radiotherapy with or without Chemotherapy in Muscle-Invasive Bladder Cancer. New England Journal of Medicine *366*, 1477-1488.

Janesick, J.R., Klaasen, K.P., and Elliott, T. (1987). Charge-Coupled-Device Charge-Collection Efficiency and the Photon-Transfer Technique. Optical Engineering *26*, 972-980.

Jazayeri, A., Balestrini, A., Garner, E., Haber, J.E., and Costanzo, V. (2008). Mre11-Rad50-Nbs1-dependent processing of DNA breaks generates oligonucleotides that stimulate ATM activity. EMBO Journal *27*, 1953-1962.

Jeggo, P., and O'Neill, P. (2002). The Greek Goddess, Artemis, reveals the secrets of her cleavage. DNA Repair *1*, 771-777.

Jenner, T.J., Delara, C.M., Oneill, P., and Stevens, D.L. (1993). Induction and Rejoining of DNA Double-Strand Breaks in V79-4 Mammalian-Cells Following Gamma-Irradiation and Alpha-Irradiation. International Journal of Radiation Biology *64*, 265-273.

Jiricny, J. (2006). The multifaceted mismatch-repair system. Nature Reviews Molecular Cell Biology *7*, 335-346.

Jowsey, P., Morrice, N.A., Hastie, C.J., McLauchlan, H., Toth, R., and Rouse, J. (2007). Characterisation of the sites of DNA damage-induced 53BP1 phosphorylation catalysed by ATM and ATR. DNA Repair *6*, 1536-1544.

Juan, G., Li, X., and Darzynkiewicz, Z. (1997). Correlation between DNA replication and expression of cyclins A and B1 in individual MOLT-4 cells. Cancer Research *57*, 803-807.

Kakarougkas, A., Ismail, A., Klement, K., Goodarzi, A.A., Conrad, S., Freire, R., Shibata, A., Lobrich, M., and Jeggo, P.A. (2013). Opposing roles for 53BP1 during homologous recombination. Nucleic Acids Research *41*, 9719-9731.

Kasparek, T.R., and Humphrey, T.C. (2011). DNA double-strand break repair pathways, chromosomal rearrangements and cancer. Seminars in Cell & Developmental Biology *22*, 886-897.

Kass, E.M., and Jasin, M. (2010). Collaboration and competition between DNA double-strand break repair pathways. FEBS Letters *584*, 3703-3708.

Kastan, M.B. (2008). DNA Damage Responses: Mechanisms and Roles in Human Disease 2007 GHA Clowes Memorial Award Lecture. Molecular Cancer Research *6*, 517-524.

Kawanishi, S., Hiraku, Y., Pinlaor, S., and Ma, N. (2006). Oxidative and nitrative DNA damage in animals and patients with inflammatory diseases in relation to inflammation-related carcinogenesis. Biological Chemistry *387*, 365-372.

Kielbassa, C., Roza, L., and Epe, B. (1997). Wavelength dependence of oxidative DNA damage induced by UV and visible light. Carcinogenesis *18*, 811-816.

Kinner, A., Wu, W.Q., Staudt, C., and Iliakis, G. (2008). gamma-H2AX in recognition and signaling of DNA double-strand breaks in the context of chromatin. Nucleic Acids Research *36*, 5678-5694.

Kleppa, L., Mari, P.O., Larsen, E., Lien, G.F., Godon, C., Theil, A.F., Nesse, G.J., Wiksen, H., Vermeulen, W., Giglia-Mari, G., and Klungland, A. (2012). Kinetics of endogenous mouse FEN1 in base excision repair. Nucleic Acids Research *40*, 9044-9059.

Koch, C.A., Agyei, R., Galicia, S., Metalnikov, P., O'Donnell, P., Starostine, A., Weinfeld, M., and Durocher, D. (2004). Xrcc4 physically links DNA end processing by polynucleotide kinase to DNA ligation by DNA ligase IV. EMBO Journal *23*, 3874-3885.

Kong, X., Mohanty, S.K., Stephens, J., Heale, J.T., Gomez-Godinez, V., Shi, L.Z., Kim, J.S., Yokomori, K., and Berns, M.W. (2009). Comparative analysis of different laser systems to study cellular responses to DNA damage in mammalian cells. Nucleic Acids Research *37*.

Krokan, H.E., and Bjoras, M. (2013). Base Excision Repair. Cold Spring Harbor Perspectives in Biology *5*.

Lan, L., Nakajima, S., Oohata, Y., Takao, M., Okano, S., Masutani, M., Wilson, S.H., and Yasui, A. (2004). In situ analysis of repair processes for oxidative DNA damage in mammalian cells. Proceedings of the National Academy of Sciences of the United States of America *101*, 13738-13743.

Lavin, M.F. (2008). Ataxia-telangiectasia: from a rare disorder to a paradigm for cell signalling and cancer (vol 9, pg 759, 2008). Nature Reviews Molecular Cell Biology *9*, 927-927.

Lavin, M.F., and Kozlov, S. (2007). ATM activation and DNA damage response. Cell Cycle *6*, 931-942.

Leatherbarrow, E.L., Harper, J.V., Cucinotta, F.A., and O'Neill, P. (2006). Induction and quantification of gamma-H2AX foci following low and high LET-irradiation. International Journal of Radiation Biology *82*, 111-118.

Lee, J.H., Cheong, H.M., Kang, M.Y., Kim, S.Y., and Kang, Y. (2009). Ser1778 of 53BP1 Plays a Role in DNA Double-strand Break Repairs. Korean Journal of Physiology & Pharmacology *13*, 343-348.

Lee, J.H., and Paull, T.T. (2005). ATM activation by DNA double-strand breaks through the Mre11-Rad50-Nbs1 complex (vol 308, pg 551, 2005). Science *308*, 1870-1870.

Lee, J.H., and Paull, T.T. (2007). Activation and regulation of ATM kinase activity in response to DNA double-strand breaks. Oncogene *26*, 7741-7748.

Lehnert, S. (2007). Biomolecular action of ionizing radiation. Biomolecular Action of Ionizing Radiation Series: Series in Medical Physics and Biomedical Engineering, ISBN: 978-0-7503-0824-3 Taylor & Francis, Edited by Shirley Lehnert *1*.

Levine, A.J., Momand, J., and Finlay, C.A. (1991). The p53 tumour suppressor gene. Nature *351*, 453-456.

LI, K. (2008), The image stabilizer plugin for ImageJ http://www.cs.cmu.edu/~kangli/code/Image_Stabilizer.html, 01/08, 2011

Lieber, M.R. (2010). The Mechanism of Double-Strand DNA Break Repair by the Nonhomologous DNA End-Joining Pathway. Annual Review of Biochemistry, Vol 79 *79*, 181-211.

Lieber, M.R., Gu, J.F., Lu, H.H., Shimazaki, N., and Tsai, A.G. (2010). Nonhomologous DNA End Joining (NHEJ) and Chromosomal Translocations in Humans. Genome Stability and Human Diseases *50*, 279-296.

Lieber, M.R., Hesse, J.E., Lewis, S., Bosma, G.C., Rosenberg, N., Mizuuchi, K., Bosma, M.J., and Gellert, M. (1988). The Defect in Murine Severe Combined Immune-Deficiency - Joining of Signal Sequences but Not Coding Segments in V(D)J Recombination. Cell *55*, 7-16.

Lieber, M.R., Ma, Y.M., Pannicke, U., and Schwarz, K. (2003). Mechanism and regulation of human non-homologous DNA end-joining. Nature Reviews Molecular Cell Biology *4*, 712-720.

Limbo, O., Chahwan, C., Yamada, Y., de Bruin, R.A.M., Wittenberg, C., and Russell, P. (2007). Ctp1 is a cell-cycle-regulated protein that functions with Mre11 complex to control double-strand break repair by homologous recombination. Molecular Cell *28*, 134-146.

Lindahl, T. (1993). Instability and Decay of the Primary Structure of DNA. Nature *362*, 709-715.

Lindahl, T., and Barnes, D.E. (2000). Repair of endogenous DNA damage. Cold Spring Harbor Symposia on Quantitative Biology *65*, 127-133.

Liu, S., Opiyo, S.O., Manthey, K., Glanzer, J.G., Ashley, A.K., Amerin, C., Troksa, K., Shrivastav, M., Nickoloff, J.A., and Oakley, G.G. (2012). Distinct roles for DNA-PK, ATM and ATR in RPA phosphorylation and checkpoint activation in response to replication stress. Nucleic Acids Research *40*, 10780-10794.

Liu, S.Z., Shiotani, B., Lahiri, M., Marechal, A., Tse, A., Leung, C.C.Y., Glover, J.N.M., Yang, X.H.H., and Zou, L. (2011). ATR Autophosphorylation as a Molecular Switch for Checkpoint Activation. Molecular Cell *43*, 192-202.

Lobrich, M., Shibata, A., Beucher, A., Fisher, A., Ensminger, M., Goodarzi, A.A., Barton, O., and Jeggo, P.A. (2010). gamma H2AX foci analysis for monitoring DNA double-strand break repair Strengths, limitations and optimization. Cell Cycle *9*, 662-669.

Lowe, S.W., Ruley, H.E., Jacks, T., and Housman, D.E. (1993). p53-dependent apoptosis modulates the cytotoxicity of anticancer agents. Cell *74*, 957-967.

Lucas, B.D., and Kanade, T. (1981). An Iterative Image Registration Technique with an Application to Stereo Vision. Paper presented at: Proceedings of Imaging Understanding Workshop.

Lukas, C., Bartek, J., and Lukas, J. (2005). Imaging of protein movement induced by chromosomal breakage: tiny 'local' lesions pose great 'global' challenges. Chromosoma *114*, 146-154.

Lukas, J., Lukas, C., and Bartek, J. (2004). Mammalian cell cycle checkpoints: signalling pathways and their organization in space and time. DNA Repair (Amst) *3*, 997-1007.

Ma, Y.M., Pannicke, U., Lu, H.H., Niewolik, D., Schwarz, K., and Lieber, M.R. (2005). The DNA-dependent protein kinase catalytic subunit phosphorylation sites in human artemis. Journal of Biological Chemistry *280*, 33839-33846.

Ma, Y.M., Pannicke, U., Schwarz, K., and Lieber, M.R. (2002). Hairpin opening and overhang processing by an Artemis/DNA-dependent protein kinase complex in nonhomologous end joining and V(D)J recombination. Cell *108*, 781-794.

Magnander, K., Hultborn, R., Claesson, K., and Elmroth, K. (2010). Clustered DNA Damage in Irradiated Human Diploid Fibroblasts: Influence of Chromatin Organization. Radiation Research *173*, 272-282.

Mahaney, B.L., Meek, K., and Lees-Miller, S.P. (2009). Repair of ionizing radiation-induced DNA double-strand breaks by non-homologous end-joining. Biochemical Journal *417*, 639-650.

Maloisel, L., Fabre, F., and Gangloff, S. (2008). DNA polymerase delta is preferentially recruited during homologous recombination to promote heteroduplex DNA extension. Molecular and Cellular Biology *28*, 1373-1382.

Marechal, A., and Zou, L. (2013). DNA Damage Sensing by the ATM and ATR Kinases. Cold Spring Harbor Perspectives in Biology *5*.

Mari, P.O., Florea, B.I., Persengiev, S.P., Verkaik, N.S., Brueggenwirth, H.T., Modesti, M., Giglia-Mari, G., Bezstarosti, K., Demmers, J.A.A., Luider, T.M., Houtsmuller, A.B., and van Gent, D.C. (2006). Dynamic assembly of end-joining complexes requires interaction between Ku70/80 and XRCC4. Proceedings of the National Academy of Sciences of the United States of America *103*, 18597-18602.

Markova, E., Schultz, N., and Belyaev, I.Y. (2007). Kinetics and dose-response of residual 53BP1/gamma-H2AX foci: co-localization, relationship with DSB repair and clonogenic survival. International Journal of Radiation Biology *83*, 319-329.

Martin, M., Genesca, A., Latre, L., Jaco, I., Taccioli, G.E., Egozcue, J., Blasco, M.A., Iliakis, G., and Tusell, L. (2005). Postreplicative joining of DNA double-strand breaks causes genomic instability in DNA-PKcs-deficient mouse embryonic fibroblasts. Cancer Research *65*, 10223-10232.

Martin, V., Chahwan, C., Gao, H., Blais, V., Wohlschlegel, J., Yates, J.R., McGowan, C.H., and Russell, P. (2006). Sws1 is a conserved regulator of homologous recombination in eukaryotic cells. EMBO Journal *25*, 2564-2574.

Masson, J.Y., Stasiak, A.Z., Stasiak, A., Benson, F.E., and West, S.C. (2001). Complex formation by the human RAD51C and XRCC3 recombination repair proteins. Proceedings of the National Academy of Sciences of the United States of America *98*, 8440-8446.

Matsuoka, S., Ballif, B.A., Smogorzewska, A., McDonald, E.R., Hurov, K.E., Luo, J., Bakalarski, C.E., Zhao, Z.M., Solimini, N., Lerenthal, Y., Shiloh, Y., Gygi, S.P., and Elledge, S.J. (2007). ATM and ATR substrate analysis reveals extensive protein networks responsive to DNA damage. Science *316*, 1160-1166.

Maxwell, J.C. (1876). Matter and Motion (London: Society for Promoting Christian Knowledge).

Maynard, S., Schurman, S.H., Harboe, C., de Souza-Pinto, N.C., and Bohr, V.A. (2009). Base excision repair of oxidative DNA damage and association with cancer and aging. Carcinogenesis *30*, 2-10.

Mazin, A.V., Mazina, O.M., Bugreev, D.V., and Rossi, M.J. (2010). Rad54, the motor of homologous recombination. DNA Repair *9*, 286-302.

McGarry, T.J., and Kirschner, M.W. (1998). Geminin, an inhibitor of DNA replication, is degraded during mitosis. Cell *93*, 1043-1053.

McGowan, A., Ruiz-Ruiz, M., Gorman, A., Lopez-Rivas, A., and Cotter, T. (1996). Reactive oxygen intermediate (s)(ROI): common mediator (s) of poly (ADP-ribose) polymerase (PARP) cleavage and apoptosis. FEBS Letters *392*, 299-303.

Mcllwraith, M.J., and West, S.C. (2008). DNA repair synthesis facilitates RAD52-mediated second-end capture during DSB repair. Molecular Cell *29*, 510-516.

McMahon, S.J., Hyland, W.B., Muir, M.F., Coulter, J.A., Jain, S., Butterworth, K.T., Schettino, G., Dickson, G.R., Hounsell, A.R., O'Sullivan, J.M., Prise, K.M., Hirst, D.G., and Currell, F.J. (2011). Biological consequences of nanoscale energy deposition near irradiated heavy atom nanoparticles. Scientific Reports *1*.

McMahon, S.J., Mendenhall, M.H., Jain, S., and Currell, F. (2008). Radiotherapy in the presence of contrast agents: a general figure of merit and its application to gold nanoparticles. Physics in Medicine and Biology *53*, 5635-5651.

Meindl, A., Hellebrand, H., Wiek, C., Erven, V., Wappenschmidt, B., Niederacher, D., Freund, M., Lichtner, P., Hartmann, L., Schaal, H., Ramser, J., Honisch, E., Kubisch, C., Wichmann, H.E., Kast, K., Deissler, H., Engel, C., Muller-Myhsok, B., Neveling, K.,

Kiechle, M., Mathew, C.G., Schindler, D., Schmutzler, R.K., and Hanenberg, H. (2010). Germline mutations in breast and ovarian cancer pedigrees establish RAD51C as a human cancer susceptibility gene. Nature Genetics *42*, 410-U465.

Meldrum, R.A., Botchway, S.W., Wharton, C.W., and Hirst, G.J. (2003). Nanoscale spatial induction of ultraviolet photoproducts in cellular DNA by three-photon near-infrared absorption. EMBO Reports *4*, 1144-1149.

Michael, B.D., Harrop, H.A., and Held, K.D. (1981). Photoreactivation of Escherichia-Coli after Exposure to Ionizing-Radiation - the Role of Uv Damage by Concomitant Cerenkov Light. International Journal of Radiation Biology *39*, 577-583.

Miller, K.A., Yoshikawa, D.M., McConnell, I.R., Clark, R., Schild, D., and Albala, J.S. (2002). RAD51C interacts with RAD51B and is central to a larger protein complex in vivo exclusive of RAD51. Journal of Biological Chemistry *277*, 8406-8411.

Miltenburger, H., Sachse, G., and Schliermann, M. (1986). S-phase cell detection with a monoclonal antibody. Developments in Biological Standardization *66*, 91-99.

Mimori, T., and Hardin, J.A. (1986). Mechanism of Interaction between Ku Protein and DNA. Journal of Biological Chemistry *261*, 375-379.

Mistry, M., Parkin, D., Ahmad, A., and Sasieni, P. (2011). Cancer incidence in the United Kingdom: projections to the year 2030. British Journal of Cancer *105*, 1795-1803.

Miyagawa, K. (2008). Clinical relevance of the homologous recombination machinery in cancer therapy. Cancer Science *99*, 187-194.

Mladenov, E., and Iliakis, G. (2011). Induction and repair of DNA double strand breaks: the increasing spectrum of non-homologous end joining pathways. Mutation Research *711*, 61-72.

Mochan, T.A., Venere, M., DiTullio, R.A., Jr., and Halazonetis, T.D. (2004). 53BP1, an activator of ATM in response to DNA damage. DNA Repair (Amst) *3*, 945-952.

Mohanty, S.K., Rapp, A., Monajembashi, S., Gupta, P.K., and Greulich, K.O. (2002). Comet assay measurements of DNA damage in cells by laser microbeams and trapping beams with wavelengths spanning a range of 308 nm to 1064 nm. Radiation Research *157*, 378-385.

Murray, A.W. (2004). Recycling the cell cycle: cyclins revisited. Cell *116*, 221-234.

Nagasawa, H., Brogan, J.R., Peng, Y.L., Little, J.B., and Bedford, J.S. (2010). Some unsolved problems and unresolved issues in radiation cytogenetics: A review and new data on roles of homologous recombination and non-homologous end joining. Mutation Research-Genetic Toxicology and Environmental Mutagenesis *701*, 12-22.

Nagasawa, H., Little, J.B., Lin, Y.F., So, S.R., Kurimasa, A., Peng, Y.L., Brogan, J.R., Chen, D.J., Bedford, J.S., and Chen, B.P.C. (2011). Differential Role of DNA-PKcs

Phosphorylations and Kinase Activity in Radiosensitivity and Chromosomal Instability. Radiation Research *175*, 83-89.

Negrini, S., Gorgoulis, V.G., and Halazonetis, T.D. (2010). Genomic instability--an evolving hallmark of cancer. Nature Reviews Molecular Cell Biology *11*, 220-228.

Nelms, B.E., Maser, R.S., MacKay, J.F., Lagally, M.G., and Petrini, J.H.J. (1998). In situ visualization of DNA double-strand break repair in human fibroblasts. Science *280*, 590-592.

Niggli, V., Schlicht, D., and Affentranger, S. (2009). Specific roles of Rac1 and Rac2 in motile functions of HT1080 fibrosarcoma cells. Biochemical and Biophysical Research Communications *386*, 688-692.

Nikjoo, H., O'Neill, P., Wilson, W.E., and Goodhead, D.T. (2001). Computational approach for determining the spectrum of DNA damage induced by ionizing radiation. Radiation Research *156*, 577-583.

Nikjoo, H., Uehara, S., Wilson, W.E., Hoshi, M., and Goodhead, D.T. (1998). Track structure in radiation biology: theory and applications. International Journal of Radiation Biology *73*, 355-364.

Nimonkar, A.V., Genschel, J., Kinoshita, E., Polaczek, P., Campbell, J.L., Wyman, C., Modrich, P., and Kowalczykowski, S.C. (2011). BLM-DNA2-RPA-MRN and EXO1-BLM-RPA-MRN constitute two DNA end resection machineries for human DNA break repair. Genes & Development *25*, 350-362.

Nimonkar, A.V., and Kowalczykowski, S.C. (2009). Second-end DNA capture in double-strand break repair How to catch a DNA by its tail. Cell Cycle *8*, 1816-1817.

Nimonkar, A.V., Ozsoy, A.Z., Genschel, J., Modrich, P., and Kowalczykowski, S.C. (2008). Human exonuclease 1 and BLM helicase interact to resect DNA and initiate DNA repair. Proceedings of the National Academy of Sciences of the United States of America *105*, 16906-16911.

Noon, A.T., Shibata, A., Rief, N., Lobrich, M., Stewart, G.S., Jeggo, P.A., and Goodarzi, A.A. (2010). 53BP1-dependent robust localized KAP-1 phosphorylation is essential for heterochromatic DNA double-strand break repair. Nature Cell Biology *12*, 177-U191.

O'Donnell, J.H., and Sangster, D.F. (1970). Principles of Radiation Chemistry.

O'Neill, P., and Wardman, P. (2009). Radiation chemistry comes before radiation biology. International Journal of Radiation Biology *85*, 9-25.

Onder, T.T., Gupta, P.B., Mani, S.A., Yang, J., Lander, E.S., and Weinberg, R.A. (2008). Loss of E-cadherin promotes metastasis via multiple downstream transcriptional pathways. Cancer Research *68*, 3645-3654.

Panier, S., and Boulton, S.J. (2014). Double-strand break repair: 53BP1 comes into focus. Nature Reviews Molecular Cell Biology *15*, 7-18.

Parsons, J.L., Dianova, I.I., Allinson, S.L., and Dianov, G.L. (2005). Poly(ADP-ribose) polymerase-1 protects excessive DNA strand breaks from deterioration during repair in human cell extracts. FEBS Journal *272*, 2012-2021.

Parsons, S.J., and Parsons, J.T. (2004). Src family kinases, key regulators of signal transduction. Oncogene *23*, 7906-7909.

Paull, T.T., Rogakou, E.P., Yamazaki, V., Kirchgessner, C.U., Gellert, M., and Bonner, W.M. (2000). A critical role for histone H2AX in recruitment of repair factors to nuclear foci after DNA damage. Current Biology *10*, 886-895.

Pawley, J.B. (2006). Handbook of biological confocal microscopy, 3rd edn (New York, NY: Springer).

Petin, V.G., Morozov, I.I., Kim, J.K., and Semkina, M.A. (2011). Quantitative estimation of UV light dose concomitant to irradiation with ionizing radiation. Radiation Physics and Chemistry *80*, 33-37.

Pires, I.M., Bencokova, Z., Milani, M., Folkes, L.K., Li, J.L., Stratford, M.R., Harris, A.L., and Hammond, E.M. (2010). Effects of Acute versus Chronic Hypoxia on DNA Damage Responses and Genomic Instability. Cancer Research *70*, 925-935.

Prasad, S.G., Parthasaradhi, K., Arbetter, S., Lee, Y., and Garces, R. (1988). Lead shielding thickness for dose reduction of 6-MeV electrons for different square fields. Medical Physics *15*, 263-266.

Purnell, P.R., Mack, P.C., Tepper, C.G., Evans, C.P., Green, T.P., Gumerlock, P.H., Lara Jr, P., Gandara, D.R., Kung, H.-J., and Gautschi, O. (2009). The Src inhibitor AZD0530 blocks invasion and may act as a radiosensitizer in lung cancer cells. Journal of thoracic oncology: official publication of the International Association for the Study of Lung Cancer *4*, 448.

Quennet, V., Beucher, A., Barton, O., Takeda, S., and Lobrich, M. (2011). CtIP and MRN promote non-homologous end-joining of etoposide-induced DNA double-strand breaks in G1. Nucleic Acids Research *39*, 2144-2152.

Rajan, S.S., Hanby, A.M., Horgan, K., Thygesen, H.H., and Speirs, V. (2014). The potential utility of geminin as a predictive biomarker in breast cancer. Breast Cancer Research and Treatment *143*, 91-98.

Rappold, I., Iwabuchi, K., Date, T., and Chen, J. (2001). Tumor suppressor p53 binding protein 1 (53BP1) is involved in DNA damage–signaling pathways. The Journal of Cell Biology *153*, 613-620.

Rasmussen, J.O. (1959). Alpha-Decay Barrier Penetrabilities with an Exponential Nuclear Potential - Even-Even Nuclei. Physical Review *113*, 1593-1598.

Rass, U., Ahel, I., and West, S.C. (2008). Molecular Mechanism of DNA Deadenylation by the Neurological Disease Protein Aprataxin. Journal of Biological Chemistry *283*, 33994-34001.

Reynolds, P., Anderson, J.A., Harper, J.V., Hill, M.A., Botchway, S.W., Parker, A.W., and O'Neill, P. (2012). The dynamics of Ku70/80 and DNA-PKcs at DSBs induced by ionizing radiation is dependent on the complexity of damage. Nucleic Acids Research *40*, 10821-10831.

Reynolds, P., Botchway, S.W., Parker, A.W., and O'Neill, P. (2013). Spatiotemporal dynamics of DNA repair proteins following laser microbeam induced DNA damage - When is a DSB not a DSB? Mutation Research-Genetic Toxicology and Environmental Mutagenesis *756*, 14-20.

Riballo, E., Kuhne, M., Rief, N., Doherty, A., Smith, G.C.M., Recio, M.J., Reis, C., Dahm, K., Fricke, A., Krempler, A., Parker, A.R., Jackson, S.P., Gennery, A., Jeggo, P.A., and Lobrich, M. (2004). A pathway of double-strand break rejoining dependent upon ATM, artemis, and proteins locating to gamma-H2AX foci. Molecular Cell *16*, 715-724.

Rich, T., Allen, R.L., and Wyllie, A.H. (2000). Defying death after DNA damage. Nature *407*, 777-783.

Riley, T., Sontag, E., Chen, P., and Levine, A. (2008). Transcriptional control of human p53-regulated genes. Nature Reviews Molecular Cell Biology *9*, 402-412.

Ristic, D., Modesti, M., Kanaar, R., and Wyman, C. (2003). Rad52 and Ku bind to different DNA structures produced early in double-strand break repair. Nucleic Acids Research *31*, 5229-5237.

Rogakou, E.P., Boon, C., Redon, C., and Bonner, W.M. (1999). Megabase chromatin domains involved in DNA double-strand breaks in vivo. Journal of Cell Biology *146*, 905-915.

Rogakou, E.P., Pilch, D.R., Orr, A.H., Ivanova, V.S., and Bonner, W.M. (1998). DNA double-stranded breaks induce histone H2AX phosphorylation on serine 139. Journal of Biological Chemistry *273*, 5858-5868.

Roos, W.P., and Kaina, B. (2006). DNA damage-induced cell death by apoptosis. Trends in Molecular Medicine *12*, 440-450.

Roots, R., and Okada, S. (1975). Estimation of Life Times and Diffusion Distances of Radicals Involved in X-Ray-Induced DNA Strand Breaks or Killing of Mammalian-Cells. Radiation Research *64*, 306-320.

Rosenberg, I. (2008). Radiation Oncology Physics: A Handbook for Teachers and Students. British Journal of Cancer *98*, 1020.

Rothkamm, K., Kruger, I., Thompson, L.H., and Lobrich, M. (2003). Pathways of DNA double-strand break repair during the mammalian cell cycle. Molecular and Cellular Biology *23*, 5706-5715.

Sage, E., and Harrison, L. (2011). Clustered DNA lesion repair in eukaryotes: relevance to mutagenesis and cell survival. Mutation Research/Fundamental and Molecular Mechanisms of Mutagenesis *711*, 123-133.

Saha, J., Wang, M., and Cucinotta, F.A. (2013). Investigation of switch from ATM to ATR signaling at the sites of DNA damage induced by low and high LET radiation. DNA Repair (Amst) *12*, 1143-1151.

Sakaue-Sawano, A., Kurokawa, H., Morimura, T., Hanyu, A., Hama, H., Osawa, H., Kashiwagi, S., Fukami, K., Miyata, T., Miyoshi, H., Imamura, T., Ogawa, M., Masai, H., and Miyawaki, A. (2008). Visualizing spatiotemporal dynamics of multicellular cell-cycle progression. Cell *132*, 487-498.

Saleh-Gohari, N., Bryant, H.E., Schultz, N., Parker, K.M., Cassel, T.N., and Helleday, T. (2005). Spontaneous homologous recombination is induced by collapsed replication forks that are caused by endogenous DNA single-strand breaks. Molecular and Cellular Biology *25*, 7158-7169.

Sartori, A.A., Lukas, C., Coates, J., Mistrik, M., Fu, S., Bartek, J., Baer, R., Lukas, J., and Jackson, S.P. (2007). Human CtIP promotes DNA end resection. Nature *450*, 509-U506.

Saxena, S., and Dutta, A. (2005). Geminin–Cdt1 balance is critical for genetic stability. Mutation Research/Fundamental and Molecular Mechanisms of Mutagenesis *569*, 111-121.

Schlegel, B.P., Jodelka, F.M., and Nunez, R. (2006). BRCA1 promotes induction of ssDNA by ionizing radiation. Cancer Research *66*, 5181-5189.

Schneider, C.A., Rasband, W.S., and Eliceiri, K.W. (2012). NIH Image to ImageJ: 25 years of image analysis. Nature Methods *9*, 671-675.

Schultz, L.B., Chehab, N.H., Malikzay, A., and Halazonetis, T.D. (2000). p53 Binding protein 1 (53BP1) is an early participant in the cellular response to DNA double-strand breaks. Journal of Cell Biology *151*, 1381-1390.

Schulz-Ertner, D., Jakel, O., and Schlegel, W. (2006). Radiation therapy with charged particles. Seminars in Radiation Oncology *16*, 249-259.

Seefeldt, B., Kasper, R., Seidel, T., Tinnefeld, P., Dietz, K.J., Heilemann, M., and Sauer, M. (2008). Fluorescent proteins for single-molecule fluorescence applications. Journal of Biophotonics *1*, 74-82.

Seymour H. Levitt, James A. Purdy, Carlos A. Perez, and Vijayakumar, S. (2008). Technical Basis of Radiation Therapy: Practical Clinical Applications, 4th edn (Springer).

Shibata, A., Conrad, S., Birraux, J., Geuting, V., Barton, O., Ismail, A., Kakarougkas, A., Meek, K., Taucher-Scholz, G., Lobrich, M., and Jeggo, P.A. (2011). Factors determining DNA double-strand break repair pathway choice in G2 phase. EMBO Journal *30*, 1079-1092.

Shiloh, Y. (2003). ATM and related protein kinases: Safeguarding genome integrity. Nature Reviews Cancer *3*, 155-168.

Shinohara, A., Ogawa, H., and Ogawa, T. (1992). Rad51 Protein Involved in Repair and Recombination in Saccharomyces-Cerevisiae Is a Reca-Like Protein. Cell *69*, 457-470.

Shiotani, B., and Zou, L. (2009). Single-Stranded DNA Orchestrates an ATM-to-ATR Switch at DNA Breaks. Molecular Cell *33*, 547-558.

Silverman, J., Takai, H., Buonomo, S.B.C., Eisenhaber, F., and de Lange, T. (2004). Human Rif1, ortholog of a yeast telomeric protein, is regulated by ATM and 53BP1 and functions in the S-phase checkpoint. Genes & Development *18*, 2108-2119.

Singleton, B.K., Torres-Arzayus, M.I., Rottinghaus, S.T., Taccioli, G.E., and Jeggo, P.A. (1999). The C terminus of Ku80 activates the DNA-dependent protein kinase catalytic subunit. Molecular and Cellular Biology *19*, 3267-3277.

Smith, G.C.M., and Jackson, S.P. (1999). The DNA-dependent protein kinase. Genes & Development *13*, 916-934.

Sordet, O., Redon, C.E., Guirouilh-Barbat, J., Smith, S., Solier, S., Douarre, C., Conti, C., Nakamura, A.J., Das, B.B., Nicolas, E., Kohn, K.W., Bonner, W.M., and Pommier, Y. (2009). Ataxia telangiectasia mutated activation by transcription- and topoisomerase I-induced DNA double-strand breaks. EMBO Reports *10*, 887-893.

Sorensen, C.S., Hansen, L.T., Dziegielewski, J., Syljuasen, R.G., Lundin, C., Bartek, J., and Helleday, T. (2005). The cell-cycle checkpoint kinase Chk1 is required for mammalian homologous recombination repair. Nature Cell Biology *7*, 195-U121.

Speit, B., Rädlein, E., Frischat, G.H., Marker, A.J., and Hayden, J.S. (1992). Radiation resistant optical glasses. Nuclear Instruments and Methods in Physics Research Section B: Beam Interactions with Materials and Atoms *65*, 384-386.

Splinter, J., Jakob, B., Lang, M., Yano, K., Engelhardt, J., Hell, S.W., Chen, D.J., Durante, M., and Taucher-Scholz, G. (2010). Biological dose estimation of UVA laser microirradiation utilizing charged particle-induced protein foci. Mutagenesis *25*, 289-297.

Sprung, C.N., Cholewa, M., Usami, N., Kobayashi, K., and Crosbie, J.C. (2011). DNA damage and repair kinetics after microbeam radiation therapy emulation in living cells using monoenergetic synchrotron X-ray microbeams. Journal of Synchrotron Radiation *18*, 630-636.

Stark, J.M., Pierce, A.J., Oh, J., Pastink, A., and Jasin, M. (2004). Genetic steps of mammalian homologous repair with distinct mutagenic consequences. Molecular and Cellular Biology *24*, 9305-9316.

Stewart, G.S. (2009). Solving the RIDDLE of 53BP1 recruitment to sites of damage. Cell Cycle *8*, 1532-1538.

Stewart, G.S., Wang, B., Bignell, C.R., Taylor, A.M.R., and Elledge, S.J. (2003). MDC1 is a mediator of the mammalian DNA damage checkpoint. Nature *421*, 961-966.

Stiff, T., Walker, S.A., Cerosaletti, K., Goodarzi, A.A., Petermann, E., Concannon, P., O'Driscoll, M., and Jeggo, P.A. (2006). ATR-dependent phosphorylation and activation of ATM in response to UV treatment or replication fork stalling. EMBO Journal *25*, 5775-5782.

Strohhofer, C., Forster, T., Chorvat, D., Kasak, P., Lacik, I., Koukaki, M., Karamanou, S., and Economou, A. (2011). Quantitative analysis of energy transfer between fluorescent proteins in CFP-GBP-YFP and its response to Ca2+. Physical Chemistry Chemical Physics *13*, 17852-17863.

Strydom, W., Parker, W., and Olivares, M. (2005). Electron beams: physical and clinical aspects. Podgorsak EB (edn) Radiation oncology physics: a handbook for teachers and students International Atomic Energy Agency (IAEA), Vienna, 273-299.

Stucki, M., and Jackson, S.P. (2006). gammaH2AX and MDC1: anchoring the DNA-damage-response machinery to broken chromosomes. DNA Repair (Amst) *5*, 534-543.

Sun, Y., Jiang, X., Chen, S., Fernandes, N., and Price, B.D. (2005). A role for the Tip60 histone acetyltransferase in the acetylation and activation of ATM. Proceedings of the National Academy of Sciences of the United States of America *102*, 13182-13187.

Sutherland, B.M., Bennett, P.V., Sidorkina, O., and Laval, J. (2000). Clustered DNA damages induced in isolated DNA and in human cells by low doses of ionizing radiation. Proceedings of the National Academy of Sciences of the United States of America *97*, 103-108.

Sutherland, B.M., Bennett, P.V., Sutherland, J.C., and Laval, J. (2002). Clustered DNA damages induced by X rays in human cells. Radiation Research *157*, 611-616.

Takata, M., Sasaki, M.S., Tachiiri, S., Fukushima, T., Sonoda, E., Schild, D., Thompson, L.H., and Takeda, S. (2001). Chromosome instability and defective recombinational repair in knockout mutants of the five Rad51 paralogs. Molecular and Cellular Biology *21*, 2858-2866.

Takeda, S., Nakamura, K., Taniguchi, Y., and Paull, T.T. (2007). Ctp1/CtIP and the MRN complex collaborate in the initial steps of homologous recombination. Molecular Cell *28*, 351-352.

Tambini, C.E., Spink, K.G., Ross, C.J., Hill, M.A., and Thacker, J. (2010). The importance of XRCC2 in RAD51-related DNA damage repair. DNA Repair *9*, 517-525.

Tanaka, K., Kagawa, W., Kinebuchi, T., Kurumizaka, H., and Miyagawa, K. (2002). Human Rad54B is a double-stranded DNA-dependent ATPase and has biochemical properties different from its structural homolog in yeast, Tid1/Rdh54. Nucleic Acids Research *30*, 1346-1353.

Tavecchio, M., Munck, J.M., Cano, C., Newell, D.R., and Curtin, N.J. (2012). Further characterisation of the cellular activity of the DNA-PK inhibitor, NU7441, reveals potential cross-talk with homologous recombination. Cancer Chemotherapy and Pharmacology *69*, 155-164.

Teo, S.H., and Jackson, S.P. (2000). Lif1p targets the DNA ligase Lig4p to sites of DNA double-strand breaks. Current Biology *10*, 165-168.

Thompson, L.H. (2012). Recognition, signaling, and repair of DNA double-strand breaks produced by ionizing radiation in mammalian cells: The molecular choreography. Mutation Research-Reviews in Mutation Research *751*, 158-246.

Tirlapur, U.K., Konig, K., Peuckert, C., Krieg, R., and Halbhuber, K.J. (2001). Femtosecond near-infrared laser pulses elicit generation of reactive oxygen species in mammalian cells leading to apoptosis-like death. Experimental Cell Research *263*, 88-97.

Tobias, F., Durante, M., Taucher-Scholz, G., and Jakob, B. (2010). Spatiotemporal analysis of DNA repair using charged particle radiation. Mutation Research *704*, 54-60.

Uematsu, N., Weterings, E., Yano, K., Morotomi-Yano, K., Jakob, B., Taucher-Scholz, G., Mari, P.O., van Gent, D.C., Chen, B.P.C., and Chen, D.J. (2007). Autophosphorylation of DNA-PKCS regulates its dynamics at DNA double-strand breaks. Journal of Cell Biology *177*, 219-229.

van Gent, D.C., and van der Burg, M. (2007). Non-homologous end-joining, a sticky affair. Oncogene *26*, 7731-7740.

van Veelen, L.R., Essers, J., van de Rakt, M.W.M.M., Odijk, H., Pastink, A., Zdzienicka, M.Z., Paulusma, C.C., and Kanaar, R. (2005). Ionizing radiation-induced foci formation of mammalian Rad51 and Rad54 depends on the Rad51 paralogs, but not on Rad52. Mutation Research-Fundamental and Molecular Mechanisms of Mutagenesis *574*, 34-49.

Vojnovic, B. (1984). A Sensitive Single-Pulse Beam Charge Monitor for Use with Charged-Particle Accelerators. Radiation Physics and Chemistry *24*, 517-522.

Vojnovic, B. (1987). Sensitive Long Pulse Beam Charge Monitor for Use with Charged-Particle Accelerators. Radiation Physics and Chemistry *29*, 409-413.

Vojnovic, B. (2011a), Development of the Gray Institute single pulse electron linear accelerator Pt 1 http://users.ox.ac.uk/~atdgroup/radiation_linac.shtml, 27/01, 2014

Vojnovic, B. (2011b), Development of the Gray Institute single pulse electron linear accelerator Pt 2 http://users.ox.ac.uk/~atdgroup/radiation_linac.shtml, 27/01, 2014

Vojnovic, B., Barber, P.R., and Newman, R.G. (2011a), A four position motorised optical path selector http://users.ox.ac.uk/~atdgroup/optical_microscopy.shtml, 27/01, 2014

Vojnovic, B., and Newman, R.G. (2007), Metering systems to determine excitation intensities in fluorescence microscopy http://users.ox.ac.uk/~atdgroup/optical_microscopy.shtml, 27/01, 2014

Vojnovic, B., and Newman, R.G. (2010), DC Motor-Encoder Position Servo Controller http://users.ox.ac.uk/~atdgroup/technicalnotes/, 27/01, 2014

Vojnovic, B., Newman, R.G., Tullis, I.D.C., and Martins, C.D. (2011b), A Magnetic Pick-up And Release System For Moving Lightweight Samples http://users.ox.ac.uk/~atdgroup/radiation_linac.shtml, 27/01, 2014

Vojnovic, B., Tullis, I.D.C., and Barber, P.R. (2008), An inverted fluorescence microscope assembly http://users.ox.ac.uk/~atdgroup/optical_microscopy.shtml, 27/01, 2014

Vojnovic, B., Tullis, I.D.C., Newman, R.G., and Prentice, J. (2012), TE300 incubator enclosure http://users.ox.ac.uk/~atdgroup/optical_microscopy.shtml, 28/01, 2014

Walker, J.R., Corpina, R.A., and Goldberg, J. (2001). Structure of the Ku heterodimer bound to DNA and its implications for double-strand break repair. Nature *412*, 607-614.

Wang, B., Matsuoka, S., Carpenter, P.B., and Elledge, S.J. (2002). 53BP1, a mediator of the DNA damage checkpoint. Science *298*, 1435-1438.

Wang, C., and Lees-Miller, S.P. (2013). Detection and repair of ionizing radiation-induced DNA double strand breaks: new developments in nonhomologous end joining. International Journal of Radiation Oncology Biology Physics *86*, 440-449.

Wang, Z.Q., Auer, B., Stingl, L., Berghammer, H., Haidacher, D., Schweiger, M., and Wagner, E.F. (1995). Mice Lacking Adprt and Poly(Adp-Ribosyl)Ation Develop Normally but Are Susceptible to Skin-Disease. Genes & Development *9*, 509-520.

Ward, I.M., and Chen, J.J. (2001). Histone H2AX is phosphorylated in an ATR-dependent manner in response to replicational stress. Journal of Biological Chemistry *276*, 47759-47762.

Ward, I.M., Minn, K., Jorda, K.G., and Chen, J.J. (2003). Accumulation of checkpoint protein 53BP1 at DNA breaks involves its binding to phosphorylated histone H2AX. Journal of Biological Chemistry *278*, 19579-19582.

Watson, J.D., and Crick, F.H. (1953). Molecular structure of nucleic acids. Nature *171*, 737-738.

West, S.C. (2003). Molecular views of recombination proteins and their control. Nature Reviews Molecular Cell Biology *4*, 435-445.

Weterings, E., and Chen, D.J. (2008). The endless tale of non-homologous end-joining. Cell Research *18*, 114-124.

Weterings, E., and van Gent, D.C. (2004). The mechanism of non-homologous end-joining: a synopsis of synapsis. DNA Repair *3*, 1425-1435.

Weterings, E., Verkaik, N.S., Bruggenwirth, H.T., Hoeijmakers, J.H.J., and van Gent, D.C. (2003). The role of DNA dependent protein kinase in synapsis of DNA ends. Nucleic Acids Research *31*, 7238-7246.

White, D.E., Negorev, D., Peng, H.Z., Ivanov, A.V., Maul, G.G., and Rauscher, F.J. (2006). KAP1, a novel substrate for PIKK family members, colocalizes with numerous damage response factors at DNA lesions. Cancer Research *66*, 11594-11599.

Wiese, C., Dray, E., Groesser, T., Filippo, J.S., Shi, I., Collins, D.W., Tsai, M.S., Williams, G.J., Rydberg, B., Sung, P., and Schild, D. (2007). Promotion of homologous recombination and genomic stability by RAD51AP1 via RAD51 recombinase enhancement. Molecular Cell *28*, 482-490.

Will, O., Gocke, E., Eckert, I., Schulz, I., Pflaum, M., Mahler, H.C., and Epe, B. (1999). Oxidative DNA damage and mutations induced by a polar photosensitizer, Ro19-8022. Mutation Research *435*, 89-101.

Wilson, P.F., Hinz, J.M., Urbin, S.S., Nham, P.B., and Thompson, L.H. (2010). Influence of homologous recombinational repair on cell survival and chromosomal aberration induction during the cell cycle in gamma-irradiated CHO cells. DNA Repair *9*, 737-744.

Wiseman, H., and Halliwell, B. (1996). Damage to DNA by reactive oxygen and nitrogen species: role in inflammatory disease and progression to cancer. Biochemical Journal *313 (Pt 1)*, 17-29.

Wold, M.S. (1997). Replication protein A: A heterotrimeric, single-stranded DNA-binding protein required for eukaryotic DNA metabolism. Annual Review of Biochemistry *66*, 61-92.

Woodbine, L., Gennery, A.R., and Jeggo, P.A. (2014). The clinical impact of deficiency in DNA non-homologous end-joining. DNA Repair.

Woodhouse, B.C., and Dianov, G.L. (2008). Poly ADP-ribose polymerase-1: An international molecule of mystery. DNA Repair *7*, 1077-1086.

Wu, L., and Hickson, I.D. (2003). The Bloom's syndrome helicase suppresses crossing over during homologous recombination. Nature *426*, 870-874.

Wyman, C., Ristic, D., and Kanaar, R. (2004). Homologous recombination-mediated double-strand break repair. DNA Repair *3*, 827-833.

Xie, A.Y., Kwok, A., and Scully, R. (2009). Role of mammalian Mre11 in classical and alternative nonhomologous end joining. Nature Structural & Molecular Biology *16*, 814-U831.

Yaneva, M., Kowalewski, T., and Lieber, M.R. (1997). Interaction of DNA-dependent protein kinase with DNA and with Ku: biochemical and atomic-force microscopy studies. EMBO Journal *16*, 5098-5112.

Yoo, H.Y., Kumagai, A., Shevchenko, A., Shevchenko, A., and Dunphy, W.G. (2007). Ataxia-telangiectasia mutated (ATM)-dependent activation of ATR occurs through phosphorylation of TopBP1 by ATM. Journal of Biological Chemistry *282*, 17501-17506.

Yoo, S., and Dynan, W.S. (1999). Geometry of a complex formed by double strand break repair proteins at a single DNA end: recruitment of DNA-PKcs induces inward translocation of Ku protein. Nucleic Acids Research *27*, 4679-4686.

You, Z., Shi, L.Z., Zhu, Q., Wu, P., Zhang, Y.-W., Basilio, A., Tonnu, N., Verma, I.M., Berns, M.W., and Hunter, T. (2009). CtIP links DNA double-strand break sensing to resection. Molecular Cell *36*, 954-969.

Yuan, S.S.F., Lee, S.Y., Chen, G., Song, M.H., Tomlinson, G.E., and Lee, E.Y.H.P. (1999). BRCA2 is required for ionizing radiation-induced assembly of rad51 complex in vivo. Cancer Research *59*, 3547-3551.

Yun, M.H., and Hiom, K. (2009). CtIP-BRCA1 modulates the choice of DNA double-strand-break repair pathway throughout the cell cycle. Nature *459*, 460-U184.

Zhao, Y., Thomas, H.D., Batey, M.A., Cowell, I.G., Richardson, C.J., Griffin, R.J., Calvert, A.H., Newell, D.R., Smith, G.C., and Curtin, N.J. (2006). Preclinical evaluation of a potent novel DNA-dependent protein kinase inhibitor NU7441. Cancer Research *66*, 5354-5362.

Zimek, Z. (1978). A single-pulse toroidal coil beam-charge monitor. Radiation Physics and Chemistry (1977) *11*, 179-181.

Zimmermann, M., Lottersberger, F., Buonomo, S.B., Sfeir, A., and de Lange, T. (2013). 53BP1 Regulates DSB Repair Using Rif1 to Control 5 ' End Resection. Science *339*, 700-704.

Ziv, Y., Bielopolski, D., Galanty, Y., Lukas, C., Taya, Y., Schultz, D.C., Lukas, J., Bekker-Jensen, S., Bartek, J., and Shiloh, Y. (2006). Chromatin relaxation in response to DNA double-strand breaks is modulated by a novel ATM and KAP-1 dependent pathway. Nature Cell Biology *8*, 870-U142.

Zou, L., and Elledge, S.J. (2003). Sensing DNA damage through ATRIP recognition of RPA-ssDNA complexes. Science *300*, 1542-1548.

Zou, L., Liu, D., and Elledge, S.J. (2003). Replication protein A-mediated recruitment and activation of Rad17 complexes. Proceedings of the National Academy of Sciences of the United States of America *100*, 13827-13832.

Appendix

A1 Photon budget calculations

A1.1 Excitation intensity

Excitation was performed with a measured power of 318 μW across the 130 x 130 μm field of view. This field of view is equal to 16900 μm^2 or 1.69 x 10^{-4} cm^2. This represents a power density of 1.88165 W/cm^2.

Excitation is performed at ~ 500 nm. The photon energy, E, is $E = hc/\lambda$, where:

h is Planck's constant = 6.626 x 10^{-34} J.s

c is the speed of light = 2.98 x 10^8 m/s

λ is the photon's wavelength = 500 x 10^{-9} m.

The photon energy is thus 3.95 x 10^{-19} J and the excitation is 4.76 x 10^{18} photons/sec/cm^2.

A1.2 Imaging collection efficiency and microscope losses

The imaging objective used had a numerical aperture of 0.9. Since the fluorophores emit isotropically, only a fraction of the light is collected. The half angle (θ/2) of collection is 64.158 degrees and the collected fraction is determined by: -1/2 (cos (θ/2) -1). The fraction of light collected is 28.2%. This collected light is further attenuated by the microscope dichroic filter, by the emission filter, by three mirrors and inevitable reflections from refractive optical surfaces. The total transmission, obtained from the filter spectra, mirror reflection efficiencies and anti-reflection coatings is calculated to be ~58%. The percentage of isotropic light impinging on the imager is thus ~16.4%.

A1.3 Imager quantum efficiency and conversion factors

The quantum efficiency of the sCMOS imager at 542 nm is 0.60. The output of the imager is presented in terms of analogue-to-digital converter units (ADUs). Each ADU corresponds to a certain number of photoelectrons. The imager was calibrated under the most commonly used operating setting (x8 gain, 2x2 pixel binning) to be 0.57 photoelectrons per ADU. The photon number per ADU is thus ~ 0.95 photons. The calibration was performed as follows. At each intensity level an image was acquired and analysed for mean and standard deviation as shown below:

I: *mean focus intensity in analogue to digital units (ADU)*
B: *mean black level intensity in ADU*
A: *photoelectrons per ADU, 0.57*
QE: *detector quantum efficiency, 0.60*

$$Photon\ no = (I - B) \times A\ /\ QE \qquad \textbf{A.1}$$

The term A in **equation A.1** was determined by evenly illuminating the camera CMOS chip with a highly diffused 525 nm LED over a range of intensity levels. The value was of A was determined from these values based on Poisson statistics (Janesick *et al.*, 1987). The value of 0.57 refers to operating the camera at a nominal gain of 8, and 2 x 2 binning, the same conditions used during experiments. QE was obtained from the ORCA Flash 2.8 datasheet. I and B were determined from image analysis.

A1.4 Fluorescence yields

The fluorescence yield F is given by:

F = σ x Q x I, where

σ = fluorophore (YFP) molecular cross-section = 4.5 x 10^{-16} cm^2 (Strohhofer *et al.*, 2011)

Q = fluorophore (YFP) quantum yield = 0.6 (Seefeldt *et al.*, 2008)

I = Excitation (calculated above) = 4.76 x 10^{18} photons/sec/cm^2

F = 4.5 x 10^{-16} cm^2 x 0.6 x 4.76 x 10^{18} photons/sec/cm^2 = 1285.2 photons/sec/molecule

This yield is attenuated by the microscope losses, calculated above, and our imager thus receives only 210.8 photons/sec/molecule. The exposure time used was 115 ms, and thus every fluorescing molecule yields 24.24 photons in a single exposure. Since the photon number per ADU (calculated above) is ~ 0.95 photons/ADU, the imager outputs 25.52 ADUs per molecule.

A2 TRI2 automated foci analysis

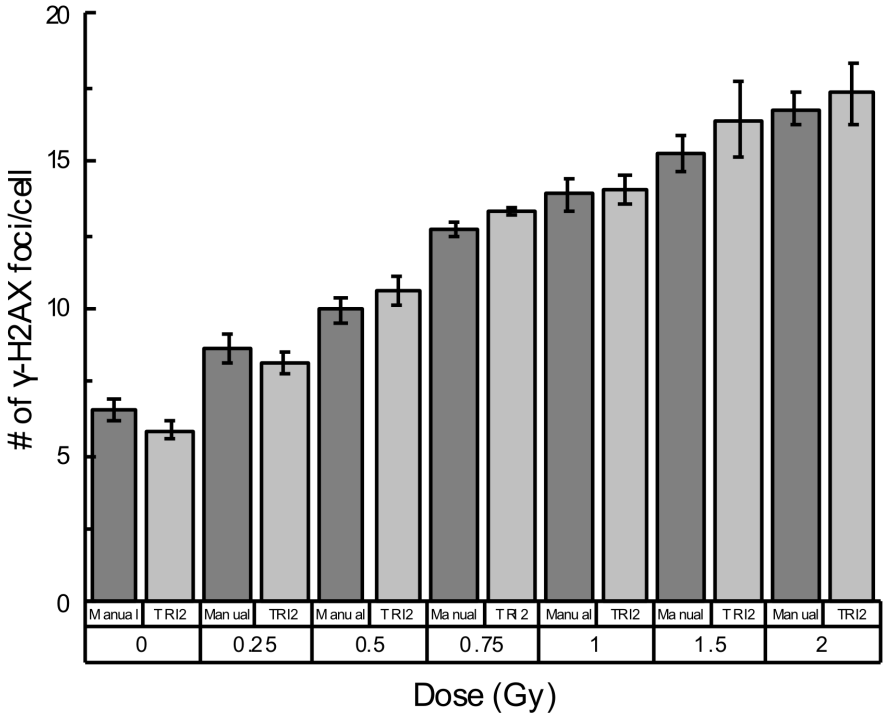


Figure A2.1 Comparison between manual and automated γ-H2AX foci count. V79-4 cells were irradiated with different doses using a ^{137}Cs source and fixed 30 min after irradiation. The number of foci per cell was counted manually and in an automated fashion using TRI2. This software uses an algorithm based on Compact Hough and Radial Map (CHARM) method for foci counting. Centres are detected with diameters of up to ~ 2.2 μm with a minimum distance of 0.2 μm between detected centres being required to distinguish individual foci. Overlapping foci by 30% or more are processed based on a shape processing criteria so that only the most intense focus is considered. The intensity of the focus is not considered as a criterion; however the image signal-to-noise ratio is important for edge detection (Barber *et al.,* 2007). The error bars represent the s.e.m. (n = 3 independent experiments).

A3 List of publications

Barber, P., Tullis, I., Rowley, M., **Martins, C.**, Weitsman, G., Lawler, K., Coffey, M., Woodman, N., Gillett, C., and Ng, T. (2014). The Gray Institute Open Microscopes applied to radiobiology and protein interaction studies. Paper presented at: SPIE BiOS (International Society for Optics and Photonics).

Stauffer, P.R., Craciunescu, O.I., Maccarini, P.F., Wyatt, C., Arunachalam, K., Arabe, O., Stakhursky, V., Soher, B., MacFall, J.R., Li, Z., Joines, W.T., Rangarao, S., Cheng, K.S., Das, S.K., **Martins, C.D.**, Charles, C., Dewhirst, M.W., Wong, T., Jones, E., and Vujaskovic, Z. (2009). Clinical Utility of Magnetic Resonance Thermal Imaging (MRTI) For Realtime Guidance of Deep Hyperthermia. Energy-Based Treatment of Tissue and Assessment V *7181*.

Martins, C. D., Tullis, I., Newman, R., Barber, P., Asaithamby, A., O'Neill, P., and Vojnovic, B. Broadcasting protein recruitment at sites of DNA damage shortly following microsecond-pulsed electron irradiation. (Manuscript to be submitted to *Nature Biotechnology*)